Printed Electromechanical Sensors

Michael R. Crump

A dissertation

Submitted in partial fulfillment of the

requirements for the degree of

Doctor of Philosophy

University of Washington

2022

Reading Committee:

John D. MacKenzie, Chair

Dwayne Arola

Guozhong Cao

Program Authorized to Offer Degree:

Materials Science and Engineering

University of Washington

Abstract

Printed Electromechanical Sensors

Michael R. Crump

Chair of the Supervisory Committee:

J. Devin MacKenzie

Department of Materials Science and Engineering

Printed electronics refers to the additive manufacture of devices with single or multiple functionalities via the deposition of inks onto flexible or deformable surfaces. This dissertation aims to utilize functional, printable materials to fabricate and characterize electromechanical sensors, which transduce a mechanical input signal to an electrical output signal. Piezoresistive-based strain sensors operating a low-frequency regime (<1 Hz) for medical simulation applications and piezoelectric-based vibration sensors operating in a high-frequency regime (> 1 Hz) for structural health monitoring applications are both described in this thesis. Monolithically integrated piezoresistive sensors can be used to quantify large deformations in lifelike tissue models. The demonstration of 3D printing of an ionogel as a stretchable, piezoresistive strain sensor embedded in an elastomer is presented as a proof-of-concept of this integrated fabrication. Subsequently, a novel class of inexpensive, conductive, non-toxic, and 3D-printable organogels was synthesized and implemented as the piezoresistive medium.

Piezoelectrics transduce electromechanical inputs and outputs for a variety of applications in sensing, actuation, and energy harvesting. The high processing temperatures, brittle mechanical properties, and toxic metal composition of high-performing piezoelectrics, such as lead zirconate titanate (PZT)-based materials, limit rapid and scalable fabrication of thin, flexible electromechanical devices. A growing class of piezoelectric materials, hybrid inorganic-organic multiaxial molecular ferroelectrics, combine a promising piezoelectric performance with solution processability. All-additively manufactured piezoelectric vibration sensors with two different molecular ferroelectric compositions were fabricated and characterized for the first time. Furthermore, powders of these materials were synthesized via ball-milling, a solvent-free and scalable synthetic approach, for the first time. The electrode material, poling conditions, humidity, and piezoelectric testing conditions affected the piezoelectric response of pressed polycrystalline samples, highlighting the need for this growing field to improve transparency of experimental methods.

Table of Contents

List of Figures

List of Tables

Chapter 1. Introduction

1.1. Motivation

Printed electronics refers to the additive manufacture of devices with single or multiple functionalities (electromechanical transduction, photovoltaic conversion, electrochemical storage, etc.) via the deposition of inks onto flexible or deformable surfaces. The inherently additive nature of printed electronics reduces material waste and overhead compared to subtractive manufacturing processes (lithography, machining, etc.), capacitates application- and person-specific customizability that accelerates product integration, and enables rapid, scalable fabrication of functional devices. Printing techniques compatible with high-throughput roll-to-roll (R2R) processing include slot-die coating [1], gravure printing [2] , and flexographic printing [3], among others [4–6]; those that allow for rapid customizability include inkjet printing [7, 8] and 3D printing [9, 10]. Many of these fabrication techniques are accessible through the Washington Clean Energy Testbeds. The steady development of novel organic [11, 12] and nanoscale materials [13–15] has underpinned the expanding plethora of printable functional materials. The scope of this thesis will focus on the fabrication and characterization of electromechanical sensors utilizing novel printable functional materials.

Electromechanical sensors transduce a mechanical input signal (strains, stresses, or torques) to an electrical output signal (voltage, current). The electromechanical transduction of strains and vibrations provides essential information regarding the health and status of structures and components across a wide range of industries, such as medicine, transportation, aerospace, and construction. For example, after the 2007 collapse of the I-35W bridge spanning the Mississippi River in Minneapolis, MN [16], the replacement bridge was equipped with a variety of strain and vibration sensors, making it one of the first “smart bridges” constructed in the U.S.

[17–19]. Mechanical strain sensing can be bifurcated into a high-frequency regime (> 1 Hz) and a low-frequency regime (< 1 Hz) depending on the specific sensing application. Structural health monitoring sensors rely on the piezoelectric to detect vibrations reflective of various bending modes with characteristic frequencies; shifts in these frequencies can reflect degradation within a structure [20–22]. Accordingly, one major thrust in my thesis has focused on the development of all-printed, low-temperature, high-throughput manufacture of piezoelectric vibration sensors for applications in structural health monitoring. In contrast, the low-frequency regime can be utilized for large strains regularly encountered in medicine [23]; accordingly, the other major thrust of my thesis will focus on the development of 3D-printed stretchable strain sensors for applications in medical education and simulation.

1.2. Organization

This dissertation includes two chapters regarding piezoresistive strain sensors and two chapters regarding printed piezoelectric sensors. Chapter 2 describes the fabrication and mechanical characterization of a 3D printable conductive ionogel embedded in an elastomeric matrix as a stretchable strain sensor. The content of Chapter 2 was published by Crump et al. in 2019 [24]. Chapter 3 describes a novel class of conductive organogels utilized as the piezoresistive medium in stretchable strain sensors, including a demonstration of monolithically integrated sensors in a realistic suture training pad. The content of Chapter 3 was published by Crump et al. in 2021 [25]. Chapter 4 describes all-printed piezoelectric vibration sensors that combine inkjet-printed interdigitated electrodes and a slot-die coated piezoelectric layer based on a manganese-based, inorganic-organic hybrid material. Chapter 5 expands on the concepts presented in Chapter 4 to iron-based, inorganic-organic hybrid materials.

Chapter 2. Ionogel Strain Sensors

2.1. Motivation

Over one third of the 700,000 deaths that occur in U.S. hospitals annually can be attributed to medical error [26], indicating a strong need for improved medical education. Reducing patient death and unforeseen complications from medical error in the operating room have driven the need for surgical simulation technologies for medical students and practitioners [27, 28]. The two-dimensional limitation of MRIs, CT scans, and other visual aids inspired the development of graspable, patient-specific 3D-printed anatomical models [29]. Many medical fields, such as cardiology [30, 31], orthopedics [32–36], radiology [37, 38], urology [39–41], plastic surgery [42, 43], and neurology [44–46] have begun adopting 3D printing to enable the fabrication of models with customizable geometries. Initial capabilities, however, were limited to rigid plastic replicas with significantly different mechanical and optical properties than those of the modeled organ [47–49]. This disparity limits the sense of realism in surgical rehearsal [47]. The wide range of currently available additive manufacturing techniques [50], such as fused deposition modeling (FDM), stereolithography (SLA), powder bed fusion, and inkjet printing, have expanded the range of printable materials from plastics [51] to metals [52], ceramics [53], composites [54], and biomaterials [55, 56]. In turn, these developments have inspired the fabrication of 3D-printed customized organs with realistic mechanical, anatomical, and optical properties; the most recent generation of 3D-printed organs include integrated functionalities, such as electronics or sensors [57, 58]. For example, Qiu *et al.* 3D-printed a prostate model generated from patient-specific MRI scans with high-fidelity mechanical and optical properties via direct-writing assembly [58]. In this study, silicones were selected to mimic tactile sensation and deformability of the prostate due to their tunable viscoelastic properties, biocompatibility, and adoptability to additive manufacturing

techniques [58, 59]. Additionally, a separately 3D-printed hydrogel pressure sensor was attached to the prostate model to quantify the applied force [58], which would provide objective feedback for the evaluation of trainee competency [60].

The next milestone development is seamless, monolithic fabrication of lifelike tissue models containing co-printed sensors with variable geometries and orientations within the model. Not only does this elegant fabrication strategy reduce the number of post-processing steps, but also it allows for precise and reproducible placement of a sensing element with geometries customized to the individual patient. The ubiquity of tissue deformation in medical examination and treatment suggests a co-printed, integrated strain sensor could be implemented widely in educational and pre-procedural simulation models. Most hollow viscus [61–63] (i.e. stomach, intestine, urinary bladder, vagina, etc.) and dermal [64–66] (i.e. skin) tissue possess a strain failure limit up to 300% tensile strain [67], so a conformable elastic stretchable strain sensor with reliable readings above 300% strain would be required for these applications.

2.2. Background

2.2.1. Definitions and Theory

Strain sensors can measure changes in the resistance of a conductive element (piezoresistive) or capacitance of a dielectric element (piezocapacitive) in response to strain [23]. Key performance metrics include the strain range, sensitivity (gauge factor), and degree of hysteresis (drift). The gauge factor of a strain sensor is defined as the relative change in electrical signal ($\Delta R/R_o$ or $\Delta C/C_o$) to strain (ε) [23]:

$$GF = \left(\frac{\frac{\Delta R}{R_O}}{\varepsilon}\right) \text{ (piezoresistive)} \qquad (1a)$$

$$GF = \left(\frac{\frac{\Delta C}{C_o}}{\varepsilon}\right) \text{ (piezocapacitive)} \qquad (1b)$$

The following sub-sections compare piezocapacitive to piezoresistive strain sensors and justify the selection of a piezoresistive strain sensor.

2.2.1.1. Piezocapacitive Strain Sensors

Piezocapacitive strain sensors measure a change in capacitance in response to strain. The gauge factor (GF) of a capacitive sensor is defined as the relative change in capacitance ($\Delta C/C_1$) to strain (ε):

$$GF = \frac{\Delta C}{\varepsilon C_1} \qquad (2a)$$

The following derivation of the theoretical gauge factor of a piezocapacitive strain sensor with the geometry of a parallel-plate capacitor has been reproduced below [23, 68]:

Assume a parallel-plate piezocapacitive structure consisting of a dielectric elastomer with an initial length x_1, width y_1, and a thickness z_1 sandwiched between two planar electrodes. The initial capacitance C_1 can be defined in terms of the permittivity of free space (e_o), the permittivity of the elastomer (e_r), and the initial geometry of the structure:

$$C_1 = e_o e_r\left(\frac{x_1 y_1}{z_1}\right) \qquad (2b)$$

If the sample is stretched uniaxially in the x-direction, the strain and new geometry of the capacitor (x_2, y_2, z_2) can be predicted by Poisson contraction:

$$\epsilon_x = \frac{\Delta x}{x} \quad (2c)$$

$$\epsilon_y = \varepsilon_z = \nu\varepsilon_x \quad (2d)$$

$$x_2 = x_1 + \Delta x = x_1 + \varepsilon_x x_1 \quad (2e)$$

$$y_2 = y_1 - \Delta y = y_1 - \nu\varepsilon_x y_1 \quad (2f)$$

$$z_2 = z_1 - \Delta z = z_1 - \nu\varepsilon_x z_1 \quad (2g)$$

where ν is Poisson's ratio. Upon stretching, the new capacitance is defined as:

$$C_2 = e_o e_r \left(\frac{x_2 y_2}{z_2}\right) = \frac{e_o e_r (x_1(1+\varepsilon_x) y_1(1-\nu\varepsilon_x))}{z_1(1-\nu\varepsilon_x)} = C_1(1+\varepsilon_x) \quad (2h)$$

The change in capacitance (ΔC) is defined as

$$\Delta C = C_2 - C_1 = C_1(1+\varepsilon_x) - C_1 = C_1\varepsilon_x \quad (2i)$$

Combining Equations 2a (where $\varepsilon = \varepsilon_x$) and 2i:

$$GF = \frac{C_1\varepsilon_x}{C_1\varepsilon_x} = 1 \quad (2j)$$

(Table 2-1) compares the gauge factor of stretchable piezocapacitive sensors from several recent works:

Table 2-1: Performance Comparison of Stretchable Piezocapacitive Sensors

Reference (Year; number of citations*)	Sensor Materials	Maximum Strain (%)	Gauge Factor
[68] (2012, 208)	CNTs / silicone	100%	0.99
[69] (2012, 573)	Ag NWs / silicone	80%	1
[70] (2013; 230)	Silver nanowires (Ag NWs) / silicone	300%	0.97
[71] (2014; 49)	Carbon Nanotubes (CNTs) / silicone	150%	1
[72] (2014, 341)	Ag NWs / silicone	50%	0.7
[73] (2015, 97)	Ionic Liquid / silicone	250%	0.35
[74] (2017, 25)	Silver-plated fabric / silicone	150%	1.23
[75] (2017, 12)	Graphene / silicone + fabric	250%	0.54-1.17
[76] (2017, 10)	Carbon black / silicone	500%	0.83-0.98
[77] (2018, 3)	Gold / adhesive elastomer (VHB)	140%	3.05

[78] (2019, 0)	Anisotropic conductive film electrodes / hydrogel	1000%	3 (0-200% strain);165 (200-1,000% strain)

*The number of citations according to the Web of Science database as of 5/9/2019

Before 2017, the gauge factor of stretchable piezocapacitive sensors did not exceed the theoretical gauge factor of 1 because these sensors utilized a parallel plate structure where the total electrode area remained constant. However, two works published in July 2017 reported sensors with gauge factors slightly surpassing unity by utilizing fabric-based substrates [75] or electrodes [74] that increased the electrode surface area in response to strain. This concept was extended further by assembling piezocapacitive sensors with out-of-plane, wrinkled gold electrodes, which pushed the peak gauge factor to 3.05 [77]. The out-of-plane, accordion-like structure of these electrodes reduced lateral contraction in response to strain, resulting in an increased electrode surface area. We note the maximum strain of all 3 works falls short of the 300% minimum strain desired for tissue models, and the reported fabrication procedures are not compatible with a monolithic 3D-printing process.

A recent communication reported higher gauge factors of 3 (0-200% strain) and 165 (200-1,000% strain) by measuring the relative change in capacitive reactance (AC mode) of a hydrogel-based piezocapacitive sensor [78]. Although this intriguing result suggests piezocapacitive sensors can achieve sensitivities comparable to piezoresistive sensors [23, 79], the underlying mechanism behind the increased gauge factor was not elucidated. In addition, significant work is required to improve sensor reliability; only 300 cycles between 50% and 150% strain were achieved before sensor failure [78].

Despite this recent progress in sensitivity, piezocapacitive strain sensors are susceptible to stray capacitive interference arising from human interactions, which can introduce false sensor responses [23, 70, 72, 80] and therefore introduce inaccuracies to medical simulation exercises. Because these exercises necessitate frequent human proximity to tissue models with embedded sensors, we were motivated to develop a piezoresistive sensor that would bypass this problem. In addition, a piezoresistive sensor requires only a single conductive trace to function, while a piezocapacitive sensor requires at least two conductive traces. Therefore, the incorporation of a piezoresistive sensor would simplify the fabrication process and limit the footprint of the sensor embedded in a tissue model.

2.2.1.2. Piezoresistive Strain Sensors

Piezoresistive strain sensors measure a change in resistance in response to deformation. The following text provides a derivation of the gauge factor of piezoresistive sensors adapted from ref. [81]:

Assume the piezoresistive sensor is composed of a conductive cylinder with a fixed volume. The initial resistance (R_1) and the final resistance (R_2) of a sensor stretched from an initial length (L_1) to a final length (L_2) can be defined as:

$$R_1 = \frac{\rho_1 L_1}{A_1} \tag{3a}$$

$$R_2 = \frac{\rho_2 L_2}{A_2} \tag{3b}$$

Where ρ_1 and ρ_2 represent the resistivities before and after deformation and A_1 and A_2 represent the cross-sectional areas before and after deformation, respectively. As the volume of the conductive cylinder is assumed to be fixed, we can define the gauge factor in the following manner:

$$GF = \Delta R/R_1 \tag{3c}$$

$$\Delta R = R_2 - R_1 \tag{3d}$$

$$V = L_1A_1 = L_2A_2 = constant \tag{3e}$$

$$GF = \frac{R_2}{R_1} - 1 = \frac{\frac{\rho_2 L_2}{A_2}}{\frac{\rho_1 L_1}{A_1}} - 1 = \frac{\rho_2}{\rho_1}\left(\frac{L_2}{L_1}\right)^2 - 1$$

$$= \left(1 + \frac{\Delta\rho}{\rho_1}\right)(\varepsilon + 1)^2 - 1 = (\varepsilon^2 + 2\varepsilon) + \left(\frac{\Delta\rho}{\rho_1}\right)(\varepsilon + 1)^2 \tag{3f}$$

For a material with a constant resistivity, the last term goes to zero, meaning the gauge factor is dependent on strain quadratically ($\varepsilon^2 + 2\varepsilon$). This expression can be modified to take contact resistance (R_c) into account:

$$GF = (\varepsilon^2 + 2\varepsilon)\frac{R_1 - 2R_c}{R_1} = \beta(\varepsilon^2 + 2\varepsilon) \tag{3g}$$

where β consolidates the contact resistance correction to a single constant. For an ideal system with zero contact resistance, $\beta = 1$. The limit of β approaches zero as the contact resistance approaches infinity.

Piezoresistive mechanisms include geometrical deformation, percolation connection/disconnection, crack propagation in films, and tunneling between conductive elements [23]. Sensors utilizing the latter three mechanisms have been explored extensively due to their superior sensitivity to sensors that rely strictly on geometrical deformation, but the following section will detail the shortcomings of sensors based on these mechanisms.

2.2.2. Percolation-based strain sensors

Typical piezoresistive sensors are composites composed of conductive fillers that form a conductive network percolating through an elastomeric matrix [23, 80, 82–85]; a wide variety of fabrication approaches [23], including micro-molding techniques [86, 87] thermal drawing [88, 89], screen printing [90, 91], spray coating [80, 92, 93] and 3D printing [94], have been utilized to manufacture stretchable sensors. As the sensor elongates, the density of interconnected conductive pathways decreases, increasing the resistance [23]. However, these composites can be highly susceptible to hysteresis and drift at large strains due to permanent changes in the conductive percolation network [23, 95, 96]. In addition, competing mechanisms that diminish and restore the conductive percolation network [97–99] during deformation result in a multi-valued response. This means a single resistance value could be attributed to multiple strain values and slopes in the resistance versus strain function could be positive and negative for a single-signed mechanical strain. These issues introduce uncertainty to the interpretation of the sensor reading and complexity to the calibration and supporting readout electronics. Therefore, sensing mechanisms that rely on a distributed network of solid fillers dispersed in an insulating matrix (percolation, crack, and tunneling) are inherently flawed.

2.2.3. Fluid- and gel-based strain sensors

The inherent challenges for stretchable sensors based on mechanically bound conductive elements inspired the development of low-hysteresis strain sensors utilizing conductive liquid sensing media, such as graphene-based conductors suspended in water [100], electrolytic solutions [101–106], or ionic liquids [107, 108]. Ionic liquids, defined as molten salts with a melting point below 100 ^{o}C [109], possess a high thermal stability and nonvolatility that make them a promising stable sensing medium. Their compositional tunability allows for the adjustment of rheological and viscoelastic properties in a manner unavailable to organic solvents or aqueous media. However, the continuously flowing liquid rheology of this class of piezoresistive conductors necessitates separately defined microfluidic structures to preserve geometrical integrity. A continuously liquid rheology also prevents the direct deposition of layers over the sensing medium. A printed piezoresistive ink that can preserve its geometrical integrity during a monolithic printing process enables the construction of embedded sensors in 3D tissue models.

Deformable, non-flowing conductors include liquid metals, hydrogels, organogels, and ionogels. Liquid metals, defined as metal alloys with a melting point below room temperature [110], have shown promise as a printable conductor because sub-melting point temperature control [111, 112] or thin metal oxides that form on the liquid surface can prevent printed feature bleeding and preserve geometrical fidelity [113, 114]. For example, Yan *et al.* reported coaxial printing of the liquid metal eutectic gallium indium (EGaIn) inside of PDMS, reaching strains up to 350%. However, the high cost of EGaIn ($70.25/mL from Sigma-Aldrich) [115] have inspired the search for alternative, low-cost conductive gels. Conductive hydrogels, defined as water-swollen polymer

networks with a conductive electrolyte or filler [116], can reach high strains as large as 1,000% [117, 118] and can be 3D-printed [119–121], but the environmental instability of hydrogels [122] inspired the substitution of water with ethylene glycol and ionic liquids to form conductive organogels [123, 124] and ionogels [125–127], respectively. In this work, an ionogel and an organogel were developed for strain sensing applications.

Truby et al. [128] demonstrated embedded 3D-printing [129] of a conductive ionogel in a liquid silicone reservoir to fabricate stretchable actuators and contact sensors, but the embedded 3D-printing process is incompatible with layer-by-layer 3D printing of patient-specific PDMS tissue models. In addition, to date there are no reports of 3D-printed ionogels utilized as the sensing medium in a high-strain, low-hysteresis, piezoresistive strain sensor. Therefore, the initial objective of this research was to fabricate the first high-strain, low-hysteresis, piezoresistive strain sensors using 3D-printed conductive ionogels as the sensing medium. We introduced the first stretchable strain sensor using a low-cost ($3 per mL), 3D-printed, conductive ionogel composed of reduced graphene oxide (rGO) dispersed in the ionic liquid 1-butyl-3-methylimidazolium tetrafluoroborate ([BMIM][BF_4]) [24]. Reduced graphene oxide not only served as an effective gelation agent but also boosted sensitivity through the disruption of the conductive percolation network. Strain sensor features include a high strain range of 350%, low hysteresis (degree of hysteresis <3.5% up to 300% strain), minimal baseline drift, a single-value response, and excellent fatigue stability (5,000 stretching cycles). In addition, we demonstrate the fabrication of sensors with stencil-printed silver/PDMS electrodes in place of direct wire contact to the gel to highlight the potential of large-scale, fully printed manufacture of these sensors. The compositional tunability of ionic liquids and the thixotropic nature of this class of conductive gels endows a far-

reaching combination of customized sensor geometry and performance that can be tailored to patient-specific, monolithically fabricated tissue models.

2.3. Methods

2.3.1. Ionogel Synthesis and Characterization

The conductive gel synthesis was adapted and scaled up from Zhang et al. [130] 30.0 mg of few-layer graphene oxide nanoplatelets with lateral dimensions of 300-800 nm (Cheap Tubes, Inc.) were sonicated in 100 mL deionized H_2O for 1.5 hours. 20.0 mL of [BMIM][BF_4] (98%, Sigma Aldrich) was added to the solution and mixed by hand for 5 minutes to induce flocculation. The product was dried via a roto evaporator at 90 ^oC for 4 hours. 100 μL of hydrazine (50-60%, Sigma Aldrich) was added, and the solution was stirred at 80 ^oC for 12 hours. The product was centrifuged at 9000 RPM for 2 hours, the ionic liquid supernatant was decanted, and centrifugation and supernatant decantation were repeated to form a freestanding gel.

For concentration calculations and thermogravimetric analysis (TGA) measurements, a small aliquot of gel was weighed and then vigorously washed with N,N-dimethylformamide (DMF). The mixture was centrifuged at 9000 RPM for 10 minutes, and the supernatant was discarded. This washing step was repeated with DMF once more followed by an IPA wash. The product was dried under vacuum at 70 ^oC overnight to remove trace amounts of solvent and weighed again. Approximately 0.10 mg of solid product was retrieved for TGA (Mettler-Toledo TGA/DSC 3+). The mass loss was measured from 40 ^oC to 700 ^oC at a heating rate of 5 ^oC/min in air. This scan was repeated for the graphene oxide.

Gel rheological properties were characterized with a rheometer (Anton Parr MCR302) at 20 ^oC. Parallel plates with a 25-mm diameter and 0.5 mm of separation were utilized, and the storage and loss moduli were measured over a frequency domain of 0.1 to 100 rad/s. Molecular vibrational characterization was carried out via Fourier Transform Infrared (FTIR) Spectroscopy (Nicolet iS10 FT-IR Spectrometer, ThermoFisher Scientific). Scanning electron microscopy

(SEM) characterization of the graphene oxide and reduced graphene oxide was carried out at an accelerating voltage of 5 kV (FEI XL830).

2.3.2. Sensor Fabrication

2.3.2.1. Printed Sensors

15 grams of PDMS Part B (Ecoflex 00-30, Smooth-On Inc.) were added to 15 grams of PDMS Part A and mixed via a planetary mixer (Thinky ARV-310) under vacuum in a cooling adapter (Figure S1) at 2000 RPM for 5 minutes, and the mixture was poured into a Teflon-coated machined aluminum mold with a pocket depth of 0.5 mm and a square edge length of 14.0 cm. The mixture was allowed to cure in the mold for 75 minutes at room temperature, forming a partially cured PDMS substrate for subsequent fabrication.

For printed sensors with wire contacts to the gel, lines of gel were dispensed onto the PDMS substrate (Video S1) via a pneumatic SmartPump® dispenser from a 3D printer (N-Scrypt 3Dn-300). Gel was carefully transferred to a pressure syringe feeding into a valve and nozzle (blunt-tip needle, 21G) assembly near the PDMS substrate, which was fixed to a two-axis translation stage. A pressure of 30 to 40 psi was applied to dispense gel through the nozzle, and lines with a length of 25 mm were printed at 4 mm/s with a clearance of 0.5 mm. Increasing the pressure increased the linewidth and decreased the aspect ratio of the printed gel line. After printing, the printer nozzle was used to trim any acute geometries (Figure S2). To make electrical contact with the gel, 38 AWG copper wires were carefully inserted 10 mm into the gel, and a fresh topcoat of PDMS was dispensed directly over the gel lines to encapsulate the sensors. Sensors were cured in an oven at 150 ºC for two hours and cooled to room temperature before removal from the pocket.

A silver flake/Ecoflex paste was prepared to fabricate sensors with stencil-printed electrodes. Equi-mass amounts of Ecoflex Parts A and B were mixed as described above, and then approximately 1 gram of Ecoflex was weighed. Silver flakes (1-3 μm, Metalor AC 4048) were added to the Ecoflex mixture until 86% Ag by weight was realized. The paste was mixed via mortar and pestle until a smooth, homogeneous texture had formed. An x-y blade cutter (Cameo 3) was used to cut electrode patterns (3 mm x 15 mm with a 25 mm spacing) into a 2-mil-thick polyimide stencil mask (Polyonics XF-101). The mask was carefully applied to a partially cured PDMS substrate, and silver/PDMS electrodes were stencil printed onto the PDMS substrate. After liftoff of the mask to reveal the electrodes, lines of the piezoresistive gel were 3D-printed between electrodes, and lines were encapsulated with PDMS as described above. Only part of the electrodes was covered to allow for electrical contact to external leads. Copper wire leads were attached to the exposed part of the Ag/PDMS electrodes via a conductive silver epoxy adhesive (MG Chemicals 8331) cured at 65 ^{o}C for 15 minutes followed by a drop of PDMS epoxy (Sil-Poxy, Smooth On) cured at 65 ^{o}C for 15 minutes to improve robustness.

2.3.2.2. Tube Sensors

Tube sensors were prepared by injecting either gel or ionic liquid into a stretchable commercial silicone tube (Orvis) with an inner diameter of 0.245 mm. Copper or nichrome leads were inserted carefully into each end of the tube to avoid trapping air bubbles and sealed with an epoxy (Sil-Poxy, Smooth-On) that cured fully in 15 minutes. In addition, sensors with platinum leads and with one platinum (reference electrode) and one copper (working electrode) lead were fabricated without an epoxy seal for cyclic voltammetry (CV) and constant-current measurements.

2.3.3. Sensor Characterization

2.3.3.1. DC-Mode Electromechanical Characterization

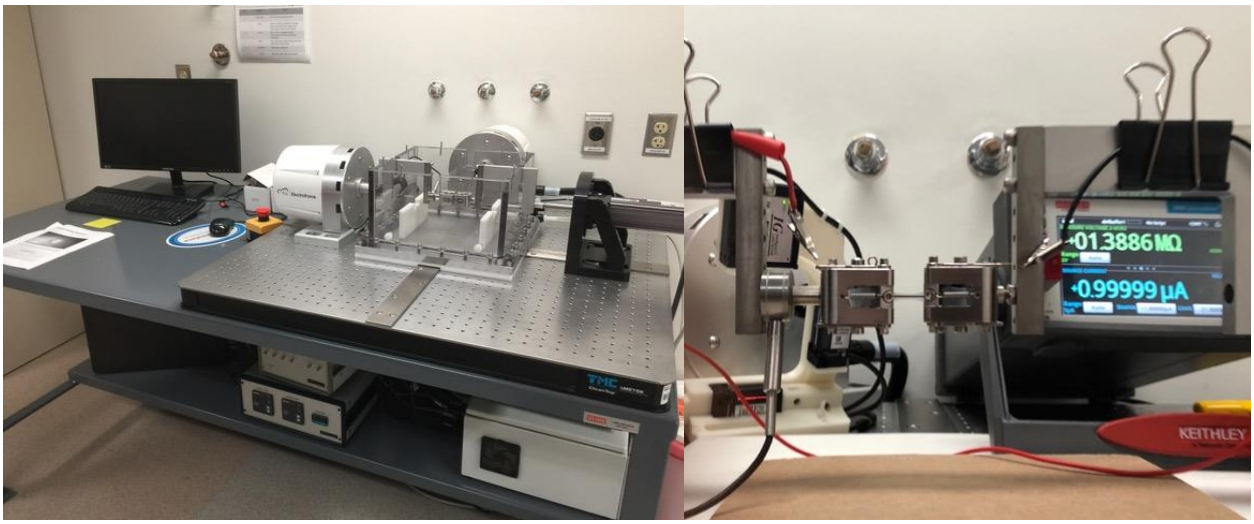

Figure 2-1. Pictures of the electromechanical characterization setup (left) and a printed ionogel sensor undergoing characterization (right).

The electromechanical characterization setup (Figure 2-1) consisted of a dynamic mechanical tester (Electroforce Testbench, TA, USA), laser micrometers (IG-028, Keyence Corp., Japan), and sourcemeter (Keithley 2450, Tektronix, USA). Sensors were cut into a dogbone shape using an ASTM D638 Type V [131, 132] cutting die. The sensors were loaded into sandpaper lined cam grips to ensure a non-slip condition. The sensors were preloaded 0.05 N, and the cross-sectional area was measured using the laser micrometers. The gage length was defined as the distance between contact points of the grips and measured using calipers. 1 µA current was forced through the sensor, and the resulting resistance reading was allowed to stabilize for 5-10 min before applying any strain. The initial resistance (R_o) was defined as the resistance of the sensor at the end of this stabilization scan.

Uniaxial mechanical testing consisted of a ramp to 400% strain at a rate of 1.0% strain/s for printed sensors and to 100% strain at the same rate for tube sensors. The stress vs. strain data

in Figure 4C was smoothed with a 5-point adjacent averaging routine. Two uniaxial dynamic mechanical tests were performed sequentially to compare the effects of amplitude and frequency. All dynamic testing included a readout stabilization period of 100 cycles to ca. 60% strain at 0.1 Hz. The initial dynamic test consisted of 10 cycles at varying amplitudes and frequencies. The test parameters were as follows: 50% strain at 0.05, 0.1, 0.2, and 0.5 Hz, 100% strain at 0.05, 0.1, 0.2, 0.5 Hz, 150% strain at 0.05, 0.1, 0.2 Hz, 200% strain at 0.05, 0.1, 0.2 Hz, 150% strain at 0.05, 0.1, 0.2 Hz, 100% strain at 0.05, 0.1, 0.2, 0.5 Hz and 50% strain at 0.05, 0.1, and 0.2 Hz. Immediately after the initial test, the second dynamic test was performed. The second dynamic test consisted of 10 cycles at 0.05 Hz with the following amplitudes: 100%, 200%, 300%, and 350% strain. Fatigue testing consisted of 5,000 stretching/releasing cycles to 100% strain at a rate of 0.2 Hz.

DC electrical characterization of the tube sensors was conducted using the same sourcemeter. 1 μA current was forced through the sensor, and the resulting resistance reading was recorded for 30 minutes.

2.3.3.2. AC-Mode Electromechanical Characterization

The electromechanical response of both tube and printed sensors were characterized using an impedance analyzer (VersaSTAT 4, Princeton Applied Research) in place of the sourcemeter in the electromechanical characterization setup. Uniaxial mechanical testing consisted of a ramp to 200% strain at a rate of 1% strain/s. An alternating square wave with an amplitude of ±2 V and a frequency of 50 Hz was applied, and the resulting current was measured at a sampling rate of 1000 Hz. Resistance vs. time results were consoiidating by taking the average resistance value of a combined positive and negative pulse (duration of 0.04 s, or a frequency of 25 Hz), and the results were synchronized manually to extrapolated strain vs. time results.

For the printed ionogel sensors, a dynamic mechanical test was carried out. This test consisted of 10 cycles at 0.05 Hz with the following amplitudes: 100%, 200%, 300%, and 400% strain.

2.3.3.3. Ionogel Cyclic Voltammetry and Constant-Current measurements

All cyclic voltammetry (CV) measurements were carried out using a PARSTAT 4000A (Princeton Applied Research). All measurements were taken from -1.5 V to 1.5 V to -1.5 V at a scan rate of 1 mV/s.

Constant current measurements were carried out for tube sensors with Cu (working) / Pt (counter) electrodes. Resistance was measured in response to a constant current of 1 μA applied for 6 hours. Subsequently, electrodes were removed, gently rinsed with dimethylformamide (DMF) and methanol (MeOH), and imaged with scanning electron microscopy (Phenon ProX Desktop SEM) at an accelerating voltage of 15 kV.

2.4. Results and Discussion

2.4.1. Ionogel Synthesis and Characterization

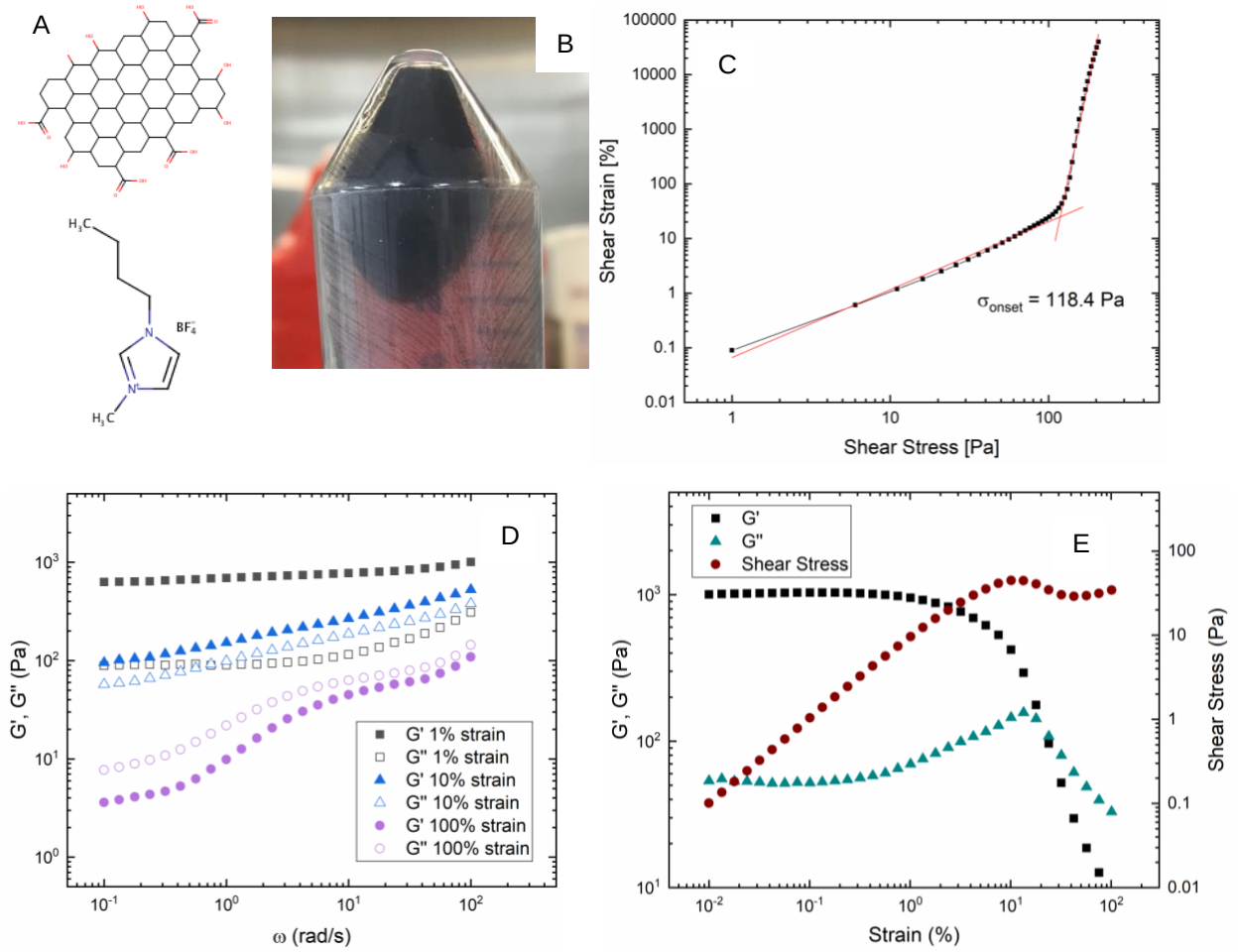

Figure 2-2. Schematic of the chemical structures of reduced graphene oxide (rGO) and 1-butyl-3-methylimidazolium tetrafluoroborate, [BMIM][BF4] (A). After centrifugation, the rGO/[BMIM][BF4] gel possesses favorable thixotropic properties as evidenced by the inversion test (B, inset) and rheology measurements (C-E). Yield stress measurements (C) revealed shear-thinning behavior with an onset yield stress of 118.4 Pa. The storage (G') and loss (G'') moduli were plotted as a function of frequency for different strain amplitudes (D) and as a function of strain for a frequency of 1 rad/s (E).

The chemical structures of rGO and [BMIM][BF_4] are shown in Figure 2-2A. The inversion test (Figure 2-2B) performed after centrifugation revealed favorable thixotropic properties of the rGO/[BMIM][BF_4] gel consistent with observations reported by *Zhang et al.*

[130] However, a second 2-hour centrifugation step was necessary to limit syneresis of excess ionic liquid from the gel, which had a concentration of 6.8 mg/mL. This low concentration (0.57 wt.%) demonstrated the efficacy of rGO as a [BMIM][BF_4] gelation agent due to its large surface area; for example, Truby et al. recently reported a conductive ionogel with 6 wt.% fumed silica particles [128]. Yield stress measurements (Figure 2-2C) and dynamic rheology measurements (Figure 2-2D and E). Yield stress measurements revealed elastic deformation and then strain thinning behavior as stress was increased, a rheological quality that is enabling for additive manufacturing techniques [133, 134]. At a strain amplitude (γ) of 0.01, the storage modulus (G') was almost independent of frequency, and the loss modulus (G'') remained below G' across all measured frequencies (Figure 7D). As γ is increased to 0.1, G' is still larger than G'' across all frequencies, but the values are within the same order of magnitude. G'' is greater than G' across all frequencies at γ = 1.0, indicating the gel behaves as a viscous fluid at this strain amplitude. Consistent with rheology measurements reported by *Zhang et al,* type III large-amplitude oscillatory shear (LAOS) behavior, or "weak strain overshoot," was observed [135] (Figure 2-2E). The initial increase in G'' suggests a resistance to applied shear up to the critical strain (0.2 here), and the decrease in G'' above the critical strain indicated a destruction of a gel structure [135]. *Zhang et al.* initially proposed that π-π interactions between the imidazolium ring of [$BMIM^+$] cation and the graphene sheets caused gelation [130]. Additionally, a recent study reported strong coulombic interactions arising between hydroxyl groups on the reduced graphene oxide and the ionic liquid [BMIM][BF_4] [136], suggesting electrostatic contributions also could play a role in gelation.

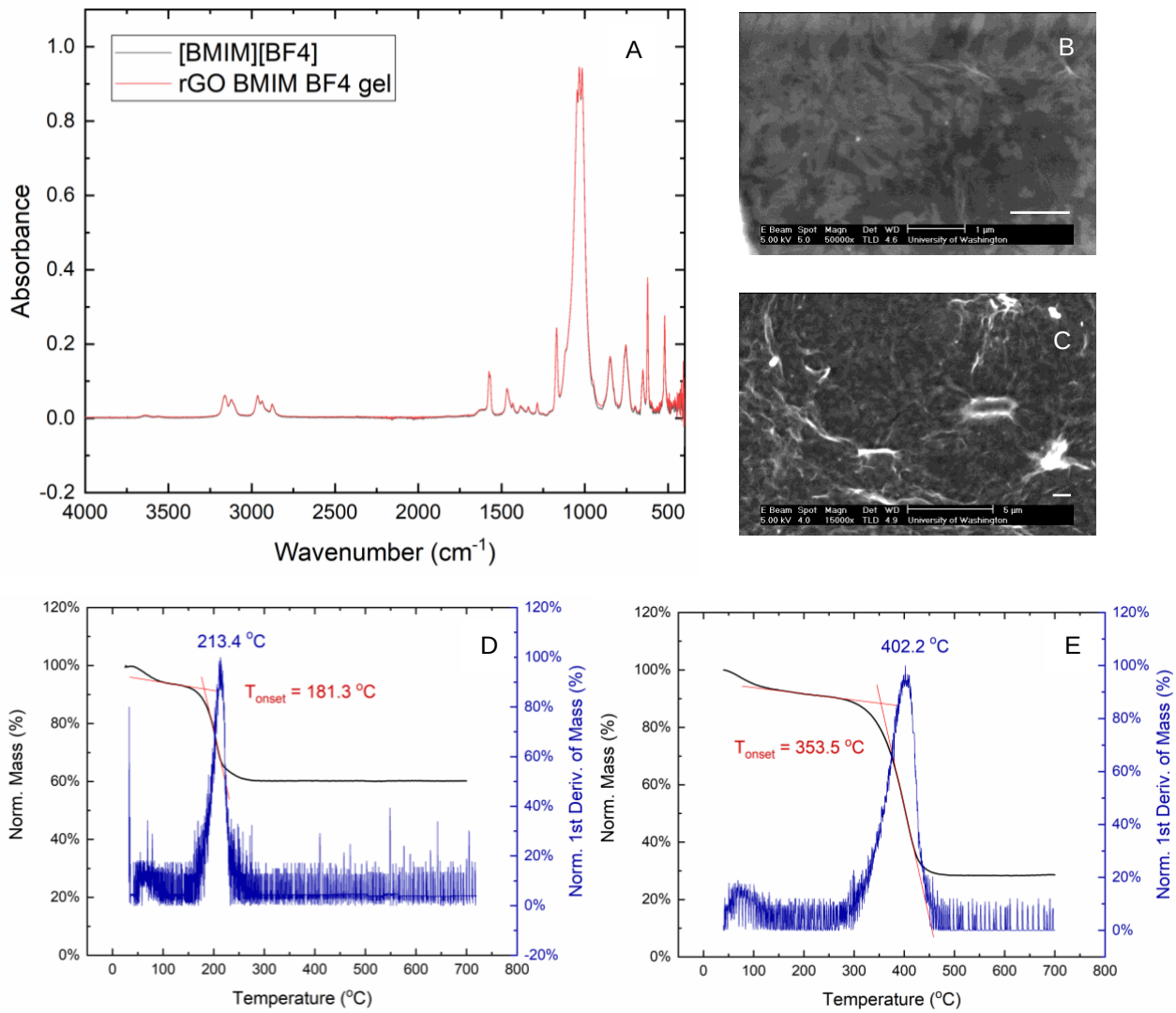

Figure 2-3. FTIR Results of the gel and the pure ionic liquid (A) do not reveal detectable chemisorption between the reduced graphene oxide and ionic liquid, SEM images of the graphene oxide (B) and the reduced graphene oxide (C) reveal flake-like structures (scale bar = 1 μm), and TGA results of the pristine graphene oxide (D) and reduced graphene oxide (E) suggest chemical reduction of graphene oxide occurred.

FTIR results (Figure 2-3A) reveal identical spectra for the gel and ionic liquid, suggesting the ionic liquid molecules could be physisorbed onto the rGO surface as observed for [BMIM][BF_4] and thermally exfoliated graphene [137]. However, the low concentration of rGO in [BMIM][BF_4] (6.8 mg/mL) could result in peak shifts indicative of chemisorption between rGO and [BMIM][BF_4] that are obscured by the much more intense [BMIM][BF_4] signal. SEM images

(Figure 2-3B and C) confirm the nanoscale plate-like structure of both the pristine and reduced graphene oxide. Thermogravimetric analysis (TGA) was used to quantify the degree of reduction in the reduced graphene oxide compared to the pristine graphene oxide (Figure 2-3D and E). The reported decomposition temperature of graphene oxide (GO) is 200 ^{o}C [138], and the decomposition temperature of graphene is as high as 2300 ^{o}C [139]. Therefore, the onset of thermal decomposition can be used to quantify the degree of reduction of reduced graphene oxide [140, 141]. The decomposition onset temperature of 352.96 ^{o}C indicated the graphene oxide had been reduced significantly, meaning oxygen-based functional groups (carboxyl, etc.) had been removed from graphene oxide [130].

2.4.2. Sensor Fabrication and DC-Mode Electromechanical Characterization

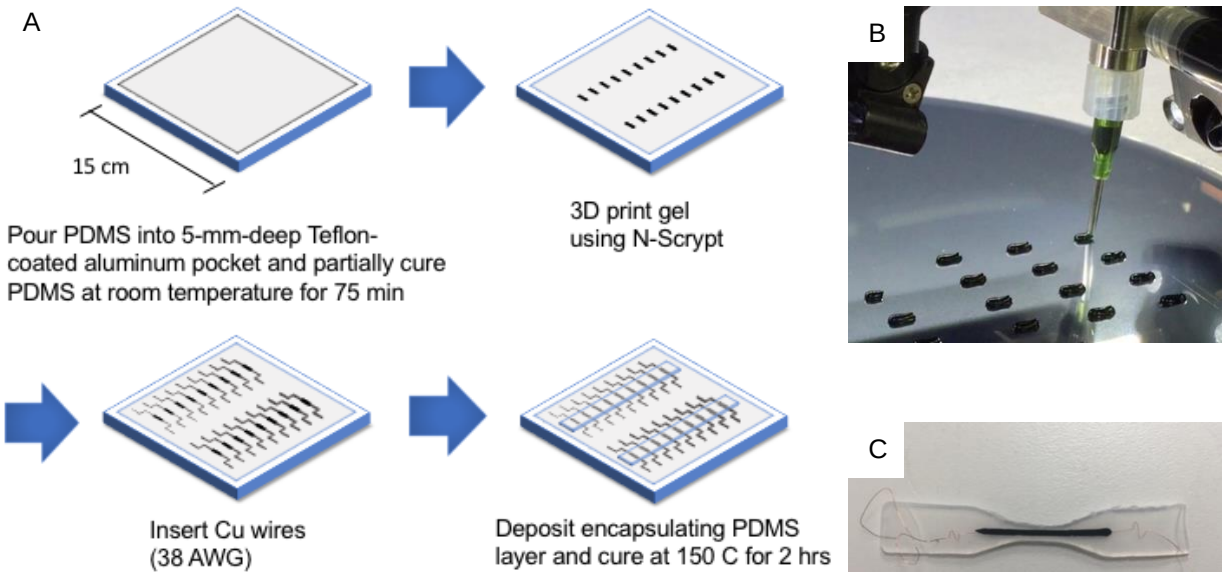

Figure 2-4. Fabrication schematic (A), photograph of gel printed on a partially cured PDMS substrate (B), and photograph of a completed strain sensor (C).

As depicted in Figure 2-4A, sensors were fabricated by printing lines of ionogel onto a partially cured PDMS substrate (Figure 2-4B). A partially cured PDMS substrate allows for stronger interlayer bonding due to the formation of covalent bonds between the top and bottom layers [142]. Lines were printed with lengths as small as 6 mm and as long as 25 mm. In addition, trimming the printed lines with the 3D printing needle removed any acute geometries that would prevent complete encapsulation of the gel (Figure 2-5). After copper wires were inserted to make electrical contact with the gel, an encapsulating layer of PDMS was syringe-deposited over the gel lines and gel/wire contacts, and sensors were placed in an oven at 150 ^{o}C for two hours to cure the PDMS. Individual sensors were punched out from the batch with a standard dog bone shape (ASTM D638 Type V) to concentrate the stress along the conductive gel channel (Figure 9C).

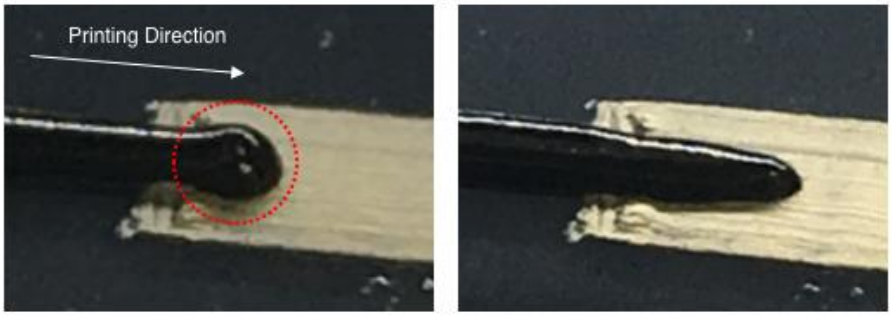

Figure 2-5. Pictures of a printed gel trace before (left) and after the trimming operation. After a trace of gel is printed, the rise of the dispensing nozzle leaves behind a cone of excess gel that prevents complete PDMS encapsulation (red circle). Re-running the printing file path without dispensing gel allows the printing nozzle to remove the cone by pushing the excess gel further to the right.

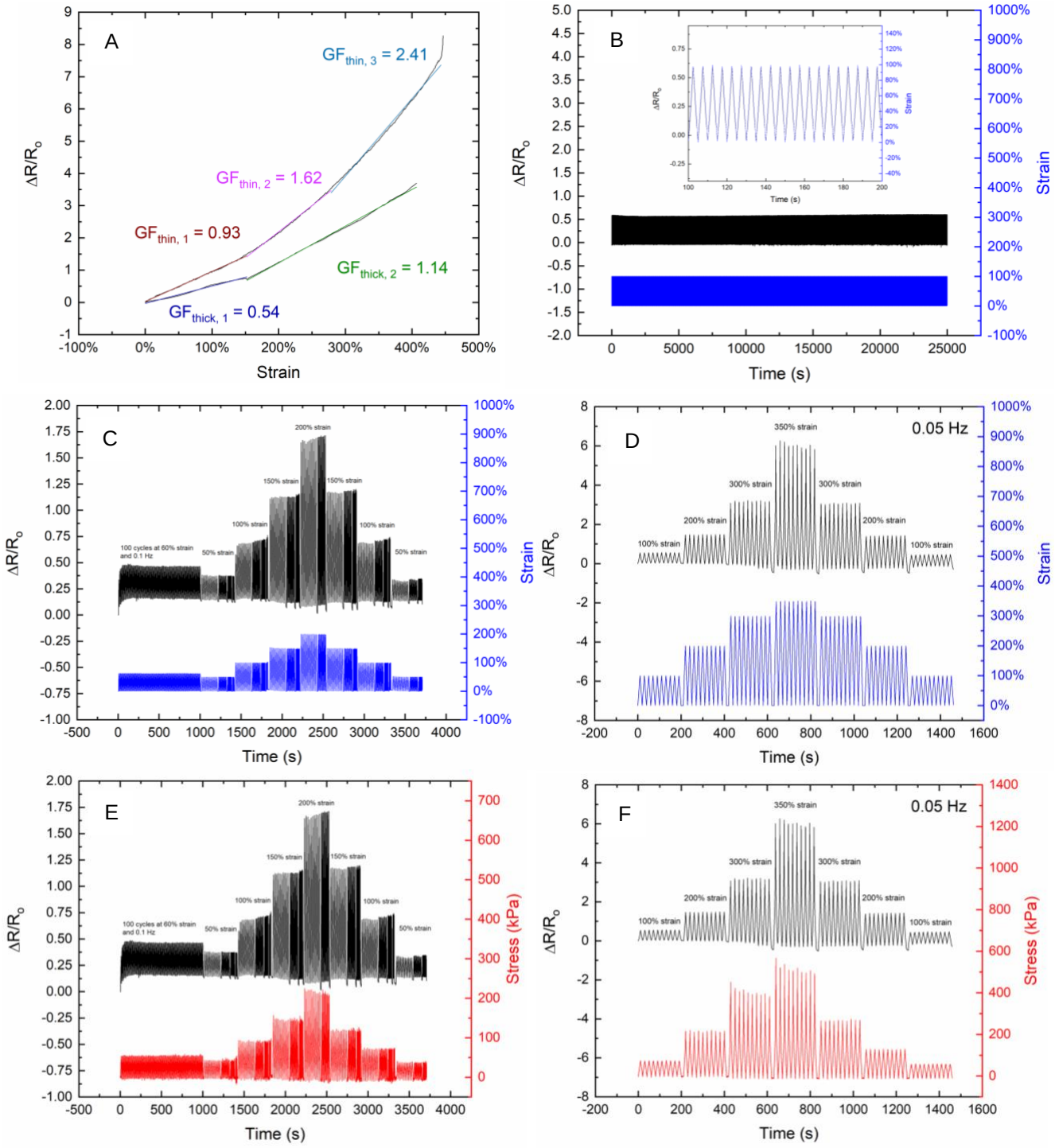

Figure 2-6. Electromechanical characterization results. Gel lines with a larger aspect ratio (length/width) showed an increased gauge factor (A). Fatigue testing conducted at 0.2 Hz and 100% strain amplitude revealed negligible drift up to 5,000 cycles (B), and closer inspection reveals excellent tracking of the strain frequency and amplitude (B, inset). Dynamic testing results (C, D) indicate a wide range of strain amplitudes (50-350%) and frequencies (0.05-1 Hz) can be detected, and corresponding plots of stress vs. time (E, F) suggest plastic deformation of the polymer, especially at high strains.

Electromechanical characterization results demonstrated excellent sensor performance. Ramp testing (Figure 2-6A) of sensors with conductive channel aspect ratios (length : width) of 40 : 1 (“thin”) and 20 : 1 (“thick”) shows that sensors with a larger aspect ratio have a higher peak gauge factor of 2.41 vs. 1.14 [143]. This result can be explained by two possible conduction mechanisms: 1) the geometric deformation of the conductive [BMIM][BF_4] channel, and/or 2) the disruption of the rGO percolation network [23]. Further elucidation of the conduction mechanism can be found in the discussion accompanying Figure 2-8, but both mechanisms predict an accelerating increase in $\Delta R/R_o$ as strain (and, by definition, the aspect ratio of the channel) is increased. Despite the higher sensitivity of the sensor with the thinner conductive channel, thicker samples were used for the fatigue and dynamic testing results due to improved reproducibility of the printed dimensions and performance results. A 5000-cycle fatigue test (100% strain, 0.2 Hz) revealed negligible drift (Figure 2-6B) and a single-valued response that linearly tracked the strain of the sensor closely was observed (Figure 2-6B, inset), unlike sensors with a piezoresistive composite composed of conductive fillers dispersed in an elastomeric matrix [97, 98, 144, 145]. The excellent cyclic durability demonstrated in the fatigue test is superior to that of composite-based sensors [97, 98, 145] and comparable to that of fluid-based sensors [106, 115, 146]. Dynamic mechanical testing results conducted over a range of frequencies (Figure 2-6C) revealed a reversible response. A 100-cycle test (60% strain, 0.1 Hz) was performed first to test initial sensor stability and stabilize the output reading, which was achieved within the first 20 cycles. Higher strain rates (higher frequencies) tended to increase the measured response slightly. Detailed studies on the viscoelastic response of the gel in response to strain rate are underway to clarify this dependence on strain rate. The corresponding stress-time plot (Figure 2-6E) showed that the measured stress required to reach 150%, 100% and 50% strain decreased after the sample was

exposed to 200% strain, suggesting creep had begun. High-strain dynamic testing performed at a strain frequency of 0.05 Hz (Figure 2-6D) demonstrated a near-symmetric response up to 350% strain, showcasing the wide strain range accessible with this gel. The corresponding stress-time plot (Figure 2-6F) showed an even larger drop in stress after exposure to 350% strain, further supporting the evidence of creep. Extracted hysteresis results reveal a degree of hysteresis less than 3.5% up to 300% strain (Figure 2-7) a performance superior to that of ionic-liquid- and liquid-metal-based strain sensors over a similar strain range [106, 146–148].

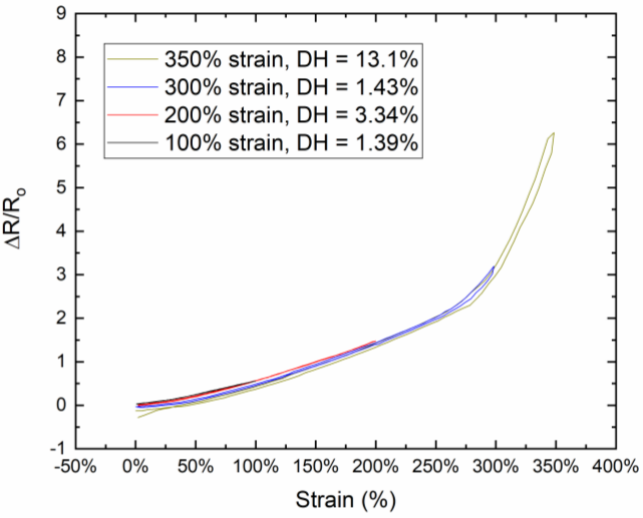

Figure 2-7. Extracted hysteresis results from Figure 3D. Each trace was taken from the second peak of the first four strain amplitudes (100%, 200%, 300%, and 350% strain). The Degree of Hysteresis is defined as (Aloading – Aunloading)/Aunloading x 100%.

2.4.3. The Sensing Mechanism

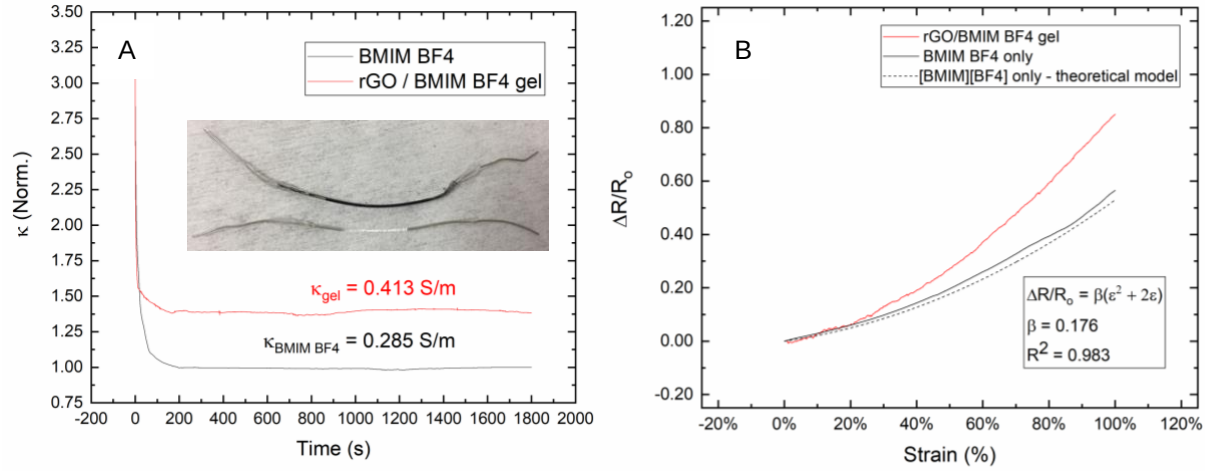

Figure 2-8. Characterization of stretchable tube sensors with gel vs. ionic liquid only (A, inset). The black tube contains gel, while the clear tube contains pure [BMIM][BF4]. The percolation of rGO NPs in the gel increase the stabilized conductivity by 45% at rest (A) and sensitivity in a ramp test (B). The equation in Figure 4B models the relative change in resistance for an incompressible and continuously deformable conductive fluid encapsulated in a cylindrical channel.

The aforementioned possibility of two conduction mechanisms necessitated a series of experiments that directly compare the electromechanical response of the gel to pure [BMIM][BF_4] (Figure 2-8). Because pure [BMIM][BF_4] is not printable, both the gel and ionic liquid were injected into stretchable silicone tubing to allow for direct comparison of the electromechanical response. DC measurements (Figure 2-8A) resulted in an average [BMIM][BF_4] conductivity of 0.285 S/m (n = 5), which is consistent with conductivities extracted from AC measurements reported in literature [149–152]. The conductivity (κ) of an ionic liquid can be described by the Vogel-Fulcher-Tammann (VFT) equation [149, 153]:

$$= \ln(A) + \frac{B}{T - T_0} \qquad (4)$$

where A and B are experimental fitting parameters and T_o is the VFT temperature. For BMIM BF_4, ln(A), B and T_o are 5.112 S/m, -806.6 K, and 167.0 K, respectively [149]. An estimated lab temperature range of 20-21 ^oC resulted in a conductivity range of 0.277-0.292 S/m, suggesting excellent agreement between our measured conductivity and previous results. The addition of rGO increased conductivity of the medium by 45%, which suggests the formation of percolating conductive pathways through rGO. Ramp tests to 100% strain further show that the inclusion of reduced graphene oxide boosts the sensitivity due to the disruption of this conducting network in addition to the geometric deformation of the [BMIM][BF_4] channel (Figure 2-8B). As the more conductive pathways in the rGO network lose contact with increasing strain [100], the relative change in resistance increases more rapidly compared to pure [BMIM][BF_4]. However, we consider geometric deformation of [BMIM][BF_4] rather than disruption of the rGO percolation network to be the primary conduction mechanism for two reasons: 1) a percolation network dispersed in a matrix results in much larger changes in conductivity (10^4-10^{11}) for an rGO concentration above the percolation threshold [154–157], and 2) therefore, the gauge factor of sensors disrupting an rGO percolation network are higher over a comparable strain range [100, 158, 159]. For example, Xu *et al.* reported rGO/water-based piezoresistive strain sensors with gauge factors of 2.5 and 31.6 in the strain intervals of 0 - 0.1% strain and 390-400% strain, respectively [100]. We also note the good fit of the quadratic model of an incompressible, continuously deformable conductor encapsulated in a cylindrical channel for the [BMIM][BF_4]-only sensor; the value of β depends on the initial resistance (R_o) and the contact resistance (R_c) between the wires and gel ($\beta = [R_o - 2R_c]/R_o$) [81, 146]. The gauge factors of printed sensors (Figure 2-6A) are comparable to those of sensors that measure the geometric deformation of a

conductive channel comprised of an ionic conductor [105, 146], organogel [122], or liquid metal [81, 115, 148].

Our sensor can be modeled electrically as an equivalent circuit with a variable resistor sandwiched in series between two electrical-double layer (EDL) capacitors that form at the electrode/ionic liquid interface [78]. Upon injection of a constant current, the capacitors accumulate charge due to the formation of the EDL, resulting in the initial decrease in conductivity observed in Figure 2-8A. The EDL capacitance (C_{EDL}) can be predicted using the following equation [78, 160]:

$$C_{EDL} = \varepsilon_o \varepsilon_r \frac{A_{EDL}}{\lambda} \qquad (5)$$

where ε_o, ε_r, A_{EDL}, and λ represent the permittivity of free space, the relative permittivity at the metal/ionic liquid interface, the metal/ionic liquid interfacial area, and the Debye screening length (a measure of EDL thickness on the order of ~1 nm), respectively [78, 160]. Equation 5 indicates that the EDL capacitance depends exclusively on quantities unaffected by strain, meaning any changes in resistance in response to strain can be attributed solely to the variable resistor element. Because sensors are operated with a fixed current of 1 μA and a fixed capacitance, the voltage (and therefore the resistance per Ohm's Law) is theoretically predicted to increase linearly with time (V = I*t/C) [161] to the voltage compliance limit of the sourcemeter (21 V). However, the voltage (and conductivity) stabilizes below this limit at 2.7 V. Initially, I speculated this pre-compliance saturation arises from the dielectric breakdown of the EDL capacitors [160], which allows for leakage current to flow through the piezoresistive channel at a constant voltage.

Regardless, upon achieving this steady-state resistance output, the sensor can be operated in a piezoresistive mode.

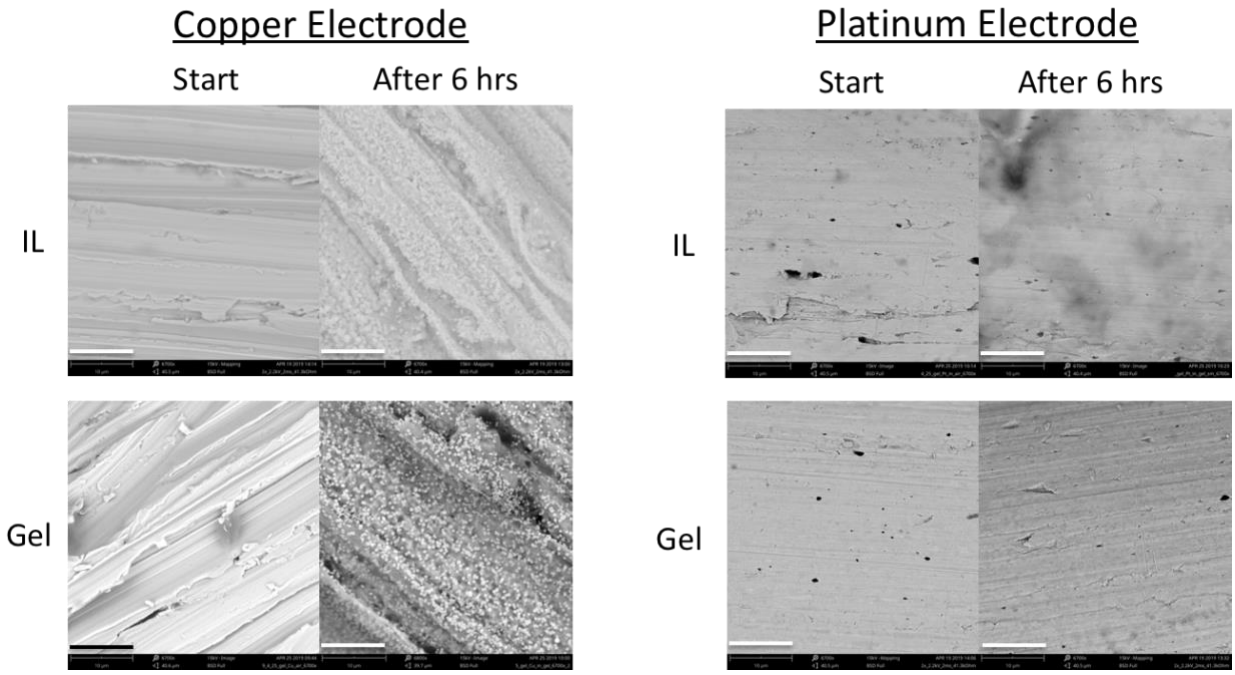

Figure 2-9. SEM images of the working electrode taken before and after a 6-hour constant current test for both gel-based and IL-based tube sensors. The copper electrode showed clear degradation and increased porosity for both the ionic liquid- and gel-based sensors, while the platinum electrode did not show any signs of degradation.

Subsequently, I hypothesized that the source of current is the electrodeposition of copper ions from one electrode to the other. Assuming a 38 AWG copper wire was inserted 1 cm into the gel, there are ~7 x 10^{18} Cu atoms available to migrate. Assuming copper is oxidized to its monovalent species rather than its divalent species, a constant current of 1 μA corresponds to ~2 x 10^{16} Cu^{+} ions per hour, or 0.3% of the available copper ions per hour. To support this hypothesis, 6-hour constant-current tests were carried out on sensors with either gel or pure ionic liquid in the channel and Pt/Cu electrodes. The Pt (counter) and Cu (working) electrodes were inspected under SEM (Figure 2-9), and clear degradation of the Cu electrodes was observed. In addition to these

SEM results, the Cu electrode had optically darkened, further corroborating the degradation of the Cu electrode.

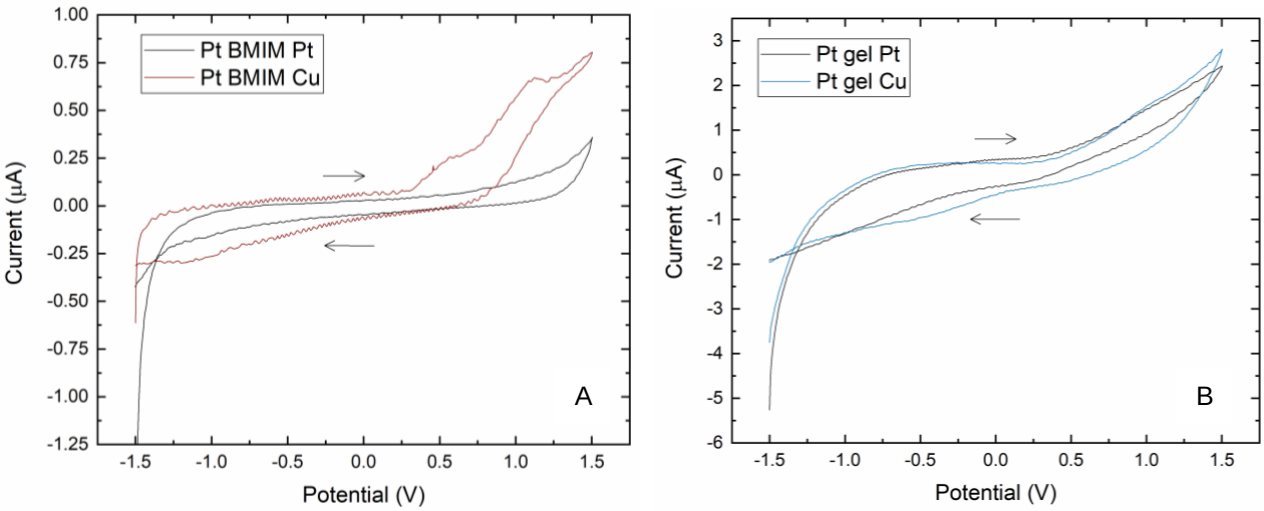

Figure 2-10. Cyclic voltammetry (CV) measurements of ionic liquid (A) and gel (B) sensors sandwiched between Pt/Pt and Pt/Cu electrodes, where the Cu electrode served as the working electrode.

Cyclic voltammetry (CV) measurements further supported the hypothesis of copper migration and electrodeposition as the source of current. Ionic liquid Sensors with Pt/Cu electrodes showed two oxidation peaks at 0.50 and 1.0 V and a reduction shoulder at -1.2 V (Figure 2-10A), while the sensors with Pt electrodes only did not display any electrochemical behavior. Sensors with the gel do not show any clear oxidation or reduction peaks (Figure 2-10B), but the much larger capacitance of the gel could mask these electrochemical events.

2.4.4. AC-Mode Electromechanical Characterization

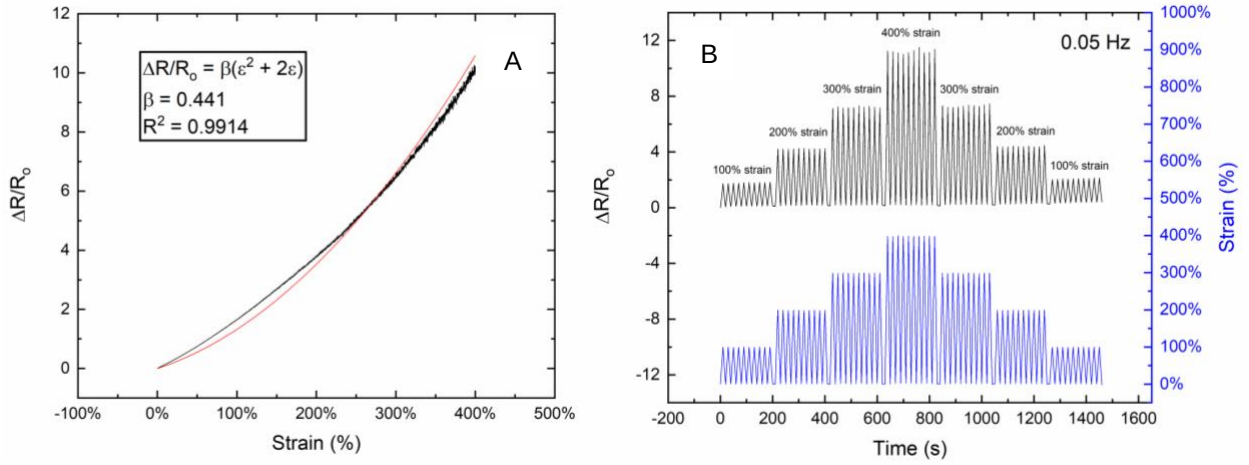

Figure 2-11: Ramp (left) and dynamic (right) electromechanical characterization of a printed ionogel strain sensor in AC mode. The sensor was stretched to 400% strain at a rate of 1% strain/s in the ramp test, and the sensor was stretched to amplitudes of 100%, 200%, 300%, and 400% strain at a frequency of 0.05 Hz.

The possibility of electrochemical activity in the gel has been established by testing with a constant current or voltage (DC mode), suggesting the development of an alternative electromechanical testing method would be necessary to avoid electrode degradation. The application of an alternating signal between 40 Hz and 10 MHz has been used in previous works to bypass electrochemical activity, so the electromechanical response of both printed and tube-based ionogel sensors were measured with an alternating square wave via an impedance analyzer (Figure 2-11) – hereafter referred to as "AC mode."

Sensors tested under AC mode demonstrated improved sensitivities compared to DC mode. Preliminary dynamic testing results (Figure 2-11B) reveal some slight drifting behavior, especially after the sensor was exposed to 400% strain. These larger strains compared to the printed sensor tested in DC mode (max strain of 350% strain – Figure 2-6D) could have contributed to this drift. Ionogel and ionic liquid tube sensors were compared in AC mode with a ramp test to 200% strain (Figure 2-12). Consistent with the DC-mode ramp test results of tube sensors, the gel-based tube sensors showed a superior sensitivity compared to those containing pure ionic liquid. Notably, the sensitivities of both species are raised due to the increased β values, suggesting that working in an AC mode decreases the contact resistance of the sensors.

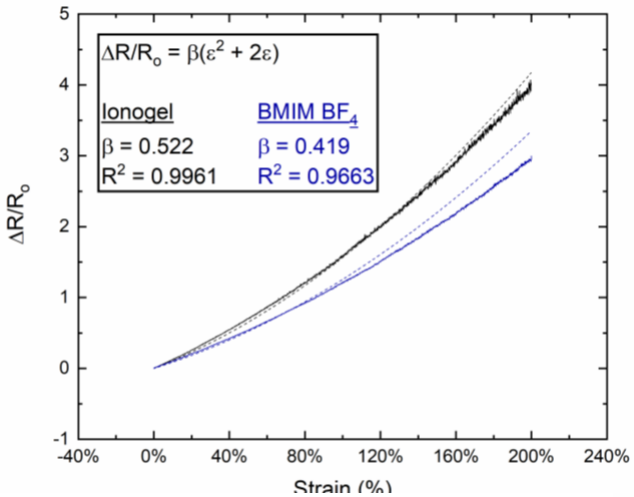

Figure 2-12. AC-mode ramp test comparing tube sensors containing ionogel vs. BMIM BF4 as the sensing medium.

2.4.5. Sensors with Printed Electrodes

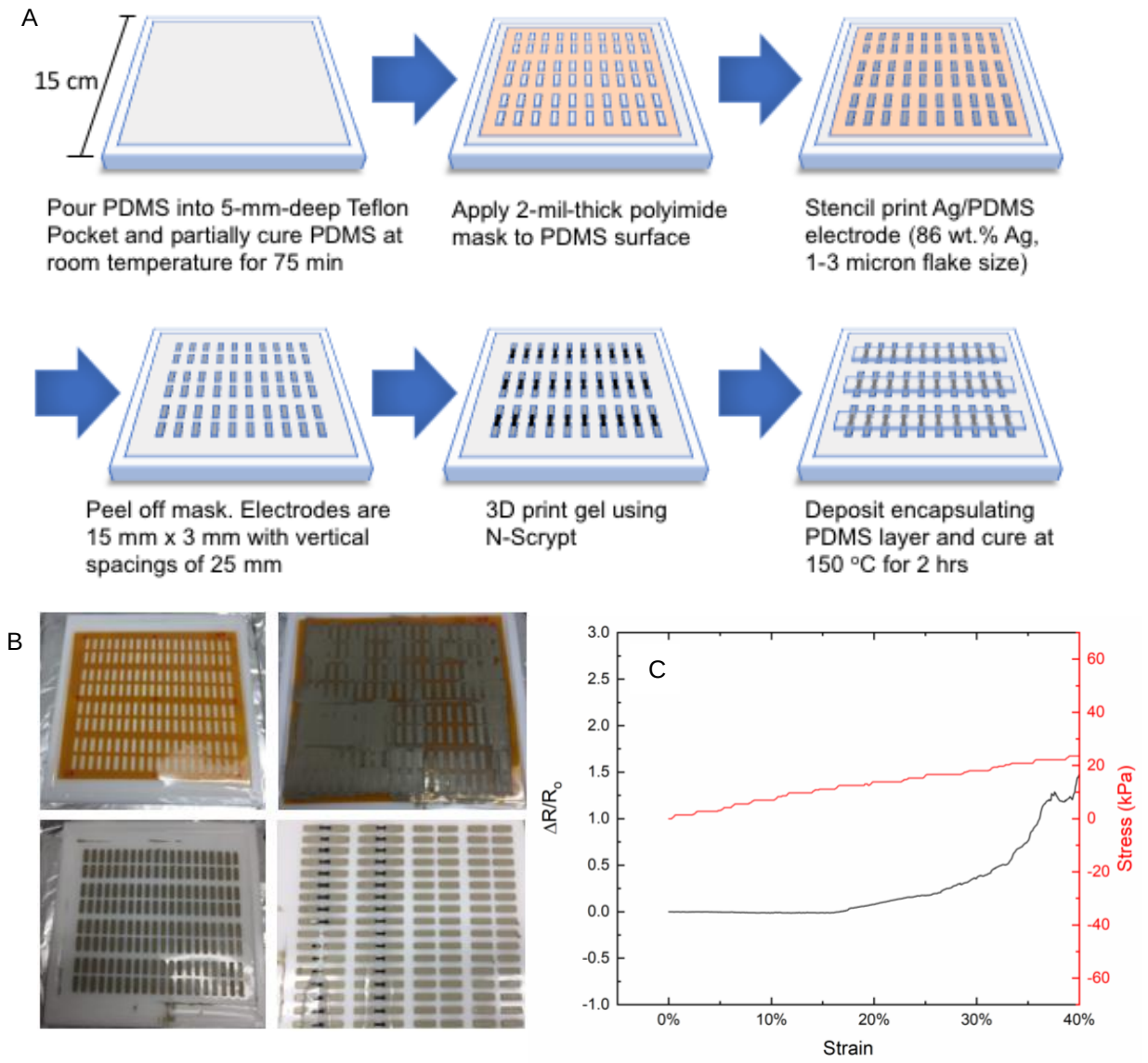

Figure 2-13. Strain sensors with Ag/PDMS electrodes. An Ag/PDMS paste (86 wt.% Ag flakes) is stencil printed through a polyimide mask onto a partially cured PDMS substrate, the mask is removed, gel is 3D-printed between electrodes, and an encapsulating layer of Eco

Strain sensors with Ag/PDMS (86 wt.% Ag) electrodes were fabricated to demonstrate an all-printed device (Figure 2-13A and B). Ag/PDMS was selected because it would cross-link with the top and bottom PDMS layers [162], allowing the gel to be encapsulated fully. The PDMS binder in the Ag electrode formulations also allows for some stretchability in the contacts

themselves, relieving strain concentrations at the electrode/substrate interfaces. An Ag flake concentration of 86 wt.% was selected due to high conductivity of the cured mixture [163]. We found using a mortar and pestle instead of a spatula and glass plate as reported by *Ruhhammer et al.* [162] to grind the mixture into a paste improved the resulting electrode conductivity. Conductivities of 2-4 x 10^3 S/m were observed. Using silver flakes with larger lateral dimensions (>10 μm) at the same concentration (86 wt.% Ag) prevented complete curing of the paste even when cured overnight at 150 ^{o}C. Preliminary ramp tests revealed a detectable strain up to 40% strain (Figure 2-13C).; the signal loses coherence above this strain, suggesting contact is lost within the silver electrode. These results show that all-printed sensors will require strain-insensitive, conductive, PDMS-compatible printable electrodes in future iterations.

2.5. Conclusion

In this chapter, we presented the first printed stretchable strain sensor using a 3D-printed ionogel with a conductive gelating agent. This showcases the potential of this material system as the embeddable sensing element in an all-printed, monolithically fabricated, patient-specific tissue model. The low drift, high-fidelity response, and high fatigue stability of the sensor merits further study and optimization of this sensing platform. The incorporation of more conductive fillers could be used to form an ionogel with a high gauge factor and low hysteresis. For example, a piezoresistive channel composed of a cracked graphene film connected by a conducting electrolyte (potassium iodide in glycerol) resulted in a gauge factor of 25.4 and a moderate degree of hysteresis of 11.13% [106]. The ionic liquid [BMIM][BF_4] could be replaced by other ionic liquids [130] that are predicted to interact strongly with reduced graphene oxide or graphene [136, 164–167] and form a printable gel. Future efforts will focus on the development of printable ionogels

with boosted sensitivity and low hysteresis. The development of PDMS-compatible, printed electrodes that maintain consistent functionality with cyclic stretching remains as a barrier to fully integrated fabrication of higher strain sensors; silver/PDMS electrodes demonstrated a limited strain range of 40% before the resistance signal loses coherence. Therefore, future efforts will focus on the development of a printed, PDMS-compatible electrode.

Additionally, the implementation of sensors to monitor biomechanical activities with large strains, such as body motion kinematics [106, 168–170] or viscus tissue expansion [171], will be pursued as part of the larger effort to 3D-print tissue models with seamless sensor integration. Sensor geometry and location would depend on the specific simulation application. For example, a longer strain sensor could be fabricated and wrapped around a bladder tissue model, and the relative change in resistance would correlate to the volumetric expansion of the model as it fills with fluid [171]. Additionally, multi-directional sensing could be realized by sequentially printing sensors with different orientations (Figure S12) [129], and 3D-printed, gel-based pressure sensors [58] could be incorporated to combine strain and pressure sensing modes.

We have demonstrated a new path to monolithic fabrication of stretchable strain sensors with 3D-printed, patient-specific tissue models. Accurately sensing the behavior of human tissues can provide objective feedback for education, medical device design, and surgical rehearsal. We contend such a development would improve the capabilities of synthetic simulated human tissue as part of a larger effort to reduce medical error.

Chapter 3. Organogel Strain Sensors

3.1. Introduction

Since Safar, Lind and Laerdal invented the first full-size medical simulator, *Resusci Anne*, in 1961 [172], the healthcare simulation field has expanded tremendously as part of a larger effort to reduce medical error [26]. To date, there exist 174 healthcare simulation centers accredited by the Society for Simulation in Healthcare [173], and, as of 2019, there were 96 accredited by the American College of Surgeons Accredited Education Institutes [174]. Healthcare simulation has improved medical skill acquisition across a wide range of practitioner seniorities [175], and a recent meta-analysis by Beal *et al.* [176] indicated that high-fidelity simulations were more effective than low-fidelity simulations in improving medical performance-based outcomes. Lifelike optical and mechanical properties of artificial tissue combined with dynamic manikin actuation driven by realistic cardiovascular physiology models distinguish the former from the latter [176]. The next significant development in healthcare simulation is the integration of sensors into high-fidelity manikins to deliver more realistic patient-provider interactions and to generate data for objective performance assessments [177]. As many medical and surgical procedures involve the manipulation and deformation of tissue, a strain sensor monolithically integrated into artificial tissue models with a minimal footprint would quantify tissue deformation in a wide range of healthcare simulation modules without sacrificing fidelity. Reconstructive surgical skin procedures such as skin flaps especially would benefit from the quantification of strain as the degree of strain experienced by a healing dermal wound influences viability of the tissue and the extent of permanent scarring [178]. Most current training simulation models use sensor-free artificial skin or pig feet for surgical practice [179]. Optically marked tissue models have delivered

objective assessment opportunities for reconstructive procedures like skin flaps [180]. We propose integrating sensorized tissue skin flap models for automated assessment.

A strain sensor is composed of a conductive channel with two electrodes connected to supporting readout electronics. Either changes in resistance (piezoresistive) or capacitance (piezocapacitive) can be measured in response to strain [23]. As detailed in our previous work [24], piezoresistive sensors are preferred for applications in medical simulation due to 1) their minimized footprint in tissue models, and 2) their insusceptibility to stray capacitive interference. Initial piezoresistive sensing channel mediums were composed of a network of solid conductors dispersed in an elastomeric matrix [23, 84, 181]. While these sensors possess high sensitivities, they suffer from significant signal drift, which arises from the permanent displacement of embedded conductors in response to applied strains [23, 95, 96]. A nonmonotonic response is observed in several recent publications [182–184], which introduces uncertainty to sensor readout interpretation and consequentially requires nontrivial signal processing.

In light of these inherent limitations of composite-based piezoresistive strain sensors, a burgeoning design strategy is to embed conductive gels or fluids in stretchable elastomers. Conductive media include liquid metals, hydrogels, ionogels, and organogels. Liquid metals include alloys, commonly eutectic gallium indium (EGaIn), that are liquids at room temperature [110]. Sensors utilizing 3D-printable EGaIn or EGaIn-based pastes have demonstrated effective performance at large strain ranges (≥100%) [185, 186], but EGaIn is expensive and possesses uncertain biocompatibility [187]. Furthermore, the U.S. Department of Interior has designated indium along with rare-earth metals as a critical material [188], which highlights the poor sustainability of EGaIn-based sensors. Recently, there has been considerable interest in conductive hydrogels as a strain sensing medium due to their low cost, enormous strain ranges (up to 1,000%),

and tunable biomimetic properties [189]. While hydrogel systems can be very stable in aquatic environments, they are prone to instability due to evaporation of water in air [189] and therefore have limitations for medical simulation applications. Ionogels, based on ionic liquids (ILs) [125, 126], have been shown to be stable, low cost, high-strain, low-hysteresis sensing media when embedded in a stretchable elastomer [24, 128]. However, the toxicity of many ionogels[190] has motivated the search for a similarly high-performance conductive gel with unequivocal biocompatibility [191].

The high cost of liquid metals, environmental instability of hydrogels, and toxicity of many ionogels have inspired the development of conductive organogels based on deep eutectic solvents (DESs) [192, 193]. DESs are liquid mixtures composed of a quaternary ammonium salt complexed with either a metal salt or a neutrally charged hydrogen bond donor (HBD) [192]; DESs possess a melting point lower than either constituent species. DESs and ILs share favorable physical properties, such as low vapor pressures, a wide liquid window, and limited flammability [194, 195]. The inexpensive, nontoxic precursor feedstocks and facile, scalable synthesis of several DES compositions [192] make them an attractive alternative to ILs as an ionically conductive liquid utilized in strain sensors. The foreseeable risk of incidental dermal contact with the conductive channel during simulation exercises necessitates the selection of a non-hazardous medium.

In this work, inexpensive, conductive, and 3D-printable organogels utilizing a DES as the liquid medium and fumed silica particles as the gelating agent are introduced. The DES used in this work is composed of an HBD, polyethylene glycol (PEG200) or propylene glycol (PG), and the quaternary ammonium salt choline chloride (ChCl) in a 5 HBD : 1 ChCl molar ratio [196, 197]. The HBDs PEG200 and PG were selected over the commonly used HBD ethylene glycol [198] due to their non-toxic nature and GRAS (generally recognized as safe) classifications by the U.S.

Food and Drug Administration [199, 200], and choline chloride is a biocompatible, mass-produced salt primarily used in animal feed [201]. In this work, we show that the surface functional group on the fumed silica particles drastically influences the DES/silica mixture rheology, and we report a class of shear-thinning organogels composed of a conductive DES and fumed silica particles with the functional group 3-trimethoxysilylpropylmethacrylate. Furthermore, we 3D-print stretchable strain sensor channels embedded in the elastomer polydimethylsiloxane (PDMS) with the PEG200-based organogel and silver-impregnated nylon thread serving as the conductive channel and electrode, respectively. Sensors achieve a large dynamic strain range (300%), negligible baseline drift, minimal hysteresis, and cyclic stability (1000 cycles at 100% strain amplitude). Finally, lifelike skin tissue models with monolithically integrated organogel strain sensors are fabricated and tested to showcase the potential applications in a dermatological surgical simulation.

3.2. Methods

3.2.1. Organogel Synthesis and Characterization

Choline chloride (≥98%), propylene glycol (PG), and poly(ethylene glycol) with a molecular weight of 200 g/mol (PEG200) were purchased from Sigma Aldrich, while all Aerosil® fumed silica particles (R711, R974, and 200) were provided gratis by Evonik. Fumed silica particles were characterized with FTIR spectroscopy in attenuated total reflectance mode (Thermo Scientific Nicolet iS10). Choline chloride was dried under vacuum at 130 ^{o}C for 72 hours and stored in a nitrogen glovebox. A deep eutectic solvent with a 1:5 molar ratio of choline chloride to PG or PEG200 was prepared and stirred for two hours at 90 ^{o}C. Fumed silica particles were added to the deep eutectic solvent with varying concentrations and mixed via a planetary mixer (Thinky ARV-310) at 2000 RPM for 10 min. The resulting gels and fluids were characterized by a rheometer (Anton Parr MCR302) at 20 ^{o}C using 25 mm parallel plates with a set height of 0.5 mm. Viscosity flow curves were taken over a shear rate domain of 0.1-500 s^{-1}. Oscillatory amplitude sweeps were carried out over a strain domain of 0.01-100% and a fixed frequency of 1 rad s^{-1}. Approximately 76.6 mg of organogel was weighed for thermogravimetric analysis (Mettler-Toledo TGA/DSC 3+). The mass loss of the sample was measured under nitrogen from 27 ^{o}C to 720 ^{o}C with a heating rate of 5 ^{o}C min^{-1}.

3.2.2. Sensor and Suture Pad Fabrication

3.2.2.1. Tube Sensor Fabrication

Organogel tube sensors were prepared by injecting the organogel into a stretchable commercial silicone tube (Orvis) with an inner diameter of 0.245 mm. Leads (30 AWG copper) were inserted carefully into each end of the tube to avoid trapping air bubbles and sealed with an epoxy (Sil-Poxy, Smooth-On) that cured fully in 15 minutes.

3.2.2.2. Printed Sensor Fabrication

Nylon fabric (L'eggs) was placed in the bottom of a 130 x 200 mm 3D printed PLA mold. 20 g of PlatSil® Gel-25 Part B silicone (Polytek) was added to a mixture of 20 g Gel-25 Part A and 20 g PlatSil® Deadener LV (Polytek). This was manually mixed for two minutes then poured into the mold and stippled into the taut nylon with a brush. The synthetic skin silicone layer was allowed to cure fully, approximately 30 minutes. Pairs of silver/nylon composite conductive threads (Agsis-Lite, Syscom Advanced Materials) were stitched into the substrates approximately 15 cm apart.

The PEG-based organogel was transferred to a syringe, and the syringe was centrifuged at 9000 RPM for 10 minutes to remove any trapped air bubbles. The syringe was then attached to the pneumatic SmartPump® on a 3D microdispenser (N-Scrypt 3Dn-300) attached to a two-axis translation stage. The silicone substrate was placed on the print chuck, and lines of organogel were dispensed onto it through a nozzle (blunt-tip needle, 20 G). 25 mm long lines were printed using a pressure of 35 psi, speed of 3 mm s^{-1}, and clearance of 0.6 mm. The sensors were then encapsulated by another layer of silicone composed of equimass amounts of Gel-25 A, Gel-25 B, and Deadener LV and allowed to cure at room temperature overnight.

3.2.2.3. Y/V Plasty Suture Training Pad Fabrication

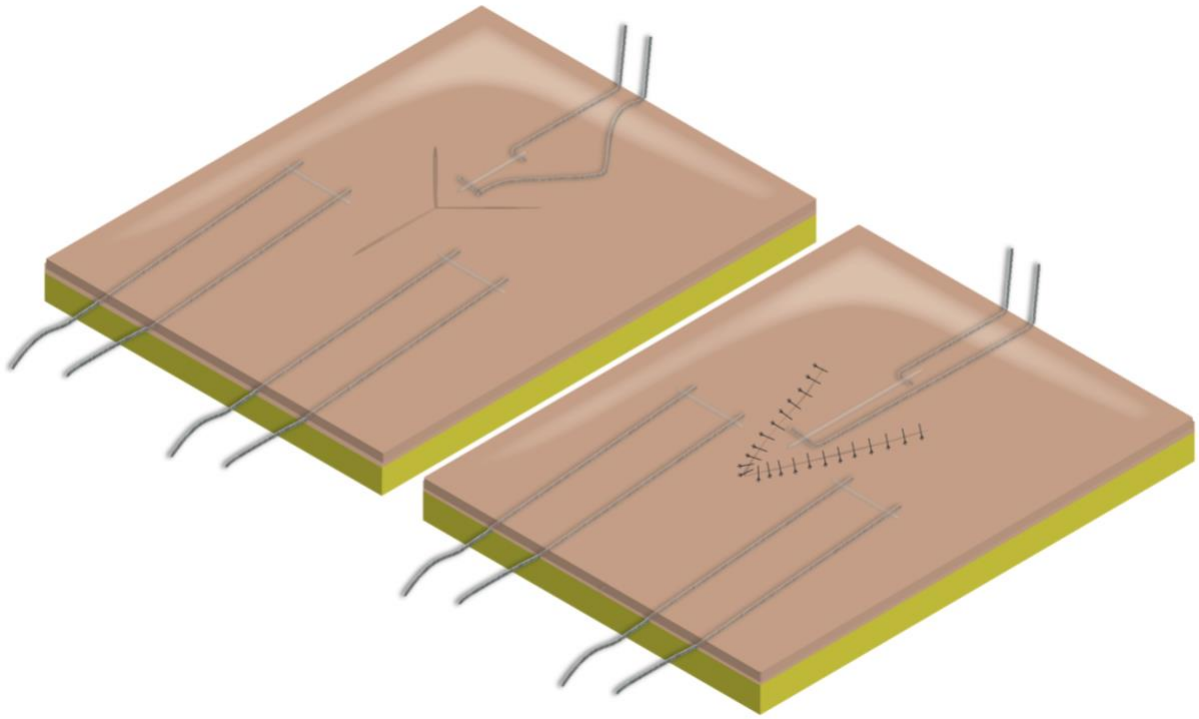

Figure 3-1. Schematic representations of the Y/V plasty suture training pads with a partially transparent top layer to reveal the location of the sensors with respect to the Y-shaped cut before (left) and after suturing (right) . A Y/V plasty involves the incision of a Y-shaped cut, and then the skin flap is pulled down into a V shape that is sutured into place. A stitched Y/V plasty training pad with sutures installed (B, right) shows the elongation of the organogel sensing channel due to the strain experienced by the Y flap.

Like the sensor fabrication, a 60 g Gel-25 skin formulation colored with 0.5 g of Silc Pig™ Flesh pigment was poured over a taut nylon layer in the same printed mold. Each mold fits two Y/V Plasty training pads. Two sets of three 20 mm organogel lines were printed on the fully cured skin layer substrate. Conductive thread electrodes were placed 5 mm into the ends of each organogel line. The sensors were then embedded by another 60 g skin layer. After curing, a thin layer of petrolatum (Vaseline) was painted onto the middle of the skin layer; a 1-cm-thick petrolatum-free perimeter was established. An 80 g PDMS fat layer of 1:1:2 Gel-25 A:Gel-25 B:Deadener LV colored with 1 g of Silc Pig™ Yellow was poured into the mold. After thirty

minutes, the suture training pad could be removed from the mold. A Y shape was cut into the skin layer by a scalpel and guided by a stencil (Figure 3-1). The size and shape of the Y cut was determined with input from two surgeons. Each line segment of the Y extends 30 mm from the nexus. Two sensors are perpendicular to the stem of the Y, 10 mm from the cut and 15 mm from the bottom of the Y. The third sensor is collinear with the stem and 27.7 mm above the Y junction.

Independent skin and fat layers were fabricated identically for mechanical characterization. Samples were cut into dog bone shapes using an ASTM D638 Type V cutting die.

3.2.2.4. Electromechanical Characterization

Rectangular sensor samples (10 mm x 64 mm) were cut from the sheet. Sensors were clamped into custom 3D printed, sandpaper lined grips on a dynamic mechanical tester (Electroforce Testbench, TA, USA). The sensors were preloaded to 0.1 N and the cross-sectional area was measured by laser micrometers (IG-028, Keyence Corp., Japan). The distance between thread electrode tips was taken as the gage length and was measured with calipers. Alternating square waves with an amplitude of ±2 V and a frequency of 50 Hz were applied by an impedance analyzer (VersaSTAT 3, Ametek, USA), and the resulting current was measured at a sampling rate of 500 Hz. The impedance analyzer was used to measure the electrical resistance of the third sensor located above the Y junction in the Y/V plasty demonstration.

The sensors first underwent a dynamic cyclic test with ten cycles at 0.05 Hz to 50%, 100%, 150%, 200%, 150%, 100%, and 50% strain, for a total of 70 cycles. This was immediately followed by a ramp to failure at 1% strain per second. Resistance vs. time results were consolidated by taking the mean resistance value of a combined negative and positive pulse (total duration of 0.04 s), and the results were synchronized manually to extrapolated strain vs. time results recorded from

the dynamic mechanical tester. All results were smoothed with a 20-point adjacent-averaging smoothing routine.

The mechanical properties of independent skin and fat layers were characterized with a uniaxial tensile test performed at two different strain rates: 0.16 mm/s (quasistatic) and 3.0 mm/s (dynamic). Samples were strained either to failure or the maximum range of the dynamic mechanical tester (150 mm). The fat layer results were smoothed with a 5-point adjacent-averaging smoothing routine.

3.2.2.5. Sensor Fabrication for Stability Study

A clear skin layer was prepared, and twelve 25-mm-long PEG-based organogel lines were dispensed using a 3D printer as described in Section 4.2. Then, conductive thread electrodes were placed directly into each line as described in Section 4.3. Then, the sensors were encapsulated using a clear skin layer of PDMS as described in sensor 4.2. The resistance of one sensor was continuously measured at 100 Hz with an LCR meter (LCR-600, Global Specialties) during the entire encapsulation process, and the first ten minutes and last 5 seconds of the 60-minute encapsulation process were recorded with a video camera (iPhone 11 Pro, Apple).

3.3. Results and Discussion

3.3.1. Organogel Synthesis and Characterization

Table 3-1. Fumed Silica Particles

Fumed Silica Product Number	BET* Surface area (m^2/g)	Surface Functional Group	Hydrophilic or Hydrophobic
Aerosil 380 ("A380")	380	hydroxyl	hydrophilic
Aerosil R974	170	methyl	hydrophobic
Aerosil R711	150	3-trimethoxysilyl methacrylate	hydrophobic

*BET refers to Brunauer-Emmett-Teller theory, which describes the physisorption of gas molecules on a surface to determine the specific surface area of a material.

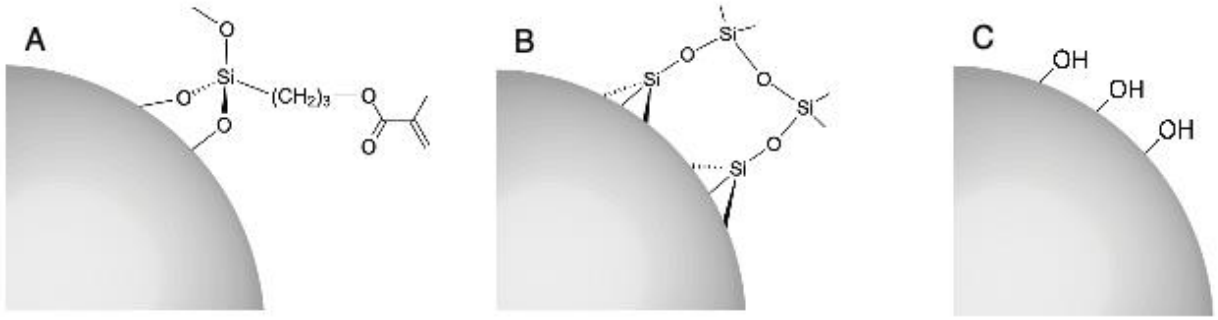

Figure 3-2. Different surface capping groups are present on Aerosil R711 (3-trimethoxysilylmethacrylate-capped), R974 (methyl-called), and 200 (hydroxyl-capped) fumed silica particles, respectively (a-c).

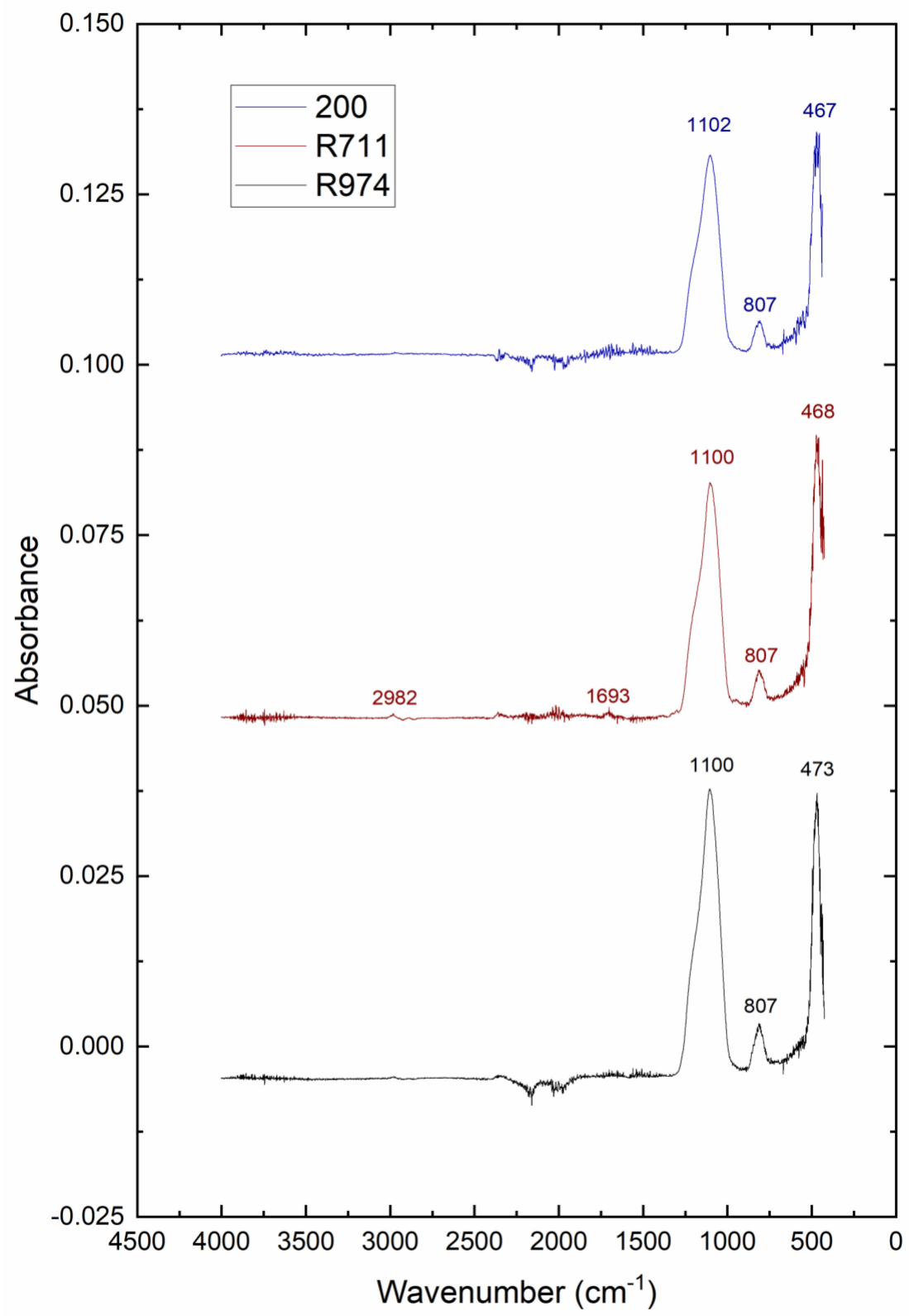

Figure 3-3. FTIR spectra of the fumed silica particles (A) revealed small C-H (2982 cm-1) and C=O (1693 cm-1) stretching regions for R711, is characteristic of a methacrylate functional group. Spectra for A380 and R974 were identical.

Fumed silica particles with different surface capping groups (Figure 3-2) were studied due to their efficacy as gelating agents in conductive ionogels [128]. A summary of the properties and FTIR spectroscopy results of the fumed silica particles investigated in this study can be found in Table 3-1. FTIR spectra (Figure 3-3) for hydrophilic A380 and hydrophobic R974 were identical, which is consistent with previous reports [202] despite the difference in surface functionalization. The peaks at 464-473 cm^{-1}, 807 cm^{-1}, and 1100-1104 cm^{-1} correspond to the bending vibrations, symmetric stretching vibrations, and asymmetric stretching vibrations of Si-O-Si, respectively [203–205] . The small peaks at 1693 cm^{-1} and 2982 cm^{-1} correspond to stretching vibrations of C=O and -CH_3 functional groups, respectively [205]. This result corroborates the manufacturer's claim that R711 has been functionalized with 3-trimethoxysilyl methacrylate.

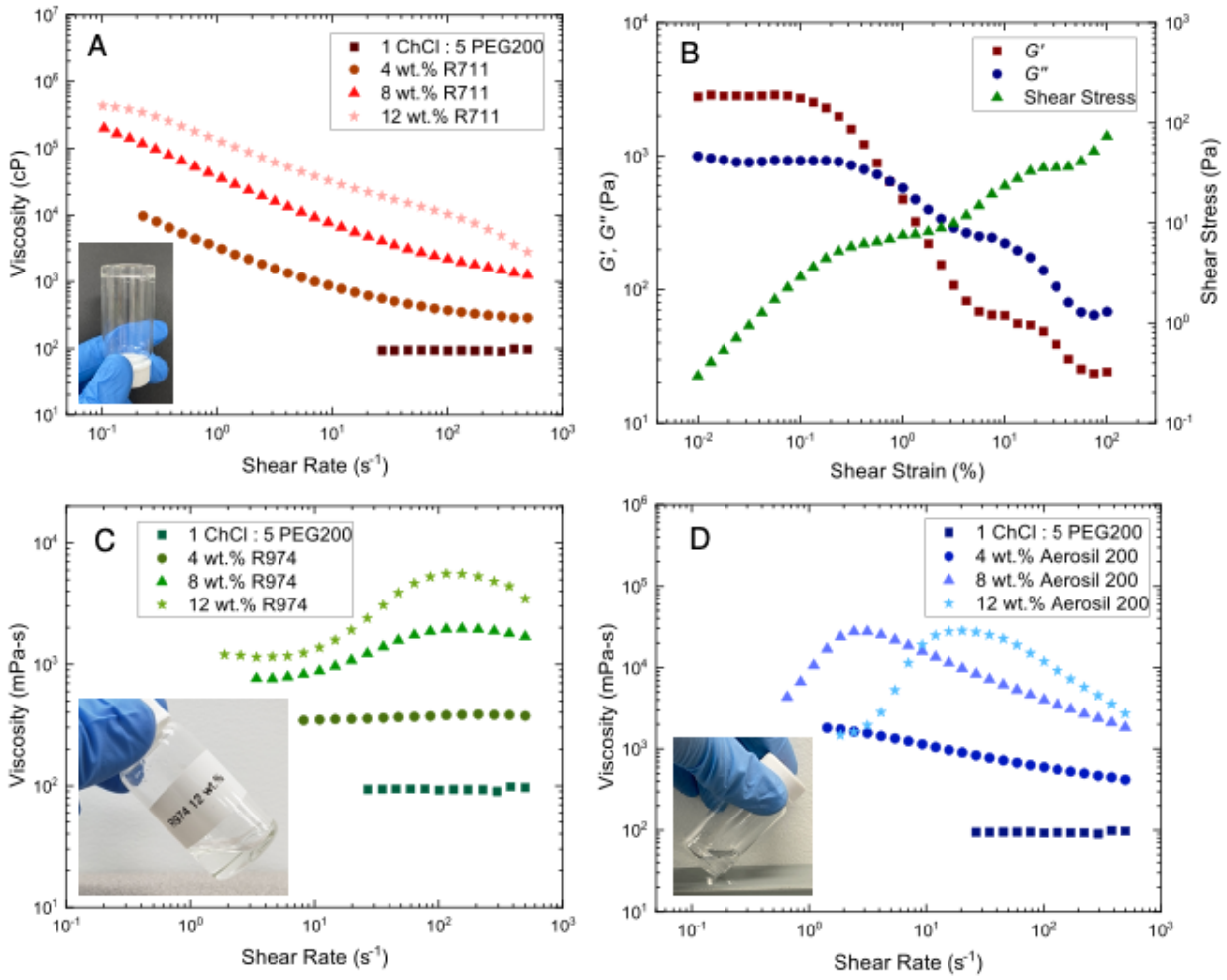

Figure 3-4. Viscosity measurements (A) and the inversion test (A, inset) revealed that the mixture formed a shear-thinning gel when 12 wt.% of the trimethoxysilylmethacrylate-coated fumed silica (R711) was added to the PEG-based deep eutectic solvent. An oscillatory amplitude sweep (B) performed on this mixture further indicated gel formation. In contrast, mixtures that used methyl-capped fumed silica (R974) consisted of shear-thickening fluids (C) when silica concentration was increased to 12 wt.%. A picture of the shear-thickening fluid with 12 wt.% R974 is shown in the inset of C. Mixtures that used hydroxyl-capped fumed silica (Aerosil 200) consisted of shear-thinning fluids at 4 wt.% and shear-thickening fluids at 8 and 12 wt.% (D). A picture of the shear-thickening fluid with 12 wt.% Aerosil 200 is shown in the inset of D.

Per viscosity flow curve measurements (Figure 3-4A) the addition of 4 or 8 wt.% R711 (3-trimethoxysilylmethacrylate-capped) fumed silica particles to the PEG-based DES converted the DES from a Newtonian fluid to shear-thinning fluids. Increasing the concentration of R711 to 12 wt.% resulted in a shear-thinning gel, a rheological quality necessary for effective 3D-printable inks[133]. The gel does not flow during the inversion test (Figure 3-4A, inset), a result indicative

of gelation. The presence of a linear viscoelastic region up to 0.1% strain followed by the crossover of the storage modulus (*G'*) and the loss modulus (*G"*) as shear strain is increased further corroborates the formation and subsequent destruction of a gel structure, respectively (Figure 3-4B) This rheological phenomenon has been observed for mixtures of a PEG400 (MW = 400 g/mol), and silica nanoparticles capped with 3-trimethoxysilylmethacrylate [206] or (3-glycidyloxypropyl)trimethoxysilane [207]. Shear-thinning, DES-based organogels utilizing cellulose nanostructures [208–210] or starch [211] as the thickening agent have been reported in literature, but shear-thinning DES-based organogels with fumed silica particles as the thickening agent have not been published. In contrast, viscosity curves for the samples containing R974 (methyl-capped) or 200 (hydroxyl-capped) fumed silica particles resulted primarily in shear-thickening fluids, or STFs (Figure 3-4C and D) This rheological phenomenon is typical of many silica particle-glycol formulations [212]. As flow increases, these fumed silica particles tend to aggregate in non-equilibrium aggregates known as hydroclusters [213]. These shear-thickening fluids are typical of hydroxyl-capped fumed silica particles mixed with PEG [214, 215]. With regards to R974, the incomplete coverage of the methyl capping group allows for hydrogen bonding between residual surface hydroxyl groups (~50%) on R974 and PEG that drive hydrocluster formation [216].

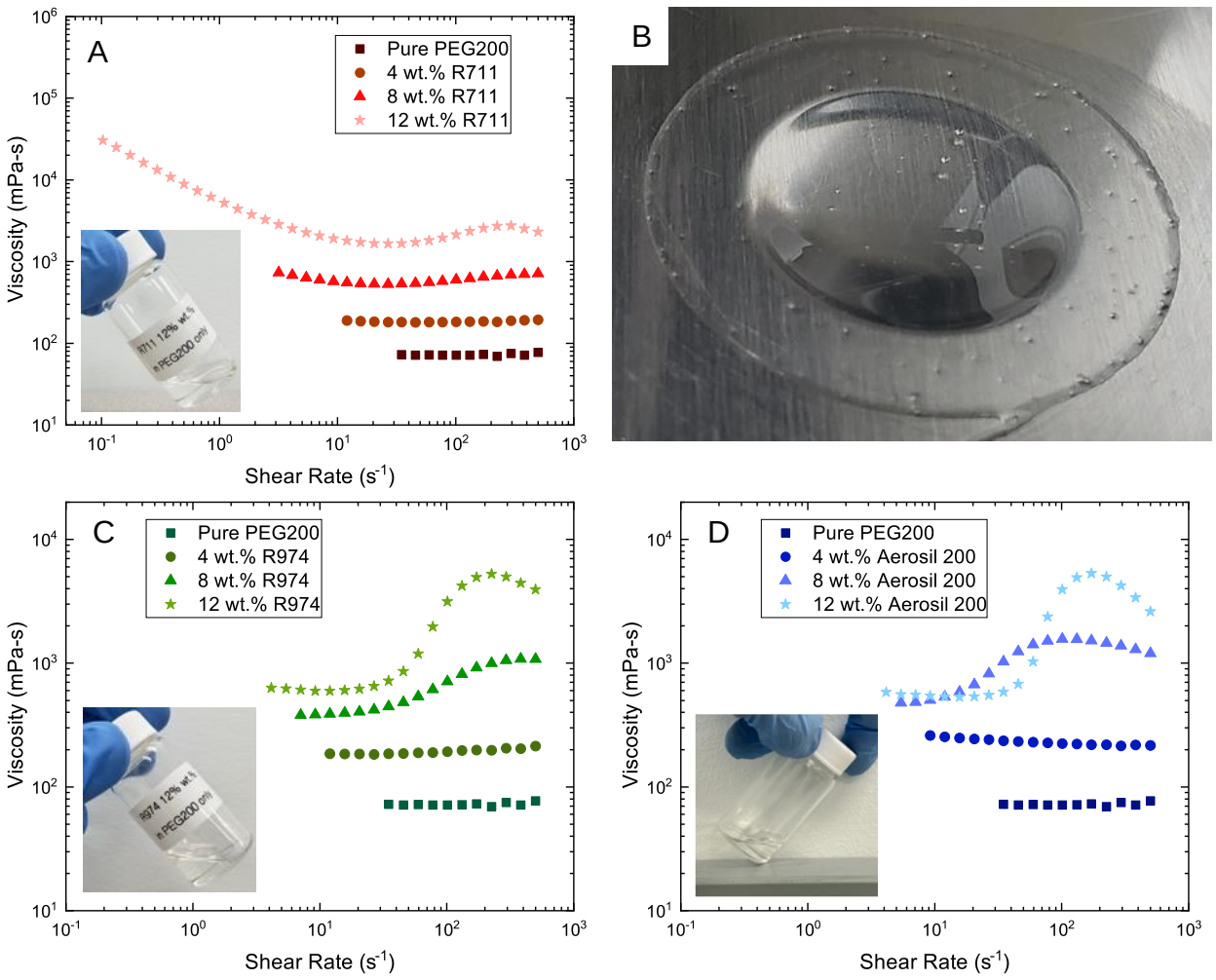

Figure 3-5. Viscosity flow curves of R711 (A), Aerosil 200 (B) and R974 (C) fumed silica mixed into pure PEG200. Mixtures with R711 resulted in fluids with predominately shear-thinning rheology (A, inset), while mixtures with R974 resulted in shear-thickening fluids (B, inset). Precipitation from PEG200 was observed on the rheometer stage for the sample containing 12 wt.% R9711 (D).

Viscosity flow curve measurements of PEG200 and fumed silica mixtures without ChCl revealed that the inclusion of ChCl increases the viscosity of the mixtures without affecting the predominant qualitative rheological trends (Figure 3-5). Mixtures of R711 and PEG200 resulted in either Newtonian or predominantly shear-thinning fluids (Figure 3-5A, inset), although a slight shear-thickening effect is noted for the liquid mixture containing 12 wt.% R711. In addition, after the viscosity flow curve measurement was taken, visible aggregates of R711 were observed

(Figure 3-5B) As no aggregates appeared in the PEG-based DES/R711 mixtures after rheological characterization or printing, this observation suggests that ChCl plays a role in inhibiting R711 aggregation. Literature suggests any electrostatic contributions to fumed silica particle stabilization in PEG would be weak [214, 216] due to the middling dielectric constant of PEG (ε ~ 8-13), [216] which reduces the electric field gradient that arises from any electric double layers (EDLs) forming around the silica particles [214]. In turn, a lowered electric field gradient results in low electrostatic repulsion between particles. Therefore, we speculate that ChCl inhibits aggregation because its presence increases the mass loading and the viscosity of the mixtures; a 1 ChCl : 5 PEG200 molar ratio corresponds to a sizeable ChCl concentration of 12.3 wt.%. Mixtures of R974 (Figure 3-5C) or Aerosil 200 (Figure 3-5D) and PEG200 resulted in either Newtonian or shear-thickening fluids. The absence of ChCl decreases viscosity values without affecting the predominate rheological trends, but the decrease is more modest than those observed in the R711/PEG200 mixtures. Similar rheological trends were reported for mixtures composed of several lithium salts in PEG300 and fumed silica particles capped with various surface functional groups [214, 216].

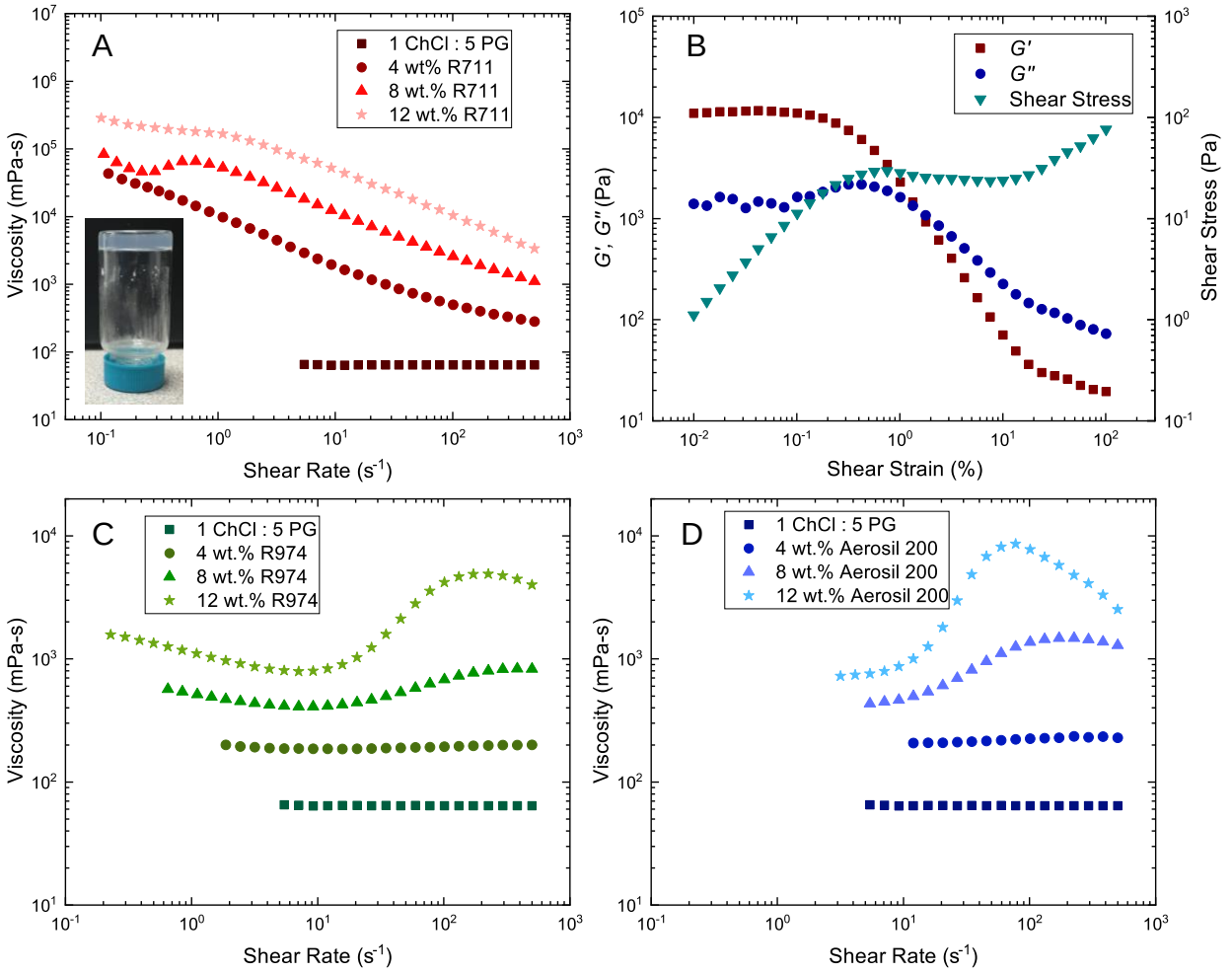

Figure 3-6. Rheology experiments of fumed silica mixed into the PG-based deep eutectic solvent. Viscosity measurements (A) and the inversion test (A, inset) revealed that the mixture formed a shear-thinning gel when 12 wt.% of the methacrylate-coated fumed silica (R711) was added to the PG-based deep eutectic solvent. An oscillatory amplitude sweep (B) performed on this mixture further indicated gel formation. In contrast, mixtures that used R974 (C) and Aerosil 200 (D) fumed silica consisted of shear-thickening fluids) when silica concentration was increased to 12 wt.%.

The rheological trends of the PG-based DES/fumed silica mixtures were similar to those of the PEG-based DES/fumed silica mixtures (Figure 3-6), which evinces a general rheological trend for mixtures consisting of fumed silica particles and deep eutectic solvents that utilize glycols as the hydrogen bond donor.

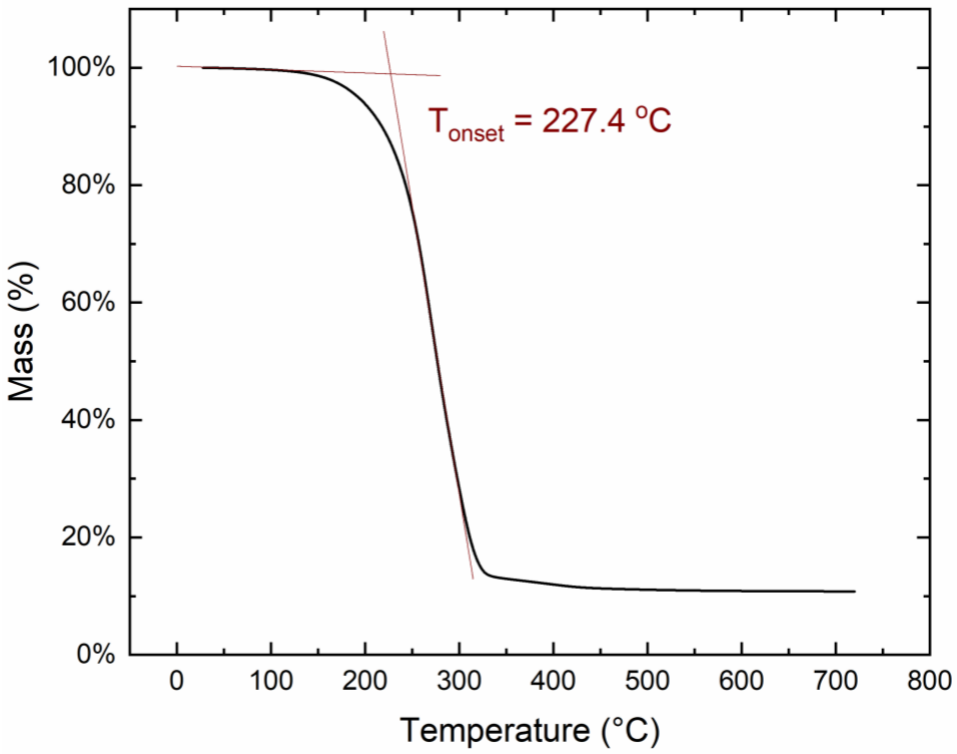

Figure 3-7. Thermogravimetric Analysis (TGA) curve of the 5 PEG200 : 1 ChCl organogel with 12 wt.% R711.

As the vapor pressure of PEG200 (1.69×10^{-2} Pa) [217] is three orders of magnitude lower than that of PG (18.9 Pa) [218] and the onset decomposition temperature of the PEG-based organogel was suitably high at 227.4 ºC (Figure 3-7) the PEG-based organogel was selected as the conductive medium in the stretchable strain sensors reported here.

3.3.2. Sensor Fabrication and Electromechanical Characterization

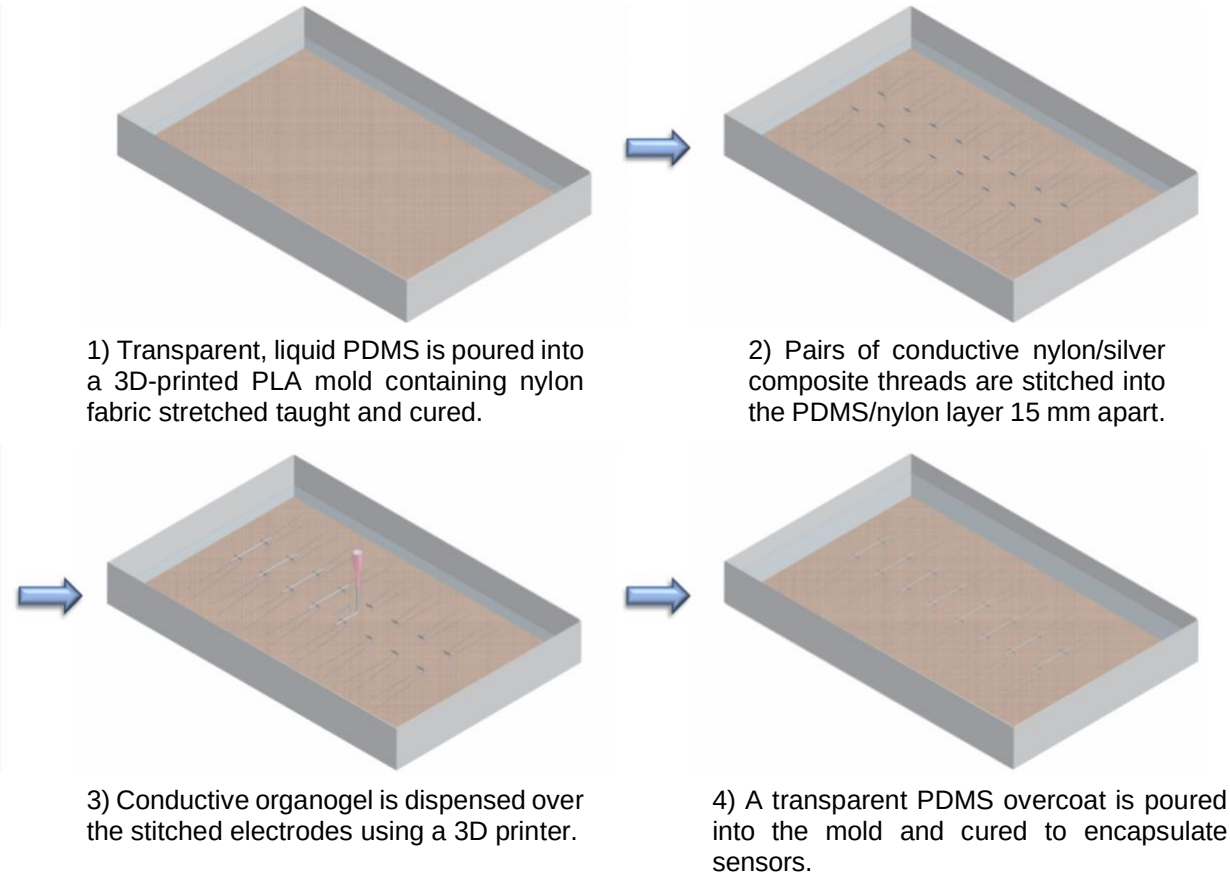

Figure 3-8. Fabrication schematic of freestanding organogel strain sensors with stitched conductive threads as electrodes.

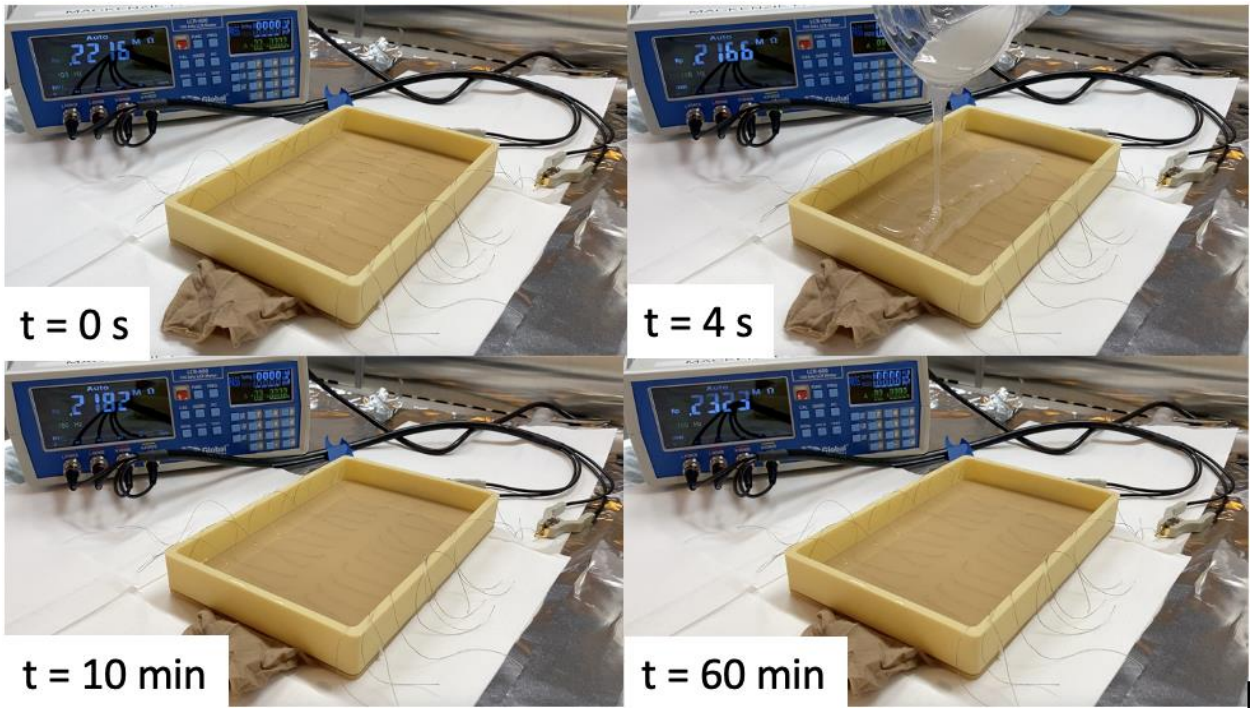

Figure 3-9. Screenshots of a video capturing the encapsulation process of organogel sensors with PDMS. All changes in resistance of the sensor (second from the top-right) were less than 5% of the starting value.

Pairs of silver/nylon conductive composite electrodes were stitched approximately 15 mm apart into the PDMS substrate containing a sheet of nylon (Figure 3-8). This sheet of nylon serves as mechanical support for both these electrodes and for stitches performed in a dermatological simulation. Next, 25 mm lines of organogel were dispensed on the PDMS substrates using the 3D printer. The extra length ensured a complete connection between pairs of stitched electrodes. After printing, deposition of the subsequent PDMS layer encapsulated the printed lines (Figure 3-9) and plugged all holes made by the stitched electrodes. Sensors were cut into 64 mm x 10 mm rectangular samples for electromechanical characterization.

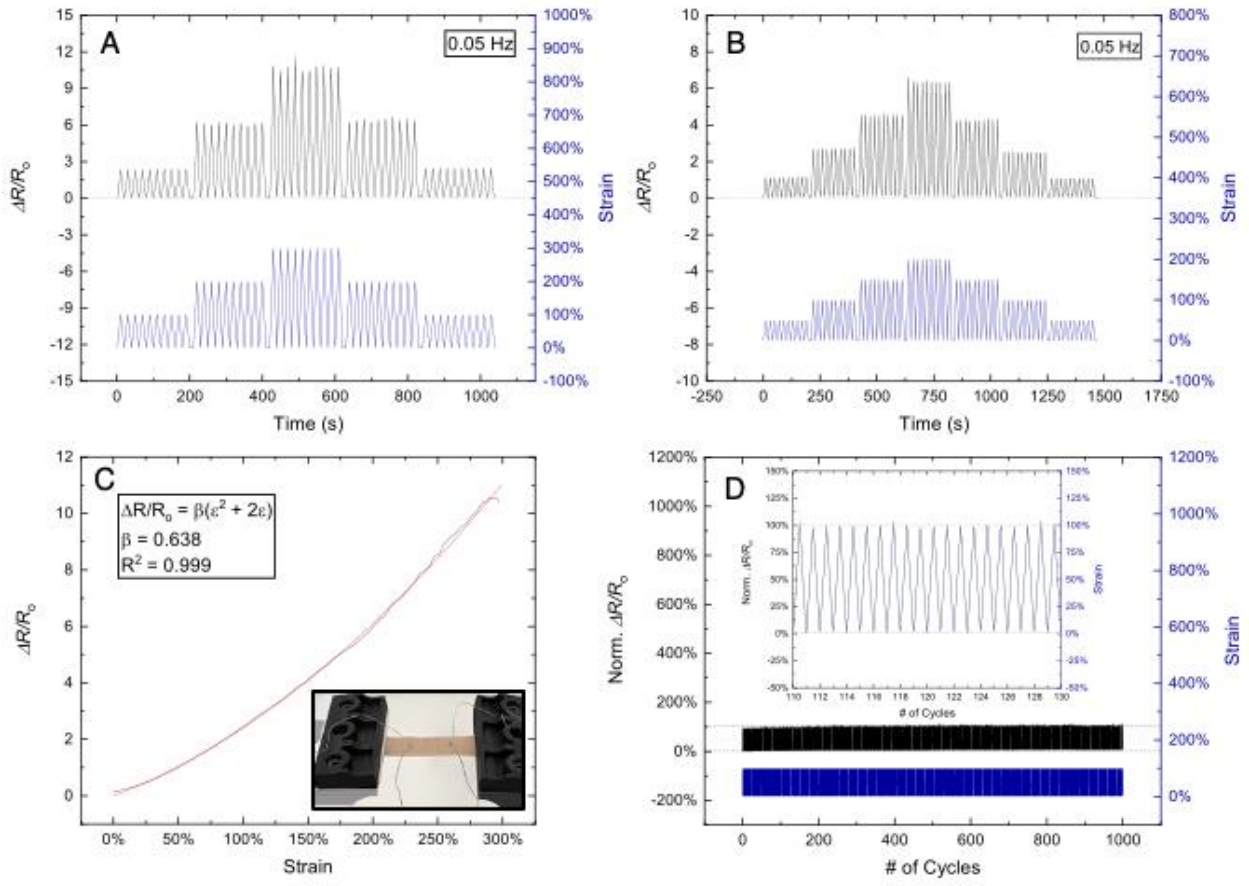

Figure 3-10. Dynamic testing results (A and B) demonstrated a consistent electrical response up to 300% strain and no baseline drift for a frequency of 0.05 Hz. Horizontal dashed lines have been added to emphasize the lack of signal drift. An example of an extracted ramp test from a C revealed a parabolic relationship between the relative change in resistance and strain up to 300% strain. A picture of a strain sensor clamped in the electromechanical testing grips is shown in the inset of c. Cyclic testing up to 100% strain and 0.3 Hz resulted in minimal drift up to 1,000 cycles (D) and normalized relative resistance results indicated excellent tracking of the amplitude and frequency of sensor actuation (D, inset).

Figure 3-10 indicated consistent, drift-free performance by the sensors. Dynamic ramp tests up to 300% strain (Figure 3-10A and Figure 3-11A) and up to 200% strain (Figure 3-10B and Figure 3-11B) show a monotonic response with a consistent return to the baseline resistance value for all ten cycles at varying amplitudes and frequencies. Furthermore, exposure to large strains do not distort the amplitudes of subsequent smaller strains. This reliable electromechanical response enables simplified sensor readout analysis compared to that required for composite-based sensors that demonstrate a nonmonotonic response [182–184]. As the strain failure limit of viscus [61] and

dermal[66] tissue falls below 300% strain [67], the 300% strain amplitude achieved by these sensors endow them with integrability in a wide range of realistic tissue models.

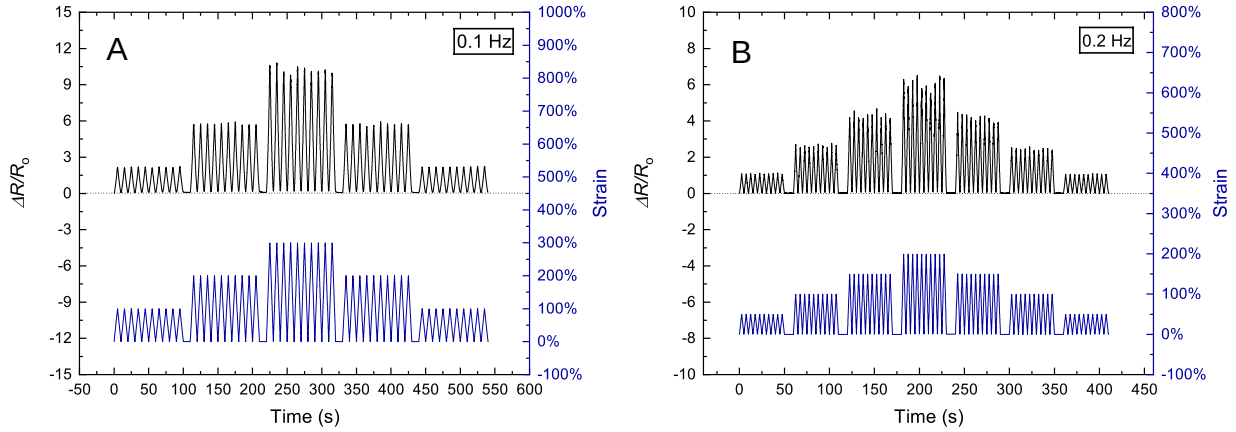

Figure 3-11. Additional dynamic electromechanical testing results of strain sensors at increased frequencies. A consistent electrical response up to 300% strain for frequencies of 0.1 Hz (a) and 0.2 Hz (b) and no baseline drift were observed. Horizontal dashed lines have been added to emphasize the lack of signal drift.

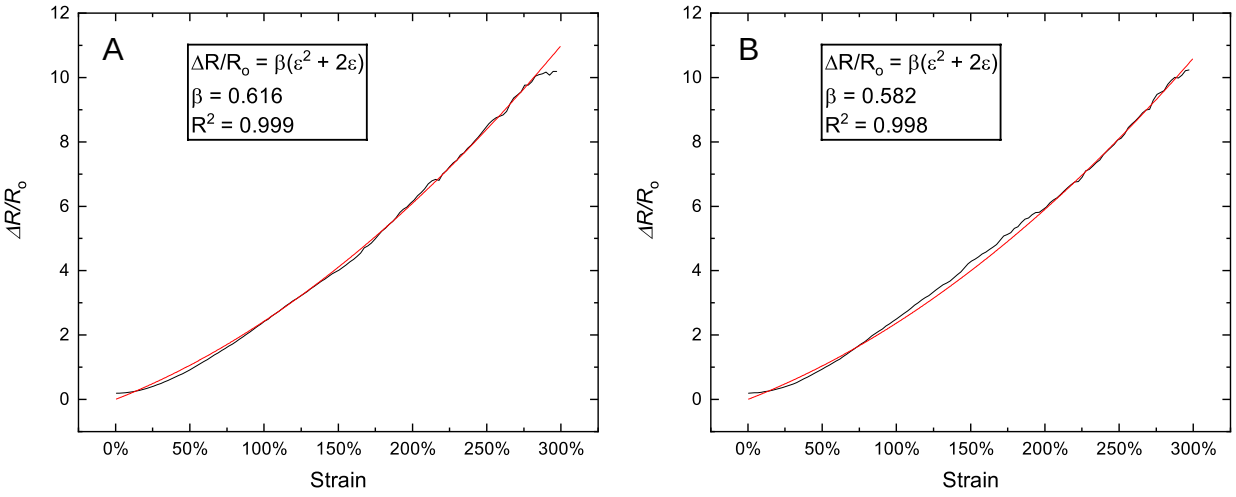

Figure 3-12. Additional ramp tests extracted from peak 6 (a) and peak 9 (b) of the 300% strain amplitude portion of Figure 3b.

Ramp tests and hysteresis analysis extracted from the twenty peaks with a strain amplitude of 300%. The ramp tests (Figure 3-10C and Figure 3-12) show a strong parabolic relationship between the relative change in resistance and strain (R^2_{avg} = 0.998 ± 0.001, n = 20). The fitting

parameter, β, reflects the contact resistance (R_c) of a strain sensor with a cylindrical sensing channel [81, 146]:

$$\beta = \frac{(R_o - 2R_c)}{R_o} \qquad (3.1)$$

where R_o represents the initial resistance of the sensor. A larger β value ($0 \leq \beta \leq 1$) indicates a lower contact resistance. The average β value of 0.621 ± 0.059 taken from the twenty peaks with a 300% strain amplitude (Fig. 3B and Supplementary Fig. 9b) is predictably lower than those of fluidic sensors that use wire electrodes (0.746-0.797 [146, 219]) due to the inferior conductivity of composite electrodes, but effective sensing is still realized, demonstrating the electromechanical robustness of the composite thread electrodes in place of wires.

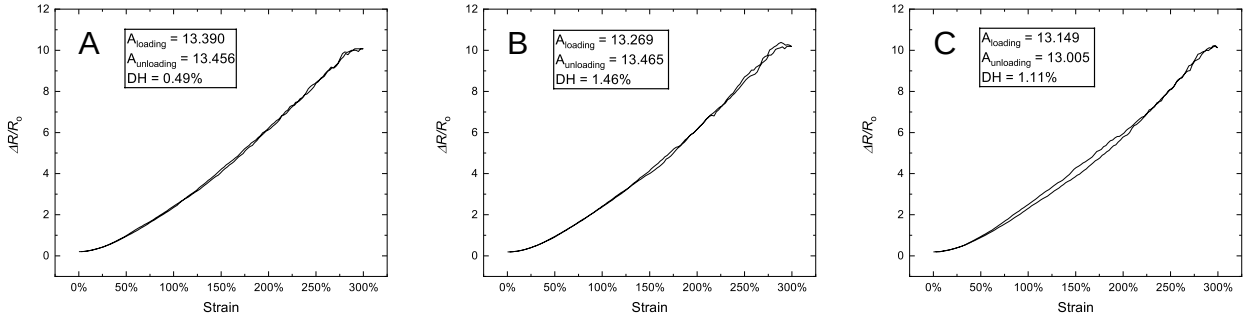

Figure 3-13. Representative extracted hysteresis results taken from peaks 3 (a), 6 (b), and 9 (c) of the 300% strain amplitude portion of Figure 3b. The degree of hysteresis (DH) is defined as DH = $A_{loading}$ - $A_{unloading}$)/$A_{unloading}$ x 100%, where $A_{loading}$ and $A_{unloading}$ are the areas underneath the loading and unloading curves, respectively.[24]

The extracted hysteresis results (Figure 3-13) show a low average degree of hysteresis of 1.34% ± 0.76% (n = 20), a value superior to those reported in fluid-based sensors using wires as electrodes over a similar strain range [24, 106, 146–148, 219]. The compliance and porosity of composite thread electrodes enables improved adhesion between the electrodes and PDMS to reduce the

degree of hysteresis. Cyclic testing **(**Figure 3-10D) revealed a stable, drift-free performance of sensors stretched to 100% strain at 0.3 Hz for 1,000 cycles, and the actuation amplitude and frequency tracked flawlessly (Figure 3-10D, inset), indicating excellent reproducibility of these sensors. In comparison, 3D-printed deep-eutectic-solvent sensors recently reported by Lai *et al.* show significant baseline drift after 100 cycles of 30% dynamic strain [210].

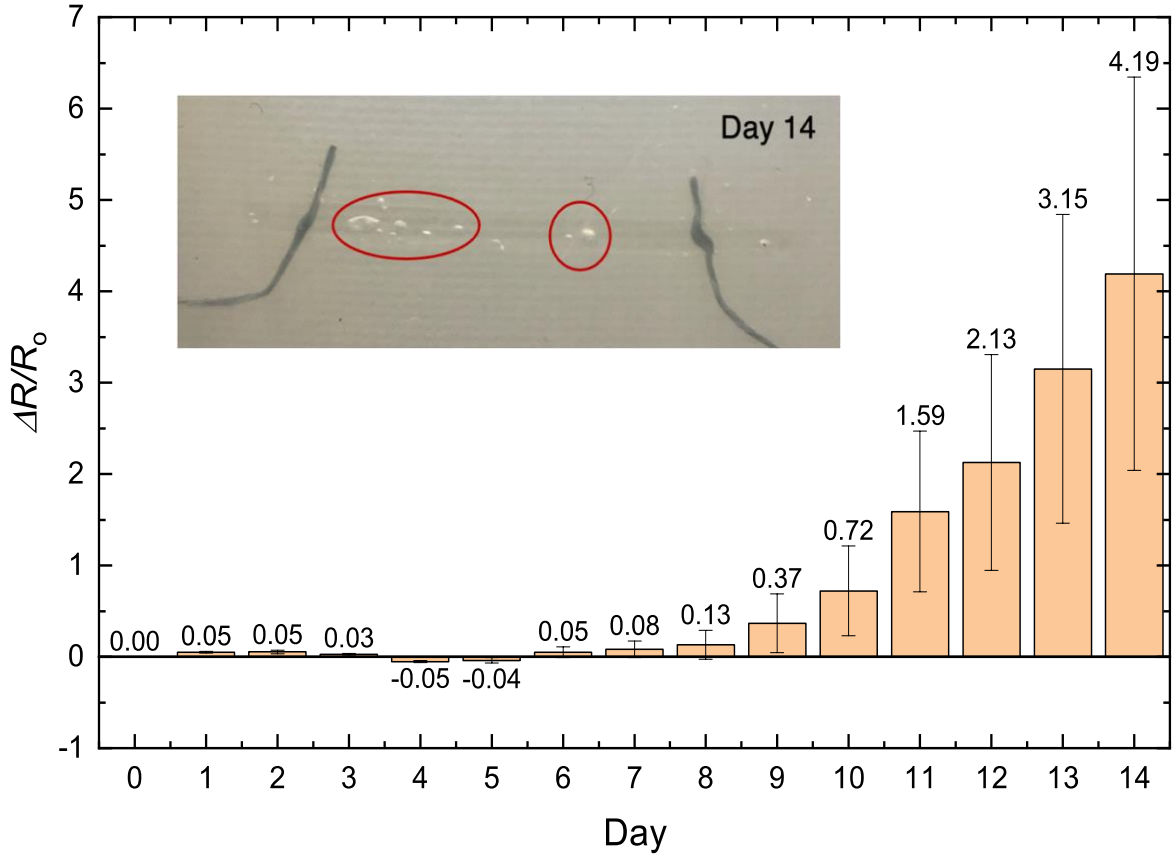

Figure 3-14. Long-term stability measurements of 12 sensors stored in a desiccator with an average relative humidity of 24% (±5%) and an average temperature of 24 °C. The relative change in resistance increased beyond 10% starting day 8, and bubbles within the channel were visible in the sensor channel on Day 14 (highlighted by red circles in the inset). The error bars represent one standard deviation.

Long-term stability measurements of twelve sensors shown in Figure 3-9 stored in a desiccator revealed stable resistance readings up to one week after fabrication (Figure 3-14) The average relative resistance of sensors increased above 10% starting Day 8; bubbles appeared in most

organogel channels by Day 14 (inset), when the average relative change in resistance had increased fourfold. The presence of bubbles introduces pinch points within the channel, which increase the relative resistance. The increase in standard deviation of readings reflects the random, irregular distribution of bubbles in the channel. I speculate bubble formation is indicative of leakage and/or syneresis, but further elucidation of this phenomenon is the subject of future investigation.

3.3.3. Y/V Plasty Demonstration

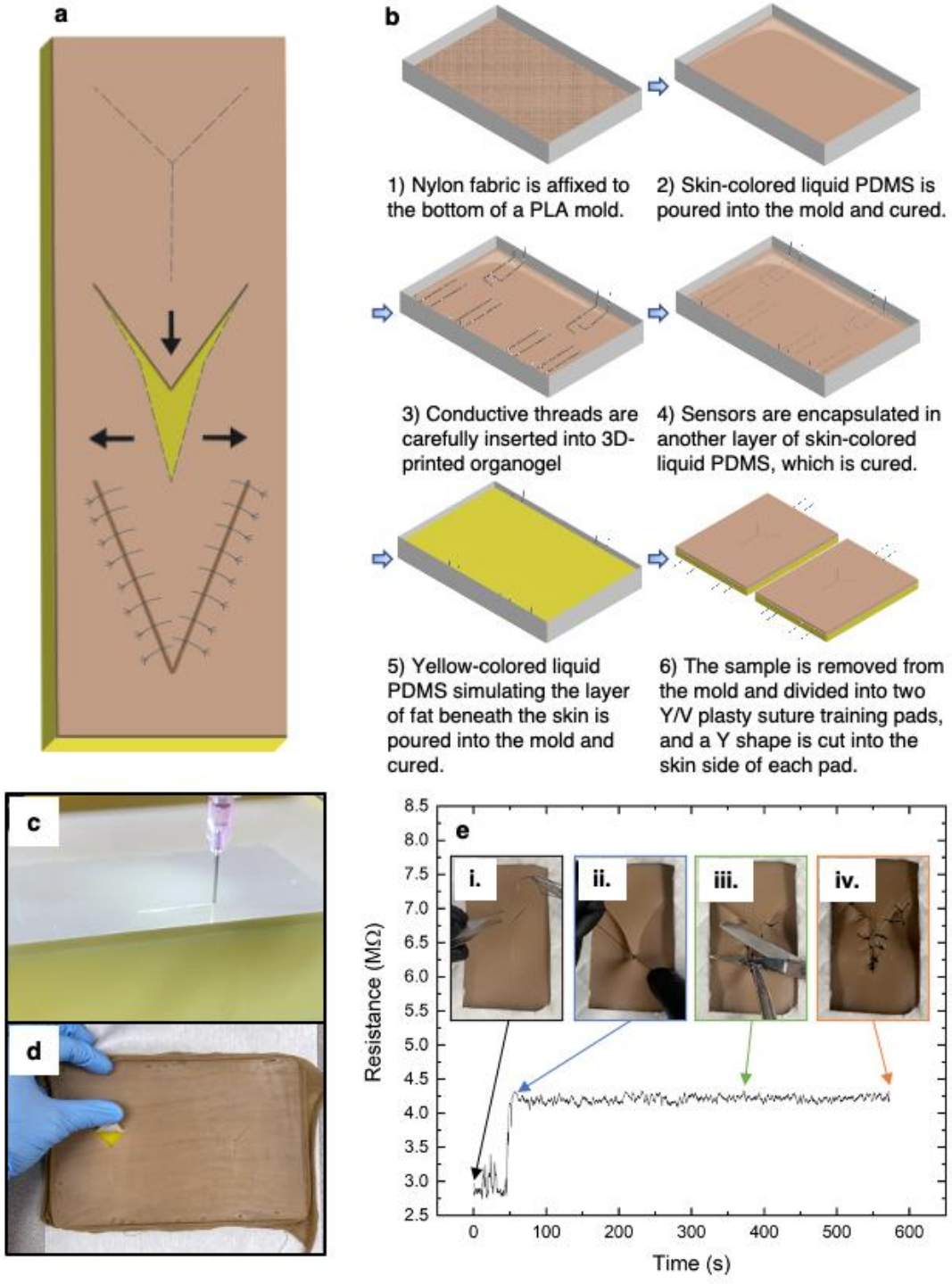

Figure 3-15. In a Y/V plasty, a Y-shaped incision with the vertex located at the site of unwanted tissue is cut into the dermal layer, and the flap in the skin layer is pulled down and sutured into a V shape after excision (A). A sensorized Y/V plasty tissue suturing pad (B) is fabricated by encapsulating a conductive organogel and conductive thread electrodes within the skin layer of the pad. This organogel is 3D-printable (C) and visually imperceptible in the skin

layer of the pad (D). The strain sensor located in the skin flap demonstrated a clear response to the elongation experienced by the flap during suturing (E).

A Y/V plasty (Figure 3-15A) is a common, versatile technique in plastic surgery utilized to excise undesired tissue and minimize the formation of hypertrophic scars arising from cutaneous wounds, so Y/V plasty training is considered an important component of surgical education[220]. Therefore, a Y/V plasty suture training pad with monolithically integrated organogel strain sensors was developed (Figure 3-15B). The pink- and yellow-colored PDMS layers represent the skin and fat layers, and the silicone recipes were selected to simulate a lifelike mechanical response and feel. Tensile tests were performed on silicone skin and fat samples (Figure 3-16). Consistent with viscoelastic materials and previous literature regarding characterization of tissue[221, 222], the elastic modulus increased for both the skin and fat samples as the strain rate increased from 0.16 mm s^{-1} (quasistatic) to 3.0 mm s^{-1} (dynamic). The fat samples possess lower elastic moduli than the skin samples due to the increased fraction of LV deadener in the silicone composition. The PEG200, R711-based organogel was 3D-printed onto the PDMS skin layer (Figure 3-15C) to serve as the strain sensing medium; conductive threaded electrodes were carefully inserted into every organogel channel and run to the edges of the pad to preserve the visual fidelity of the tissue model (Figure 3-15D). A Y/V plasty suturing procedure was performed on a tissue model with monolithically integrated strain sensors (Figure 3-15E) the resistance of the strain sensor located in the flap was selected for measurement. The resistance of this sensor rapidly increased in response to the initial elongation experienced by the flap (Figure 3-15E, insets i. and ii.). As more sutures were stitched, the resistance of the sensor remained constant (Figure 3-15E, insets iii. and iv.). This was indicative of a successful suturing procedure as loosening sutures would result in retraction of the flap and a corresponding decrease in resistance.

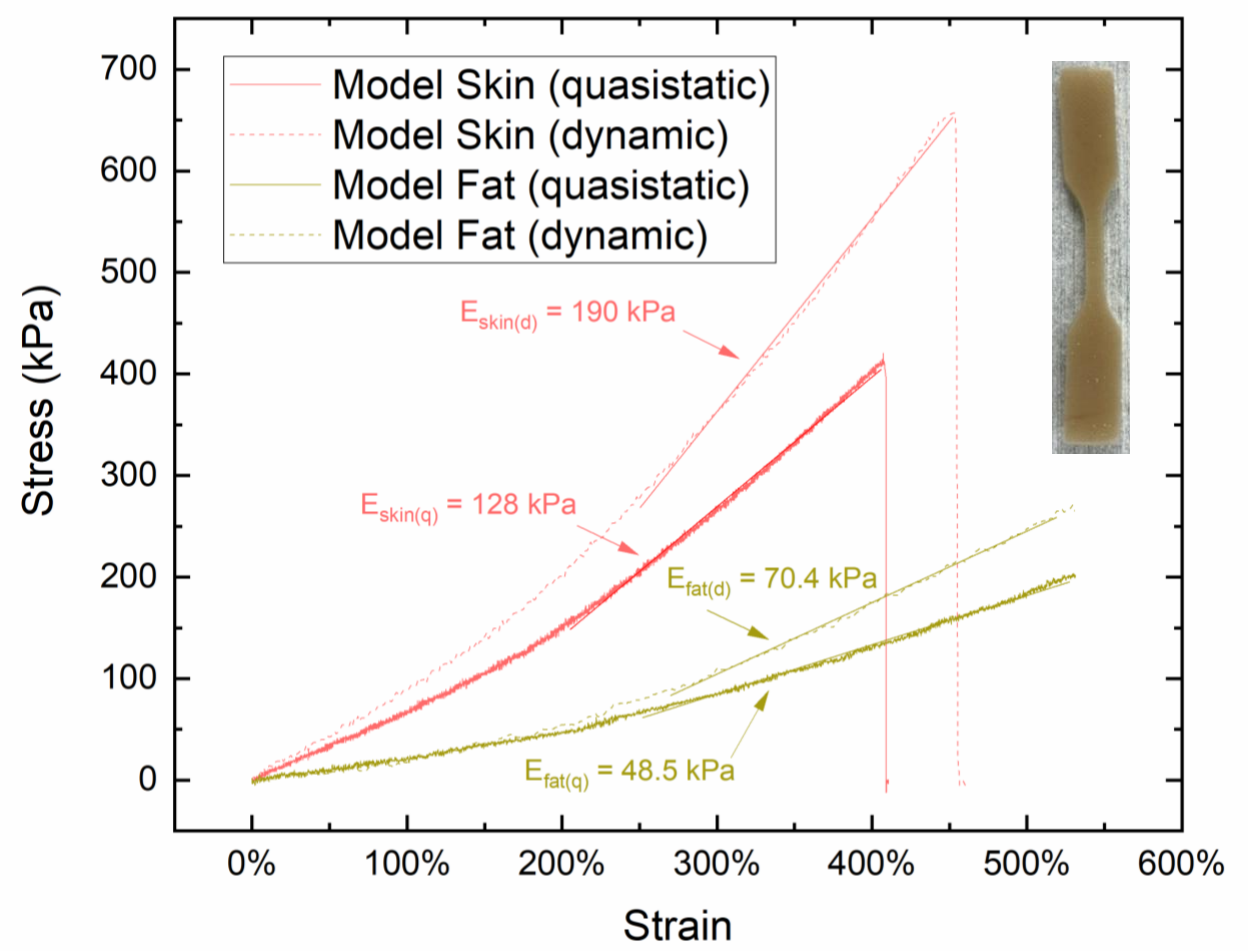

Figure 3-16. Stress-strain results from uniaxial tensile tests on dog bone samples of the model skin and fat tissue used in the Y/V Plasty tissue model. $E_{skin(d)}$, $E_{skin(q)}$, $E_{fat(d)}$, and $E_{fat(q)}$ are the elastic moduli of the skin samples tested at 3 mm/s, skin samples tested at 0.16 mm/s, fat samples tested at 3 mm/s, and fat samples tested at 0.16 mm/s, respectively. The inset shows a picture of a model skin sample cut into a dog bone shape with an ASTM D638 Type V cutting die.

3.4. Conclusion

In this chapter, I introduced a novel class of shear-thinning organogels, which combine fumed silica particles with a deep eutectic solvent comprised of choline chloride and biofriendly glycols. In addition, I report a stretchable strain sensor using this 3D-printable and inexpensive organogel as the sensing medium and conductive composite threads as the electrodes. Finally, I showcase a Y/V plasty suture training pad with monolithically integrated organogel strain sensors; the small sensor footprint preserves the fidelity of the simulation. The lack of drift, achievable

strain amplitudes of 300% strain, and simple, monotonic response of these sensors suggests widespread applicability of this sensing technology to the quantification of soft tissue deformation in medical simulation. Reliable quantification of tissue deformation can generate real-time, objective feedback for surgical rehearsal and medical education. We expect sensorized tissue models such as the additively manufactured one reported here to improve practitioner skill and confidence, leading to lower medical error rates. Future studies will focus on the development of organogel compositions with improved stability. Also, future work will focus on the development of simulation modules that require simultaneous multi-sensor detection of strain, as recent studies have reported such capabilities using piezoresistive ionogel-based soft sensors[128, 223]. In addition, future work will include validation studies of the Y-V model with surgical trainees and also will expand on applications and capabilities using this 3D-printable gel. As the surface of the fumed silica utilized to induce a shear-thinning rheology is capped with the UV-sensitive 3-trimethoxysilylpropylmethacrylate, UV-enabled technologies, such as sensors using 3D-printed auxetic frameworks [224] or UV-curable supercapacitors [225], will be explored.

Chapter 4. All-Printed Piezoelectric Sensors

4.1. Motivation

Piezoelectrics, which deform elastically in response to an electric field, have demonstrated versatile applications in sensing [226], energy harvesting [227], actuation [228], and tissue regeneration [229], among many others. Flexible, ultralight, low cost, and non-toxic piezoelectric sensors can enable the structural health monitoring and impact detection on curvilinear and dynamic surfaces, such as architectural structures, vehicles, and industrial equipment. Vibrational data from these sensors can be used to optimize performance and safety, reduce failure and maintenance downtime, and identify threat location. Current state-of-the-art options, however, require tradeoffs between flexibility, performance, toxicity, and cost. The ferroelectric ceramic lead zirconate titanate (PZT) has been widely implemented in commercial piezoelectric applications because of its superior piezoelectric coefficient (d_{33} of 500-600 pC/N) [230]. However, the large lead content (>60% Pb by weight), high processing temperatures (>150 ^{o}C), and brittle nature of PZT (fracture for strains <1%) [231] have limited its integration as thin films in a broader range of sensors, medical devices, human electronics interfaces and flexible electronics. These inherent limitations have inspired the search for alternative piezoelectric materials that are non-toxic, solution-processable at low temperatures, and flexible [232–235]. Inorganic ceramic alternatives, such as barium titanate (BTO) [236] or potassium sodium niobate (KNN) [237], suffer from similar processing problems that plague PZT and furthermore possess inferior piezoelectric coefficients of 191 pC/N [238] and 416 pC/N [230], respectively. The polymer polyvinylidene fluoride (PVDF) [239] and its various copolymers [240] represent the most promising non-ceramic alternative to inorganic ceramic piezoelectrics due to their chemical stability, flexibility and potential for scalable processing [241]. However, their low piezoelectric

coefficients (d_{33} of 13-38 pC/N) [242–244] and low-temperature processing challenges [245–248] have limited their efficacy in commercial applications. Organic molecular ferroelectrics, such as diisopropylammonium bromide (d_{33} of 18 pC/N) [249–252] and imidazolium perchlorate (d_{33} of 41 pC/N) [253–255], also are an intriguing, solution processable option. However, organic molecular ferroelectrics are not suitable for rapid, solution-processable fabrication due to their uniaxial piezoelectric axis. This property necessitates slow, careful processing to grow piezoelectric domains with textured long-range order that induces macro-scale piezoelectric effects [256, 257]. In addition, their piezoelectric coefficients are either comparable or inferior to those of PVDF and its copolymers.

Inorganic-organic hybrids, such as lead halide perovskites, have received increasing attention due their promising functional properties, low temperature solution processing capabilities, and an exciting range of compositional and molecular tuning [233, 235, 258]. Unlike their organic counterparts, inorganic-organic hybrid molecular ferroelectrics possess large d_{33} values ranging from 80 to 1540 pC/N, and the low dielectric constant of these hybrids (ε_r ~10-20) results in extraordinarily large piezoelectric voltage coefficients (g_{33}) ranging from 660 to 1,318 V-m/N [259–261]; exceeding the g_{33} values of commercial piezoelectrics, such as PZT (20-40 x 10^{-3} V-m/N) [262] and PVDF (286 x 10^{-3} V-m/N) [260]. The g_{33} coefficient is used to compare the sensing performance of piezoelectrics. Furthermore, these high-performing inorganic-organic hybrids possess multiple (4-12) equivalent ferroelectric axes [263–268]. Multiaxial ferroelectricity simplifies fabrication by relaxing the requirement for aligned crystal orientation. Polycrystalline samples with randomly oriented ferroelectric domains can be poled with an electric field to align domains along the same direction after fabrication. In turn, recent reports have responded to calls for demonstrations of practical applications of polycrystalline molecular ferroelectrics [269, 270]

by showcasing piezoelectric nanogenerators [259–261, 271–275] and sensors [274, 276, 277]. All reported devices use a three-layer structure consisting of a poled polycrystalline ferroelectric or a poled, ferroelectric-based composite sandwiched between two electrodes. Piezoelectric nanogenerators harvest electricity generated by ambient vibrations, while sensors detect local changes in strain or pressure. However, the synthesis and fabrication techniques used for the piezoelectric component, such as drop-casting thin films from solution or slow evaporation of solvent to induce single crystal growth, are not rapid nor readily scalable despite the compatibility of these materials with high-throughput fabrication processes. Demonstrations of scalable synthesis of these piezoelectric materials and rapid fabrication of devices are lacking in the field.

4.2. Background

4.2.1. *Basic Theory of Dielectrics, Piezoelectrics, and Ferroelectrics*

A brief overview of dielectrics, piezoelectrics, and ferroelectrics is given here; detailed reading can be found in [278]. A dielectric material is defined as an electrical insulator that can be polarized by an electric field. The electric displacement field D_i in the 'i' direction can be defined as [278]:

$$D_i = \varepsilon_o E_i + P_i \quad (1)$$

Where E_i is the applied electric field, ε_o is the permittivity of free space, and $\boldsymbol{P_i}$ is the polarization (the total dipole moment per unit area). In the case of a homogeneous, linear dielectric, the polarization can be defined as [278]:

$$P_i = \chi_{ij} E_j \quad (2)$$

Where χ_{ij}, a second-rank tensor, is the electric susceptibility of a material. Combining equations (1) and (2) yields:

$$D_i = \varepsilon_o E_i + \chi_{ij} E_j = \varepsilon_o \delta_{ij} E_j + \chi_{ij} E_j = \varepsilon_{ij} E_j \quad (3)$$

Where δ_{ij} is the Kronecker delta and the dielectric constant ε_{ij} is approximate to χ_{ij} in ferroelectric materials (as $\chi_{ij} >> \varepsilon_o \delta_{ij}$). Polarization in dielectrics is driven by three distinct mechanisms: 1) electronic polarization (the shifting of electron cloud density within atoms), 2) ionic polarization (the displacement of ions), and 3) orientational polarization (rotation of a molecule with a permanent dipole moment). Polarization depends on the frequency of an applied oscillating electric field. As the frequency increases, the orientational polarization response will drop out first followed by ionic polarization followed by electronic polarization.

Piezoelectrics are a subset of dielectrics that generate an electric charge in response to an applied stress (the direct piezoelectric effect) or deform in response to an electric field (the converse piezoelectric effect). For the direct piezoelectric effect, the dielectric displacement of a piezoelectric is defined as:

$$D_i = d_{ij} T_j \quad (4)$$

$$d_{ij} = \begin{bmatrix} d_{11} & d_{12} & d_{13} & d_{14} & d_{15} & d_{16} \\ d_{21} & d_{22} & d_{23} & d_{24} & d_{25} & d_{26} \\ d_{31} & d_{32} & d_{33} & d_{34} & d_{35} & d_{36} \end{bmatrix} \quad (5)$$

Where d_{ij} is a third-order tensor representing the piezoelectric coefficient (with units of C/N), and T_j represents the stress applied to the piezoelectric. Short-hand notation ('d_{ij}') is used here rather than long-hand ('d_{ijk}') notation as stress and strain are symmetrical tensors (implying $d_{ijk} = d_{ikj}$), reducing the number of independent coefficients from 27 to 18. The subscripts '1, 2, and 3' refer to normal forces acting in the x-, y-, and z- directions, while the subscripts '4, 5 and 6' refer to shear forces with rotations centered about the x-, y-, and z- axes The most common piezoelectric coefficient reported in literature is the d_{33} coefficient, which corresponds to the dielectric displacement in the z-direction in response to a normal force applied in the same direction.

For the converse piezoelectric effect, the strain induced in a piezoelectric by an applied electric field, x_j, is defined as:

$$x_i = d_{ij}E_j \quad (6)$$

In this case, d_{ij} has units of m/V, which is equivalent to C/N; this reflects the thermodynamic identicalness of the direct and converse piezoelectric effects [278]. For completeness, strain and stress are related via the fourth-rank compliance tensor, s_{ij}:

$$x_i = s_{ij}T_j \quad (7)$$

Where the indices i,j = 1-6.

Ferroelectrics are a subset of piezoelectrics that possess a permanent reversible spontaneous dipole. The direction of this dipole can be switched via an applied electric field. Per Neumann's principle, the symmetry properties of a material must include its crystallographic point group. Crystallographic point groups contain all non-translational symmetry operations that can be performed on a crystal: reflection, rotation, or rotoinversion. There exist 32 classes of crystallographic point groups. 20 of these 32 groups are non-centrosymmetric, meaning any material with a crystal structure in this point group can show the piezoelectric effect. Ten of these point groups (1, 2, *m*, *2mm*, 4, 4*mm*, 3, 3*m*, 6, and 6*mm*) possess a unique polar axis, meaning all ferroelectric materials must belong in one of these point groups [278]. Also, ferroelectrics only keep their ferroelectric properties for a given temperature range. As the temperature is increased beyond a threshold temperature (the Curie Temperature, T_c), a ferroelectric will change phases and become paraelectric as the crystal symmetry is increased in the new phase. Dielectric anomalies accompany the structural transition at this temperature. Therefore, the Curie temperature determines the thermal operating range of a ferroelectric material [278].

4.2.2. *Polycrystalline Ferroelectrics, Poling, PE Loops, and Piezoelectric Characterization*

As described in the previous section, ferroelectricity and piezoelectricity are tensor properties and therefore depend on the symmetry of the crystal. Crystals with more symmetry require fewer coefficients to describe their piezoelectric properties sufficiently. For example, the solid solution ceramic lead zirconate titanate (PZT), which contains competing phases with hexagonal/tetragonal symmetries, possesses only three distinct non-zero piezoelectric coefficients: d_{33}, d_{31}, and d_{15}. As the symmetry of a crystal structure is reduced, additional non-zero terms

appear. However, utilizing symmetry elements to describe the piezoelectricity of a material is not sufficient for polycrystalline ferroelectrics synthesized in a rapid, scalable fashion. Polycrystalline ferroelectrics are composed of crystallographic grains divided into ferroelectric domains, which are defined as regions where the spontaneous dipole direction is aligned [278]. Often polycrystalline ferroelectric samples or thin films will not show a piezoelectric effect as fabricated because the individual ferroelectric dipoles are randomly oriented, resulting in a net zero dipole. The application of an electric field after deposition can orient dipoles along the same direction, resulting in a net dipole and measurable piezoelectricity; this process is called poling. Poling does not reorient the grains, only the domains. Typical electric fields of 1-100 kV/cm are applied, and the polarization remaining after switching off the electric field is called the remnant polarization. The maximum remnant polarization of a polycrystalline material is typically a portion of its single-crystal value given that all dipoles may not align perfectly along the direction of the applied electric field due to competing internal stresses imposed by the sample morphology [278].

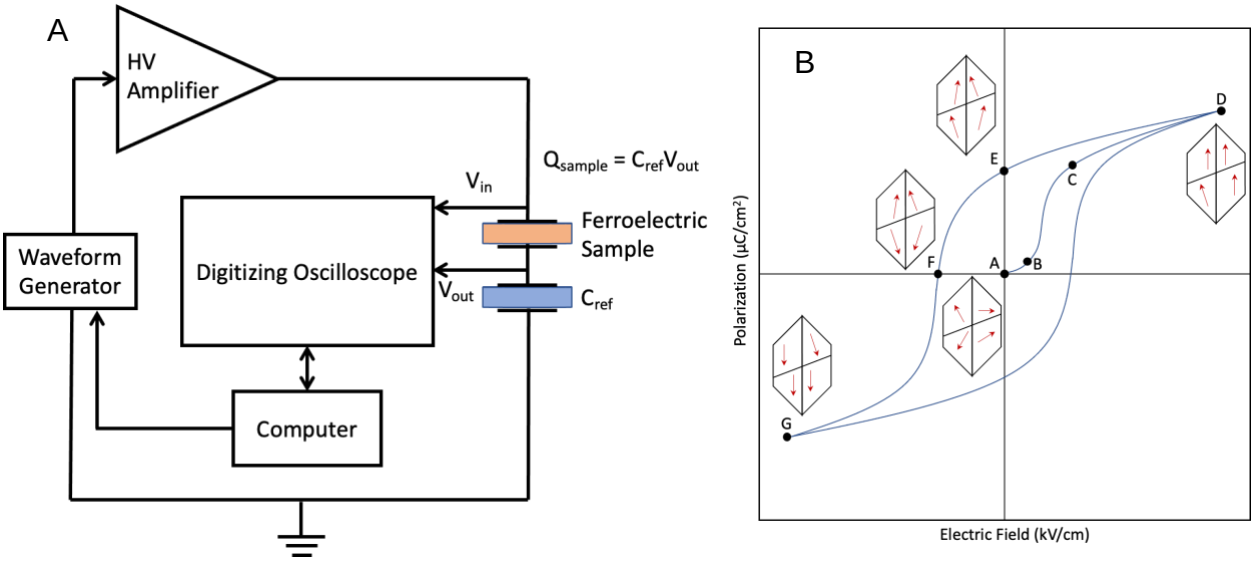

Figure 4-1. Simplified schematic of a Sawyer-Tower circuit (A) used to reveal the characteristic polarization-electric field hysteresis loop of ferroelectrics (B). Point E in the PE Loop corresponds to the remnant polarization, while point F in the PE Loop corresponds to the coercive electric field.

Ferroelectric hysteresis loops experimentally measured via a Sawyer-Tower circuit are used to determine the remnant polarization of a ferroelectric (Figure 4-1A). A Sawyer-Tower circuit is comprised of two capacitors in parallel: a reference capacitor (C_{ref}) and the ferroelectric sample. The capacitance of the reference is selected to be much larger than that of the sample to ensure most of the voltage drop occurs over the sample ($Q = C_{ref}V_{ref} + C_{sample}V_{sample}$). A pulse is delivered to the reference capacitor and sample via a pulse generator (V_{in}) , and the voltage across the reference capacitor (V_{out}) is measured to calculate the charge (Q). The electric field (E) and polarization (P) of the sample can be calculated knowing the thickness (t) and area (A) of the sample, respectively:

$$E = \frac{V_{in}}{t} \tag{7}$$

$$P = \frac{Q}{A} = \frac{C_{ref}V_{out}}{A} \tag{8}$$

The resulting polarization-electric field loop ('PE Loop') is shown in Figure 4-1B. As the electric field increases (point A → B), the polarization increases linearly until sufficiently large electric fields switch the domains, resulting in a non-linear response (B → C) until all domains are maximally aligned, resulting in a return to the linear regime (C → D). Upon decreasing the electric field to zero (point E), the polarized domains will remain aligned; this polarization is deemed the remnant polarization (P_r). Subsequent application of an electric field in the reverse direction will result in domain switching; the electric field required to eliminate any polarization is known as the coercive electric field (point F). At this point, the net polarization disappears as the domains cancel each other out. Further increases in the electric field in the reverse direction will result in polarization in the opposite direction (point G). Applying an electric field in the forward direction

will result in switching of the dipoles again (point D), completing the loop. Ferroelectric loops are essential for piezoelectrics because they elicit the coercive electric field required to align dipoles. Typically, piezoelectrics are poled at 2-3x the coercive electric field to ensure ferroelectric domains are aligned.

The piezoelectric properties of a polycrystalline ferroelectric sample can be characterized through the quasi-static Berlincourt method (Figure 4-2). A sample is clamped between two conductive electrodes that are oscillated at a fixed frequency and force. A frequency of 110 Hz is typically used to avoid any likely sample resonances but also ensure a measurement is completed within a few seconds. This quasi-static approach also avoids the issue of thermal drift inherent with a static load. A minimal preload force of 2-5 N is required to ensure the sample does not rattle or shift in response to the oscillating force (typically 0.025 or 0.25 N). A reference capacitor with a capacitance much larger than the sample is used in parallel to measure the charge output from the sample. Then, a calibrated reference piezoelectric located in line with the oscillating load is used to calculate the force, allowing the calculation of the d_{33} value of the sample. The term 'd_{33}' is still used to quantify the piezoelectric response of polycrystalline samples as the applied force and charge polarization lie in the z-direction. This measurement is independent of sample geometry, enabling direct comparison of different compositions [279].

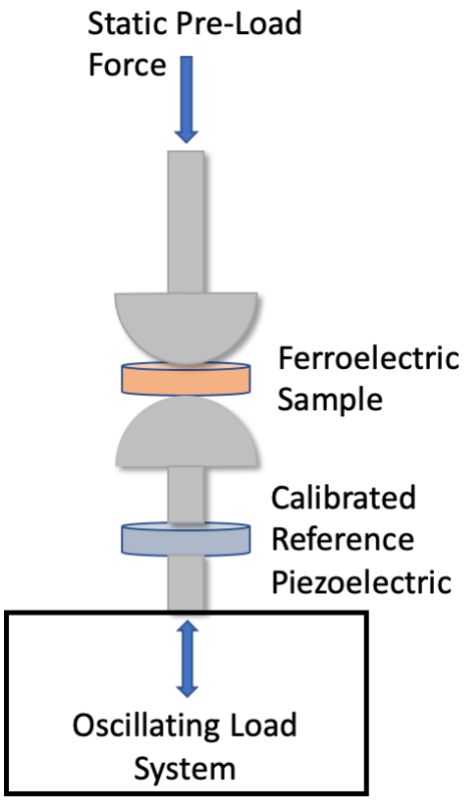

Figure 4-2. Schematic depicting the operating principle of the quasi-static d33 measurement.

4.2.3. Scalable Synthesis of Molecular Ferroelectrics and All-Printed Piezoelectric Sensors

As detailed in section 4.1, the promising piezoelectric and processing properties inorganic-organic multiaxial molecular ferroelectrics suggested that these materials were compatible with scalable synthetic and rapid fabrication techniques. In this work, ball milling was selected to demonstrate scalable synthesis of an inorganic-organic hybrid multiaxial ferroelectric, while slot die coating and inkjet printing were utilized to demonstrate rapid fabrication of all-printed devices for the first time.

4.2.3.1. Ball Milling

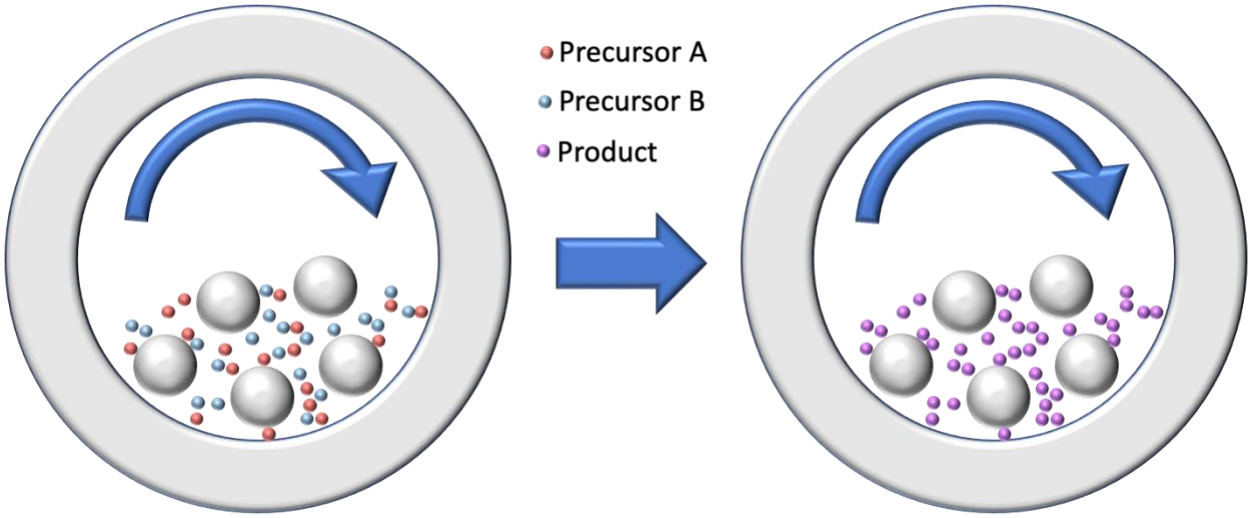

Figure 4-3. Schematic of ball milling utilized to drive forward a solvent-free mechanochemical reaction.

Ball milling is a mechanosynthetic technique that utilizes continuous mechanical grinding to decrease particle size and size distribution. Particles are loaded into jars with milling media and rotated until the desired particle size distribution is achieved. However, the mechanical energy

imparted via ball milling also can be utilized to drive chemical reactions, which Wilhelm Ostwald referred to as mechanochemistry in his 1919 textbook on chemistry [280, 281]. Michael Faraday first described the reduction of silver chloride via mechanical grinding in 1820 [282], and Carey Lea carried out a series of experiments in mechanochemistry that studied the decomposition of metal halides into their metal and halogen constituents after trituration in the 1880s; in contrast, simple thermal heating of these metal halide compounds resulted in sublimation or melting, requiring a distinction classification for mechanochemical reactions [283]. Ball milling has expanded to fields such as organic synthesis [284], metal complexes [285], and metal-organic frameworks [286] due to efficient transfer of mass and energy, resulting in solvent-free scalable synthesis. Ball milling and other mechanochemical approaches have been utilized to synthesize hybrid inorganic-organic lead halide perovskites for optoelectronic applications [287, 288], but ball-milled hybrid inorganic-organic molecular ferroelectrics have not been reported to date.

4.2.3.2. Slot-die coating

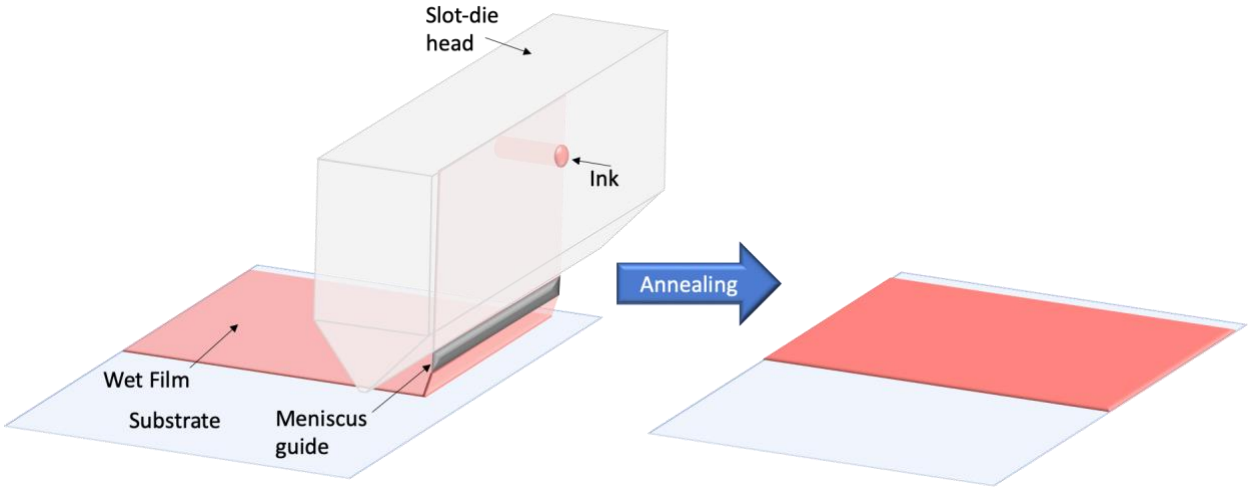

Figure 4-4. Schematic of slot-die coating.

Slot-die coating combines rapid processing with flexible substrates to allow for low cost, low-carbon-footprint manufacturing of large-area functional films, devices and device arrays [4, 5]. As depicted in Figure 4-4, a syringe pump pushes ink into a slot-die head, and a liquid meniscus is formed on a substrate with the help of a meniscus guide as the slot die head translates across the substrate. Slot-die coating is a pre-metered process, meaning the syringe pump rate and speed of the slot die head can be adjusted to tune the thickness of rectangular wet film deposited onto the substrate. Subsequently, wet films are annealed to form functional thin films. Both the efficient deposition of ink and meter-per-second coating speeds achievable with slot-die coating [289, 290] make this fabrication technique an attractive alternative to more wasteful and less scalable solution-processing approaches, such as spin-coating. Slot-die coating has been utilized to fabricate large areas of inorganic-organic hybrid lead halide perovskites for applications in photovoltaics [291–294]. Therefore, we hypothesized that slot-die coating could be utilized to demonstrate scalable fabrication of polycrystalline multiaxial molecular ferroelectric films for piezoelectric sensors. Slot-die coated molecular ferroelectrics have not been reported to date.

4.2.3.3. Inkjet Printing

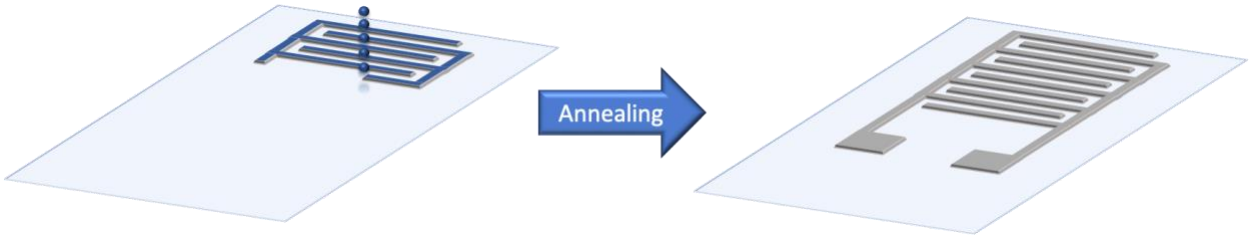

Figure 4-5. Schematic of inkjet-printed interdigitated electrodes.

Piezoelectric device fabrication can be further simplified for scalable manufacture by replacing the top-bottom electrodes with interdigitated electrodes (IDEs), enabling all-printed piezoelectric devices [295]. In this architecture, only one electrode layer must be printed. Additionally, the requirements for piezoelectric film coverage and quality are relaxed as gaps or pinholes in the film no longer result in sensor failure due to short-circuit pathways. Additive manufacturing techniques, such as inkjet printing, can be used to fabricate IDEs at low temperatures on flexible substrates (Figure 4-5). Inkjet printing is a drop-on-demand fabrication technique that enables rapid fabrication of arbitrary functional geometries on a substrate. Piezoelectric actuators in an inkjet head generate pulses that eject droplets from a nozzle containing an ink reservoir; droplets are ejected at acoustic frequencies (1-20 kHz) [296]. Picoliter-scale droplet volumes are jettable, resulting in resolutions as small as 20 μm [297]. Annealing inkjet-printed patterns decomposes the ink, resulting in conductive traces. Inkjet printing represents another low-waste and scalable additive manufacturing technique.

4.2.3.4. The molecular ferroelectric TMCM $MnCl_3$

In this chapter, two-step scalable fabrication of all-printed piezoelectric vibration sensors utilizing a multiaxial molecular ferroelectric was demonstrated for the first time. A molecular ferroelectric was slot-die coated over inkjet-printed interdigitated electrodes to reduce the number of processing steps. The organic-inorganic molecular ferroelectric trimethylchloromethyl ammonium trichloromanganese (TMCM $MnCl_3$) stands out as a scalable, printable piezoelectric because of its exceptional piezoelectric and processing properties [264]. TMCM $MnCl_3$ possesses a single-crystal d_{33} of 185 pC/N a high Curie temperature of 406 K, six equivalent piezoelectric axes, and solubility in water and methanol [298]. The schematics of the molecular structures

highlight the free rotation of the TMCM cation and corresponding increase in symmetry as TMCM $MnCl_3$ transitions from its ferroelectric phase to its paraelectric phase above the Curie temperature. These outstanding material properties makes this molecular ferroelectric an intriguing candidate for low-cost, rapid printing of flexible piezoelectric sensors [269]. In this chapter, the first all-printed, flexible vibration sensor using a multiaxial molecular ferroelectric and interdigitated electrodes are showcased. Then, sensors with a top-bottom electrode architecture were fabricated and characterized to quantify the piezoelectric response of slot-die coated and poled TMCM $MnCl_3$. Then, we describe the first mechanochemical synthesis of a lead-free multiaxial hybrid molecular ferroelectric by ball milling TMCM $MnCl_3$ powder and characterizing its structural and thermal properties. The structural, morphological, and piezoelectric properties of pressed TMCM $MnCl_3$ pellets are characterized, resulting in the first d_{33} measurements of polycrystalline TMCM $MnCl_3$ pellets. A peak d_{33} value of +/- 4.0 pC/N was measured.

4.3. Methods

4.3.1. Materials

Rolls of PET substrates (Melinex ST 505, Dupont) were supplied by Tekra LLC, and 10 cm square ITO substrates with a sheet resistivity of 12-15 Ω-sq were purchased from MSE Supplies. Manganese chloride (>99.99%, anhydrous, Sigma Aldrich), trimethylamine solution (25 wt.% in dH_2O, Sigma Aldrich), dichloromethane (>99.5%, ACS reagent, Sigma Aldrich), acetonitrile (99.5%, ACS reagent, Sigma Aldrich), poly(methyl methacrylate) (MW 100,000 g/mol, Sigma Aldrich), anisole (99%, ReagentPlus, Sigma Aldrich), silver nanoparticle ink (Silverjet DGP-40LT-15C, Advanced Nano Products), conductive silver paste (Dupont PE874, Insulectro), and epoxy (ATACS 5103A/B, Atacs Products Inc.) were purchased without further

purification. $MnCl_2$ was dried under vacuum overnight and stored in a nitrogen glovebox. Trimethylchloromethyl ammonium chloride (TMCM Cl) was prepared by stirring equimolar quantities of trimethylamine solution and dichloromethane in acetonitrile at room temperature for 48 hours. TMCM Cl was precipitated via rotary evaporation, dried under vacuum overnight at 70 ^oC, and stored in a nitrogen glovebox.

4.3.2. Thin film fabrication and characterization

For initial solvent screening experiments, equimolar quantities of $MnCl_2$ and TMCM Cl were weighed in a nitrogen glovebox and dissolved in DMSO, DMF, acetonitrile, ethanol, and ethylene glycol at a concentration of 0.5 M. Solutions were stirred overnight.

To prepare the precursor ink for slot die coating experiments, equimolar quantities of $MnCl_2$ and TMCM Cl were weighed in a nitrogen glovebox and dissolved in DMSO (1.6 M) or an equivolume mixture of ethanol and water (1.6 M) by stirring at 80 ^oC overnight. All slot-die coating was performed in an environment control room with an adjustable humidity (10-60% RH) and temperature; the temperature of the room was fixed at 21 ^oC. PET substrates were cleaned with a cleaning roller, treated with UV-ozone (lamp time of 5 minutes), and affixed to a temperature-variable vacuum chuck. A stainless-steel slot die head with a 10-mm-wide stainless-steel shim and meniscus guide was used to coat the precursor solution onto the substrate. The guide-substrate gap was set to 152 μm, and the slot-die coating chuck temperature (80, 120 ^oC) and humidity (15 and 55% RH) were varied. The rate of the precursor solution injected into the slot die head via a motorized syringe pump was scaled with the coating speed proportionately. All films were dried at 120 ^oC on the vacuum chuck for one hour prior to characterization.

The crystal structure of TMCM $MnCl_3$ films was characterized with both 1D and 2D x-ray diffractometers (D8 Discover Microfocus, Bruker), and the film morphology was characterized via a scanning electron microscope (Sirion XL30, FEI).

4.3.3. *All-printed sensor fabrication and characterization*

PET substrates were cleaned with a cleaning roller, and silver interdigitated electrodes were printed using a Dimatix DMP-2800 inkjet printer and a cartridge with a 10-pL drop size. All geometries were inkjet-printed at a bed temperature of 60 ^{o}C, a cartridge temperature of 40 ^{o}C, a drop spacing of 20 μm, and a jetting frequency of 5 kHz. Four passes were printed. After annealing at 60 ^{o}C, interdigitated electrodes were annealed at 120 ^{o}C for 30 minutes. The geometries of IDEs were measured with a laser confocal scanning profilometer (LEXT OLS4100, Olympus). TMCM $MnCl_3$ precursor solution was slot die coated at 120 ^{o}C and 15% RH and subsequently annealed at 120 ^{o}C for 60 minutes. 38 AWG copper wires were attached to piezoelectric sensors with silver epoxy followed by a 2-part epoxy (5103A/B, ATACS) to reinforce adhesion. Sensors were cut to size and affixed to 2 cm x 50 cm aluminum beams with a thickness of 0.50 mm via epoxy and cured overnight. Sensors were poled in a nitrogen glovebox at varying electric fields overnight.

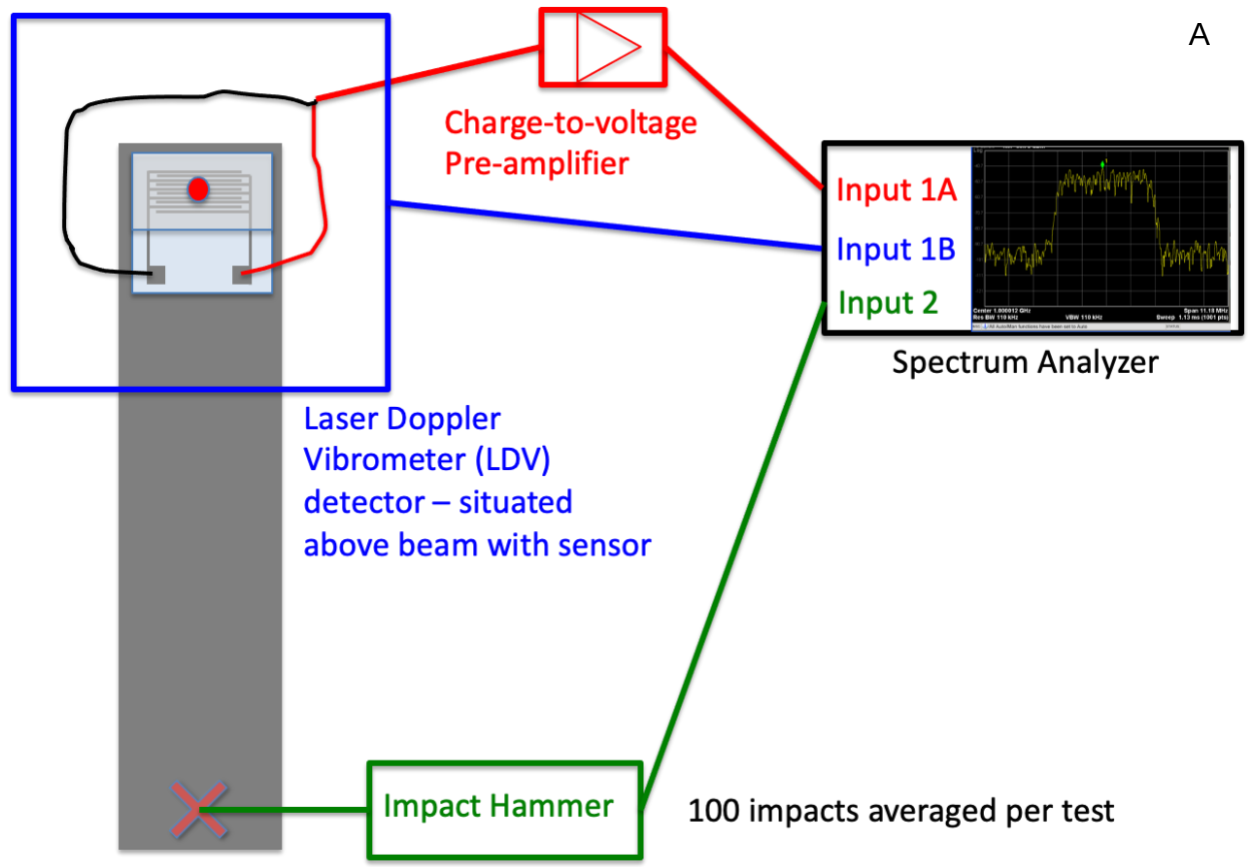

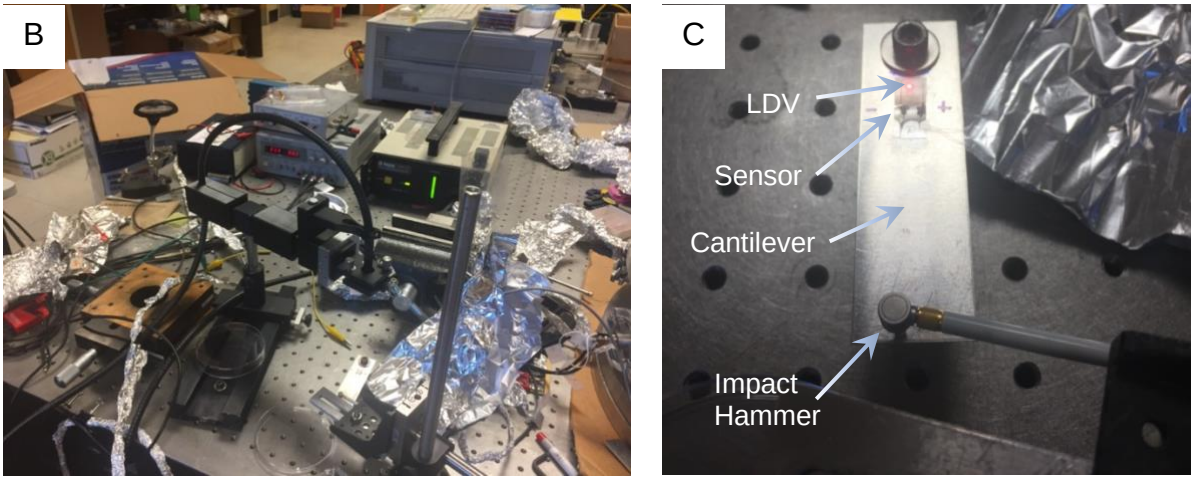

Figure 4-6. Schematic (A) and Picture (B) of the impact test. A closeup of the sensor on an aluminum beam shows the laser doppler vibrometer over the IDEs (C).

All sensor characterization experiments were designed and performed by Dr. Weiwei Xu (Figure 4-6). Two types of tests were designed and implemented: an impact test and a shaker test. For vibration testing, sensors were affixed to a cantilever with epoxy. An impact hammer struck

the end of the cantilever, and the polarization response was converted to a voltage via a preamplifier (100 V/pC) and recorded in a spectrum analyzer. A laser doppler vibrometer (LDV) was used to detect the mechanical deflection of cantilever as a control. A commercial strain gauge connected to a Wheatstone bridge completion module (Omega BCM-1) was used to measure the strain of the beam independently.

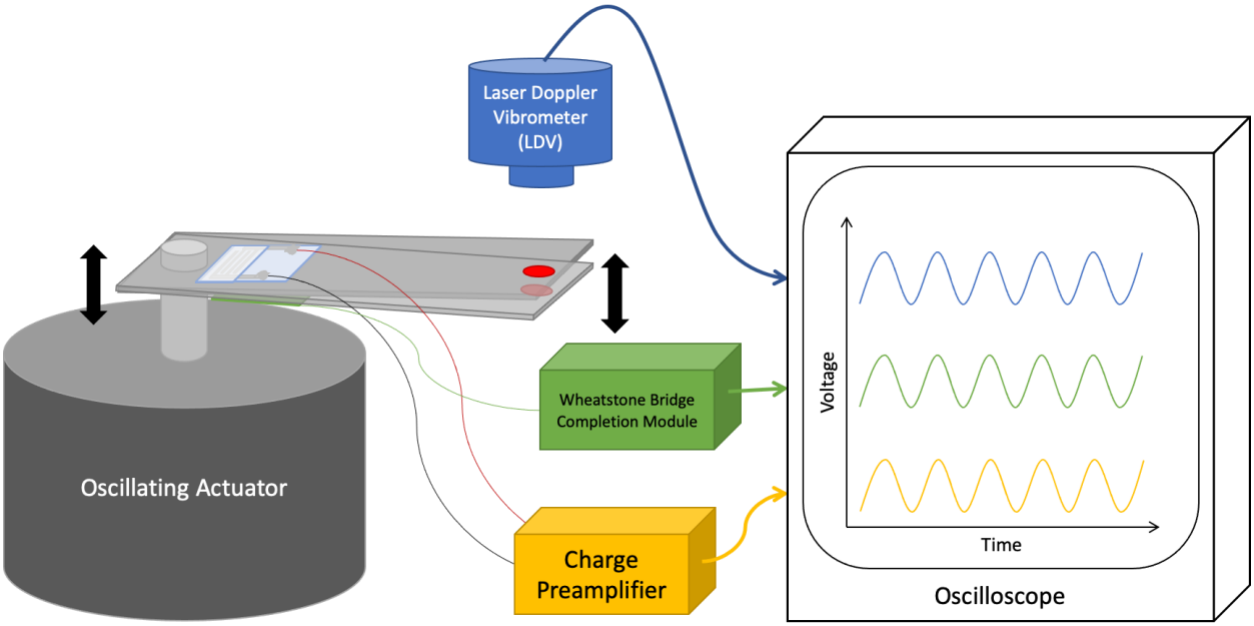

Figure 4-7. Schematic of the shaker test used to characterize all-printed sensors.

In the shaker test, sensors attached to aluminum beams via epoxy were affixed to an electromechanical oscillator (Arbor Scientific) driven by a function generator. The beam is oscillated at its first natural frequency (ca. 130 Hz). Time domain signals from a laser doppler vibrometer (LDV), the voltage output from the Wheatstone bridge completion module and the sensor response from the charge amplifier are collected and analyzed by a digital oscilloscope (Tektronix TDS540A).

4.3.4. Top-Bottom electrode sensor fabrication and characterization

ITO/glass substrates were cleaned with 2% detergent in dH_2O, dH_2O, acetone, and IPA, treated with UV-ozone (lamp time of 5 minutes), and affixed to a temperature-variable vacuum chuck. A stainless-steel slot die head with a 10-mm-wide stainless-steel shim and meniscus guide was used to coat the TMCM $MnCl_3$ precursor solution onto the substrate with a guide-substrate gap of 152 μm, chuck temperature of 120 ^oC, and humidity of 15% RH. One to six passes were slot-die coated with 5-minute gaps between each coat, and the film was annealed at 120 ^oC for 60 min. A PMMA precursor solution (8 wt.% in anisole) was prepared by stirring at 80 ^oC overnight, and the solution was slot-die coated over the TMCM $MnCl_3$ layer using a stainless-steel slot die head with a 13-mm-wide stainless-steel shim and meniscus guide. The gap, chuck temperature, and humidity were set to 152 μm, 80 ^oC, and 15% RH. One to three passes were fabricated with a wait time of 15 minutes. Films were annealed at 130 ^oC for an hour. 400 nm silver electrodes were thermally evaporated through PET masks with an 8 x 16 mm rectangular mask. 38 AWG copper wires were attached with silver pate and cured at 90 ^oC for 15 minutes. Then, non-conducting epoxy (ATACS) was deposited over the wires and on the silver electrode as a pad for the impact hammer.

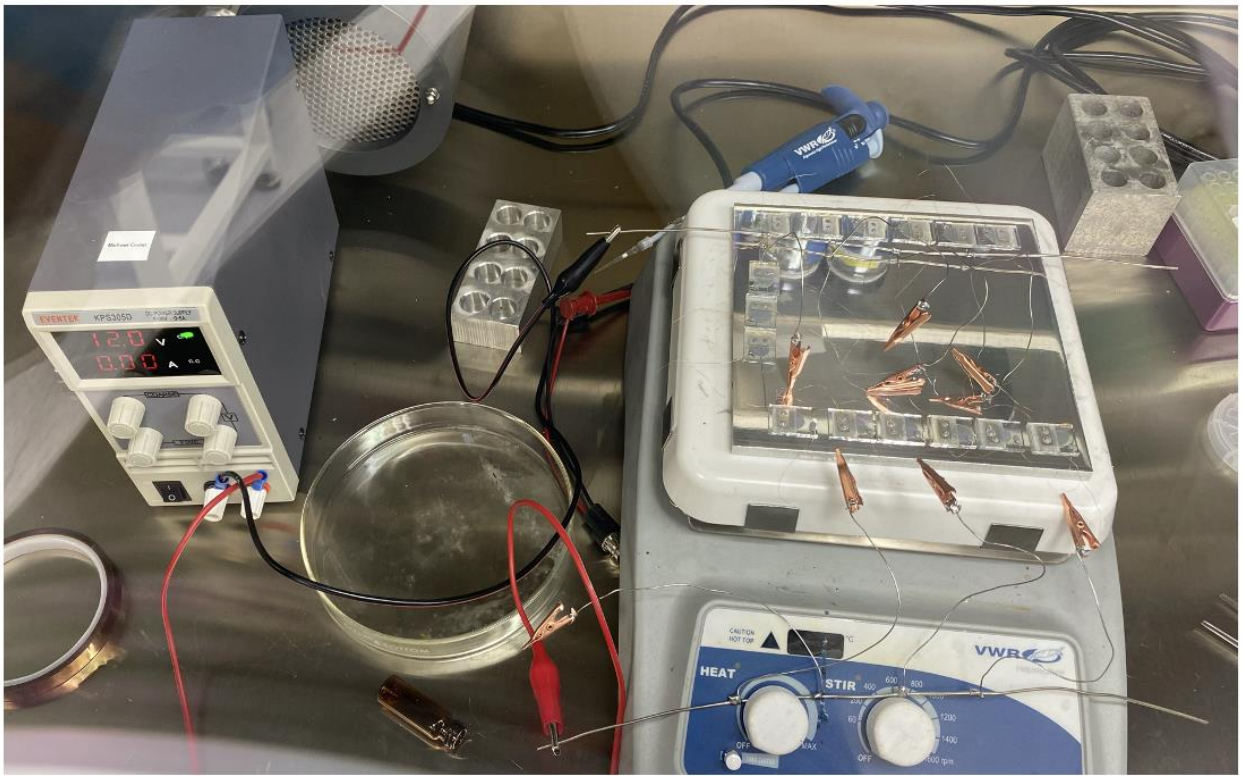

Figure 4-8. Poling of top-bottom devices attached to an aluminum plate.

Devices were attached to an aluminum plate (152 mm x 152 mm x 6.35 mm) with the non-conducting epoxy and allowed to cure for 12 hours before poling in a nitrogen glovebox (Figure 4-8).

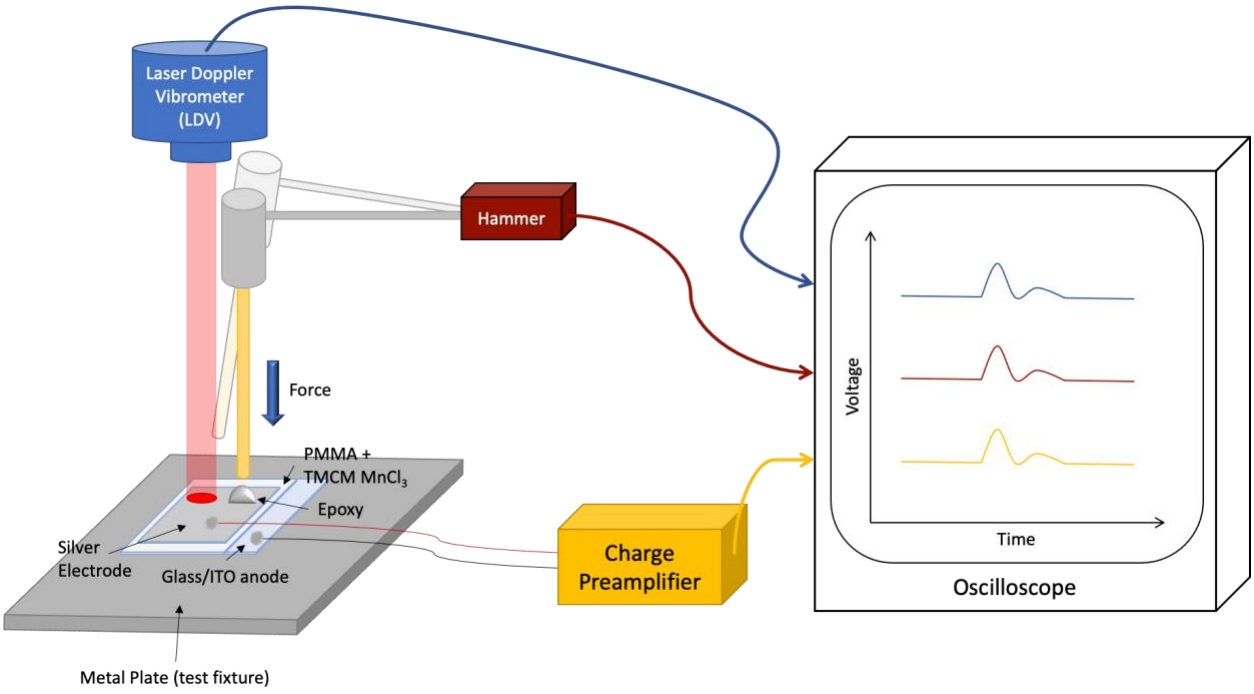

Figure 4-9. Schematic of the hammer test.

The hammer technique was adapted from previous work by the Shen group [299] to quantify the piezoresponse of PZT nanoparticle composite films (Figure 4-9). A force through a wooden stick is applied to the top surface of the silver electrode and measured by a load cell. The charge across the film is captured by a charge amplifier and recorded in an oscilloscope. To withstand the applied force, a droplet of epoxy (about 1-2 mm in thickness) is applied onto the top silver electrode for protection. The charge response is recorded for forces of varying magnitude.

4.3.5. Ball milling and characterization of TMCM $MnCl_3$ powder

50 mL yttria-stabilized zirconia (YSZ) ball milling jars and media (JA0205 and BA0125, MSE Supplies) were dried under vacuum overnight and transferred into a glovebox. Equimolar quantities of $MnCl_2$ and TMCM Cl were weighed and added to the jar. Jars were sealed with electrical tape and then ball-milled in open air using a planetary ball mill (MA0103, MSE Supplies)

for 15 minutes. Jars were transferred into the glovebox to break up caked powder in the bottom of the jar. 4, 8 or 12 ball milling cycles were completed.

The pink product was characterized with XRD (D8 Advance, Bruker) using Cu Kα radiation (λ = 0.15418 nm). A 2-theta range of 10-50°, a step size of 0.02°, and a step time of 0.5 second were utilized. The product also characterized with TGA and SEM. All product was stored in a nitrogen glovebox.

4.3.6. Fabrication and characterization of TMCM $MnCl_3$ pellets

Varying masses of TMCM $MnCl_3$ powder was weighed in a glovebox and added to a stainless-steel pellet die with a 6.35 mm diameter (PR0101, MSE Supplies). Die inserts were covered with polyimide tape to prevent corrosion of the inserts. Pellets were pressed at a force of 60 MPa for 60 seconds, and the pellet die set was cleaned with 2% detergent in dH_2O, dH_2O, and IPA immediately after pressing and liberating the pellet. The thickness of pellets was measured with digital calipers, and pellets were characterized with XRD and SEM. Conductive carbon paste (DM-CAP-4701S, Dycotec Materials) was painted on each face and cured at 100 °C for 10 minutes. Ferroelectric properties were characterized with a P-E Loop system based on a modified Sawyer-Tower circuit (PolyK Technologies). Dielectric properties were characterized with an impedance analyzer (PARSTAT 4000A, Princeton Applied Research). Pellets were poled in a silicone oil bath using a 3 kV power supply, and the piezoelectric properties were measured using a d_{33} meter (PolyK Technologies).

4.4. Results and Discussion

4.4.1. Fabrication and Characterization of slot-die coated TMCM $MnCl_3$ films

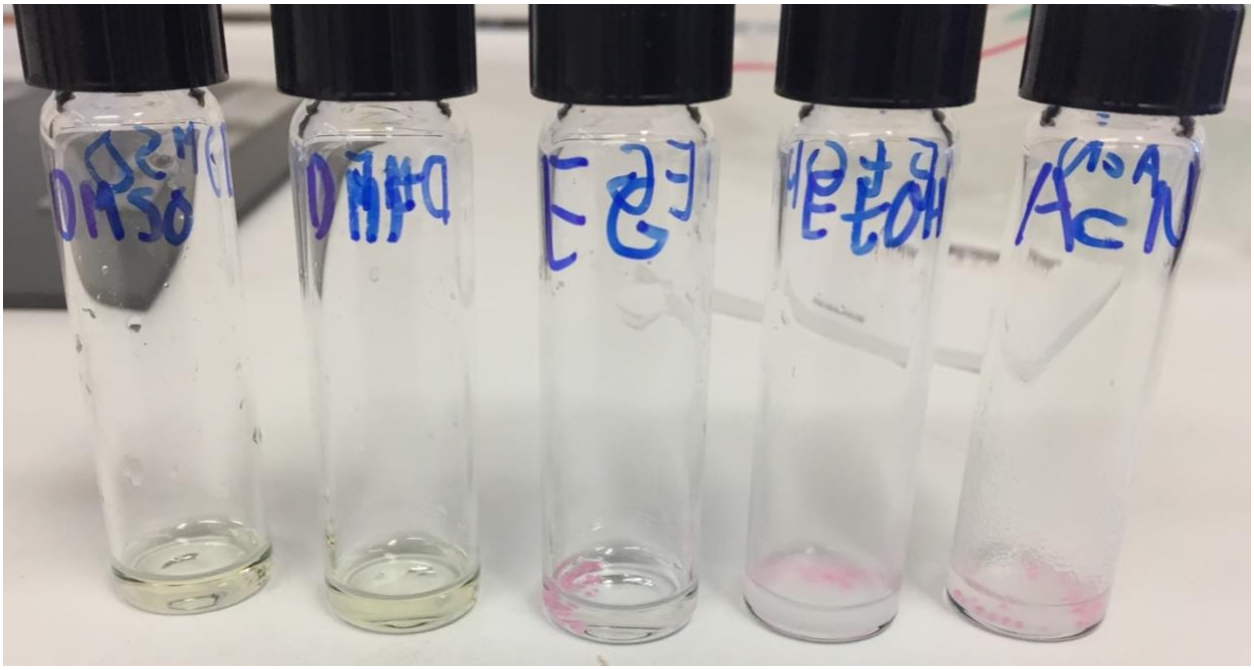

Figure 4-10. 0.5 M TMCM MnCl3 precursor solutions in DMSO, DMF, ethylene glycol, ethanol, and acetonitrile (left to right).

Preparing a proper precursor solution is necessary to slot-die coat functional thin films. Both precursors, $MnCl_2$ and TMCM Cl are readily soluble in water; previous literature reports the slow single-crystal growth of TMCM $MnCl_3$ from aqueous solution [298]. However, the rapid precipitation of TMCM $MnCl_3$ from aqueous solutions can result in phase impurities in the film (refer to the section on ball-milled for further exploration of this topic). Furthermore, the high surface tension of water (72 mN m^{-1} [300]) can result in rapid de-wetting of slot-die coated aqueous films on PET [301, 302]. De-wetting is defined as the retraction of coated wet film into droplets prior to evaporation of the solvent, resulting in the formation of films with minimal coverage. Therefore, I was motivated to identify non-aqueous polar solvents that could be used to prepare TMCM $MnCl_3$ solutions for slot-die coating. Equimolar quantities of the precursors $MnCl_2$ (a pink powder) and TMCM Cl (a white powder) were dissolved in dimethylsulfoxide (DMSO),

dimethylformamide (DMF), ethylene glycol (EG), ethanol (EtOH), and acetonitrile (AcN). Both precursors fully dissolved in DMSO and DMF after stirring overnight, forming a pale transparent yellow solution. DMSO and DMF have been reported to form pale yellow complexes with $MnCl_2$ [303, 304]. TMCM Cl dissolved in ethylene glycol, but $MnCl_2$ did not dissolve as evidenced by the pink precipitate. Neither precursor dissolved in ethanol or acetonitrile as evidenced by the formation of a cloudy mixture with a pink precipitate. Subsequent solubility experiments showed that peak solubilities of 1.6 M and 1.2 M were achieved in DMSO and DMF. A higher concentration was desired to form a thicker layer, so DMSO was selected as the best solvent for slot-die coating TMCM $MnCl_3$ thin films.

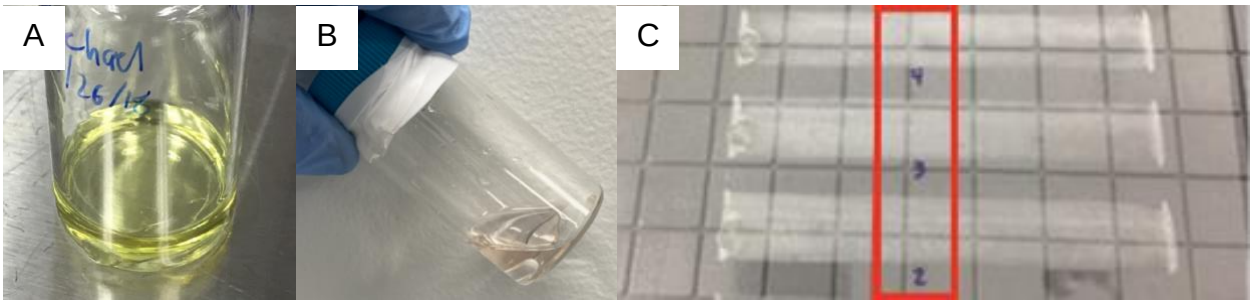

Figure 4-11. Pictures of TMCM $MnCl_3$ precursor solutions in DMSO (A) and an equivolume binary mixture of water and ethanol (B). Slot-die coated films of TMCM $MnCl_3$ from DMSO are shown in C; the middle of the coated films was characterized as depicted by the red rectangle.

1.6 M TMCM $MnCl_3$ precursor solutions were prepared in DMSO (Figure 4-11A) and a equivolume binary mixture of water and ethanol (Figure 4-11B) to test the hypothesis if presence of water was detrimental to the formation of phase-pure TMCM $MnCl_3$ films. The addition of ethanol was used to reduce the water fraction, and furthermore the addition of alcohols to aqueous

solutions has been shown to reduce the surface tension of water, resulting in slot-die coating of functional inks from water-containing solutions without de-wetting [301].

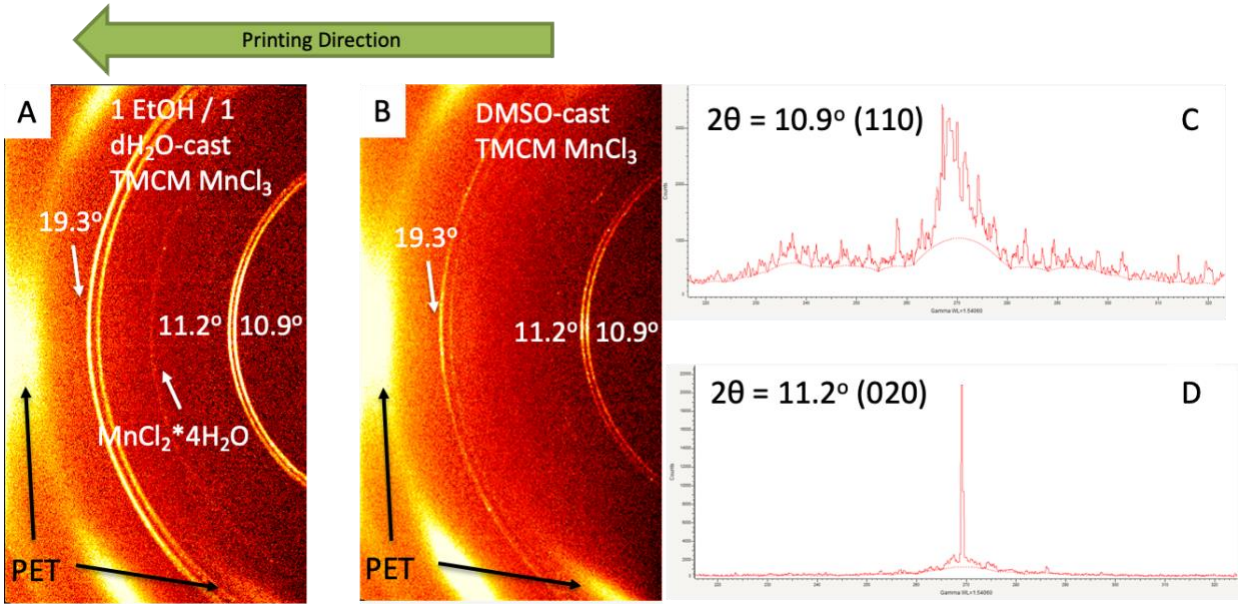

Figure 4-12. 2D-XRD results of TMCM $MnCl_3$ films slot-die coated from a 1 EtOH : 1 dH_2O (v/v) mixture (A) and DMSO (B). Gamma-integrated plots of the rings at 10.9° (C) and 11.2° (D) are shown.

2D XRD characterization was used to assess phase purity of slot-die coated films. The XRD peaks at 10.9°, 11.2°, 18.7°, and 19.3° correspond to the (110), (020), (200), and (130) planes of TMCM $MnCl_3$, the crystal structure of which belongs to the monoclinic space group *Cc* [298]. However, the peak at 16.0° corresponds to the (200) plane of the impurity $MnCl_2*4H_2O$ [305]. In contrast, XRD revealed only phase-pure TMCM $MnCl_3$ is slot-die coated from DMSO. Furthermore, 2D XRD shows that slot-die coated films from DMSO possess texture, as confirmed by the gamma-integrated plots. In contrast, the films slot-die coated from dH_2O/ethanol show a mostly uniform distribution of diffraction intensity as a function of gamma, indicating a lack of preferred orientation. All subsequent fabrication and characterization of TMCM $MnCl_3$ films were cast from DMSO due to the phase purity of films cast from DMSO.

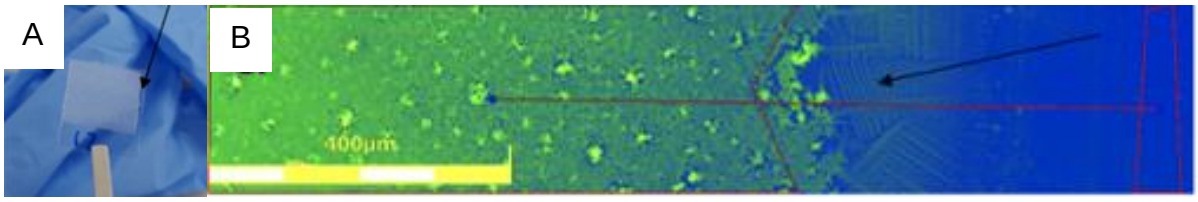

Figure 4-13. Picture of a cross-section of TMCM MnCl3 (A) prepared for optical profilometry characterization (B).

The thickness and roughness of slot-die-coated TMCM MnCl3 films were characterized with optical profilometry using a laser scanning confocal microscopy. Samples were prepared by cutting them into 15-mm-wide samples and etching away one edge using a DMSO-soaked cotton swab so the middle of the TMCM MnCl3 film could be measured (Figure 4-13A). A 405-nm laser is rastered over a sample to construct a 2D image, and the z-height is varied to change the focal point. As different features come into focus at different heights, a 3D image of a sample can be reconstructed with 1-nm resolution in the z-direction. Because the etching process can influence the morphology of the film near the edge, 5 scans were performed and stitched into a single image, enabling the measurement of film thicknesses and roughnesses as a function of slot-die coating temperature and humidity.

Table 4-1. Thickness and Root-mean-square (RMS) roughness of TMCM MnCl3 films slot die coated from different environmental conditions

	80 ℃ Bed Temperature	120 ℃ Bed Temperature
15% Relative Humidity	thickness: 1.87 µm RMS roughness: 0.534 µm	thickness: 1.14 µm RMS roughness: 0.113 µm
55% Relative Humidity	thickness: 1.76 µm RMS roughness: 0.607 µm	thickness: 1.23 µm RMS roughness: 0.356 µm

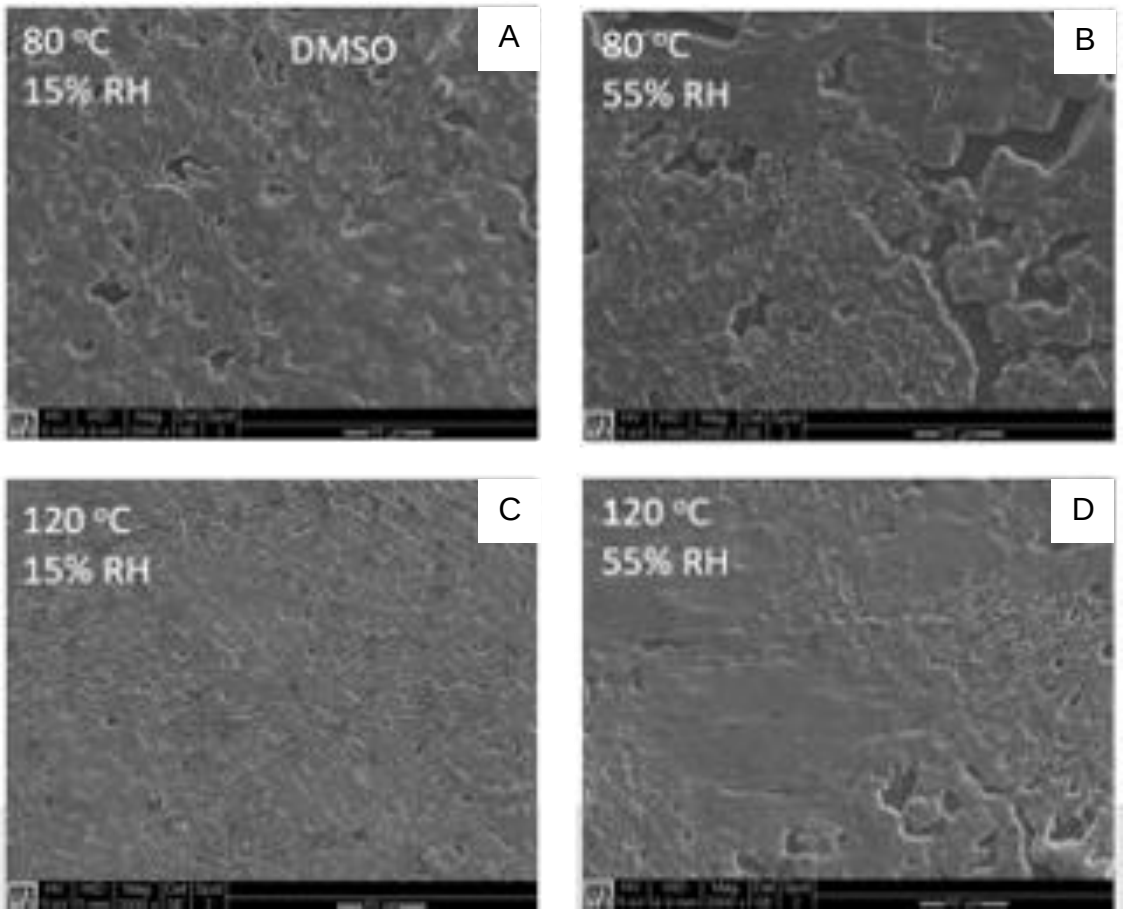

Figure 4-14. SEM images of TMCM $MnCl_3$ films slot-die coated at 80 °C and 15% RH (A), 80 °C and 55% RH (B), 120 °C and 15% RH (C), and 120 °C and 55% RH (D).

I hypothesized that driving nucleation over grain growth would increase surface coverage and reduce film roughness as observed in lead-based organic-inorganic hybrid perovskites. Nucleation itself is encouraged by maximizing the supersaturation of precursors in solution. Supersaturation was maximized in three ways: 1) maximizing the concentration of precursors in solution near the solubility limit of 1.6 M, 2) printing and annealing at elevated temperatures to drive off DMSO rapidly, and 3) printing at low relative humidity. As indicated in Table 2, decreasing the humidity and increasing the bed temperature decreased the root-mean-square roughness of the films, which indicates increased nucleation. I speculate that the decreases in

thickness at larger printing temperatures and lower humidity could be due to the evolution of any persistent DMSO trapped in the films, as the boiling point of DMSO is 189 ^{o}C. scanning electron microscopy (SEM) was utilized to inspect the coverage and morphology of slot-die coated films (Figure 4-14). The grain size decreased, and film coverage improved as the printing temperature increased and the relative humidity decreased, which corroborates the conclusions drawn from profilometry results.

4.4.2. Fabrication and Characterization of All-Printed Devices

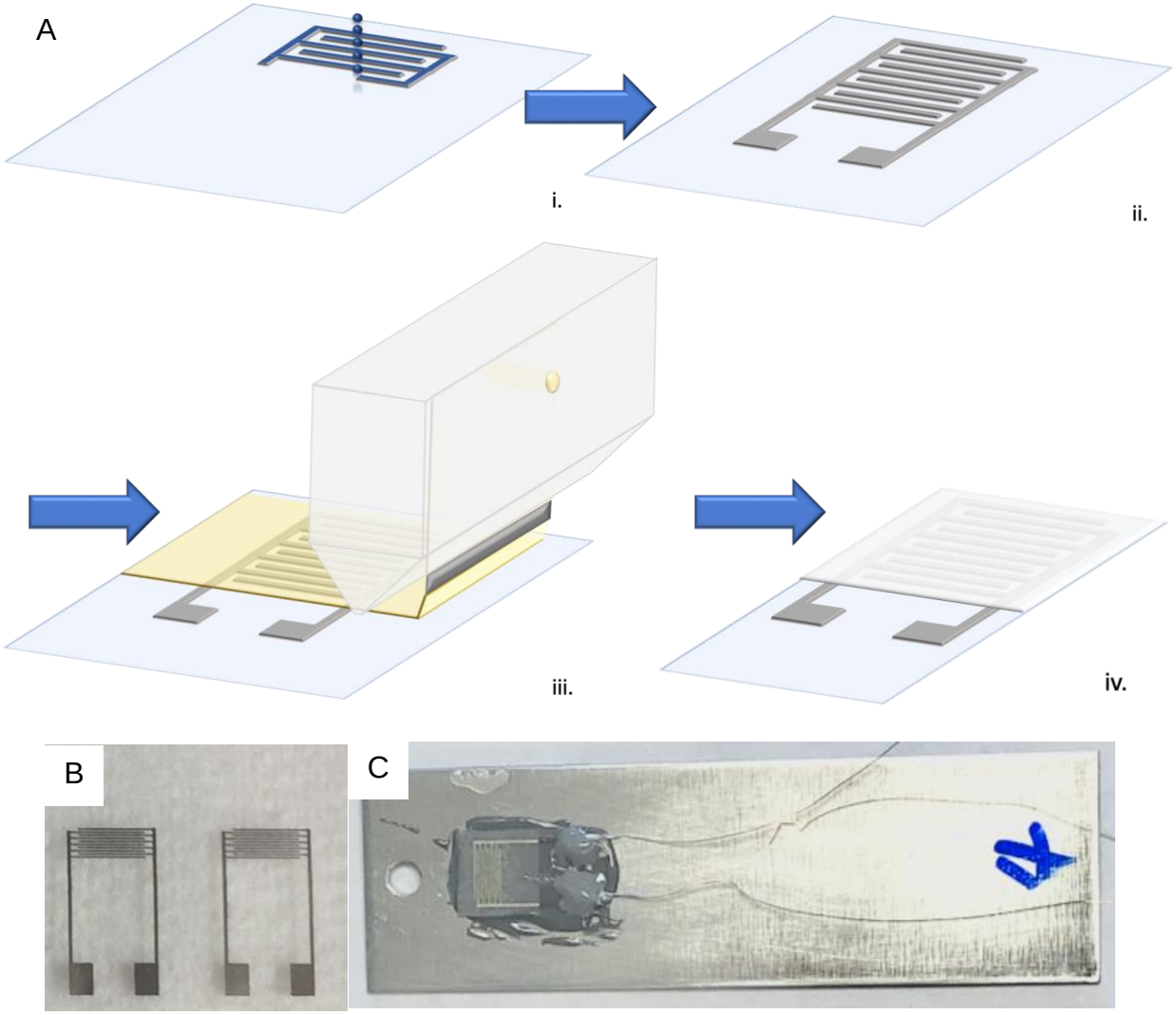

Figure 4-15. Fabrication schematic of all-printed piezoelectric sensors (A), a picture of IDE electrodes (B), and a picture of an all-printed sensor attached to an aluminum beam for vibration testing (C).

All-printed sensors were fabricated in several short steps (Figure 4-15). First, interdigitated electrodes (IDEs) were fabricated by inkjet printing a silver nanoparticle onto a PET substrate and then annealed. The IDE finger length, overlapping length, width, line spacing, and thickness are 4.5 mm, 4.0 mm, 120 µm, 115 µm, and 70 nm, respectively. Then, TMCM $MnCl_3$ was slot die coated over the interdigitated electrodes and annealed. After attaching wires to sensors, sensors

were attached to an aluminum beam for several vibration characterization tests, which were designed and executed by Dr. Weiwei Xu.

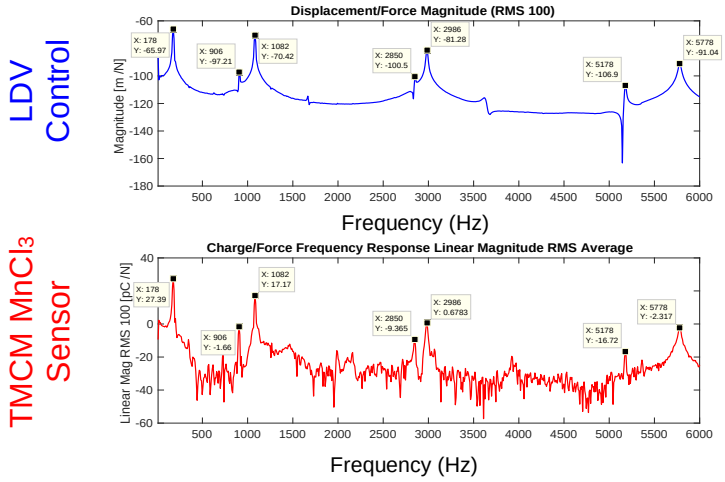

Mode	Exp. Freq.	FEA. Freq.	FEA Mode Shapes
1	178	174	
2	914	939	
3	1082	1082	
4	N/A	2978	
5	2994	3033	
6	N/A	4230	
7	5266	5470	
8	5834	5941	

Figure 4-16. Impact vibration testing results (prepared by Dr. Weiwei Xu).

Impact testing results demonstrate that the piezoelectric sensor detected seven distinct vibrational modes of the beam after 100 cumulative impacts (Figure 4-16), which were modeled in the accompanying table using finite element analysis (FEA). The heat maps in the table depict the shape of the deformation at each mode. Seven of eight FEA-predicted mode shapes of were detected experimentally. The charge/force response from the sensor is notably noisier, and the response does include several peaks at ca. 2.0 kHz and 3.9 kHz that do not appear in the LDV control or is predicted to appear in FEA analysis.

Interestingly, this response was detected without poling the sensors, indicating that the TMCM $MnCl_3$ films as fabricated possess a non-zero net polarization in the direction between the fingers of the IDEs. This direction, defined as the 'y' direction, is perpendicular to the slot-die coating direction (the 'x' direction). The texture observed in slot-die coated films (Figure 4-12B)

showed a sharp (020) peak oriented parallel to the slot-die coating direction. Given that the [020] direction is orthogonal to the [102] direction previously reported to be the polar axis in TMCM $MnCl_3$ [298], it's possible there is a non-zero dipole moment aligned in the y-direction, enabling the detection of a piezo-response.

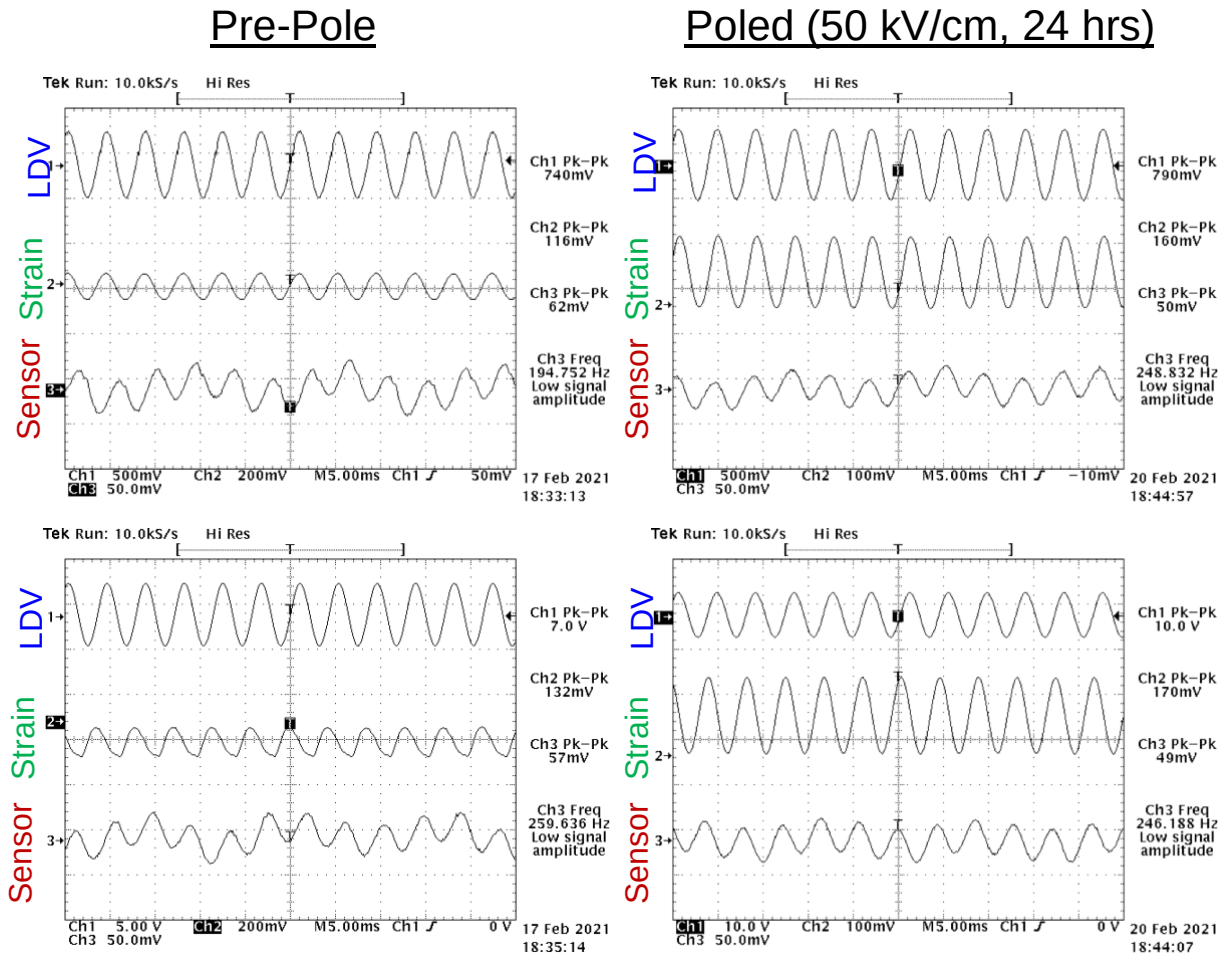

Figure 4-17. Comparison of sensor performance before and after poling (credit: Dr. Weiwei Xu)

Table 4-2. Comparison of sensor performance before and after poling (credit: Dr. Weiwei Xu)

Sample	Strain Output μϵ	Charge Output (pC)	Charge-to-strain Ratio (10^3 pC/ϵ)
Pre-Pole	~120-140	~0.35	~2.54-2.89
Poled	~170-180	~0.45	~2.54-2.7

Shaker tests performed at the first resonant frequency of the aluminum beam compare the time-domain response of the laser Doppler vibrometer (top trace), the commercial strain gauge attached to the bottom of the beam (middle trace), and the all-printed sensor attached on the top side of the aluminum beam (bottom trace). The frequency of all three output signals match (Figure 4-17), indicating that the piezoelectric sensor is detecting the charge generated by the oscillator. The signal from the charge is low and contains larger undulations due to 60-Hz noise contributions. (Table 4-2) shows the strain output, charge output, and charge to strain ratio calculated for this sensor. The strain output was calculated based on the strain-voltage equation used for commercial strain gauges:

$$\varepsilon = \frac{4V}{BV\ x\ GF\ x\ G}$$

Where V is the output voltage of the strain gauge, *BV* is the bridge excitation voltage (5 V), *GF* is the gauge factor (2.05), and *G* is the amplifier gain (187). The charge output of the sensor is calculated based on the sensitivity of the charge amplifier (100 pC/V). Then, a sensor sensitivity

in the form of a charge-to-strain ratio was defined to quantify the response of the sensor. Interestingly, sensors poled at 50 kV/cm for 24 hours, which is more than twice the coercive electric field reported for TMCM $MnCl_3$ single crystals (23 kV/cm) [298], did not show an increase in the charge-to-strain ratio. These initial tests were unable to show clear improvements in performance with poling, but these results represented the first demonstration of an all-printed and flexible vibration sensor utilizing TMCM $MnCl_3$ as the piezoelectric material.

4.4.3. Fabrication and Characterization of Top-Bottom Devices

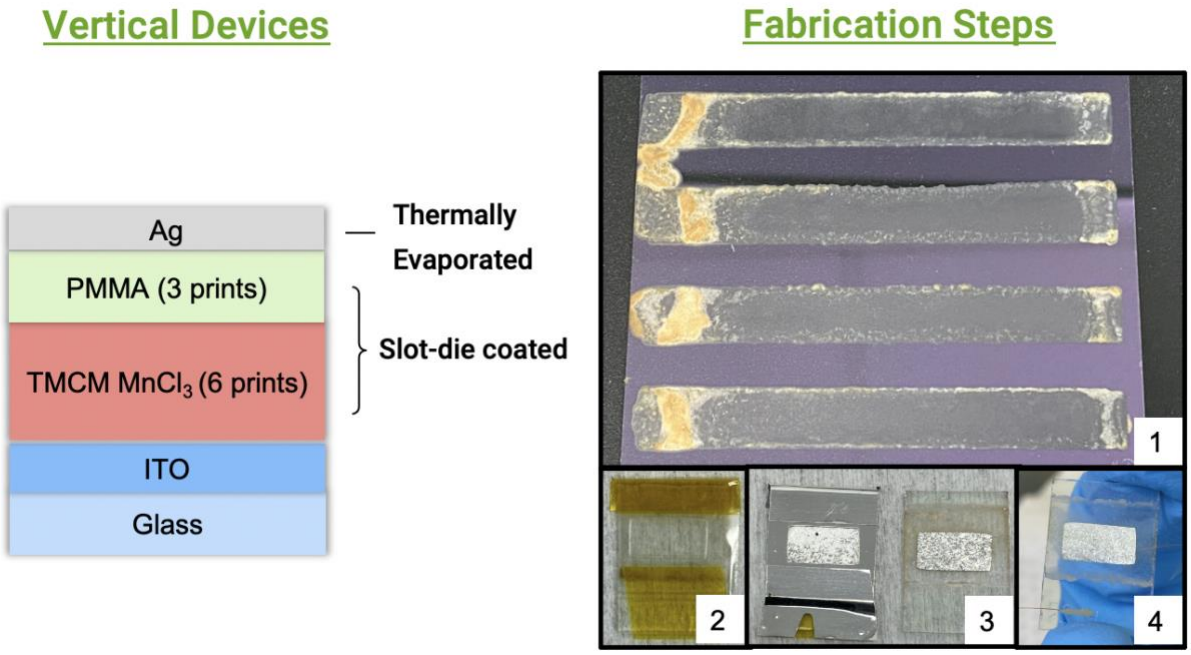

Figure 4-18. Schematic (left) and pictures (right) of top-bottom devices

Another approach used to study the piezoresponse of slot-die coated, TMCM $MnCl_3$ films is the fabrication of devices with a top/bottom electrode structure. Such a structure increases the signal by increasing the electrode surface area, resulting in 100-1,000x increases in the capacitance. Furthermore, the piezoresponse of a device with this architecture can be characterized

with the 'hammer measurement' pioneered by Prof. Steve Shen of the UW Mechanical Engineering department [299]. Pictures of TMCM $MnCl_3$ slot-die coated with three layers of PMMA on an ITO/glass substrate are shown in frame 1, and the thermal evaporation of silver onto PMMA is shown in steps 2-4, resulting in complete devices (Figure 4-18).

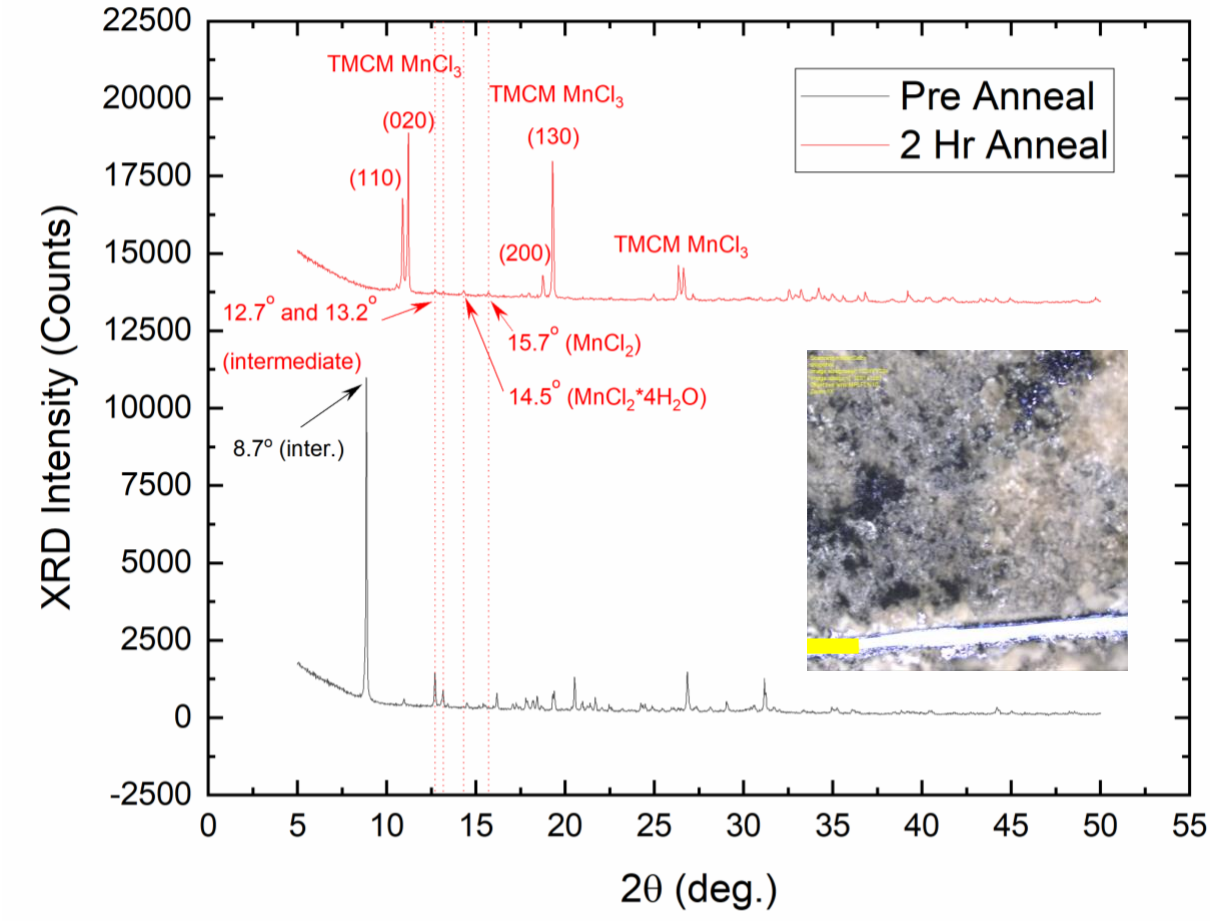

Figure 4-19. XRD Plot of TMCM $MnCl_3$ films before and after annealing at 120 C for two hours. The inset shows a picture of the film (scale bar is 200 µm).

First, TMCM $MnCl_3$ films were slot-die coated from DMSO onto ITO glass and characterized with XRD (Figure 4-19). The dominant feature of the XRD spectrum for the sample prior to annealing is a large peak at 8.7°. However, after annealing at 120 °C for two hours,

primarily TMCM $MnCl_3$ peaks emerge and this large peak (as well as the ones at 12.7°, 13.2°, etc.) disappear. The low 2θ value of the first peak is reminiscent of PbI_2*DMSO intermediates that degrade after annealing as DMSO evaporates [306]. Optical imaging (Figure 4-19, inset) shows that despite the presence of 6x layers, film coverage isn't quite complete. Obtaining complete coverage is necessary to prevent any short circuit pathways between the top and bottom electrode. Therefore, PMMA was selected as an intermediate polymer layer to ensure complete separation of the ITO and silver layers.

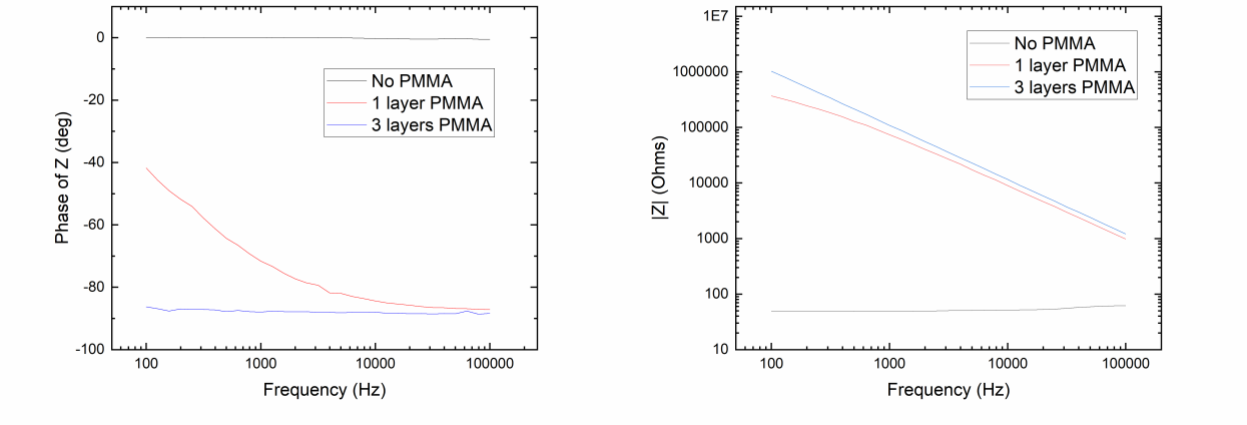

Figure 4-20. Impedance results for ITO/TMCM MnCl3/PMMA/silver sensors with 0, 1, and 3 layers of PMMA.

Impedance measurements indicated that three slot-die coated layers of PMMA prevented any short-circuit pathways between the ITO and silver electrodes (Figure 4-20). A well-behaving dielectric will show a linear increase in impedance as frequency decreases on a log-log plot, and the phase angle is typically less than -85° (an ideal capacitor has a phase angle of -90°). Devices with three layers of PMMA show this behavior, while devices with a single layer of PMMA showed a non-linear increase and a phase angle of -20° to -10° at low frequencies, indicative of a leaky capacitor. A device with PMMA showed a phase angle near 0° and an impedance <100 Ω, which is indicative of direct contact between the electrodes as an ideal resistor has a phase angle

of 0°. All devices characterized with the hammer test had three layers of PMMA (thickness of 4.8 µm).

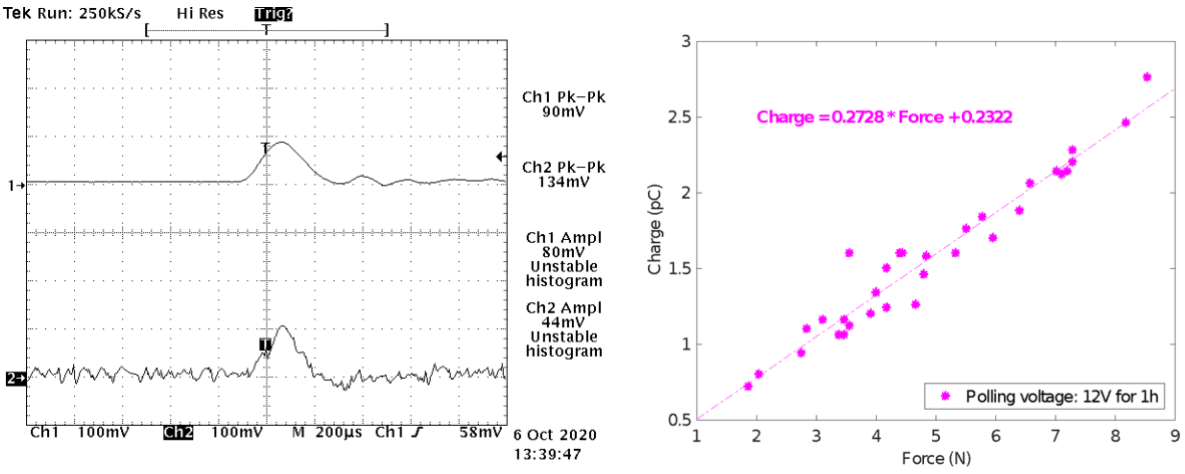

Figure 4-21. Sample time-domain plot (left) and charge vs. force plot (right) from a hammer test of a sample poled for one hour (credit: Dr. Weiwei Xu).

A sample time domain plot (Figure 4-21, left) shows the detection of charge maps the displacement of the laser doppler vibrometer. The force of the impact hammer was varied between 2-9 N to generate a charge-force plot (Figure 4-21, right), revealing a linear piezoelectric response after poling at 50 kV/cm for one hour. The charge/force ratio (slope) is 0.27 pC/N.

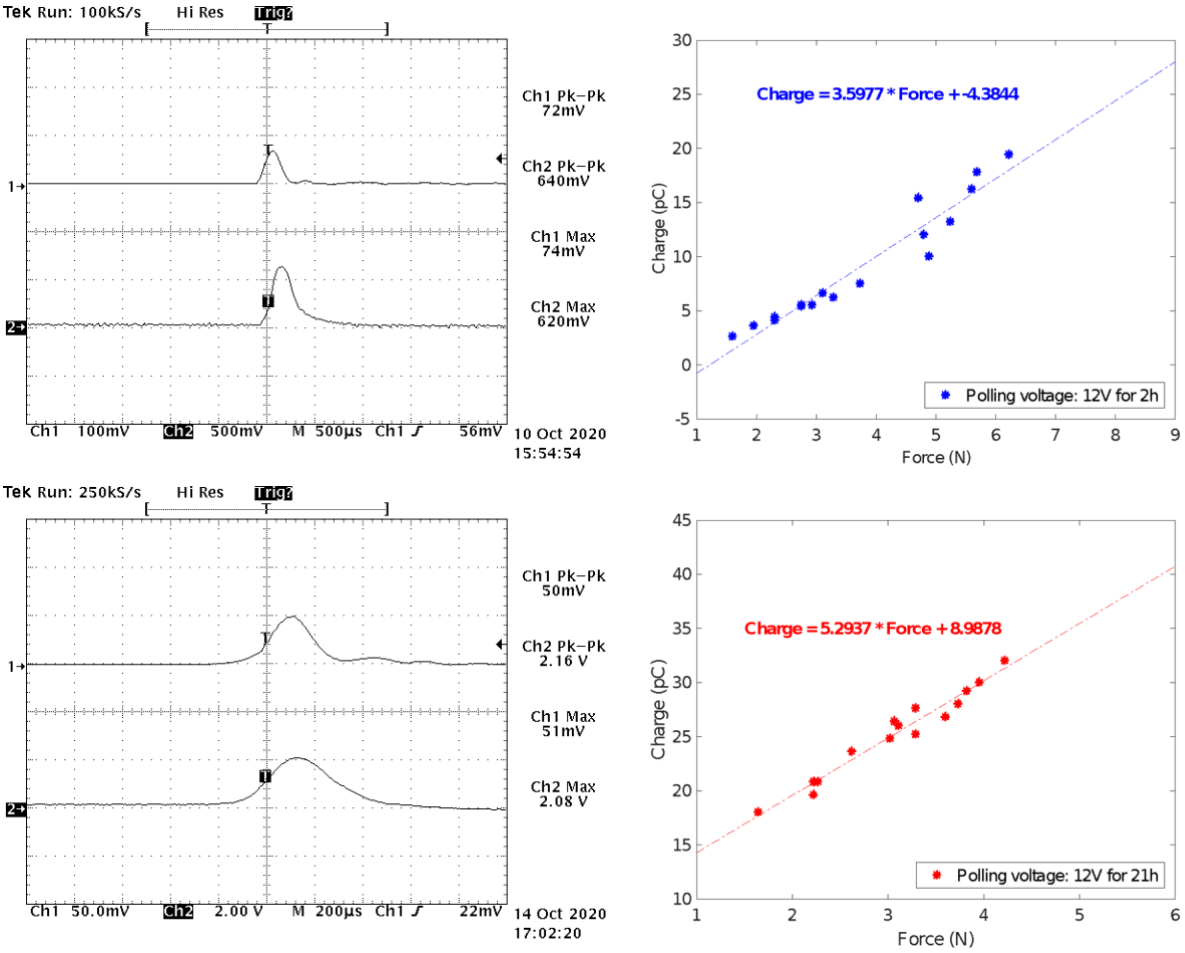

Figure 4-22. Sample time-domain plot (left) and charge vs. force plot (right) from a hammer test of a sample poled for 3 cumulative hours (top row) and 24 cumulative hours (bottom row). Credit to Dr. Weiwei Xu.

Poling this sample at 50 kV/cm for 2 additional hours (3 cumulative hours) increased the charge/force slope to 3.60 pC/N, and poling of this sample at 50 kV/cm for 21 additional hours (24 cumulative hours) increased the charge/force slope to 5.29 pC/N (Figure 4-22). The responses of the samples are still linear, indicating that detected charge in due to the piezoelectric effect. The higher slopes correspond to less noise in the accompanying time-domain plots.

Table 4-3. Comparison of poling electric fields on charge/force response as a function of cumulative poling time (prepared by Weiwei Xu)

Sample (poling electric field)	*Pre-Pole Charge/Force Ratio (pC/N)*	*1 hr poling Charge/Force Ratio (pC/N)*	*3 hrs poling Charge/Force Ratio (pC/N)*	*24 hrs poling Charge/Force Ratio (pC/N)*
1741 (25 kV/cm)	0.301	0.397	0.439	0.731
1742 (25 kV/cm)	0.539	0.491	0.306	0.601
1752 (25 kV/cm)	0.362	0.297	0.297	0.868
Average (25 kV/cm)	**0.401**	**0.395**	**0.347**	**0.733**
1811 (50 kV/cm)	0.230	0.273	3.598	5.294
1812 (50 kV/cm)	0.423	0.466	0.258	1.771
1732 (50 kV/cm)	0.194	0.390	0.614	1.525
Average (50 kV/cm)	**0.282**	**0.376**	**1.49**	**2.86**

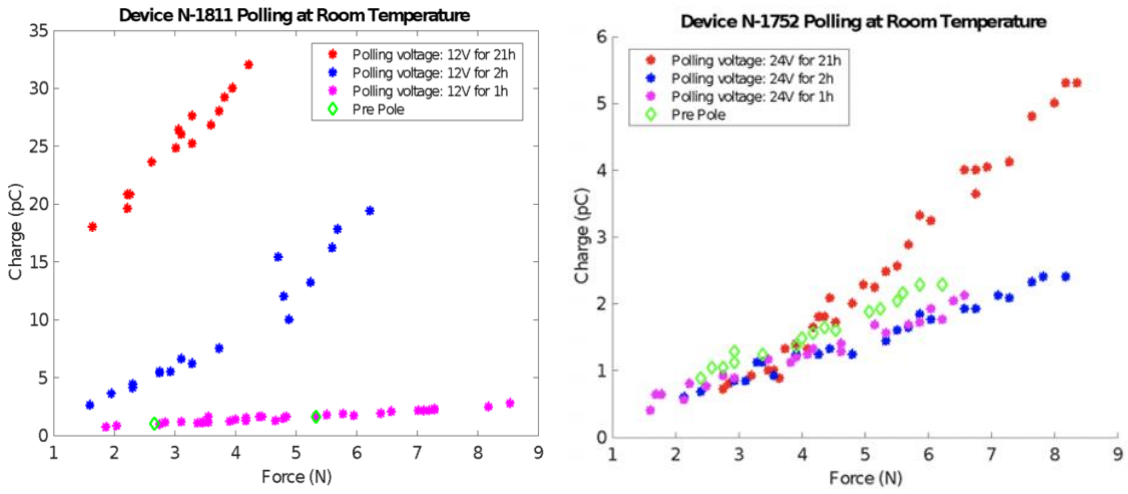

Figure 4-23. Charge vs. force plots of sensors poled at 50 kV/cm (left) and 25 kV/cm (right). Credit to Dr. Weiwei Xu.

All charge-force plots are combined to show the increase in slope as a function of poling time (Figure 4-23, left), and a similar plot was generated for a sensor poled at 25 kV/cm (Figure 4-23, right). Furthermore, the average charge/force ratios from three sensors poled under each condition was summarized (Table 4-3). The charge/force ratio of sensors poled at 50 kV/cm showed an average increase from 0.282 pC/N to 2.86 pC/N, representing a 10x increase in the response when poled a cumulative 24 hours. The charge/force ratio of sensors poled at 25 kV/cm showed a more modest increase of nearly 100% when poled a cumulative 24 hours; no significant poling is observed within the first 3 cumulative poling hours.

Overall, the results of this hammer test show that slot-die coated TMCM $MnCl_3$ can be poled to increase the charge-to-force ratio, indicating that the TMCM $MnCl_3$ films are piezoelectric. Note that the charge/force ratios measured here are not equivalent to a d_{33} value as the charge-to-force ratio is dependent on the geometry of the sample. Per the technique developed by the Shen group, finite element analysis is required to take into account the geometry of the sample and sample-substrate coupling [299], but such analysis is difficult to accomplish given that the full experimental piezoelectric tensor, compliance tensor, and dielectric tensor of TMCM $MnCl_3$ has not been published. Therefore, a calculated d_{33} value is limited compared to a d_{33} value measured via more direct approaches.

4.4.4. Fabrication and Characterization of Powder and Pellets

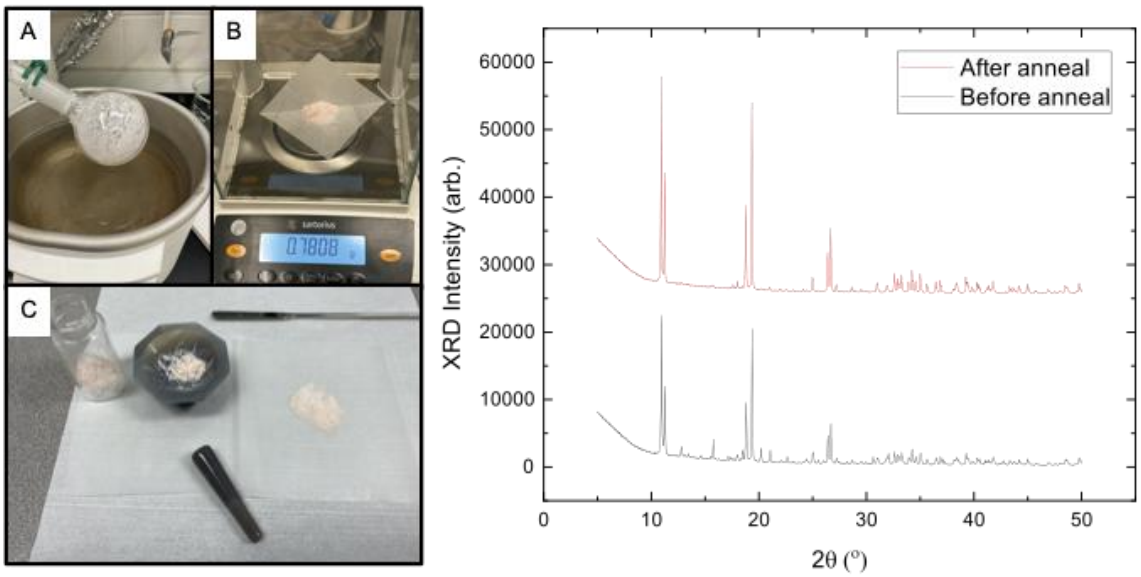

Figure 4-24. Pictures of synthesis of TMCM MnCl3 via rotary evaporation and XRD spectra of product before and after annealing for 48 hours.

Evidence of a piezoelectric response in slot-die coated TMCM $MnCl_3$ films has been demonstrated in the previous two sections, but one shortcoming of this approach is the requirement of FEA simulation to estimate the d_{33} of the piezoelectric layer without a complete piezoelectric tensor, compliance tensor, and dielectric tensor of TMCM $MnCl_3$. Although determining the d_{33} of printed polycrystalline films would be ideal, the effective d_{33} of polycrystalline TMCM $MnCl_3$ has not been reported to date. Therefore, we were inspired to synthesize TMCM $MnCl_3$ powder and press pellets. Initially, a pink powder was synthesized via rotary evaporation of an aqueous solution with a percent yield of 78% (Figure 4-24A and B). Ground up powder was characterized via XRD, revealing primarily a TMCM $MnCl_3$ phase with impurities (Figure 4-24C and Figure 4-24, right). However, annealing the product under vacuum at 100 ^oC for 48 hours drove off the impurities, resulting in a phase-pure TMCM $MnCl_3$ powder.

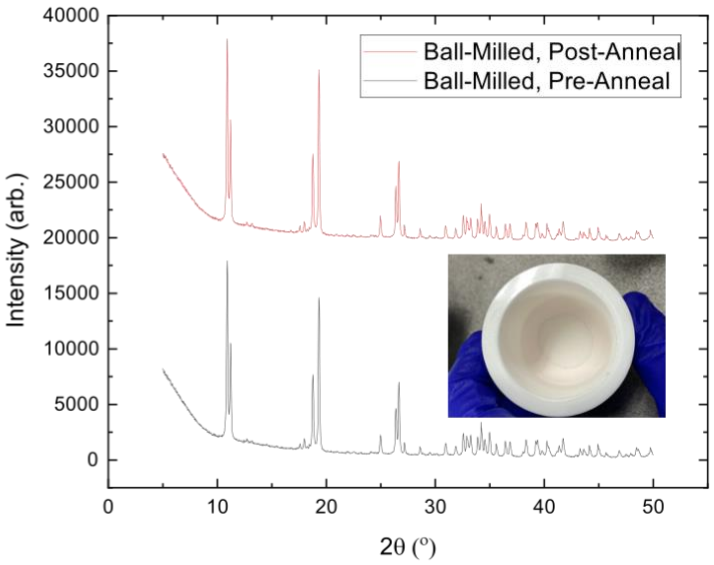

Figure 4-25. Picture of the planetary ball mill (left), an XRD plot of the TMCM $MnCl_3$ product before and after ball milling, and a picture of the powder in the jar.

The lengthy annealing step required to obtain phase-pure powder inspired a different synthetic approach: ball milling. Ball milling resulted in direct synthesis of TMCM $MnCl_3$ from precursors without the need for solvents (Figure 4-25, right). Sample phase purity was preserved after drying under vacuum for two hours to ensure any remaining water was removed. One key step required to ensure a phase-pure product had formed was de-caking the product periodically. $MnCl_2$ and TMCM Cl precursors were ball-milled for the same amount of time without de-caking, and XRD results showed mostly $MnCl_2$ with minimal TMCM $MnCl_3$ phase forming (Figure 4-26).

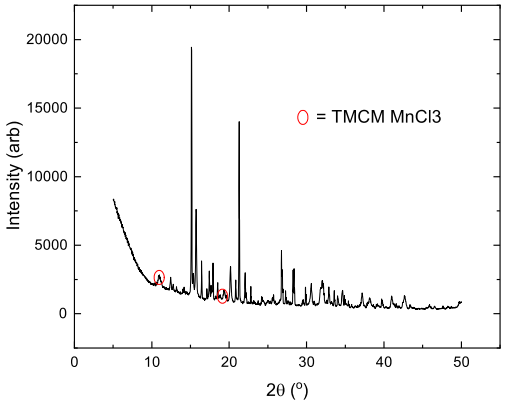

Figure 4-26. XRD of ball-milled TMCM $MnCl_3$ without de-caking.

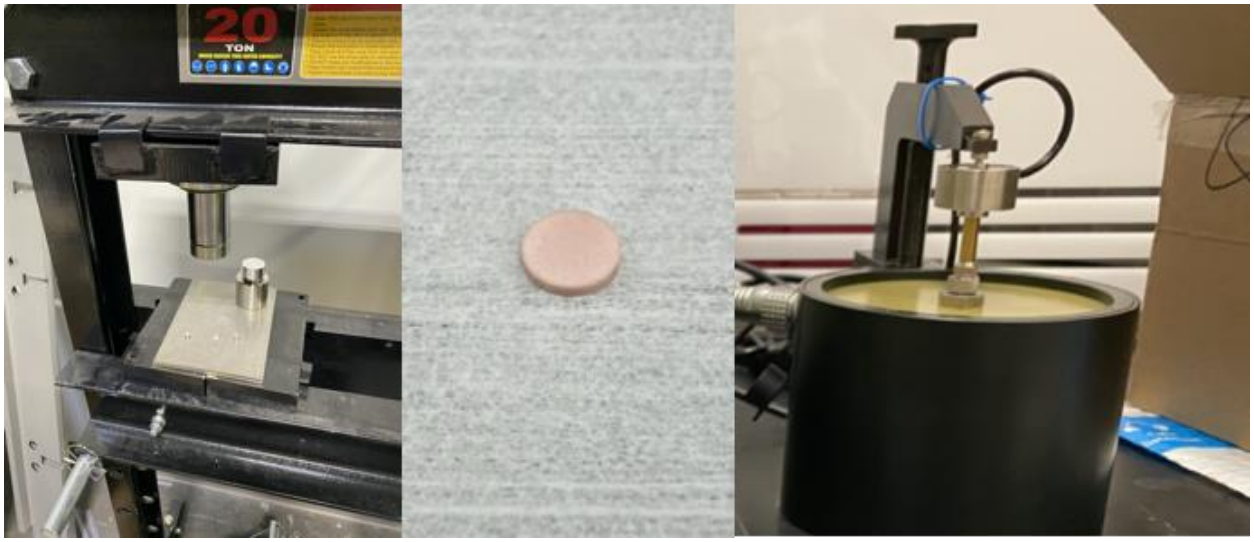

Figure 4-27. Pictures of the pellet press (left), pellets (center), and pellet in a d_{33} meter (right).

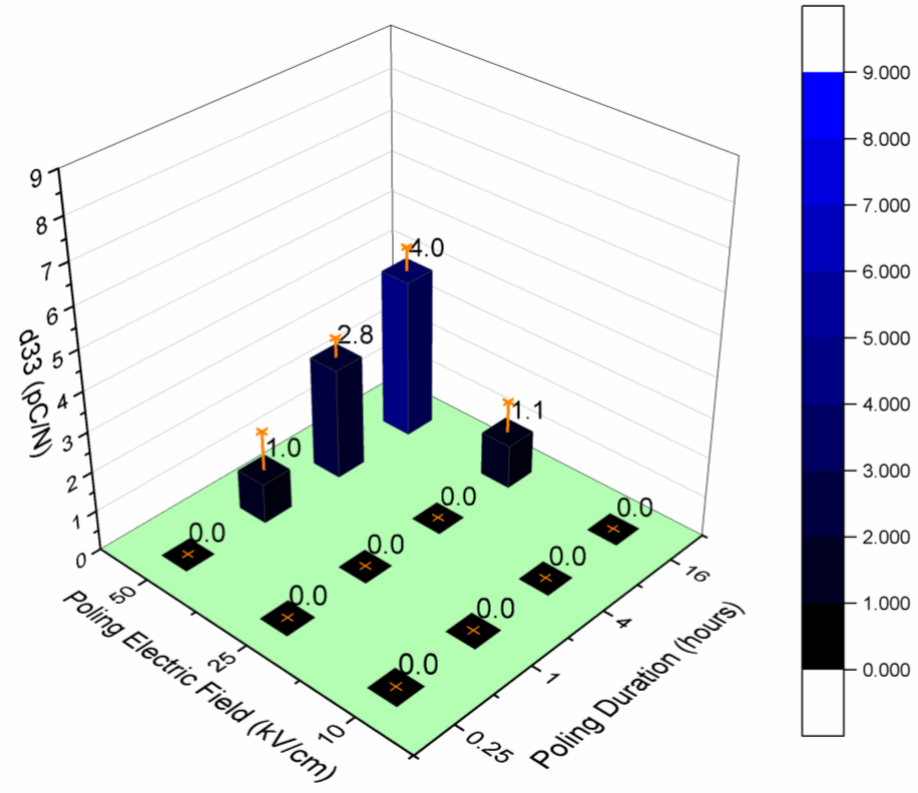

Figure 4-28. d_{33} vs. poling electric field and poling duration for TMCM $MnCl_3$ pellets

Poling electric fields of 10, 25, and 50 kV/cm were applied with cumulative poling durations of 15 min, 1 hour, 4 hours, and 16 hours (n = 5). All unpoled pellets showed a d_{33} of 0-1 pC/N and did not change sign when the pellet was flipped, indicative of insufficient poling. As depicted in Figure 4-28, pellets poled at 50 kV/cm for 24 hours showed a maximum d_{33} of 4.0 pC/N and changed sign when flipped, indicative of successful poling. Electric fields >50 kV/cm resulted in shorting. Shorting also occurred at elevated poling temperatures of 85 ^{o}C and 140 ^{o}C at 25 kV/cm. We speculate that temperature-driven ionic conductivity enabled by defects or vacancies in the TMCM $MnCl_3$ lattice as well as grain boundaries could explain the short circuiting observed at elevated temperatures.

Although a d_{33} value less than the reported single-crystal value of 185 pC/N was expected, a peak d_{33} of 4.0 pC/N was surprisingly low given that TMCM $MnCl_3$ is a multiaxial ferroelectric that should be poled to realize a sizable fraction of the single-crystal value. Theoretically, multiaxial polycrystalline ferroelectrics with a tetragonal crystal structure with six equivalent domain directions can possess a theoretical maximum remnant polarization of $0.83P_s$ (where P_s is the remnant polarization of the single-crystal value), those with a rhombohedral crystal structure with eight equivalent directions can possess a maximum theoretical polarization of $0.87P_s$, and those with an orthorhombic crystal structure with twelve equivalent directions can possess a maximum theoretical polarization of $0.91P_s$ [278]. This trend indicates that as the symmetry of a ferroelectric decreases, the maximum theoretical polarization approaches that of the single-crystal value. The actual realized value is expected to be significantly decreased due to the presence of

internal electric fields/stresses and the ability for some domains to switch back after turning off the poling field.

The large single-crystal d_{33} value of TMCM $MnCl_3$ has not been reproduced in literature by any other groups to date. Ghosh et al. [307] used first-principles simulations to study the piezoelectricity of TMCM $MnCl_3$ as they noted the spontaneous polarization is an order of magnitude smaller than that of $BaTiO_3$, which suggests the expected intrinsic d_{33} would be an order of magnitude less than that of $BaTiO_3$ (105 pC/N in the [001] direction [298]). In their work, they predicted the formation of a ground state with a *Cc* monoclinic structure and spontaneous polarization of 5.2 $\mu C/cm^2$, which matches favorable with experimentally reported structure and P_s (4.0 $\mu C/cm^2$). The intrinsic d_{33} coefficient was predicted to be 1.36 pC/N, two orders of magnitude less than the value reported by You et al. [298]. In addition, Ghosh predicted a second metastable orthorhombic phase with an energy only 27 meV/f.u. higher in energy than the predicted ground state as well as a d_{33} value of -3.16 pC/N. Thus, they concluded that the measured d_{33} values are not intrinsic and considered extrinsic contributions. Ghosh simulated the phase transition from the ground to the metastable phases via stress, and a large spontaneous polarization accompanies this phase transition. Their simulations then predict a d_{33} of 185 pC/N along the polar direction, indicating that phase competition could drive anomalously large piezoelectric response; this mechanism is similar to the one boosting the piezoelectric response of ceramic solution solutions with a morphotropic phase boundary, such as lead zirconate titanate [307]. Based on the proposed mechanism, the authors predict that increasing the static load in the quasi-static

Berlincourt measurement would induce a sudden increase in the piezoresponse. However, in this work we did not observe an increase above 4 pC/N for static loads ranging from 1 to 10 N.

4.5. Conclusion

In this chapter, all-printed piezoelectric sensors based on a multi-axial molecular ferroelectric are fabricated and characterized for the first time, showing the ability to detect multiple bending modes of an aluminum beam in an impact test and a matching frequency response to the first bending mode of a shaker test. Sensors with top/bottom electrodes were fabricated and characterized, demonstrating that the charge/force response can be increased in response to an electric field. Furthermore, polycrystalline TMCM $MnCl_3$ powder was synthesized via ball-milling for the first time, and pressed pellets showed a maximum d_{33} value of 4 pC/N, which is slightly more than 2% of the single-crystal value of 185 pC/N reported previously [298]. This represents the first effort to characterize and quantify the piezoelectric response of polycrystalline TMCM $MnCl_3$.

Chapter 5. Iron-Based Molecular Ferroelectrics

5.1. Introduction

In the previous chapter, all-printed piezoelectric devices were developed using a manganese-based multiaxial molecular ferroelectric. However, the low polycrystalline d_{33} value of TMCM $MnCl_3$ pellets and low signal from all-printed sensors indicated a modest performance for this material in its polycrystalline form. Therefore, I was inspired to search for additional candidates with the potential for improved performance. The molecular ferroelectric tetramethylammonium trichlorobromoferrate(III) (TM $FeBrCl_3$) appeared to be a strong candidate because it possesses reportedly strong polycrystalline d_{33} and g_{33} values (110 pC/N and 731 x 10^{-3} V-m/N, respectively), twelve equivalent polarization axes along the <110> family of directions, processability from green solvents, and a fluorine- and toxic-metal-free composition [308–311]. In addition, Walker et al. carried out detailed ferroelectric characterization studies of TM $FeBrCl_3$ [309–311], making it one of the few newly reported ferroelectrics to be studied by multiple groups.

Notably, Walker et al. did not publish any piezoelectric characterization in their three studies on TM $FeBrCl_3$, but a d_{33} value of 7 pC/N for pressed polycrystalline samples was disclosed in the thesis of one of the coauthors, Simon Scherrer [312]. This large discrepancy in piezoelectric performance was notable, so I believed further characterization of this material was necessary to identify the reason for this discrepancy. The research carried out by Harada et al. and Walker et al. were compared, and the following significant discrepancies were identified as possible explanations for the difference in piezoelectric performance: 1) electrical poling conditions, 2) uncontrolled humidity during ferroelectric and piezoelectric characterization, 3) unknown static loads applied to the samples during piezoelectric characterization, and 4) the compatibility of the electrode material with the sample.

Harada discloses that pellets were poled, but the poling electric field, duration, and temperature were not disclosed. Scherrer did not disclose whether the TM $FeBrCl_3$ samples were poled or not. The detection of a non-zero d_{33} value implied either 1) poling was performed, or 2) a net polarization existed in the piezoelectric samples after fabrication. Neither possible explanation for the observation of a non-zero d_{33} value was provided. Arguably the most important parameter space to explore is the poling conditions as the poling conditions directly influence the ferroelectric and piezoelectric properties in well-studied ceramic and polymer piezoelectrics. For example, the d_{33} coefficient of barium zirconate titanate-barium calcinate titanate solid solutions (BZT-BCT) varied from 150 pC/N to 650 pC/N depending on the magnitude of the poling electric field [313]. In the case of polycrystalline PZT thick films, Radzi et al. reported the d_{33} coefficient increased from 0 to 12 pC/N within the first 5 minutes of poling, and reach saturation value of 25 pC/N after 25 minutes of poling at 4 MV/mm [314]. In general, larger electric fields and poling times increase the d_{33} value.

Another approach utilized to pole piezoelectrics is called field cooling, in which a piezoelectric sample is cooled from an elevated temperature while continuously exposed to an electric field. Typically, the starting elevated temperature is above the Curie temperature, T_C, meaning the ferroelectric dipoles are easily rotatable in response to an electric field at this temperature. This non-180^o domain motion is known as ferroelastic domain motion. Then, as the sample is cooled below the Curie temperature to room temperature under the poling field, the rotated dipoles are "locked in" along the direction of the poling field. For example, Kounga et al. reported a ~40x increase in the d_{33} of commercial PZT by field cooling from 300 ^{o}C (above the Curie temperature) vs. 50 ^{o}C (below the Curie temperature) with a poling electric field of 0.2

kV/mm [315]. Detailed, systematic poling studies have not been performed on any previously published organic-inorganic hybrid molecular ferroelectrics to date.

Furthermore, there is a lack of detail regarding the relative humidity in the ferroelectric and piezoelectric measurements reported by Harada and Scherrer. One publication by Walker and Scherrer [309] indicated the strong impact of water on the ferroelectric properties of TM $FeBrCl_3$. First, Walker notes leakage currents orders of magnitude higher in TM$FeBrCl_3$ films dried on a hot plate vs. under vacuum at the same temperature, suggesting that the presence of water plays a significant role in the dielectric quality of the TM $FeBrCl_3$ samples [309, 310]. Dried samples still showed significant leakage current contributions, which were speculated to be halide vacancies as they are the most mobile species in inorganic-organic metal halide perovskites [310]. However, in this work, Walker also noted that ferroelectric measurements "an insulating oil was avoided as the long and short-term effects of the oil on the $[N(CH3)_4][FeBrCl_3]$ material were unknown. This resulted in some arcing during measurement which contributed to noise in the current signal." It is assumed these ferroelectric measurements were performed in open air as no further description on the environmental conditions (e.g. low humidity, glovebox, etc.) was detailed, suggesting the possibility of ambient moisture degrading the polycrystalline samples during ferroelectric characterization. Furthermore, Harada noted that "contributions of electric conductivity were eliminated by adjusting a variable resistor, which afforded compensated hysteresis loops with straight lines in the high-electric field corners [316] In other words, the P-E loop that Harada reported was compensated to eliminate the rounding observed due to leakage current. Uncompensated P-E loops were not published. In either case, P-E characterization of samples in silicone oil, a standard practice in ferroelectric characterization, would limit exposure of samples to ambient humidity. In addition, even if samples were characterized and poled in silicone oil,

piezoelectric characterization with a quasi-static d_{33} meter cannot be performed with samples in oil. I hypothesized that elevated humidity levels could reduce the d_{33} coefficient due to the potential increase in leakage current. Therefore, the d_{33} coefficient was measured as a function of humidity by carrying out all testing in an Environment Control room with a programmable humidity (10-60% relative humidity).

In addition, neither Harada nor Scherrer describe the static force applied to the sample during piezoelectric characterization, only the dynamic load (0.25 N, 110 Hz). Given that these samples can be compressed in response to mild pressures, it is possible that an overly aggressive static load could dampen/clamp the piezoelectric response, resulting in an artificially low d_{33} value. Furthermore, another key issue is that neither Harada nor Scherrer describe the number of samples characterized. Often studies of piezoelectric ceramics and polymer will report the average d_{33} value of multiple samples. Therefore, it is unclear if reported measurements are an anomaly or truly representative of the material.

Finally, we note that Harada and Walker/Scherrer used different electrode materials. Harada reported the use of conductive carbon electrodes deposited on each face of the pressed TM $FeBrCl_3$ sample, while Scherrer and Walker sputtered gold electrodes. While the difference appears to be trivial *prima facie* given that both electrode materials are chemically inert when in contact with most materials, polycrystalline gold can react with $FeCl_3$ in the presence of excess bromide to form $AuCl_2^-$ species. For example, gold plasmonic nanorods have been reported to be shortened by $FeCl_3$ with excess Br. Furthermore, Scherrer acknowledged "electrode degradation caused by the known corrosivity of [$FeBrCl_3$]" [312]. Therefore, it's plausible that leakage currents were boosted due to the degrading electrode, which in turn could result in a poorer dielectric with

a lower d_{33} coefficient. Therefore, the ferroelectric and piezoelectric properties of samples with carbon and gold electrodes were compared.

In this chapter, first all-printed vibration sensors with TM $FeBrCl_3$ as the piezoelectric material were fabricated and characterized. Then, TM $FeBrCl_3$ powder was synthesized via ball milling, and pellets were fabricated to characterize the material's ferroelectric and piezoelectric properties. The goal of this fundamental characterization was to identify the reason for the discrepancy in the d_{33} values reported by Harada and Scherrer. The peak d_{33} value measured in TM $FeBrCl_3$ pellets, 5.1 pC/N, is substantially lower than the value of 110 pC/N reported by Harada [316] but is consistent with the value of 7 pC/N reported by Scherrer [312]. The aforementioned piezoelectric poling and testing discrepancies between Harada and Scherrer were examined and addressed experimentally, allowing the elimination of several explanations for this discrepancy. The results of this series of experiments inspire a larger discussion on the lack of transparency and reproducibility in this burgeoning field and potential remedies that will enable this field to blossom.

5.2. Methods

5.2.1. Materials

PET substrates (Melinex ST 505, Dupont) were supplied by Tekra LLC. Ferric chloride (reagent grade, 97%), tetramethylammonium bromide (ACS reagent, ≥98%), ethanol, trimethylamine solution (28% in dH_2O), chlorobromomethane, acetonitrile, and silver nanoparticle ink (Silverjet DGP-40LT-15C, Advanced Nano Products) were purchased from Sigma Aldrich. Ferric chloride and tetramethylammonium bromide were dried under vacuum overnight and stored

in a nitrogen glovebox. Trimethylchloromethyl ammonium bromide (TMCM Br) was prepared by stirring equimolar quantities of trimethylamine solution and chlorobromomethane in acetonitrile at room temperature for 48 hours. TMCM Br was precipitated via rotary evaporation, dried under vacuum overnight, and stored in a nitrogen glovebox.

5.2.2. Thin film fabrication and characterization

To prepare the precursor ink, equimolar quantities of $FeCl_3$ and TMAB were weighed in a nitrogen glovebox and dissolved via stepwise addition of dH_2O (*caution: the dissolution of $FeCl_3$ in dH_2O is exothermic*). Upon observing a transparent red solution that had cooled to room temperature, ethanol was added such that a 4 dH_2O : 1 ethanol mixture by volume with a precursor concentration of 400 mg per mL of total solvent was realized. All slot-die coating was performed in an environment control room with an adjustable humidity (10-60% RH) and temperature; the temperature of the room was fixed at 21 ^oC. PET substrates were cleaned with a cleaning roller, treated with UV-ozone (lamp time of 5 minutes), and affixed to a temperature-variable vacuum chuck. A polyether ether ketone (PEEK) slot die head with a 10-mm-wide tantalum-coated stainless-steel shim and meniscus guide was used to coat the precursor solution onto PET. The guide-substrate gap was set to 152 μm, and the slot-die coating chuck temperature (50, 70, and 90 ^oC), coating speed (30, 60, 120, and 240 cm/min), and humidity (15, 35, and 55% RH) were varied systematically. The rate of the precursor solution injected into the slot die head via a motorized syringe pump was scaled with the coating speed at a 1 cm/min : 1 μL/min ratio (e.g. a coating speed of 30 cm/min corresponded to an injection rate of 30 μL/min). All films were dried at 90 ^oC on the vacuum chuck for one hour prior to characterization.

The crystal structure of $TMFeBrCl_3$ films was characterized with a 2D x-ray diffractometer (D8 Discover Microfocus, Bruker), and the morphology of $TMFeBrCl_3$ films was characterized via a scanning electron microscope (Sirion XL30, FEI).

5.2.3. *All-printed device fabrication and characterization*

For all-printed devices, PET substrates were cleaned with a cleaning roller, and silver interdigitated electrodes were printed using a Dimatix DMP-2800 inkjet printer and a cartridge with a 10-pL drop size. All geometries were inkjet-printed at a bed temperature of 60 ^{o}C, a cartridge temperature of 40 ^{o}C, a drop spacing of 20 μm, and a jetting frequency of 5 kHz. One or four passes were printed. After annealing at 60 ^{o}C, interdigitated electrodes were annealed at 120 ^{o}C for 30 minutes. The geometries of IDEs were measured with a laser confocal scanning profilometer (LEXT OLS4100, Olympus). $TMFeBrCl_3$ was slot die coated at 70 ^{o}C and 15% RH and subsequently annealed at 70 ^{o}C for 60 minutes. 38 AWG copper wires were attached to piezoelectric sensors with silver epoxy followed by a 2-part epoxy (5103A/B, ATACS) to reinforce adhesion. Sensors were cut to size and affixed to 2 cm x 50 cm aluminum beams with a thickness of 0.50 mm via epoxy and cured overnight. Poled sensors were poled in a nitrogen glovebox at an electric field of 60 kV/cm for 30 min.

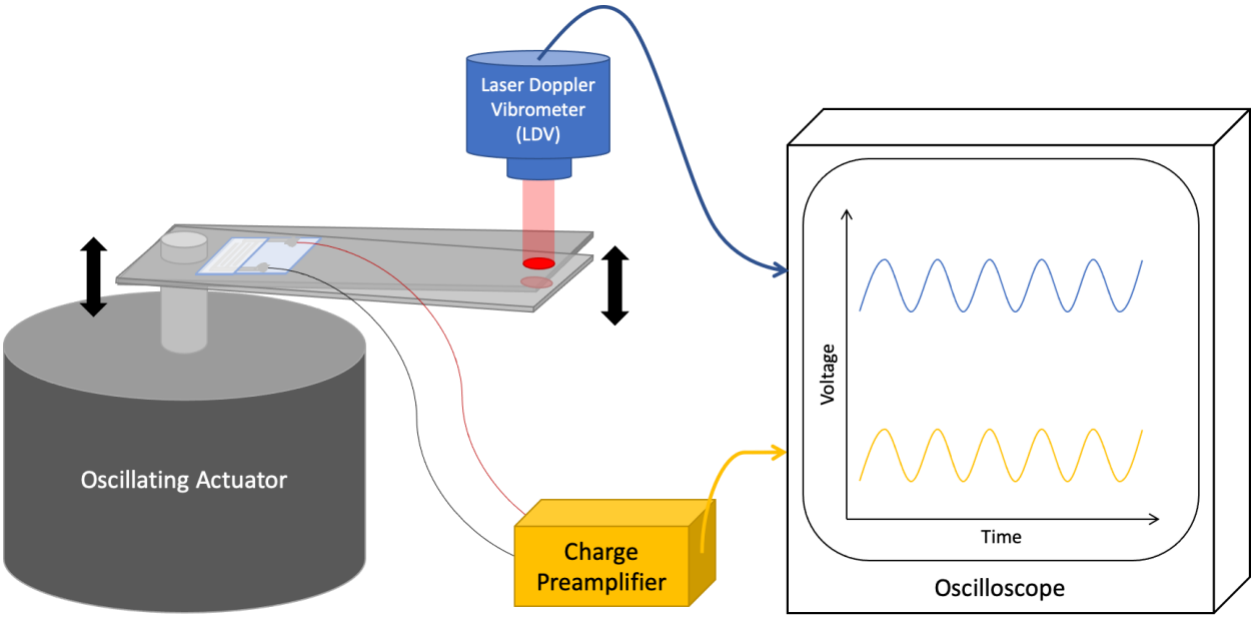

Figure 5-1. Schematic of the shaker test used to confirm the piezoelectric response of all-printed sensors.

All sensor characterization experiments were designed and performed by Dr. Weiwei Xu. Sensors attached to beams via epoxy were affixed to an electromechanical oscillator (Arbor Scientific) driven by a function generator (Figure 5-1). The beam is oscillated at its first natural frequency (ca. 130 Hz). Time domain signals from a laser doppler vibrometer (LDV) and the sensor response from the charge amplifier (Bruel and Kjaer Type 2663, 100 mV/pC) were collected and analyzed by a digital oscilloscope (Tektronix TDS540A) or a spectrum analyzer.

For corrosion experiments, 120-mm-long silver traces were inkjet-printed onto PET as described previously. Traces with 1, 2, 3, 4, 6, 8, and 10 passes were inkjet-printed. Traces with multiple passes were annealed at 60 ^{o}C for five minutes prior to the deposition of the next layer. All traces were annealed at 120 ^{o}C for 15 minutes. Then, silver contacts were deposited by hand along each trace using a screen-printing silver ink (Dupont PE874), and the traces and contacts were annealed at 120 ^{o}C for 30 minutes. The resistivity of each segment was measured on the slot-die bed (set to 70 ^{o}C), and then TM $FeBrCl_3$ was slot-die coated perpendicular to each segment at

a bed temperature of 70 ºC, a relative humidity of 15% RH, a coating speed of 30 cm/min, and an injection rate of 30 µL/min. After allowing the films to anneal at 70 ºC for 10 min, the resistance of each line segment was re-measured.

5.2.4. Mechanosynthesis and Characterization of TM $FeBrCl_3$ Powders

50 mL yttria-stabilized zirconia (YSZ) ball milling jars and media (JA0205 and BA0125, MSE Supplies) were dried under vacuum overnight and transferred into a glovebox. Equimolar quantities of $FeCl_3$ and TMAB were weighed and added to the jar. Jars were sealed with electrical tape and then ball-milled in open air using a planetary ball mill (MA0103, MSE Supplies) for 10 minutes. Jars were transferred into the glovebox to break up caked powder in the bottom of the jar. 6 ball milling cycles were completed. Product was dried under vacuum overnight; some undried product was reserved for ferroelectric characterization.

The orange-brown product was characterized with XRD (D8 Advance, Bruker) using Cu Kα radiation (λ = 0.15418 nm). A 2-theta range of 10-50º, a step size of 0.02º, and a step time of 0.5 second were utilized. The product also characterized with DSC (DSC 3+, Bruker) with a temperature range of -25 ºC to 150 ºC, a scan rate of 5 ºC/min, and a 15-minute hold time at the minimum and maximum temperature. All product was stored in a nitrogen glovebox.

5.2.5. Fabrication and Characterization of TM $FeBrCl_3$ and TMCM $FeBrCl_3$ Pellets

Varying masses of TM $FeBrCl_3$ powder was weighed in a glovebox and added to a stainless-steel pellet die with a 6.35 mm diameter (PR0101, MSE Supplies). Die inserts were

covered with polyimide tape to prevent corrosion of the inserts. Pellets were pressed at a pressure of 60 MPa for 60 seconds, and the pellet die set was cleaned with 2% detergent in dH_2O, dH_2O, and IPA immediately after pressing and liberating the pellet. The thickness of pellets was measured with digital calipers. Conductive carbon paste (DM-CAP-4701S, Dycotec Materials) was painted on each face and cured at 100 ^oC for 10 minutes to form electrodes. Or, 100 nm of gold were sputtered through a 4.5-mm-diameter mask onto each face to form electrodes. Ferroelectric properties of both dried and undried pellets were characterized with a P-E Loop system based on a modified Sawyer-Tower circuit (PolyK Technologies). Pellets were poled in a silicone oil bath using a 10 kV power supply, and the piezoelectric properties were measured using a d_{33} quasi-static meter (PolyK Technologies). All fabrication and characterization steps were performed in an environment control room with a programmable humidity (10-60% relative humidity).

5.3. Results

5.3.1. Slot-Die Coating and Characterization of TMFeBrCl$_3$ film

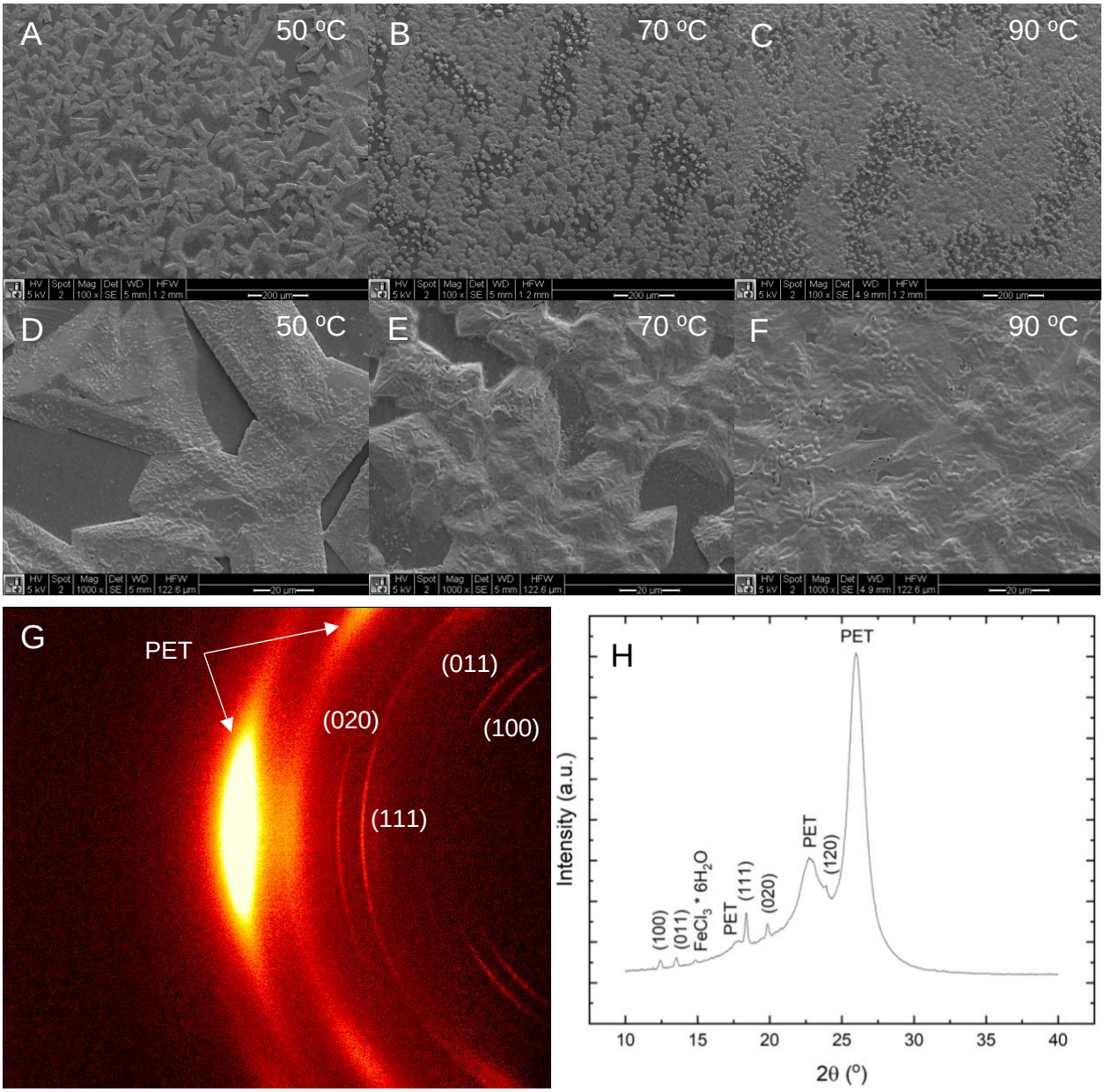

Figure 5-2. SEM images of TM FeBrCl$_3$ films slot die coated at 50 °C (A, D), 70 °C (B, E), and 90 °C (C, F) reveal increasing film coverage as temperature increases. 2D XRD (G) and the integrated scan (H) of the films slot die coated at 70 °C and 15% RH revealed a textured TM FeBrCl$_3$ film.

TM $FeBrCl_3$ films were slot-die coated from water as the organic salt TMAB is poorly soluble in all other solvents. as the solubility of the organic precursor tetramethylammonium bromide is limited in non-aqueous solvents. Ethanol was added to decrease the surface tension of the aqueous solution [317] and improve the wetting of the wet film on the substrate. The addition of 10-30% alcohol by volume is a common approach utilized to slot-die coat uniform films. The slot die bed temperature and humidity were varied to identify the optimal processing conditions. The slot-die bed temperature played a central role in affecting the morphology of TM $FeBrCl_3$ films (Figure 5-2, A-C) A rectangular wet film was achieved with an injection rate of 30 μL/min and coating speed of 30 cm/min. Optical and SEM imaging of slot-die coated TM $FeBrCl_3$ films revealed that increasing the bed temperature from 50 ^oC to 70 ^oC resulted in the formation of a denser microstructure and increased coverage. A higher slot die coating temperature accelerates solvent evaporation, resulting in an increased drying and nucleation rate for the piezoelectric from solution and a reduced time for liquid flow-based de-wetting. However, slot-die coating at 90 ^oC resulted in visibly streaky films, indicative of overly volatile solvent evaporation. Therefore, a slot-die coating temperature of 70 ^oC was deemed optimal for sensor fabrication.

2D XRD results revealed that the room-temperature-stable ferroelectric phase of TM $FeBrCl_3$ [308, 310] primarily formed for the slot-die coated film coated at 70 ^oC (Figure 5-2D); a small peak detected at ~14.8^o from the integrated scan (Figure 5-2E) was assigned to $FeCl_3*6H_2O$ as the primary printing solvent is water. Furthermore, the incomplete Debye-Scherrer rings indicated texture, suggesting that slot-die coating can impart a preferred orientation in the polycrystalline films. This processing-structure relationship has been reported for other inorganic-organic hybrids, such as lead halide perovskites [291] and TMCM $MnCl_3$ as described in the previous chapter. In this case, the ferroelectric axes are in the <011> family of directions, so the

orientation of the (001) plane with a 45^{o} angle to the slot-die coating direction indicates a non-zero component of the ferroelectric axis lies perpendicular to the slot-die coating direction (the direction necessary to observe a piezoelectric response between the positive and negative IDEs). These results, along with slot-die coated TMCM $MnCl_3$ described in Chapter 4, represent the first report of this processing-structure relationship resulting in textured ferroelectric films.

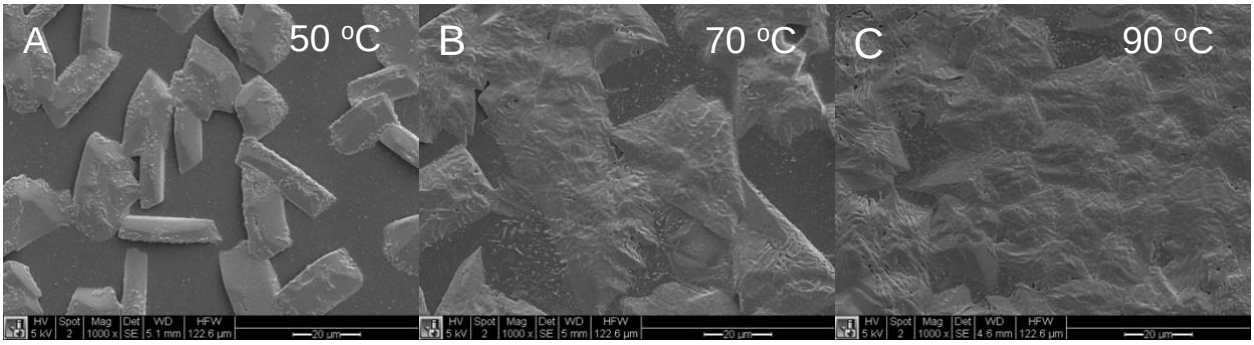

Figure 5-3. SEM images of slot-die coated TMFeBrCl3 at 55% relative humidity at slot die coating temperatures of 50 °C (A), 70 °C (B), and 90 °C (C).

SEM images of films slot-die coated at 55% RH resulted in fewer, larger domains (Figure 5-3). An elevated humidity decelerated solvent evaporation, which promoted crystal growth over nucleation.

5.3.2. Fabrication and Characterization of All-Printed Devices and Corrosion Experiments

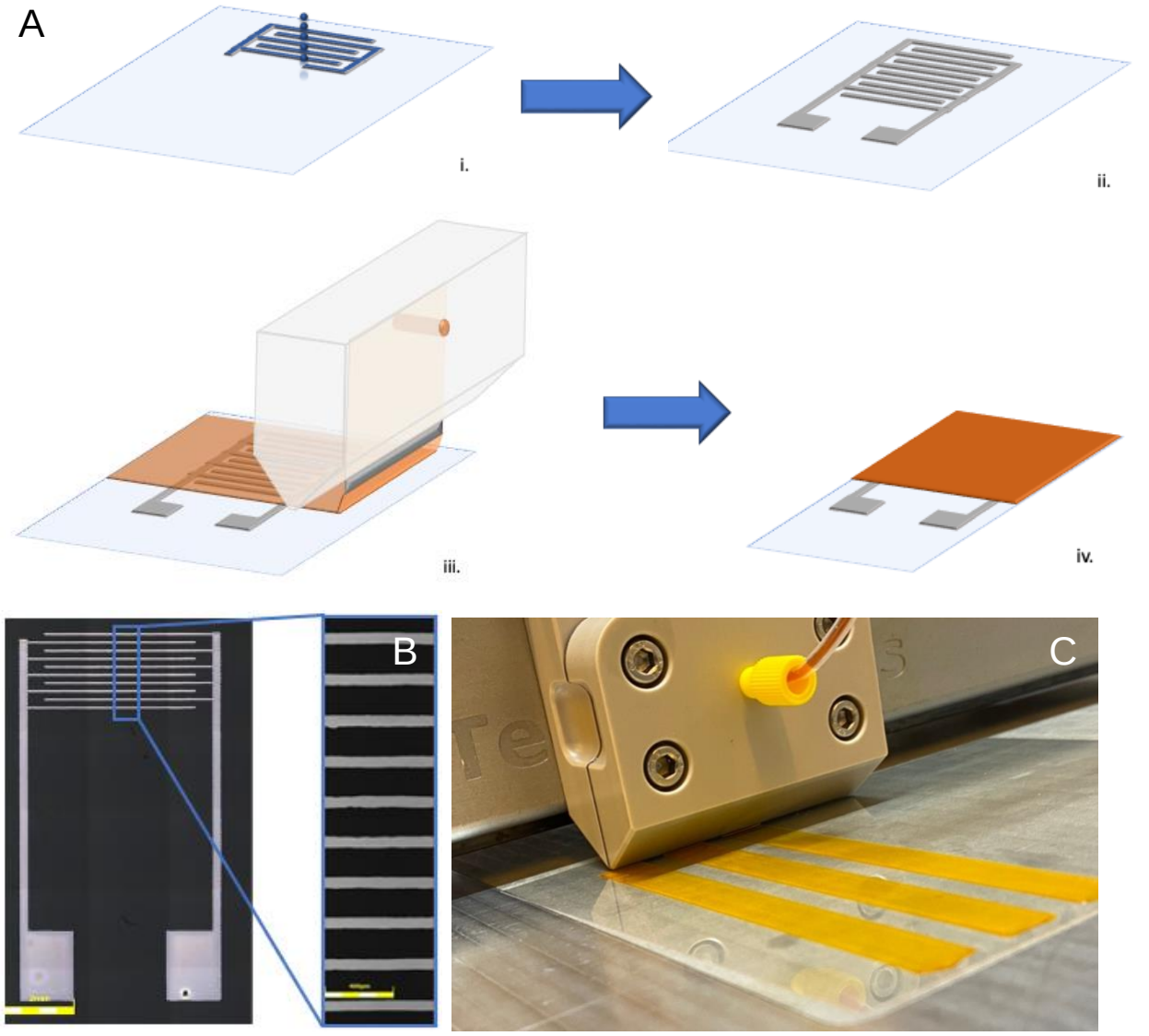

Figure 5-4. Schematic of the all-printed vibration sensor. Interdigitated electrodes (IDEs) are inkjet-printed onto a PET substrate (A, i) and annealed at 120 ºC for 15 min (A, ii), and then TM FeBrCl3 is slot-die coated over the interdigitated electrodes (A, iii.) and annealed (A, iv.). Optical images of IDEs (B) reveal a linewidth of 90 microns and a line spacing of 150 microns, and slot die coating represents a scalable technique to fabricate piezoelectric films (C).

All-printed piezoelectric vibration sensors were fabricated in several manufacturing steps (Figure 5-4A). First, silver interdigitated electrodes (IDEs) were inkjet-printed onto a flexible PET substrate (Figure 5-4A, i) at a substrate temperature of 60 ºC and inkjet cartridge temperature of 50 ºC to drive off solvent and prevent bleeding and overlap of the IDE digits, which would result

in device failure. A commercial silver nanoparticle ink was selected due to its low sintering temperature of 120 °C and rheological properties tailored for inkjet printing. After inkjet printing, all patterns were cured at 120 °C for 15 min (Figure 5-4A, ii). The IDE finger length, width, separation, and thickness were 4.5 mm, 90 µm, 150 µm, and 400 nm, respectively after four printing passes (100 nm per pass). Then, a TM $FeBrCl_3$ solution was prepared and slot-die coated over the interdigitated electrodes (Figure 5-4A, iii. and Figure 5-4C).

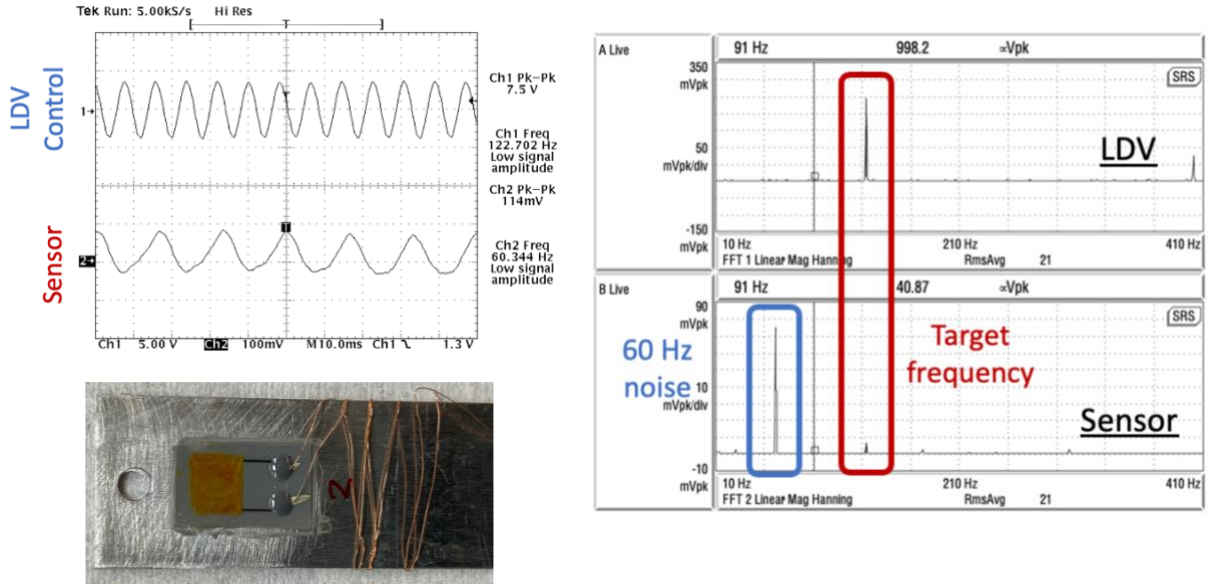

Figure 5-5. Time-domain (upper left) and frequency-domain (right) response of an all-printed sensor (lower left).

Shaker tests as described in the previous chapter were performed to confirm if the sensors show a piezoresponse. Eight sensors with IDEs that had only one printing pass did not show a response using an oscilloscope; only 60 Hz noise was detected (Figure 5-5). Replacing the oscilloscope with a spectrum analyzer confirmed that the sensor was detecting primarily 60 Hz noise. A small peak was detected at the target frequency, the first bending mode of the oscillating beam. While such a response could be piezoelectric, triboelectric contributions from vibrating

wires could generate a small signal, indicating it's possible the integrity of the silver traces was compromised.

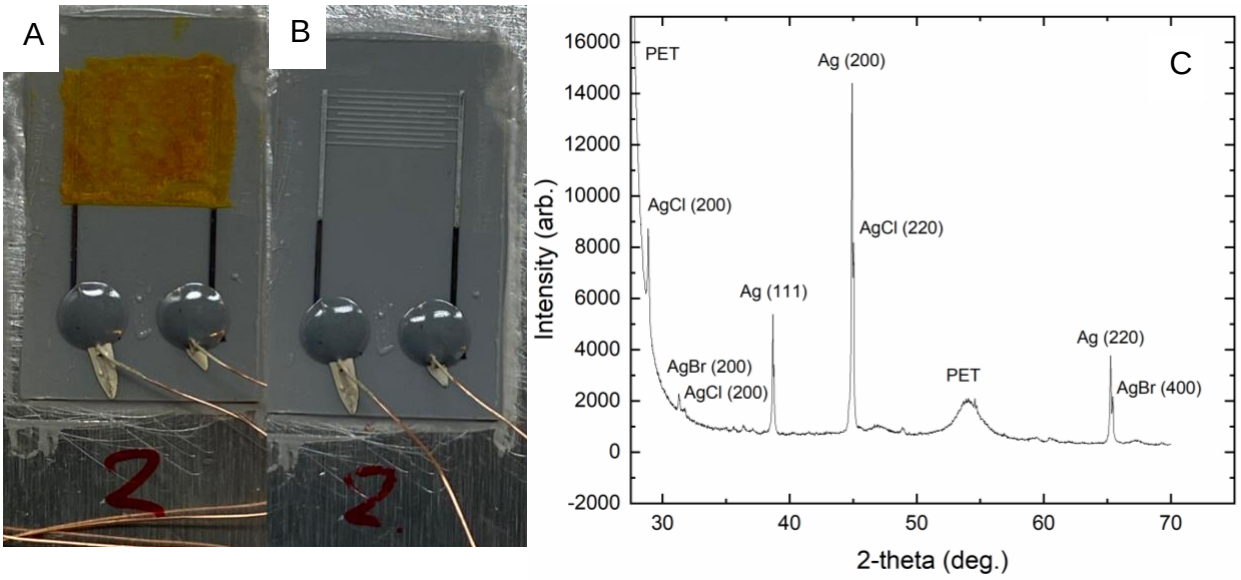

Figure 5-6. Pictures of an all-printed sensor before (A) and after (B) the dH_2O wash and the corresponding XRD plot of the exposed IDE fingers

To investigate the integrity of the silver traces, one of the non-responsive sensors was dipped in dH_2O to dissolve the TM $FeBrCl_3$ (Figure 5-6A), leaving behind exposed silver IDE electrodes (Figure 5-6B). XRD scans of these exposed electrodes (Figure 5-6C) revealed silver peaks at 38.678° (111), 44.918° (200), and 65.253° (220). Clear XRD peaks for AgCl at 28.879° (111), 31.293° (200), and AgBr at 32.029° (200) and 65.437° were also detected, indicating that the slot-die coated silver was forming a metal halide interfacial layer. It is possible that the corrosion of the silver traces results in disruptions in trace conductivity, leading to dramatic decreases in the measured response as the surface area between electrodes is reduced.

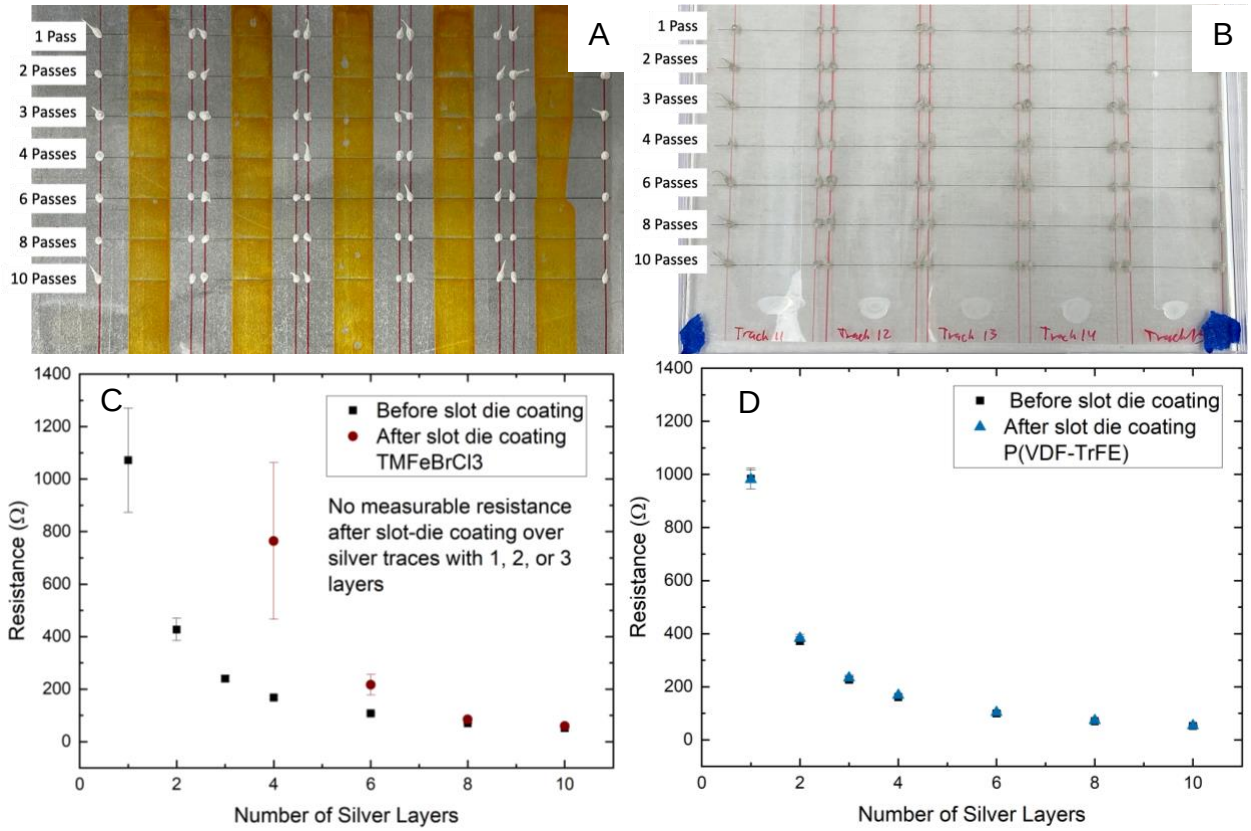

Figure 5-7. Comparing the effects of slot-die coated TM FeBrCl3 (A, C) vs. P(VDF-TrFE) (B, D) on the resistance of inkjet-printed silver traces as a function of number of printed silver layers.

Given that the TM $FeBrCl_3$ layer has been shown to corrode the silver electrodes, experiments were taken to determine the minimum number of inkjet printing passes required to maintain conductivity in printed silver traces. Long silver traces with increasing numbers of passes were inkjet-printed, and the resistance of traces was measured for ten line segments. Then, TM $FeBrCl_3$ was slot die coated over silver traces with increasing number of silver passes (Figure 5-7A), and the resistance was remeasured. I hypothesized 1) the resistance would increase due to the replacement of conductive silver with non-conductive AgCl and AgBr species, and 2) the relative increase in resistance would decrease as the thickness of the silver layer increases. Both trends were observed (Figure 5-7B). Silver traces with one, two, and three passes were rendered non-conductive after slot-die coating. Silver traces with four passes showed a nearly 4x increase

in the average resistance (n = 10), while the resistance of those with six passes doubled after slot-die coating TM $FeBrCl_3$. The resistance of traces with eight and ten passes showed minimal increases in the average resistance after slot-die coating. The latter result suggested that corrosion rather than physical removal of printed silver by the slot-die coating process was responsible for the increase in resistance. Such a possibility must be considered as silver traces with poor adhesion to a substrate can be removed due to subsequent processing steps. To further support the hypothesis that corrosion rather than displacement was responsible for the increase in resistance, the co-polymer poly(vinylidene-co-trifluoroethylene), known as P(VDF-TrFE), was slot die coated from DMF (2 wt.%) over silver traces (n = 5) under identical slot-die coating processing conditions. P(VDF-TrFE) was selected due to its inert chemical nature. The traces showed no change in resistance, indicating that the slot-die coating process did not physically displace silver lines.

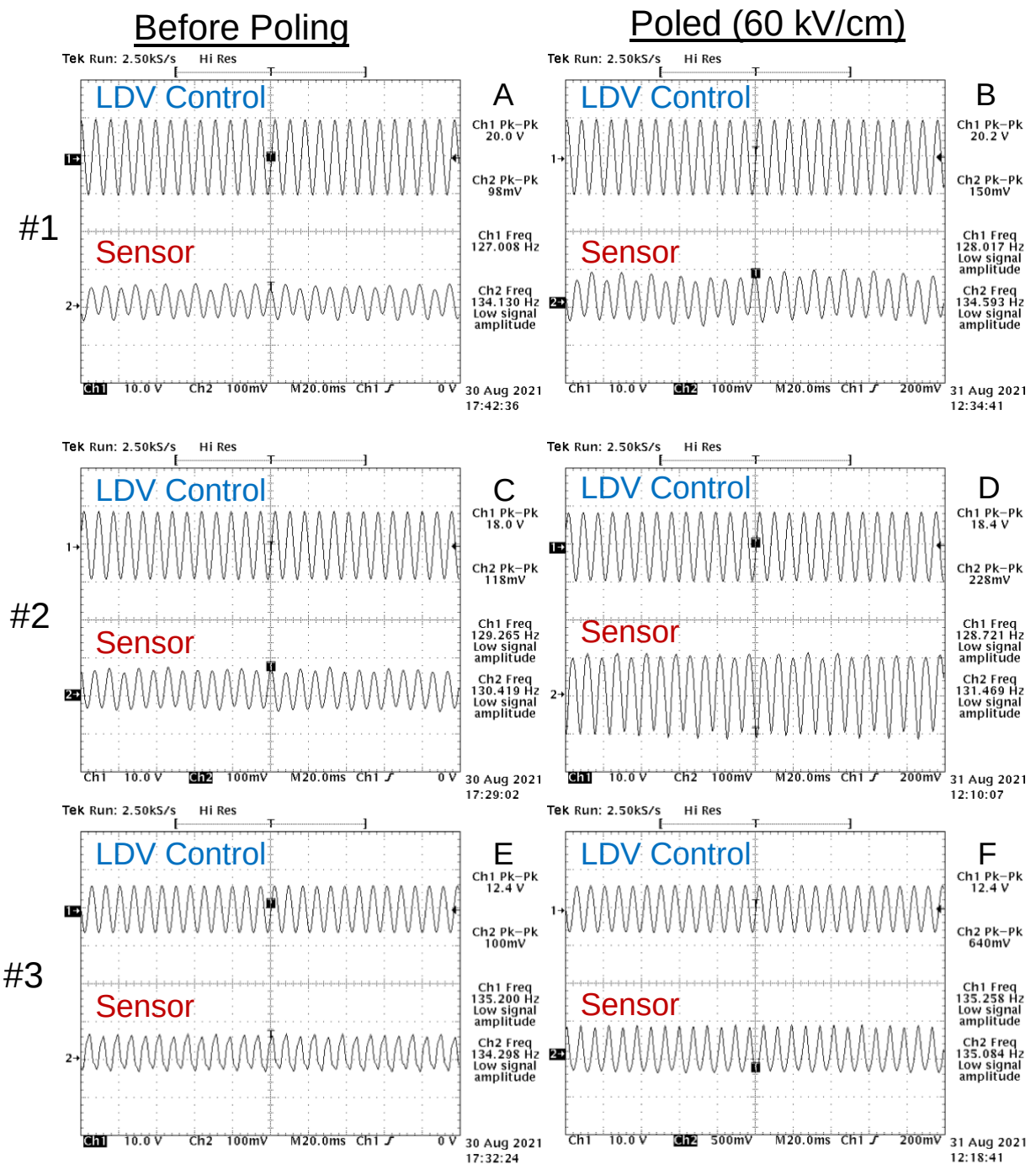

Figure 5-8. Shaker test results for three sensors before (A, C, and E) and after poling (B, D, and F). The top trace in each plot corresponds to the LDV signal, while the bottom trace corresponds to the charge output from the sensor (credit: Dr. Weiwei Xu).

The shaker test developed by Dr. Weiwei Xu was used to validate the sensor response (Figure 5-8). As described in the previous chapter, sensors were attached to an aluminum beam, and the beam was affixed to a dynamic oscillator. The beam was vibrated near its first natural frequency (ca. 135 Hz) to generate a response that is recorded by an oscilloscope. The frequency of the charge generated from the sensor matches the frequency of the displacement independently measured by a laser doppler vibrometer, indicating the piezoelectric sensors were operational. Notably, sensors showed a piezoelectric response prior to poling. The aforementioned 2D XRD results revealed a textured polycrystalline film, so we hypothesize. shear forces from slot-die coating induce a self-polarized ferroelectric film with a net ferroelectric dipole. Self-polarized thin films have been reported for several classes of ferroelectrics, including oxide perovskites [318–320], PVDF and its derivatives [321–323], and, more recently, the organic molecular ferroelectric [Hdabco]ClO_4 (dabco = 1,4-diazabicyclo[2.2.2]octane) [324]. Processing conditions have been reported to influence self-polarization in ferroelectrics. For example, the high shear forces of spin coating induced a self-polarized thin film of the ferroelectric polymer P(VDF-TrFE) [321]. Detailed studies on this self-poling mechanism are in progress. Furthermore, the average magnitude of the signal detected by the sensors doubled after poling sensors at 60 kV/cm for 30 min, indicating that post-fabrication poling increased dipole alignment and boosted sensor performance. This result represents the first demonstration of an all-printed vibration sensor using TM $FeBrCl_3$ as the piezoelectric sensing layer.

5.3.3. TM $FeBrCl_3$ Powder Synthesis and Characterization

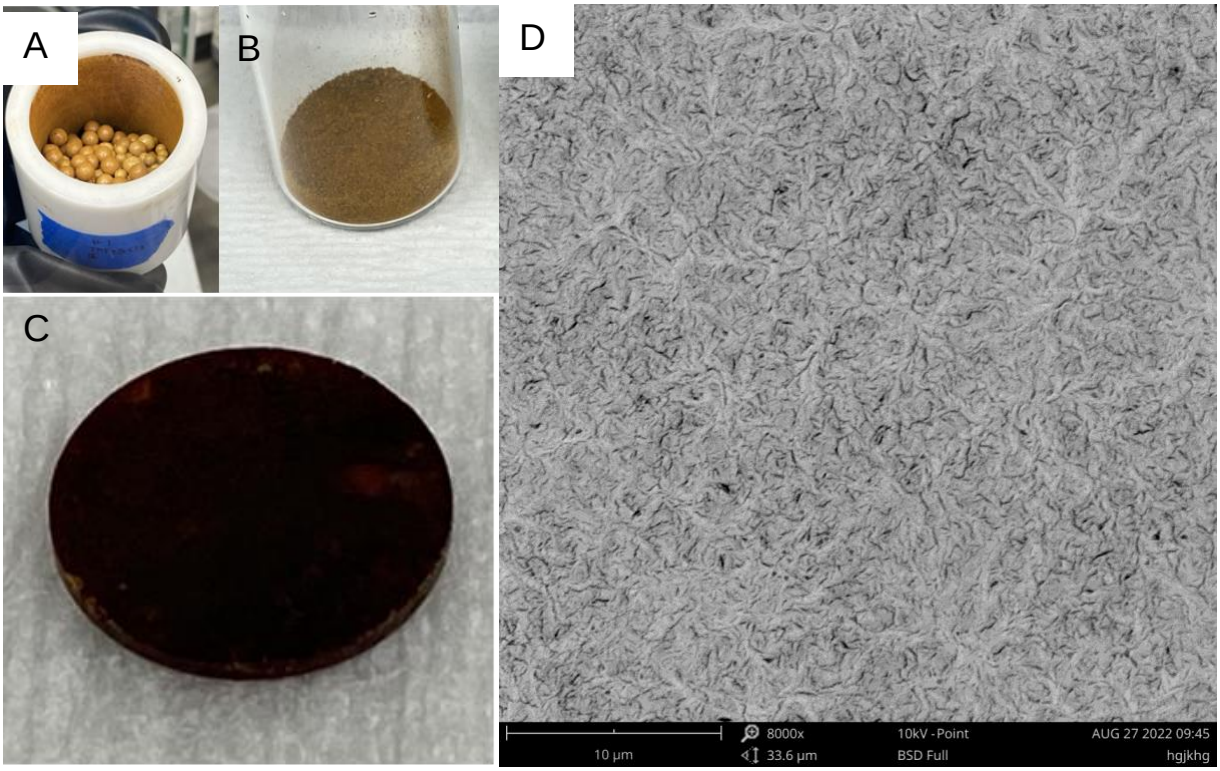

Figure 5-9. Pictures of ball-milled TM $FeBrCl_3$ powder (A, B) and a pressed pellet (C), and an SEM image of a pressed pellet (D).

As discussed in the previous chapter, it is difficult to measure the d_{33} of printed polycrystalline TM $FeBrCl_3$ given that the full experimental piezoelectric tensor, compliance tensor, and dielectric tensor of this material has not been published. Given these limitations, I was motivated to synthesize powder via the ball-milling technique introduced in Chapter 4 (Figure 5-9A and B) to measure the d_{33} in bulk powder form, which likely would not possess the same texture as slot-die coated films. A uniform orange/brown powder formed after three cycles of ball milling and de-caking, but powder was ball milled for six cycles to ensure all reagents were consumed. Then, powder was pressed into 6.35-mm-diameter pellets for ferroelectric and

piezoelectric characterization (Figure 5-9C). SEM images revealed a uniform microstructure with micron-scale domain sizes.

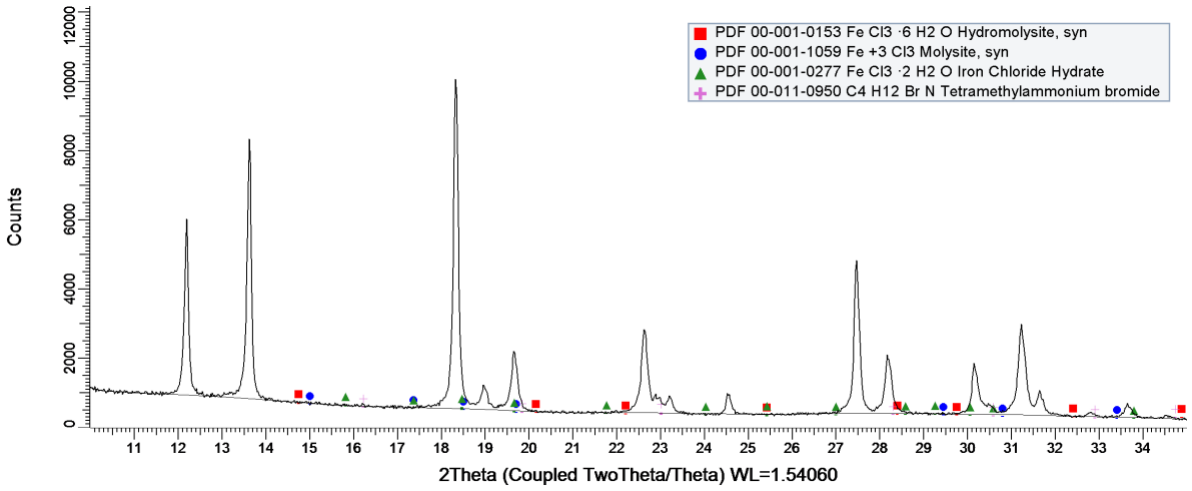

Figure 5-10. XRD scan of the TM FeBrCl3 powder.

XRD scans of the powder (Figure 5-10) revealed that the phase-pure orthorhombic *Amm2* structure of TM $FeBrCl_3$ had formed [309], although it's possible trace amounts of impurities exist in the film that escape the resolution of the diffractometer. Additional markers of precursors ($FeCl_3$ and TMAB) and common impurities ($FeCl_3$*$6H_2O$ and $FeCl_3$*$2H_2O$) were included to emphasize the lack of impurities or unreacted precursors.

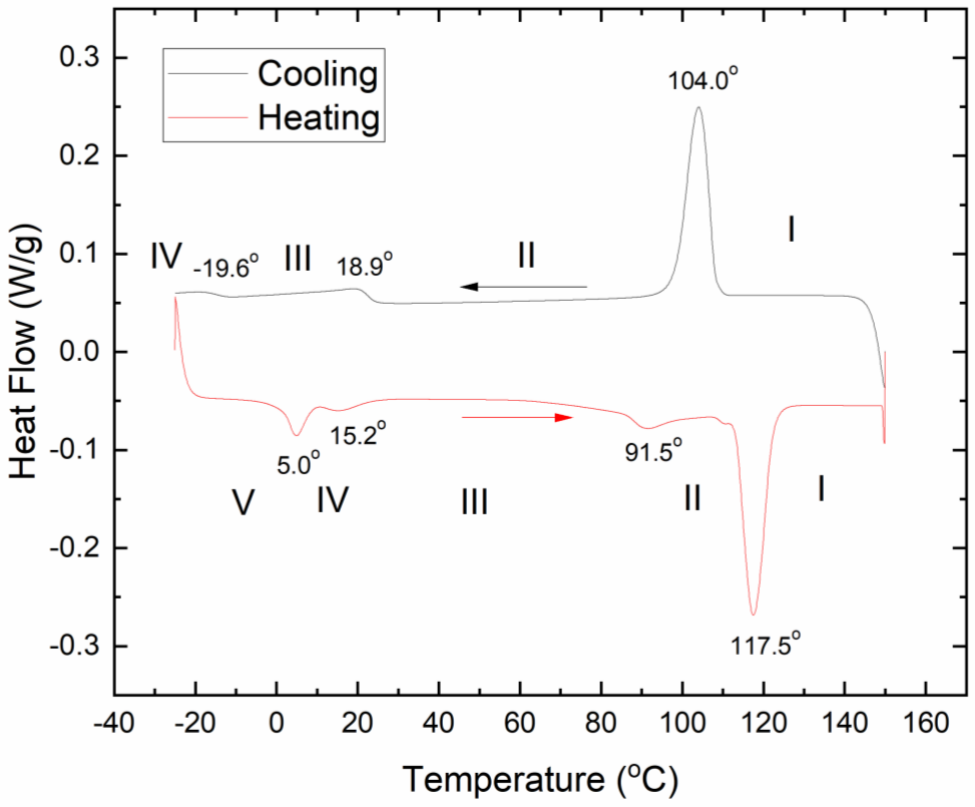

Figure 5-11. DSC plot of TM $FeBrCl_3$ powder. The roman numerals correspond to the five phases reported by Harada and Walker.

A DSC scan of the TM $FeBrCl_3$ powder was taken (Figure 5-11). Notably, alumina crucibles rather than aluminum crucibles were used due to the corrosivity of TM $FeBrCl_3$, meaning that there was slower heat transfer to the sample. In turn, this resulted in 5-15° rightward shifts of exothermic peaks during the heating run and similar 5-15° leftward shifts of the endothermic peaks during the cooling run when comparing to the results collected by Walker [311].

5.3.4. Ferroelectric and Piezoelectric Characterization of TM $FeBrCl_3$ Pellets

5.3.4.1. Ferroelectric Properties of TM $FeBrCl_3$ pellets

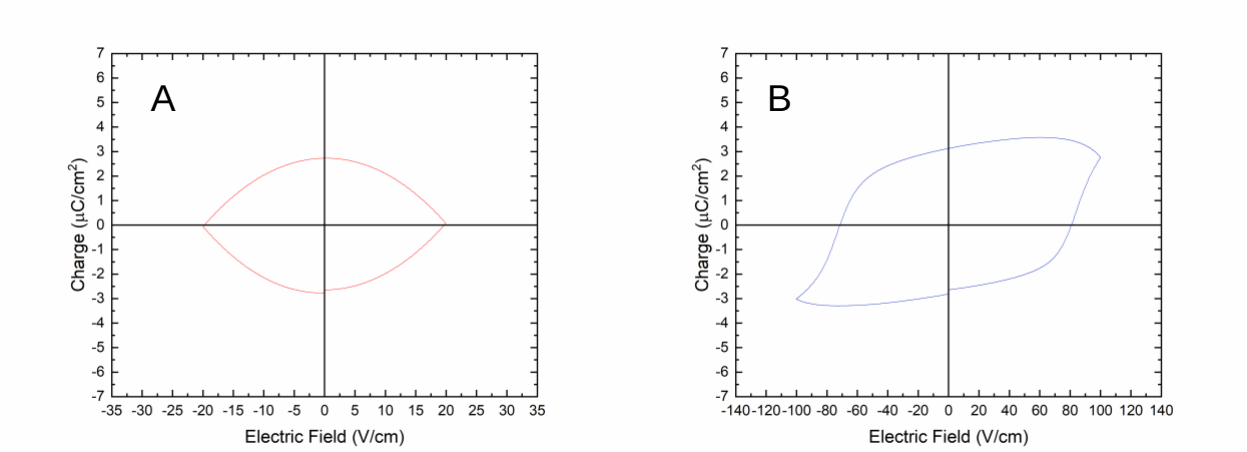

Figure 5-1. P-E Loops for TM $FeBrCl_3$ pellets using undried powder (A) and powder dried under vacuum overnight (B).

The ferroelectric properties of TM $FeBrCl_3$ pellets pressed from powder dried overnight vs. un-dried were compared (Figure 5-1). The undried powder (Figure 5-1A) showed a near-ideal resistor response, while the dried powder (Figure 5-1B) showed a ferroelectric hysteresis loop with some leakage current as evidenced by the rounded corners at each end of the loop. As underscored by Walker et al [309, 310], these results highlighted the importance of drying TM $FeBrCl_3$ powder prior to pressing as the presence of water can cause local dissolution within the sample, enabling the formation and transport of ionic species, such as vacancies in the lattice [310]. All powders were dried overnight under vacuum for subsequent characterization experiments.

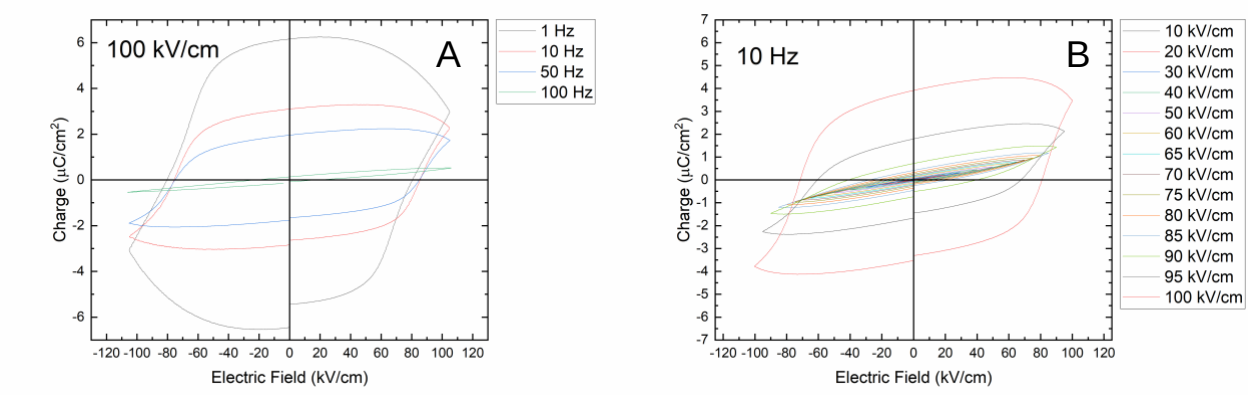

Figure 5-2. P-E Loops for a TM FeBrCl3 pellet at a constant maximum electric field of 100 kV/cm (A) and a frequency of 10 Hz (B).

The frequency and maximum magnitude of the applied electric field were varied for a representative pellet (Figure 5-2). As the frequency of the loop increases, the area in the loop decreases, characteristic of ferroelectric materials as less polarization can be achieved at larger frequencies. TM $FeBrCl_3$ hysteresis loops were compared to those reported in literature. The measured coercive electric fields (~60-80 kV/cm) are comparable to those reported by Walker et al. [310] and roughly double those reported by Harada [316] at 10 Hz. Ferroelectric with significant leakage current will show larger coercive electric fields in uncompensated hysteresis loops. In addition, the remnant polarization (3.6 $\mu C/cm^2$) was consistent with the range of remnant polarization values reported by Walker (2.9-3.8 $\mu C/cm^2$) [310] and slightly lower than that reported by Harada (4.5 $\mu C/cm^2$) [316].

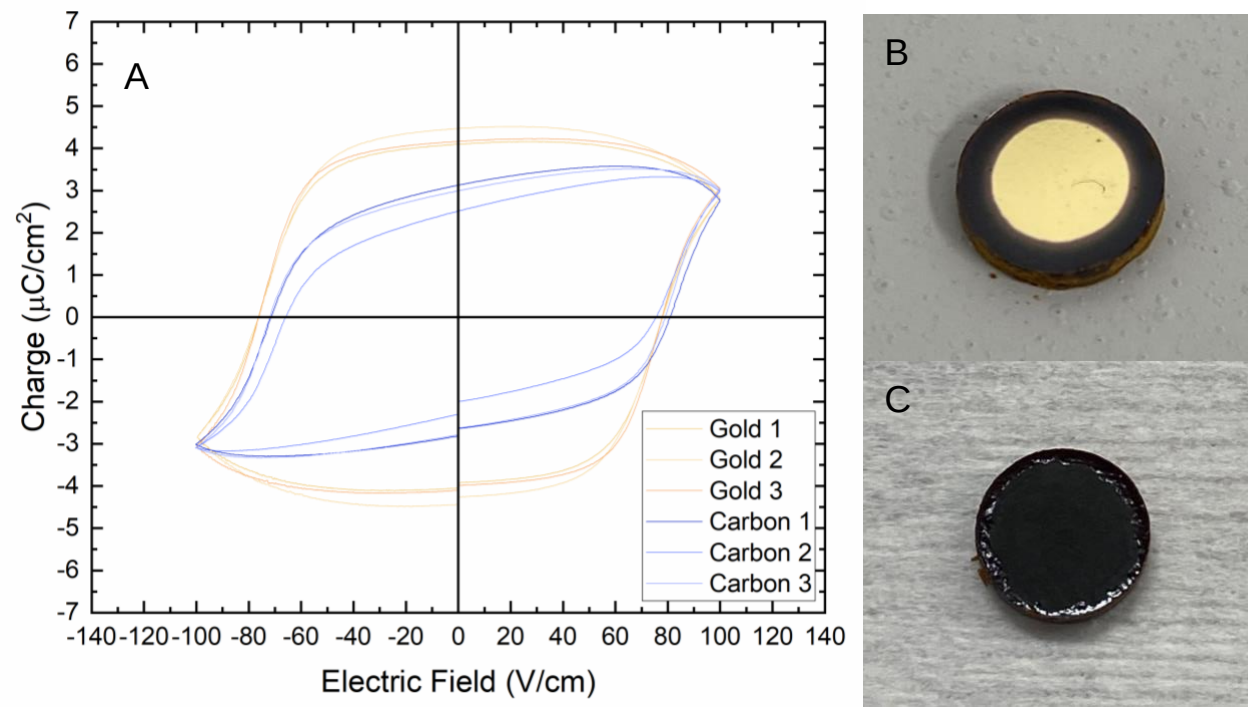

Figure 5-3. P-E Hysteresis Loops (A) of three TM $FeBrCl_3$ pellets with gold electrodes (B) and conductive carbon electrodes (C).

The ferroelectric response of TM $FeBrCl_3$ pellets with 100 nm sputtered gold vs. painted carbon electrodes were compared at 10 Hz and a peak electric field of 100 kV/cm (Figure 5-3). The polarization at each end of the loop was similar for all samples (~3 μC/cm^2), but the apparent remnant polarization for the samples with gold electrodes (3.9-4.3 μC/cm^2) was roughly 40% larger than that of samples with carbon electrodes (2.5-3.1 μC/cm^2). The larger apparent remnant polarization of the samples with gold electrodes indicated the leakage current was significantly higher for three different samples with gold electrodes compared to the leakage current of the samples with carbon electrodes. As Scherrer disclosed previously, TM $FeBrCl_3$ corroded the gold electrode in their experiments [312]. Although Scherrer or Walker did not specify the corrosion reaction in their work, previous literature has shown that $AuCl_2^-$ species can form in aqueous solutions containing gold nanorods, $FeCl_3$, and excess bromide [325]. Therefore, we speculate this corrosion generates additional mobile species in the form of $AuCl_2^-$ and/or halide vacancies,

resulting in the increase in leakage current. A direct comparison of the leakage current in the hysteresis loops reported by Harada et al. could not be made because Harada reported only compensated loops that eliminate leakage current, while the loops described here and reported by Walker/Scherrer were uncompensated. All subsequent ferroelectric and piezoelectric characterization experiments were carried out using conductive carbon electrodes rather than sputtered gold to minimize the leakage current.

5.3.4.2. Effects of Poling Conditions on d_{33} of TM $FeBrCl_3$ Pellets

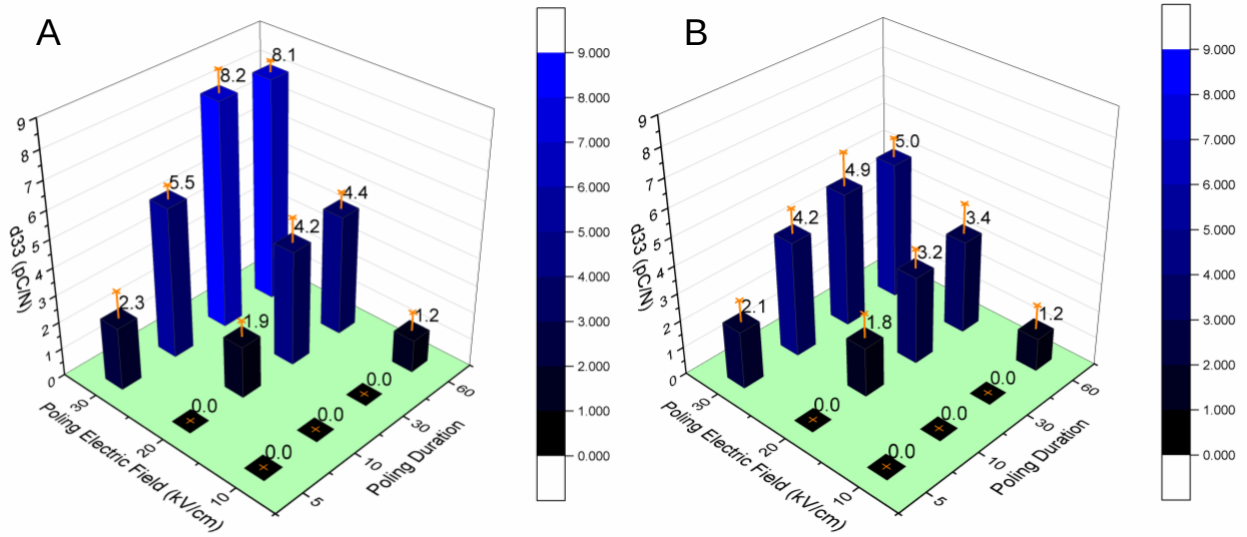

Figure 5-4. Plots of the average d_{33} value of TM $FeBrCl_3$ pellets as a function of poling electric field and duration for samples with carbon electrodes (A) vs. gold electrodes (B).

Having identified the electrode material to be potentially deleterious to the piezoelectric properties of TM $FeBrCl_3$, the piezoelectric coefficient d_{33} was measured via the quasi-static method after poling at several electric fields (10, 20 and 30 kV/cm) and durations (5, 10, 30, and 60 minutes) as depicted in Figure 5-4. Five pellets were poled at each combination of poling field and duration except for 30 kV/cm and 60 minutes with gold electrodes (n = 3), in which two of the

samples short-circuited before poling had completed. The minimum recordable d_{33} value was 1.0 pC/N, so any value <1 pC/N was assumed to be 0 pC/N. Poling fields larger than 30 kV/cm led to short circuits occurring within 5 minutes of poling for samples with either electrode material. The apparent coercive electric field was measured to be ca. 60-80 kV/cm at 10 Hz, but the increase in leakage current at lower frequencies (as evidenced by the large increase in apparent remnant polarization at 1 Hz in Figure 5-2A) indicated that the true coercive electric field of TM $FeBrCl_3$ was likely lower. In fact, the corresponding current-electric field plots Walker presents alongside the P-E loops showed coercive electric fields as low as 30 kV/cm when the frequency is 0.1 Hz [310]. Therefore, it is reasonable to expect poling to occur at electric fields lower than the apparent electric fields measured via polarization – electric field loops. Saturation was achieved after 30 minutes of poling for the samples with carbon electrodes; increased poling times to 60 minutes did not yield additional increases in the d_{33} value. A peak d_{33} value of 5.0 pC/N was measured for samples with gold electrodes, a peak value more comparable to that measured by Scherrer (7 pC/N) [312] than Harada (110 pC/N). The peak d_{33} value of 8.2 pC/N was measured for samples with carbon electrodes. At a poling electric field of 30 kV/cm, the d_{33} value of TM $FeBrCl_3$ samples with carbon electrodes was consistently larger than those with gold electrodes. This result implies that a decreased leakage current results in an increased d_{33} response, a trend that has been observed in polycrystalline oxide piezoelectrics [326].

Although Walker et al. demonstrated that the resistivity of TM $FeBrCl_3$ increased by three orders of magnitude at elevated temperatures required to access the paraelectric phase for field cooling (120 ^{o}C) [311], field cooling was still attempted for pellets because previous ferroelectric characterization showed that the usage of gold electrodes contributed to elevated leakage current. However, all samples with carbon or gold electrodes poled at 10 kV/cm at 70 ^{o}C short-circuited

within 30 seconds of turning on the electric field. One potential explanation for the immediate short-circuits would be the increase in conductivity as a function of temperature, a trend previously reported by Walker [311]. Going forward, pellets with carbon electrodes were poled at 30 kV/cm for 30 minutes for subsequent experiments.

5.3.4.3. Effects of Static Load and humidity on TM $FeBrCl_3$ Piezoelectric Properties

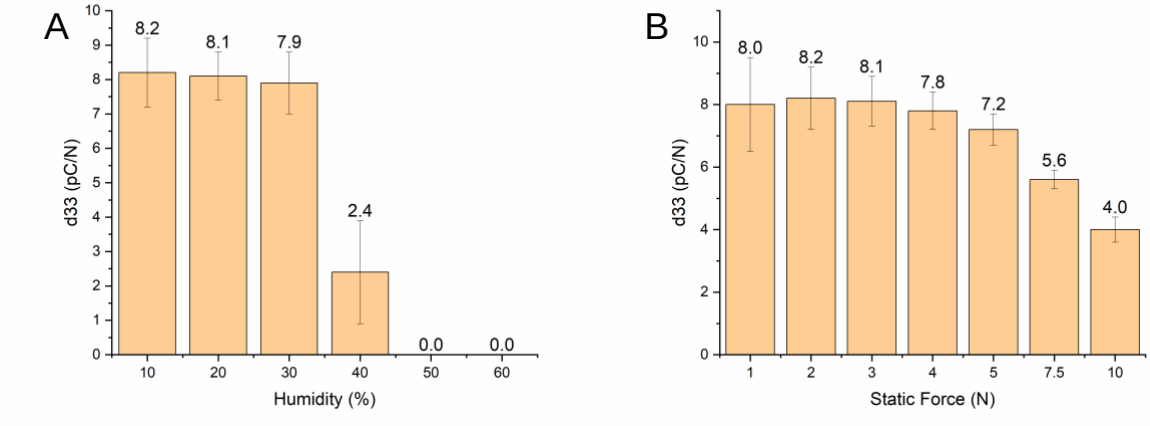

Figure 5-5. d_{33} as a function of humidity (A) and static force applied to the sample (B)

Pellets poled at 30 kV/cm for 30 minutes with carbon electrodes were tested at different relative humidity with a static force of 2 N (n = 5) as depicted in Figure 5-5A. The sample was allowed to equilibrate at a given relative humidity level for 15 minutes prior to testing. The piezoelectric performance is mostly preserved to 30% relative humidity, but the average d_{33} value decreased to 2.4 pC/N when measured at 40% relative humidity. Then, the piezoelectric response completely disappeared when the relative humidity was increased to 50 and 60%. This result is consistent with previous results reported on the influence of the leakage current on ferroelectric properties (where undried samples showed only a resistive response), further demonstrating the sensitivity of the dielectric properties of TM $FeBrCl_3$ to water.

The static pre-load force applied to the sample during the quasi-static measurement also was shown influence the d_{33} value (Figure 5-5B). The pre-load force was varied between 1-10 N at 10% relative humidity (n = 5), and samples show a decreased d_{33} response as the static load increased. This indicated that additional clamping of the sample resulted in a reduced response, a trend previously observed in soft piezoelectric materials [279].

5.4. Discussion

In the previous section on TM $FeBrCl_3$ pellets, several series of experiments were performed to identify the cause for the large discrepancy in the reported value for d_{33} numbers. Poling conditions and poling times were explored for samples with gold and carbon-based electrodes, resulting in a maximum d_{33} values of 5.1 and 8.2 pC/N for samples with gold- and carbon-based electrodes. Ferroelectric P-E loops indicated that samples with gold electrodes possessed larger leakage currents, which could explain the decreased d_{33} values. However, this pair of d_{33} values is closer in magnitude to the d_{33} value reported by Scherrer (7 pC/N) rather than Harada (110 pC/N). Increasing the static load and the relative humidity both decreased the peak d_{33} value of 8.2 pC/N. Therefore, we conclude that that the discrepancy between the values reported by Harada and Scherrer is not due to poling or testing conditions but rather other causes.

One potential explanation for the large discrepancy in piezoelectric performance could be the TM $FeBrCl_3$ morphology and piezoelectric response of polycrystalline TM $FeBrCl_3$. The effect of grain size on inorganic-organic hybrid polycrystalline molecular ferroelectrics has not been studied to date. In oxide ferroelectrics, one common strategy utilized to boost the d_{33} is domain miniaturization. When domains are miniaturized to <10 μm, enhanced ferroelastic switching and domain wall motion are observed, mechanisms that enable the generation of a large extrinsic

piezoelectric response. For example, polycrystalline $BaTiO_3$ with an optimal grain size range of 1-2 μm possess a d_{33} value that is up to 5x larger than that of polycrystalline $BaTiO_3$ samples with grain sizes on the order of 10-100 μm [327, 328]. In the case of $BaTiO_3$, the decrease in grain size below 10 μm increases the density of 90° domain walls, the displacement of which results in an enhanced piezoelectric response [329]. Large grains (>10 μm) can show large back-switching of domains after turning off the electric field, resulting in a decreased d_{33} [330]. Submicron grain sizes results in the clamping of these 90° domain walls, and the larger density of grain boundaries introduce strain gradients and other effects that will reduce the d_{33} coefficient [327]. Although inorganic-organic hybrids may not follow the microstructural trends of $BaTiO_3$ due to the softer nature of these inorganic-organic hybrids, a greater understanding of the relationships between microstructure and the d_{33} would be helpful. Neither Harada nor Walker reported the grain size of their pressed polycrystalline films. Therefore, one promising route forward to resolve this discrepancy would be to study the relationship of grain size vs. maximum d_{33} value. A systematic study drawing relationships between the pressure and temperature of pressed polycrystalline samples and the resulting grain size followed by d_{33} characterization could explain the discrepancy in piezoelectric performance for TM $FeBrCl_3$.

A larger issue that has emerged over the course of this research is the lack of transparency and reproducibility in the growing field of molecular ferroelectrics. For example, the first 2017 TMCM $MnCl_3$ study with a d_{33} value of 185 pC/N [298] was cited over 600 times as of November 2022, but not a single publication has reproduced the d_{33} value reported in this work experimentally. The initial report by Harada followed by the studies by Walker represent the only case where two independent groups studied the same material, TM $FeBrCl_3$. Other promising compositions, such as TMCM $CdCl_3$ (d_{33} of 220 pC/N) [298], TMBM $MnBr_3$ (112 pC/N) [265],

and TM $GaCl_4$ (80 pC/N) [331], have not been reproduced by other groups yet. Most research efforts simply report the structure and properties of a new ferroelectric compound. While this research is useful and necessary to demonstrate the exciting compositional tunability available to this field, it will be important for the field to show that the compounds can be synthesized and characterized in multiple labs, especially given that many of these compounds are water-sensitive. The following disclosures and practices standard in the established fields of oxide and polymer piezoelectrics are recommended:

1. **Disclose poling conditions**. At a minimum, stating the electric field and poling time would improve transparency.

2. **Disclose d_{33} testing conditions**. Although the dynamic force and frequency regularly are reported in literature, additional details include the static pre-load force and the humidity. The sample fixture type (acorn nut vs. flat) also would be useful for reproducing d_{33} values; flat fixtures typically are used for thin samples prone to fracture from standard acorn nut fixtures. It is understandable that humidity has scarcely been reported given that most classes of piezoelectrics (ceramics and polymers) are stable in ambient conditions, but it is important to disclose humidity for inorganic organic hybrids. For example, humidity can affect the processing and stability of solar cells using inorganic-organic hybrid lead halide perovskites [332].

3. **Disclose uncompensated P-E hysteresis loops.** Reporting only the compensated hysteresis loops clouds the true ferroelectric nature of these hybrid materials.

Including uncompensated loops paints a complete picture on the ferroelectric quality.

4. **Increase and/or disclose sample size**. Most publications fail to report the sample size of d_{33} values as no averages or standard deviations are given, so the sample size is assumed to be one.

Despite the call for increased scientific rigor in this field, there exist several promising future directions, including:

1. **Molecular ferroelectrics with morphotropic phase boundaries**. One of the most exciting developments in this field was the first report of molecular ferroelectrics with morphotropic phase boundaries: $TMFM_{0.27}TMCM_{0.73}CdCl_3$, which had an outstanding d_{33} of 1,570 pC/N [268]. A morphotropic phase boundary (MPB) is a solid solution with two competing phases; lead zirconate titanate (PZT) shows a large boost in the piezoelectric effect for compositions near the MPB. The substitution of an A-site cation, TMCM with a similarly sized cation, trimethylfluoromethyl ammonium (TMFM) resulted in a 7x increase in d_{33} at the MPB. However, a precursor used to synthesize the cation, chlorofluoroethylene, is a banned CFC in the U.S, and this molecular ferroelectric is toxic due to the presence of cadmium. Therefore, there is strong interest in identifying MPBs with nontoxic species. Scherrer made the first attempt to identify a composition with a MPB by mixing tetraethylammonium (TE) with tetramethylammonium to form the

solid solution TE_xTM_{1-x} $FeBrCl_3$ (x = 0, 0.1, 0.2…0.9, 1), but a piezoelectric response was not recorded for compositions with a relative TE molar fraction > 0.2 as TE $FeBrCl_3$ is not ferroelectric [312]. Also, a morphotropic phase boundary region was not identified as described by You et al. Given that our development of ball-milled molecular ferroelectrics enabled high-throughput search for novel compositions, I attempted to form solid solutions of TM_xTMCM_{1-x} $FeBrCl_3$ (x = 0, 0.1, 0.2…0.9, 1) as the TMCM cation was closer in size to the TM cation. However, all compositions containing TMCM formed leaky dielectrics with PE Loops with a shape similar to those shown in Figure 5-1A, indicative of high leakage current. Given the observed and reported degradation in ferroelectric quality due to the presence of moisture in the powder, I speculate the increased hygroscopicity of the TMCM cation exacerbated this issue. Preparation and characterization of powders exclusively in a moisture-free environment (rather than brief exposures to an environment with 10% relative humidity) would isolate the effects of moisture on the ferroelectric properties of these compositions.

2. **Mixed-anion compositions with hydrophobic organic components for vibrational energy harvesting**. A recent study reported a tri-anion composition $PTMACdBr_2Cl_{0.75}I_{0.25}$ with d_{33} of 367 pC/N [333]. This composition contains a more hydrophobic A-site salt, phenyltrimethyl ammonium (PTMA), which also reduces the dielectric constant of the material to 9 and decreases the softness below that of PVDF (0.8 vs. 2.0 GPa). This results in a giant piezoelectric voltage coefficient (g_{33}) of 3,595 x 10^{-3} V/mN. This enables a high-performing vibrational

energy harvester with an output power density of 1.1 mW/cm^2, which represents a ~100x increase over the best performances achieved with PZT or PVDF to date. Vibrational energy harvesters convert ambient mechanical vibrations into electricity, and high-performing energy harvesters also make for ideal piezoelectric sensor materials. Therefore, development of a cadmium-free, mixed-anion composition that could be printed from solution would be an interesting direction to pursue, especially one with more hydrophobic A-site cations.

3. **Molecular ferroelectric / elastomer composites**. One strategy used to bypass the moisture sensitivity of these materials is to prepare composites. Typically, 10 wt.% of the molecular ferroelectric powder is mixed into silicones to fabricate piezoelectric vibrational energy harvesters. Recent examples from literature include TMCM $GaCl_4$ (d_{33} of 226 pC/N) [261], TMCM $SnCl_6$ (d_{33} of 137 pC/N) [259], and copper- [334] and bismuth-based [335] molecular ferroelectrics.

5.5. Conclusion

In this chapter, the first all-printed vibration sensor using slot-die-coated TM $FeBrCl_3$ was reported. Four inkjet printing passes of silver traces was necessary to ensure electrodes remained conductive due to the corrosive nature of TM $FeBrCl_3$. Pre-poled sensors showed a clear frequency-matching response to the oscillating beam, and the charge output of all sensors increased after poling. Ball-milled TM $FeBrCl_3$ powder was synthesized for the first time, demonstrating another pathway towards scalable fabrication of this class of materials. Polarization-electric field characterization of pressed TM $FeBrCl_3$ pellets confirmed the

ferroelectric nature of this material. A comparison of pellets with gold electrodes showed increased leakage current and decreased piezoelectric response compared to pellets with carbon electrodes. A maximum d_{33} of 8.2 pC/N was measured for pellets with carbon electrodes, which is notably lower than the value published in the first publication of this material (110 pC/N) but consistent with the value disclosed in a subsequent report (7 pC/N). Several routes forward are proposed to explain the discrepancy in the reported d_{33} values, a list of best practices and disclosures is detailed, and a perspective on the prospects of this field is provided.

Chapter 6. Acknowledgements

I would like to thank my mom, dad, and sister for their love and support during my graduate studies. I would also like to thank my grandparents, Ralph and Marjorie, for their love and support. I would not have been able to finish without the support I received from my Aunt Marla as well as my other grandparents, aunts, uncles, and cousins, including Arlene, Scott, Lisa, Sydney, Connye, Peter, Dan, and Henry.

I would like to thank Prof. J. Devin MacKenzie for his mentorship and support, Profs. Dwayne Arola, Guozhong Cao, and Alshakim Nelson for serving on my doctoral supervisory committee, and UW Materials Science and Engineering for their academic, financial, and administrative support.

I wouldn't be able to complete this research without the contributions and efforts of my collaborators, especially Dr. Weiwei Xu and Prof. Steve Shen, who designed and performed all piezoelectric characterization experiments in Chapters 4 and 5 of this dissertation. I'm also grateful to have collaborated with Sophia Bidinger, Alex Gong, Dr. Robert Sweet and the rest of the team at the Center for Research in Education and Simulation Technologies (CREST) on the research described in Chapters 2 and 3 of this dissertation. I'm also thankful for the opportunity to study alongside Holly Brunner, Brandon Rotondo, Ted Cohen, Taichong Ma, and Oliver Nakano-Baker in the MacKenzie group. I also feel fortunate to have the opportunity to mentor many talented and hardworking students, including Allison Tuuri, Sophia Bidinger, Daniel Chai, and Abdullatif Jazzar. Finally, this research wouldn't have been possible without the support of the Washington Clean Energy Testbeds staff past and present, including Felippe Pavinatto, Phillip Cox, Mike Pomfret, Joey Law, Kristine Parra, Le Cai, and Dr. Hadi Zareie.

Furthermore, I received tremendous support from peer mentors, including Spencer Williams and Matt Cast. Also, I'm grateful for my Seattle friends, including Elliot Boschwitz, Riley Kimball, Emma Nyland, Meritt Petersen, Richard Ryder, Ellen Murphy, and many others keeping me grounded!

I also would like to thank Prof. Cherie Kagan and Prof. Aaron Fafarman for their mentorship of my undergraduate and graduate studies at the University of Pennsylvania. I feel incredibly fortunate for the support and guidance I received from Lois Fruen and Prof. Russell Holmes during my research experience at the University of Minnesota.

I also would like to thank SEMI-FlexTech, the Washington Clean Energy Institute (CEI), the Washington Research Foundation, the state of Washington, the Center for Research in Education and Simulation Technologies (CREST), the U.S. Department of Defense, and Jack Norfleet of the U.S. Army Research Laboratory for their support of the research that went into this dissertation.

Chapter 7. References

[1] Khan S, Lorenzelli L, Dahiya R S 2015 Technologies for printing sensors and electronics over large flexible substrates: A review *IEEE Sens. J.* **15** 3164–85.

[2] Grau G, Cen J, Kang H, Kitsomboonloha R, Scheideler W J, Subramanian V 2016 Gravure-printed electronics: recent progress in tooling development, understanding of printing physics, and realization of printed devices *Flex. Print. Electron.* **1** 23002.

[3] Krebs F C, Fyenbo J, Jørgensen M 2010 Product integration of compact roll-to-roll processed polymer solar cell modules: methods and manufacture using flexographic printing, slot-die coating and rotary screen printing *J. Mater. Chem.* **20** 8994–9001.

[4] Søndergaard R, Hösel M, Angmo D, Larsen-Olsen T T, Krebs F C 2012 Roll-to-roll fabrication of polymer solar cells *Mater. today* **15** 36–49.

[5] Søndergaard R R, Hösel M, Krebs F C 2013 Roll-to-Roll fabrication of large area functional organic materials *J. Polym. Sci. Part B Polym. Phys.* **51** 16–34.

[6] Abbel R, Galagan Y, Groen P 2018 Roll-to-Roll Fabrication of Solution Processed Electronics *Adv. Eng. Mater.* **20** 1701190.

[7] Calvert P 2001 Inkjet printing for materials and devices *Chem. Mater.* **13** 3299–305.

[8] Cummins G, Desmulliez M P Y 2012 Inkjet printing of conductive materials: a review *Circuit world* **38** 193–213.

[9] Gul J Z, Sajid M, Rehman M M, Siddiqui G U, Shah I, Kim K-H, et al 2018 3D printing for soft robotics–a review *Sci. Technol. Adv. Mater.* **19** 243–62.

[10] Boydston A J, Cao B, Nelson A, Ono R J, Saha A, Schwartz J J, et al 2018 Additive manufacturing with stimuli-responsive materials *J. Mater. Chem. A* **6** 20621–45.

[11] Berggren M, Nilsson D, Robinson N D 2007 Organic materials for printed electronics *Nat. Mater.* **6** 3.

[12] Kim C-H, Kymissis I 2017 Graphene–organic hybrid electronics *J. Mater. Chem. C* **5** 4598–613.

[13] Kamyshny A, Magdassi S 2019 Conductive nanomaterials for 2D and 3D printed flexible electronics *Chem. Soc. Rev.* **48** 1712–40.

[14] Kamyshny A, Magdassi S 2014 Conductive nanomaterials for printed electronics *Small* **10** 3515–35.

[15] Perelaer J, Smith P J, Mager D, Soltman D, Volkman S K, Subramanian V, et al 2010 Printed electronics: the challenges involved in printing devices, interconnects, and contacts based on inorganic materials *J. Mater. Chem.* **20** 8446.

[16] Zhu S, Levinson D, Liu H X, Harder K 2010 The traffic and behavioral effects of the I-35W Mississippi River bridge collapse *Transp. Res. part A policy Pract.* **44** 771–84.

[17] Inaudi D, Bolster M, Deblois R, French C E, Phipps A, Sebasky J, et al 2009. Structural health monitoring system for the new I-35W St Anthony Falls Bridge In: *4th International Conference on Structural Health Monitoring of Intelligent Infrastructure, SHMII 2009*.

[18] Inaudi D, Favez P, Belli R, Posenato D 2011. Dynamic monitoring systems for structures under extreme loads In: *Applied Mechanics and Materials* Trans Tech Publ; p. 804–9.

[19] Agdas D, Rice J A, Martinez J R, Lasa I R 2015 Comparison of visual inspection and structural-health monitoring as bridge condition assessment methods *J. Perform. Constr. Facil.* **30** 4015049.

[20] Giurgiutiu V 2007. Structural health monitoring: with piezoelectric wafer active sensors Elsevier;

[21] Sun Y, Gu F 2017 Compressive sensing of piezoelectric sensor response signal for phased array structural health monitoring *Int. J. Sens. Networks* **23** 258–64.

[22] Liu T, Zou D, Du C, Wang Y 2017 Influence of axial loads on the health monitoring of concrete structures using embedded piezoelectric transducers *Struct. Heal. Monit.* **16** 202–14.

[23] Amjadi M, Kyung K U, Park I, Sitti M 2016 Stretchable, Skin-Mountable, and Wearable Strain Sensors and Their Potential Applications: A Review *Adv. Funct. Mater.* **26** 1678–98.
[24] Crump M R, Gong A T, Chai D, Bidinger S L, Pavinatto F J, Reihsen T E, et al 2019 Monolithic 3D-Printing of embeddable and highly stretchable strain sensors using conductive ionogels *Nanotechnology* **30** 364002.
[25] Crump M R, Bidinger S L, Pavinatto F J, Gong A T, Sweet R M, MacKenzie J D 2021 Sensorized tissue analogues enabled by a 3D-printed conductive organogel *npj Flex. Electron.* **5** 1–8.
[26] Makary M A, Daniel M 2016 Medical error—the third leading cause of death in the US *Bmj* **353** i2139.
[27] Badash I, Burtt K, Solorzano C A, Carey J N 2016 Innovations in surgery simulation: a review of past, current and future techniques *Ann. Transl. Med.* **4** .
[28] Acton R D 2015 The evolving role of simulation in teaching surgery in undergraduate medical education *Surg. Clin.* **95** 739–50.
[29] Rengier F, Mehndiratta A, Von Tengg-Kobligk H, Zechmann C M, Unterhinninghofen R, Kauczor H-U, et al 2010 3D printing based on imaging data: review of medical applications *Int. J. Comput. Assist. Radiol. Surg.* **5** 335–41.
[30] Ventola C L 2014 Medical applications for 3D printing: current and projected uses *Pharm. Ther.* **39** 704.
[31] Markert M, Weber S, Lueth T C 2007. A beating heart model 3D printed from specific patient data In: *Engineering in Medicine and Biology Society, 2007 EMBS 2007 29th Annual International Conference of the IEEE* IEEE; p. 4472–5.
[32] Starosolski Z A, Kan J H, Rosenfeld S D, Krishnamurthy R, Annapragada A 2014 Application of 3-D printing (rapid prototyping) for creating physical models of pediatric orthopedic disorders *Pediatr. Radiol.* **44** 216–21.
[33] Eltorai A E M, Nguyen E, Daniels A H 2015 Three-dimensional printing in orthopedic surgery *Orthopedics* **38** 684–7.
[34] Tam M D, Laycock S D, Bell D, Chojnowski A 2012 3-D printout of a DICOM file to aid surgical planning in a 6 year old patient with a large scapular osteochondroma complicating congenital diaphyseal aclasia *J. Radiol. Case Rep.* **6** 31.
[35] Windisch G, Salaberger D, Rosmarin W, Kastner J, Exner G U, Haldi-Brändle V, et al 2007 A model for clubfoot based on micro-CT data *J. Anat.* **210** 761–6.
[36] Niikura T, Sugimoto M, Lee S Y, Sakai Y, Nishida K, Kuroda R, et al 2014 Tactile surgical navigation system for complex acetabular fracture surgery *Orthopedics* **37** 237–42.
[37] Mitsouras D, Liacouras P, Imanzadeh A, Giannopoulos A A, Cai T, Kumamaru K K, et al 2015 Medical 3D printing for the radiologist *Radiographics* **35** 1965–88.
[38] Ballard D H, Trace A P, Ali S, Hodgdon T, Zygmont M E, DeBenedectis C M, et al 2018 Clinical applications of 3D printing: primer for radiologists *Acad. Radiol.* **25** 52–65.
[39] Youssef R F, Spradling K, Yoon R, Dolan B, Chamberlin J, Okhunov Z, et al 2015 Applications of three-dimensional printing technology in urological practice *BJU Int.* **116** 697–702.
[40] Zhang Y, Ge H, Li N, Yu C, Guo H, Jin S, et al 2016 Evaluation of three-dimensional printing for laparoscopic partial nephrectomy of renal tumors: a preliminary report *World J. Urol.* **34** 533–7.
[41] Silberstein J L, Maddox M M, Dorsey P, Feibus A, Thomas R, Lee B R 2014 Physical models of renal malignancies using standard cross-sectional imaging and 3-dimensional printers: a pilot study *Urology* **84** 268–73.
[42] Chae M P, Rozen W M, McMenamin P G, Findlay M W, Spychal R T, Hunter-Smith D J 2015 Emerging applications of bedside 3D printing in plastic surgery *Front. Surg.* **2** 25.
[43] Kamali P, Dean D, Skoracki R, Koolen P G L, Paul M A, Ibrahim A, et al 2016 The current role of three-dimensional printing in plastic surgery *Plast. Reconstr. Surg.* **137** 1045–55.
[44] Klein G T, Lu Y, Wang M Y 2013 3D printing and neurosurgery—ready for prime time? *World Neurosurg.* **80** 233–5.
[45] Ploch C C, Mansi C S S A, Jayamohan J, Kuhl E 2016 Using 3D printing to create personalized brain models for neurosurgical training and preoperative planning *World Neurosurg.* **90** 668–74.
[46] Pucci J U, Christophe B R, Sisti J A, Connolly Jr E S 2017 Three-dimensional printing: technologies, applications, and limitations in neurosurgery *Biotechnol. Adv.* **35** 521–9.
[47] Wurm G, Tomancok B, Pogady P, Holl K, Trenkler J 2004 Cerebrovascular stereolithographic biomodeling for aneurysm surgery *J. Neurosurg.* **100** 139–45.
[48] D'Urso P S, Thompson R G, Atkinson R L, Weidmann M J, Redmond M J, Hall B I, et al 1999 Cerebrovascular biomodelling: a technical note *Surg. Neurol.* **52** 490–500.
[49] Kenedi R M, Gibson T, Evans J H, Barbenel J C 1975 Tissue mechanics *Phys. Med. Biol.* **20** 699.
[50] Ngo T D, Kashani A, Imbalzano G, Nguyen K T Q, Hui D 2018 Additive manufacturing (3D printing): A

review of materials, methods, applications and challenges *Compos. Part B Eng.*
[51] Ligon S C, Liska R, Stampfl J, Gurr M, Mülhaupt R 2017 Polymers for 3D printing and customized additive manufacturing *Chem. Rev.* **117** 10212–90.
[52] Wang X, Xu S, Zhou S, Xu W, Leary M, Choong P, et al 2016 Topological design and additive manufacturing of porous metals for bone scaffolds and orthopaedic implants: a review *Biomaterials* **83** 127–41.
[53] Hwa L C, Rajoo S, Noor A M, Ahmad N, Uday M B 2017 Recent advances in 3D printing of porous ceramics: A review *Curr. Opin. Solid State Mater. Sci.* **21** 323–47.
[54] Wang X, Jiang M, Zhou Z, Gou J, Hui D 2017 3D printing of polymer matrix composites: A review and prospective *Compos. Part B Eng.* **110** 442–58.
[55] Guvendiren M, Molde J, Soares R M D, Kohn J 2016 Designing biomaterials for 3D printing *ACS Biomater. Sci. Eng.* **2** 1679–93.
[56] Chia H N, Wu B M 2015 Recent advances in 3D printing of biomaterials *J. Biol. Eng.* **9** 4.
[57] Qiu K, Haghiashtiani G, McAlpine M C 2018 3D Printed Organ Models for Surgical Applications *Annu. Rev. Anal. Chem.*
[58] Qiu K, Zhao Z, Haghiashtiani G, Guo S-Z, He M, Su R, et al 2017 3D Printed Organ Models with Physical Properties of Tissue and Integrated Sensors *Adv. Mater. Technol.* **1700235** 1700235.
[59] Liravi F, Toyserkani E 2018 Additive manufacturing of silicone structures : A review and prospective *Addit. Manuf.* **24** 232–42.
[60] Sweet R M 2017 The CREST simulation development process: training the next generation *J. Endourol.* **31** S-69.
[61] Kemper A R, Santago A C, Stitzel J D, Sparks J L, Duma S M 2012 Biomechanical response of human spleen in tensile loading *J. Biomech.* **45** 348–55.
[62] Dahms S E, Piechota H J, Dahiya R, Lue T F, Tanagho E A 1998 Composition and biomechanical properties of the bladder acellular matrix graft: comparative analysis in rat, pig and human. *Br. J. Urol.* **82** 411–9.
[63] Jansen L H, Rottier P B 1958 Some Mechanical Properties of Human Abdominal Skin Measured on Excised Strips *Dermatology* **117** 65–83.
[64] Dunn M G, Silver F H, Swann D A 1985 Mechanical Analysis of Hypertrophic Scar Tissue: Structural Basis for Apparent Increased Rigidity *J. Invest. Dermatol.* **84** 9–13.
[65] Daly C H, Odland G F 1979 Age-related Changes in the Mechanical Properties of Human Skin *J. Invest. Dermatol.* **73** 84–7.
[66] Ottenio M, Tran D, Ní Annaidh A, Gilchrist M D, Bruyère K 2015 Strain rate and anisotropy effects on the tensile failure characteristics of human skin *J. Mech. Behav. Biomed. Mater.* **41** 241–50.
[67] Joodaki H, Panzer M B 2018 Skin mechanical properties and modeling: A review *Proc. Inst. Mech. Eng. Part H J. Eng. Med.* **232** 323–43.
[68] Cohen D J, Mitra D, Peterson K, Maharbiz M M 2012 A highly elastic, capacitive strain gauge based on percolating nanotube networks *Nano Lett.* **12** 1821–5.
[69] Xu F, Zhu Y 2012 Highly conductive and stretchable silver nanowire conductors *Adv. Mater.* **24** 5117–22.
[70] Cai L, Song L, Luan P, Zhang Q, Zhang N, Gao Q, et al 2013 Super-stretchable, transparent carbon nanotube-based capacitive strain sensors for human motion detection *Sci. Rep.* **3** 3048.
[71] Shin U-H, Jeong D-W, Park S-M, Kim S-H, Lee H W, Kim J-M 2014 Highly stretchable conductors and piezocapacitive strain gauges based on simple contact-transfer patterning of carbon nanotube forests *Carbon* **80** 396–404.
[72] Yao S, Zhu Y 2014 Wearable multifunctional sensors using printed stretchable conductors made of silver nanowires *Nanoscale* **6** 2345–52.
[73] Frutiger A, Muth J T, Vogt D M, Mengüç Y, Campo A, Valentine A D, et al 2015 Capacitive soft strain sensors via multicore–shell fiber printing *Adv. Mater.* **27** 2440–6.
[74] Atalay A, Sanchez V, Atalay O, Vogt D M, Haufe F, Wood R J, et al 2017 Batch fabrication of customizable silicone-textile composite capacitive strain sensors for human motion tracking *Adv. Mater. Technol.* **2** 1700136.
[75] White E L, Yuen M C, Case J C, Kramer R K 2017 Low-Cost, Facile, and Scalable Manufacturing of Capacitive Sensors for Soft Systems *Adv. Mater. Technol.* **2** 1700072.
[76] Shintake J, Piskarev E, Jeong S H, Floreano D 2018 Ultrastretchable strain sensors using carbon black-filled elastomer composites and comparison of capacitive versus resistive sensors *Adv. Mater. Technol.* **3** 1700284.
[77] Nur R, Matsuhisa N, Jiang Z, Nayeem M O G, Yokota T, Someya T 2018 A Highly Sensitive Capacitive-type Strain Sensor Using Wrinkled Ultrathin Gold Films *Nano Lett.* **18** 5610–7.
[78] Xu H, Lv Y, Qiu D, Zhou Y, Zeng H, Chu Y 2019 An ultra-stretchable, highly sensitive and biocompatible

capacitive strain sensor from an ionic nanocomposite for on-skin monitoring *Nanoscale* **11** 1570–8.
[79] Qiu A, Li P, Yang Z, Yao Y, Lee I, Ma J 2019 A Path Beyond Metal and Silicon: Polymer/Nanomaterial Composites for Stretchable Strain Sensors *Adv. Funct. Mater.* 1806306.
[80] Amjadi M, Yoon Y J, Park I 2015 Ultra-stretchable and skin-mountable strain sensors using carbon nanotubes-Ecoflex nanocomposites *Nanotechnology* **26** .
[81] Matsuzaki R, Tabayashi K 2015 Highly stretchable, global, and distributed local strain sensing line using GaInSn electrodes for wearable electronics *Adv. Funct. Mater.* **25** 3806–13.
[82] Amjadi M, Pichitpajongkit A, Lee S, Ryu S, Park I 2014 Highly stretchable and sensitive strain sensor based on silver nanowire-elastomer nanocomposite *ACS Nano* **8** 5154–63.
[83] Abshirini M, Charara M, Liu Y, Saha M, Altan M C 2018 3D Printing of Highly Stretchable Strain Sensors Based on Carbon Nanotube Nanocomposites *Adv. Eng. Mater.* **20** 1800425.
[84] Yamada T, Hayamizu Y, Yamamoto Y, Yomogida Y, Izadi-Najafabadi A, Futaba D N, et al 2011 A stretchable carbon nanotube strain sensor for human-motion detection *Nat. Nanotechnol.* **6** 296.
[85] Giffney T, Bejanin E, Kurian A S, Travas-Sejdic J, Aw K 2017 Highly stretchable printed strain sensors using multi-walled carbon nanotube/silicone rubber composites *Sensors Actuators A: Phys.* **259** 44–9.
[86] Han C-J, Chiang H-P, Cheng Y-C 2018 Using Micro-Molding and Stamping to Fabricate Conductive Polydimethylsiloxane-Based Flexible High-Sensitivity Strain Gauges *Sensors* **18** 618.
[87] Kong J-H, Jang N-S, Kim S-H, Kim J-M 2014 Simple and rapid micropatterning of conductive carbon composites and its application to elastic strain sensors *Carbon* **77** 199–207.
[88] Yan W, Page A, Nguyen-Dang T, Qu Y, Sordo F, Wei L, et al 2019 Advanced multimaterial electronic and optoelectronic fibers and textiles *Adv. Mater.* **31** 1802348.
[89] Qu Y, Nguyen-Dang T, Page A G, Yan W, Das Gupta T, Rotaru G M, et al 2018 Superelastic multimaterial electronic and photonic fibers and devices via thermal drawing *Adv. Mater.* **30** 1707251.
[90] Emon M, Choi J-W 2017 Flexible piezoresistive sensors embedded in 3D printed tires *Sensors* **17** 656.
[91] Lee C, Jug L, Meng E 2013 High strain biocompatible polydimethylsiloxane-based conductive graphene and multiwalled carbon nanotube nanocomposite strain sensors *Appl. Phys. Lett.* **102** 183511.
[92] Luo S, Liu T 2013 Structure–property–processing relationships of single-wall carbon nanotube thin film piezoresistive sensors *Carbon* **59** 315–24.
[93] Ferreira A, Lanceros-Mendez S 2016 Piezoresistive response of spray-printed carbon nanotube/poly (vinylidene fluoride) composites *Compos. Part B Eng.* **96** 242–7.
[94] Huang P, Xia Z, Cui S 2018 3D printing of carbon fiber-filled conductive silicon rubber *Mater. Des.* **142** 11–21.
[95] Sekitani T, Noguchi Y, Hata K, Fukushima T, Aida T, Someya T 2008 A rubberlike stretchable active matrix using elastic conductors *Science* **321** 1468–72.
[96] Truby R L, Lewis J A 2016 Printing soft matter in three dimensions *Nature* **540** 371.
[97] Zheng Y, Li Y, Dai K, Wang Y, Zheng G, Liu C, et al 2018 A highly stretchable and stable strain sensor based on hybrid carbon nanofillers/polydimethylsiloxane conductive composites for large human motions monitoring *Compos. Sci. Technol.* **156** 276–86.
[98] Yamaguchi K, Busfield J J C, Thomas A G 2003 Electrical and mechanical behavior of filled elastomers. I. The effect of strain *J. Polym. Sci. Part B Polym. Phys.* **41** 2079–89.
[99] Liu H, Li Y, Dai K, Zheng G, Liu C, Shen C, et al 2016 Electrically conductive thermoplastic elastomer nanocomposites at ultralow graphene loading levels for strain sensor applications *J. Mater. Chem. C* **4** 157–66.
[100] Xu M, Qi J, Li F, Zhang Y 2018 Highly stretchable strain sensors with reduced graphene oxide sensing liquids for wearable electronics *Nanoscale* **10** 5264–71.
[101] Russo S, Ranzani T, Liu H, Nefti-Meziani S, Althoefer K, Menciassi A 2015 Soft and stretchable sensor using biocompatible electrodes and liquid for medical applications *Soft Robot.* **2** 146–54.
[102] Gosline A H, Arabagi V, Kassam A, Dupont P E 2013. Achieving biocompatibility in soft sensors for surgical robots In: *Proc Hamlyn Symp Med Robot* p. 5–6.
[103] Cheung Y-N, Zhu Y, Cheng C-H, Chao C, Leung W W-F 2008 A novel fluidic strain sensor for large strain measurement *Sensors Actuators A: Phys.* **147** 401–8.
[104] Xu S, Vogt D M, Hsu W, Osborne J, Walsh T, Foster J R, et al 2019 Biocompatible Soft Fluidic Strain and Force Sensors for Wearable Devices *Adv. Funct. Mater.* **29** 1807058.
[105] Chossat J-B, Park Y-L, Wood R J, Duchaine V 2013 A soft strain sensor based on ionic and metal liquids *IEEE Sens. J.* **13** 3405–14.
[106] Liu C, Han S, Xu H, Wu J, Liu C 2018 Multifunctional Highly Sensitive Multiscale Stretchable Strain Sensor

Based on a Graphene/Glycerol–KCl Synergistic Conductive Network *ACS Appl. Mater. Interfaces* **10** 31716–24.
[107] Keulemans G, Pelgrims P, Bakula M, Ceyssens F, Puers R 2014 An ionic liquid based strain sensor for large displacements *Procedia Eng.* **87** 1123–6.
[108] Zhu Y, Chao C, Cheng C-H, Leung W W-F 2009 A novel ionic-liquid strain sensor for large-strain applications *Ieee electron device Lett.* **30** 337–9.
[109] Watanabe M, Thomas M L, Zhang S, Ueno K, Yasuda T, Dokko K 2017 Application of ionic liquids to energy storage and conversion materials and devices *Chem. Rev.* **117** 7190–239.
[110] Daeneke T, Khoshmanesh K, Mahmood N, de Castro I A, Esrafilzadeh D, Barrow S J, et al 2018 Liquid metals: fundamentals and applications in chemistry *Chem. Soc. Rev.* **47** 4073–111.
[111] Fassler A, Majidi C 2013 3D structures of liquid-phase GaIn alloy embedded in PDMS with freeze casting *Lab Chip* **13** 4442–50.
[112] Gannarapu A, Gozen B A 2016 Freeze-Printing of Liquid Metal Alloys for Manufacturing of 3D, Conductive, and Flexible Networks *Adv. Mater. Technol.* **1** 1600047.
[113] Dickey M D 2017 Stretchable and Soft Electronics using Liquid Metals *Adv. Mater.* **29** 1–19.
[114] Ladd C, So J, Muth J, Dickey M D 2013 3D printing of free standing liquid metal microstructures *Adv. Mater.* **25** 5081–5.
[115] Yan H, Chen Y, Deng Y, Zhang L, Hong X, Lau W, et al 2016 Coaxial printing method for directly writing stretchable cable as strain sensor *Appl. Phys. Lett.* **109** 83502.
[116] Ahmed E M 2015 Hydrogel: Preparation, characterization, and applications: A review *J. Adv. Res.* **6** 105–21.
[117] Liu S, Li L 2017 Ultrastretchable and self-healing double-network hydrogel for 3D printing and strain sensor *ACS Appl. Mater. Interfaces* **9** 26429–37.
[118] Cai G, Wang J, Qian K, Chen J, Li S, Lee P S 2017 Extremely Stretchable Strain Sensors Based on Conductive Self-Healing Dynamic Cross-Links Hydrogels for Human-Motion Detection *Adv. Sci.* **4** 1600190.
[119] Odent J, Wallin T J, Pan W, Kruemplestaedter K, Shepherd R F, Giannelis E P 2017 Highly elastic, transparent, and conductive 3D-printed ionic composite hydrogels *Adv. Funct. Mater.* **27** 1701807.
[120] Tian K, Bae J, Bakarich S E, Yang C, Gately R D, Spinks G M, et al 2017 3D printing of transparent and conductive heterogeneous hydrogel–elastomer systems *Adv. Mater.* **29** 1604827.
[121] Yin X, Zhang Y, Cai X, Guo Q, Yang J, Wang Z 2019 3D Printing of Ionic Conductors for High-Sensitivity Wearable Sensors *Mater. Horizons*.
[122] Zhang H, Niu W, Zhang S 2018 Extremely Stretchable, Stable, and Durable Strain Sensors Based on Double-Network Organogels *ACS Appl. Mater. Interfaces* **10** 32640–8.
[123] Lee Y, Kang H, Gwon S H, Choi G M, Lim S, Sun J, et al 2016 A Strain-Insensitive Stretchable Electronic Conductor: PEDOT: PSS/Acrylamide Organogels *Adv. Mater.* **28** 1636–43.
[124] Rong Q, Lei W, Chen L, Yin Y, Zhou J, Liu M 2017 Anti-freezing, Conductive Self-healing Organohydrogels with Stable Strain-Sensitivity at Subzero Temperatures *Angew. Chemie Int. Ed.* **56** 14159–63.
[125] Le Bideau J, Viau L, Vioux A 2011 Ionogels, ionic liquid based hybrid materials *Chem. Soc. Rev.* **40** 907–25.
[126] Marr P C, Marr A C 2016 Ionic liquid gel materials: applications in green and sustainable chemistry *Green Chem.* **18** 105–28.
[127] Ding Y, Zhang J, Chang L, Zhang X, Liu H, Jiang L 2017 Preparation of High-Performance Ionogels with Excellent Transparency, Good Mechanical Strength, and High Conductivity *Adv. Mater.* **29** 1704253.
[128] Truby R L, Wehner M, Grosskopf A K, Vogt D M, Uzel S G M, Wood R J, et al 2018 Soft somatosensitive actuators via embedded 3D printing *Adv. Mater.* **30** 1706383.
[129] Muth J T, Vogt D M, Truby R L, Mengüç Y, Kolesky D B, Wood R J, et al 2014 Embedded 3D printing of strain sensors within highly stretchable elastomers *Adv. Mater.* **26** 6307–12.
[130] Zhang B, Ning W, Zhang J, Qiao X, Zhang J, He J, et al 2010 Stable dispersions of reduced graphene oxide in ionic liquids *J. Mater. Chem.* **20** 5401.
[131] Oliva-Avilés A I, Avilés F, Sosa V 2011 Electrical and piezoresistive properties of multi-walled carbon nanotube/polymer composite films aligned by an electric field *Carbon* **49** 2989–97.
[132] Tigelaar D M, Waldecker J R, Peplowski K M, Kinder J D 2006 Study of the incorporation of protic ionic liquids into hydrophilic and hydrophobic rigid-rod elastomeric polymers *Polymer (Guildf).* **47** 4269–75.
[133] Highley C B, Rodell C B, Burdick J A 2015 Direct 3D printing of shear-thinning hydrogels into self-healing hydrogels *Adv. Mater.* **27** 5075–9.
[134] Ouyang L, Highley C B, Rodell C B, Sun W, Burdick J A 2016 3D printing of shear-thinning hyaluronic acid hydrogels with secondary cross-linking *ACS Biomater. Sci. Eng.* **2** 1743–51.
[135] Hyun K, Kim S H, Ahn K H, Lee S J 2002 Large amplitude oscillatory shear as a way to classify the complex

fluids *J. Nonnewton. Fluid Mech.* **107** 51–65.
[136] Wang Y, Huo F, He H, Zhang S 2018 The confined [Bmim][BF4] ionic liquid flow through graphene oxide nanochannel: A molecular dynamics study *Phys. Chem. Chem. Phys.*
[137] Tamilarasan P, Remya T S, Ramaprabhu S 2013 Ionic liquid functionalized graphene for carbon dioxide capture *Graphene* **1** 3–10.
[138] Stankovich S, Dikin D A, Piner R D, Kohlhaas K A, Kleinhammes A, Jia Y, et al 2007 Synthesis of graphene-based nanosheets via chemical reduction of exfoliated graphite oxide *Carbon* **45** 1558–65.
[139] Kim K, Regan W, Geng B, Alemán B, Kessler B M, Wang F, et al 2010 High-temperature stability of suspended single-layer graphene *Phys. status solidi (RRL)–Rapid Res. Lett.* **4** 302–4.
[140] Mei X, Ouyang J 2011 Ultrasonication-assisted ultrafast reduction of graphene oxide by zinc powder at room temperature *Carbon* **49** 5389–97.
[141] Zheng H, Neo C Y, Mei X, Qiu J, Ouyang J 2012 Reduced graphene oxide films fabricated by gel coating and their application as platinum-free counter electrodes of highly efficient iodide/triiodide dye-sensitized solar cells *J. Mater. Chem.* **22** 14465.
[142] Eddings M A, Johnson M A, Gale B K 2008 Determining the optimal PDMS–PDMS bonding technique for microfluidic devices *J. Micromechanics Microengineering* **18** 67001.
[143] Chen S, Liu H, Liu S, Wang P, Zeng S, Sun L, et al 2018 Transparent and Waterproof Ionic Liquid-Based Fibers for Highly Durable Multifunctional Sensors and Strain-Insensitive Stretchable Conductors *ACS Appl. Mater. Interfaces* **10** 4305–14.
[144] Shi G, Zhao Z, Pai J, Lee I, Zhang L, Stevenson C, et al 2016 Highly sensitive, wearable, durable strain sensors and stretchable conductors using graphene/silicon rubber composites *Adv. Funct. Mater.* **26** 7614–25.
[145] Wang Y, Jia Y, Zhou Y, Wang Y, Zheng G, Dai K, et al 2018 Ultra-stretchable, sensitive and durable strain sensors based on polydopamine encapsulated carbon nanotubes/elastic bands *J. Mater. Chem. C* **6** 8160–70.
[146] Choi D Y, Kim M H, Oh Y S, Jung S H, Jung J H, Sung H J, et al 2017 Highly stretchable, hysteresis-free ionic liquid-based strain sensor for precise human motion monitoring *ACS Appl. Mater. Interfaces* **9** 1770–80.
[147] Yoon S G, Park B J, Chang S T 2017 Highly sensitive microfluidic strain sensors with low hysteresis using a binary mixture of ionic liquid and ethylene glycol *Sensors Actuators A: Phys.* **254** 1–8.
[148] Wu Y, Zhen R, Liu H, Liu S, Deng Z, Wang P, et al 2017 Liquid metal fiber composed of a tubular channel as a high-performance strain sensor *J. Mater. Chem. C* **5** 12483–91.
[149] Stoppa A, Zech O, Kunz W, Buchner R 2009 The conductivity of imidazolium-based ionic liquids from (− 35 to 195) CA Variation of cation's alkyl chain *J. Chem. Eng. Data* **55** 1768–73.
[150] Stoppa A, Hunger J, Buchner R 2008 Conductivities of binary mixtures of ionic liquids with polar solvents *J. Chem. Eng. Data* **54** 472–9.
[151] Kanakubo M, Harris K R, Tsuchihashi N, Ibuki K, Ueno M 2007 Effect of pressure on transport properties of the ionic liquid 1-butyl-3-methylimidazolium hexafluorophosphate *J. Phys. Chem. B* **111** 2062–9.
[152] Widegren J A, Saurer E M, Marsh K N, Magee J W 2005 Electrolytic conductivity of four imidazolium-based room-temperature ionic liquids and the effect of a water impurity *J. Chem. Thermodyn.* **37** 569–75.
[153] Angell C A 1995 Formation of glasses from liquids and biopolymers *Science* **267** 1924–35.
[154] Stankovich S, Dikin D A, Dommett G H B, Kohlhaas K M, Zimney E J, Stach E A, et al 2006 Graphene-based composite materials *Nature* **442** 282.
[155] Potts J R, Shankar O, Du L, Ruoff R S 2012 Processing–morphology–property relationships and composite theory analysis of reduced graphene oxide/natural rubber nanocomposites *Macromolecules* **45** 6045–55.
[156] Yousefi N, Gudarzi M M, Zheng Q, Aboutalebi S H, Sharif F, Kim J-K 2012 Self-alignment and high electrical conductivity of ultralarge graphene oxide–polyurethane nanocomposites *J. Mater. Chem.* **22** 12709–17.
[157] Zheng D, Tang G, Zhang H-B, Yu Z-Z, Yavari F, Koratkar N, et al 2012 In situ thermal reduction of graphene oxide for high electrical conductivity and low percolation threshold in polyamide 6 nanocomposites *Compos. Sci. Technol.* **72** 284–9.
[158] Liu Q, Chen J, Li Y, Shi G 2016 High-performance strain sensors with fish-scale-like graphene-sensing layers for full-range detection of human motions *ACS Nano* **10** 7901–6.
[159] Wang Y, Hao J, Huang Z, Zheng G, Dai K, Liu C, et al 2018 Flexible electrically resistive-type strain sensors based on reduced graphene oxide-decorated electrospun polymer fibrous mats for human motion monitoring *Carbon* **126** 360–71.
[160] Kim S H, Hong K, Xie W, Lee K H, Zhang S, Lodge T P, et al 2013 Electrolyte-gated transistors for organic and printed electronics *Adv. Mater.* **25** 1822–46.
[161] Shi L, Crow M L 2008. Comparison of ultracapacitor electric circuit models In: *2008 IEEE Power and Energy*

Society General Meeting-Conversion and Delivery of Electrical Energy in the 21st Century IEEE; p. 1–6.
[162] Ruhhammer J, Zens M, Goldschmidtboeing F, Seifert A, Woias P 2015 Highly elastic conductive polymeric MEMS *Sci. Technol. Adv. Mater.* **16** 15003.
[163] Niu X Z, Peng S L, Liu L Y, Wen W J, Sheng P 2007 Characterizing and patterning of PDMS-based conducting composites *Adv. Mater.* **19** 2682–6.
[164] Fedorov M V, Lynden-Bell R M 2012 Probing the neutral graphene–ionic liquid interface: insights from molecular dynamics simulations *Phys. Chem. Chem. Phys.* **14** 2552–6.
[165] Ghatee M H, Moosavi F 2011 Physisorption of hydrophobic and hydrophilic 1-alkyl-3-methylimidazolium ionic liquids on the graphenes *J. Phys. Chem. C* **115** 5626–36.
[166] Pensado A S, Malberg F, Gomes M F C, Pádua A A H, Fernández J, Kirchner B 2014 Interactions and structure of ionic liquids on graphene and carbon nanotubes surfaces *RSC Adv.* **4** 18017–24.
[167] Li H, Wood R J, Endres F, Atkin R 2014 Influence of alkyl chain length and anion species on ionic liquid structure at the graphite interface as a function of applied potential *J. Phys. Condens. Matter* **26** 284115.
[168] Yeo J C, Yap H K, Xi W, Wang Z, Yeow C, Lim C T 2016 Flexible and stretchable strain sensing actuator for wearable soft robotic applications *Adv. Mater. Technol.* **1** 1600018.
[169] Wu Y, Karakurt I, Beker L, Kubota Y, Xu R, Ho K Y, et al 2018 Piezoresistive stretchable strain sensors with human machine interface demonstrations *Sensors Actuators A: Phys.* **279** 46–52.
[170] Mai H, Mutlu R, Tawk C, Alici G, Sencadas V 2019 Ultra-stretchable MWCNT–Ecoflex piezoresistive sensors for human motion detection applications *Compos. Sci. Technol.* **173** 118–24.
[171] Yan D, Bruns T M, Wu Y, Zimmerman L L, Stephan C, Cameron A P, et al 2019 Ultra-compliant carbon nanotube stretchable direct bladder interface *bioRxiv* 580902.
[172] Grenvik A, Schaefer J 2004 From Resusci-Anne to Sim-Man: the evolution of simulators in medicine *Crit. Care Med.* **32** S56–7.
[173] Seam N, Lee A J, Vennero M, Emlet L 2019 Simulation Training in the ICU *Chest* **156** 1223–33.
[174] 2020 Accredited Education Institutes [Internet]
[175] McGaghie W C, Issenberg S B, Cohen M E R, Barsuk J H, Wayne D B 2011 Does simulation-based medical education with deliberate practice yield better results than traditional clinical education? A meta-analytic comparative review of the evidence *Acad. Med. J. Assoc. Am. Med. Coll.* **86** 706.
[176] Beal M D, Kinnear J, Anderson C R, Martin T D, Wamboldt R, Hooper L 2017 The effectiveness of medical simulation in teaching medical students critical care medicine: a systematic review and meta-analysis *Simul. Healthc.* **12** 104–16.
[177] Noureldin Y A, Lee J Y, McDougall E M, Sweet R M 2018 Competency-based training and simulation: making a "valid" argument *J. Endourol.* **32** 84–93.
[178] Harn H I, Ogawa R, Hsu C, Hughes M W, Tang M, Chuong C 2019 The tension biology of wound healing *Exp. Dermatol.* **28** 464–71.
[179] Dai J, Bordeaux J S, Miller C J, Sobanko J F 2016 Assessing surgical training and deliberate practice methods in dermatology residency: a survey of dermatology program directors *Dermatologic Surg.* **42** 977–84.
[180] Sajan J A, Hilger P A, Sidman J D, Walsh W E, Chaffin P L, Reihsen T, et al 2013 Validated Assessment Tools for Reconstructing Facial Defects in Simulation *Otolaryngol. Neck Surg.* **149** P44–5.
[181] Lim H, Kim H S, Qazi R, Kwon Y, Jeong J, Yeo W 2019 Advanced Soft Materials, Sensor Integrations, and Applications of Wearable Flexible Hybrid Electronics in Healthcare, Energy, and Environment *Adv. Mater.* 1901924.
[182] Zheng Y, Li Y, Zhou Y, Dai K, Zheng G, Zhang B, et al 2019 High-Performance Wearable Strain Sensor Based on Graphene/Cotton Fabric with High Durability and Low Detection Limit *ACS Appl. Mater. Interfaces* **12** 1474–85.
[183] Zhao M, Li D, Huang J, Wang D, Mensah A, Wei Q 2019 A multifunctional and highly stretchable electronic device based on silver nanowire/wrap yarn composite for a wearable strain sensor and heater *J. Mater. Chem. C* **7** 13468–76.
[184] Zhou C-G, Sun W-J, Jia L-C, Xu L, Dai K, Yan D-X, et al 2019 Highly Stretchable and Sensitive Strain Sensor with Porous Segregated Conductive Network *ACS Appl. Mater. Interfaces* **11** 37094–102.
[185] Votzke C, Daalkhaijav U 2018. Highly-Stretchable Biomechanical Strain Sensor using Printed Liquid Metal Paste In: *IEEE Biomedical Circuits and Systems Conference (BioCAS)*.
[186] Malakooti M H, Bockstaller M R, Matyjaszewski K, Majidi C 2020 Liquid Metal Nanocomposites *Nanoscale Adv.*
[187] Kim J-H, Kim S, So J-H, Kim K, Koo H-J 2018 Cytotoxicity of Gallium–Indium Liquid Metal in an Aqueous Environment *ACS Appl. Mater. Interfaces* **10** 17448–54.

[188] Ellis L 2018 US Department of the Interior - Office of the Secretary: Final List of Critical Minerals 2018 *Fed. Regist.* **83** 23295–6.
[189] Wang Z, Cong Y, Fu J 2020 Stretchable and tough conductive hydrogels for flexible pressure and strain sensors *J. Mater. Chem. B.*
[190] Costa S P F, Azevedo A M O, Pinto P C A G, Saraiva M L M F S 2017 Environmental impact of ionic liquids: recent advances in (eco) toxicology and (bio) degradability *ChemSusChem* **10** 2321–47.
[191] Gomes J M, Silva S S, Reis R L 2019 Biocompatible ionic liquids: fundamental behaviours and applications *Chem. Soc. Rev.* **48** 4317–35.
[192] Smith E L, Abbott A P, Ryder K S 2014 Deep eutectic solvents (DESs) and their applications *Chem. Rev.* **114** 11060–82.
[193] Paiva A, Craveiro R, Aroso I, Martins M, Reis R L, Duarte A R C 2014 Natural deep eutectic solvents–solvents for the 21st century *ACS Sustain. Chem. Eng.* **2** 1063–71.
[194] Wu S-H, Caparanga A R, Leron R B, Li M-H 2012 Vapor pressure of aqueous choline chloride-based deep eutectic solvents (ethaline, glyceline, maline and reline) at 30–70 C *Thermochim. Acta* **544** 1–5.
[195] Shahbaz K, Mjalli F S, Vakili-Nezhaad G, AlNashef I M, Asadov A, Farid M M 2016 Thermogravimetric measurement of deep eutectic solvents vapor pressure *J. Mol. Liq.* **222** 61–6.
[196] Kuehn K M, Massmann C M, Sovell N R 2017 Choline Chloride Eutectics: Low Temperature Applications *J. Undergrad. Res.* **15** 5.
[197] Troter D Z, Todorović Z B, Đokić-Stojanović D R, Veselinović L M, Zdujić M V, Veljković V B 2018 Choline chloride-based deep eutectic solvents in CaO-catalyzed ethanolysis of expired sunflower oil *J. Mol. Liq.* **266** 557–67.
[198] Ibrahim R K, Hayyan M, AlSaadi M A, Ibrahim S, Hayyan A, Hashim M A 2019 Physical properties of ethylene glycol-based deep eutectic solvents *J. Mol. Liq.* **276** 794–800.
[199] LaKind J S, McKenna E A, Hubner R P, Tardiff R G 1999 A review of the comparative mammalian toxicity of ethylene glycol and propylene glycol *Crit. Rev. Toxicol.* **29** 331–65.
[200] Zhou T, Xiao X, Li G, Cai Z 2011 Study of polyethylene glycol as a green solvent in the microwave-assisted extraction of flavone and coumarin compounds from medicinal plants *J. Chromatogr. A* **1218** 3608–15.
[201] Frauenkron M, Aktiengesellschaft B, RUIDER G Ü N, HO H 2012 Ethanolamines and propanolamines *Environ. Prot.* **421** 8.
[202] Monteiro M S de S de, Cucinelli Neto R P, Santos I C S, Silva E O da, Tavares M I B 2012 Inorganic-organic hybrids based on poly (ε-Caprolactone) and silica oxide and characterization by relaxometry applying low-field NMR *Mater. Res.* **15** 825–32.
[203] Deshmukh P K 2013 Dissolution enhancement of rosuvastatin calcium by liquisolid compact technique *J. Pharm.* **2013** .
[204] Sanaeishoar H, Sabbaghan M, Mohave F 2015 Synthesis and characterization of micro-mesoporous MCM-41 using various ionic liquids as co-templates *Microporous Mesoporous Mater.* **217** 219–24.
[205] Zhang J, Ge X, Wang M, Wu M, Yang J, Wu Q 2012 Facile fabrication of flower-like nanocomposite microparticles via seeded miniemulsion polymerization *Polym. Chem.* **3** 2011–7.
[206] Yu M, Qiao X, Dong X, Sun K 2018 Effect of particle modification on the shear thickening behaviors of the suspensions of silica nanoparticles in PEG *Colloid Polym. Sci.* **296** 1767–76.
[207] Pattanayek S K, Ghosh A K 2018 Dynamic shear rheology of colloidal suspensions of surface-modified silica nanoparticles in PEG *J. Nanoparticle Res.* **20** 53.
[208] Sirviö J A 2018 Cationization of lignocellulosic fibers with betaine in deep eutectic solvent: Facile route to charge stabilized cellulose and wood nanofibers *Carbohydr. Polym.* **198** 34–40.
[209] Selkälä T, Sirviö J A, Lorite G S, Liimatainen H 2016 Anionically stabilized cellulose nanofibrils through succinylation pretreatment in urea–lithium chloride deep eutectic solvent *ChemSusChem* **9** 3074–83.
[210] Lai C-W, Yu S-S 2020 3D printable strain sensors from deep eutectic solvents and cellulose nanocrystals *ACS Appl. Mater. Interfaces* **12** 34235–44.
[211] Selvanathan V, Azzahari A D, Halim A A A, Yahya R 2017 Ternary natural deep eutectic solvent (NADES) infused phthaloyl starch as cost efficient quasi-solid gel polymer electrolyte *Carbohydr. Polym.* **167** 210–8.
[212] Gürgen S, Kuşhan M C, Li W 2017 Shear thickening fluids in protective applications: a review *Prog. Polym. Sci.* **75** 48–72.
[213] Liu X-Q, Bao R-Y, Wu X-J, Yang W, Xie B-H, Yang M-B 2015 Temperature induced gelation transition of a fumed silica/PEG shear thickening fluid *Rsc Adv.* **5** 18367–74.
[214] Raghavan S R, Walls H J, Khan S A 2000 Rheology of silica dispersions in organic liquids: new evidence for solvation forces dictated by hydrogen bonding *Langmuir* **16** 7920–30.

[215] Warren J, Offenberger S, Toghiani H, Pittman Jr C U, Lacy T E, Kundu S 2015 Effect of temperature on the shear-thickening behavior of fumed silica suspensions *ACS Appl. Mater. Interfaces* **7** 18650–61.
[216] Raghavan S R, Riley M W, Fedkiw P S, Khan S A 1998 Composite polymer electrolytes based on poly (ethylene glycol) and hydrophobic fumed silica: dynamic rheology and microstructure *Chem. Mater.* **10** 244–51.
[217] Krieger U K, Siegrist F, Marcolli C, Emanuelsson E U, Gøbel F M, Bilde M, et al 2018 A reference data set for validating vapor pressure measurement techniques: homologous series of polyethylene glycols *Atmos. Meas. Tech.* **11** 49–63.
[218] Verevkin S P, Emel'yanenko V N, Nell G 2009 1, 2-Propanediol. Comprehensive experimental and theoretical study *J. Chem. Thermodyn.* **41** 1125–31.
[219] Chen G, Wang H, Guo R, Duan M, Zhang Y, Liu J 2020 Superelastic EGaIn Composite Fiber Sustaining 500% Tensile Strain with Superior Electrical Conductivity for Wearable Electronics *ACS Appl. Mater. Interfaces*.
[220] Khalil P N, Siebeck M, Mutschler W, Kanz K G 2009 The use of chicken legs for teaching wound closure skills *Eur. J. Med. Res.* **14** 459.
[221] Kalra A, Lowe A 2016 Mechanical Behaviour of Skin: A Review *J. Mater. Sci. Eng.* **5** .
[222] Manschot J F M, Brakkee A J M 1986 The measurement and modelling of the mechanical properties of human skin in vivo—II. The model *J. Biomech.* **19** 517–21.
[223] Truby R L, Katzschmann R K, Lewis J A, Rus D 2019. Soft Robotic Fingers with Embedded Ionogel Sensors and Discrete Actuation Modes for Somatosensitive Manipulation In: *2019 2nd IEEE International Conference on Soft Robotics (RoboSoft)* IEEE; p. 322–9.
[224] Wong J, Gong A T, Defnet P A, Meabe L, Beauchamp B, Sweet R M, et al 2019 3D Printing Ionogel Auxetic Frameworks for Stretchable Sensors *Adv. Mater. Technol.* **4** 1900452.
[225] Qin H, Panzer M J 2017 Chemically Cross-Linked Poly (2-hydroxyethyl methacrylate)-Supported Deep Eutectic Solvent Gel Electrolytes for Eco-Friendly Supercapacitors *ChemElectroChem* **4** 2556–62.
[226] Muralt P 2000 Ferroelectric thin films for micro-sensors and actuators: a review *J. Micromech. Microeng.* **10** .
[227] Bowen C R, Kim H A, Weaver P M, Dunn S 2014 Piezoelectric and ferroelectric materials and structures for energy harvesting applications *Energy Environ. Sci.* **7** 25–44.
[228] Near C D 1996. Piezoelectric actuator technology In: *Smart Structures and Materials 1996: Smart Structures and Integrated Systems* International Society for Optics and Photonics; p. 246–59.
[229] Rajabi A H, Jaffe M, Arinzeh T L 2015 Piezoelectric materials for tissue regeneration: A review *Acta Biomater.* **24** 12–23.
[230] Saito Y, Takao H, Tani T, Nonoyama T, Takatori K, Homma T, et al 2004 Lead-free piezoceramics *Nature* **432** 84.
[231] Tanimoto T, Okazaki K, Yamamoto K 1993 Tensile stress-strain behavior of piezoelectric ceramics *Jpn. J. Appl. Phys.* **32** 4233.
[232] Horiuchi S, Tokura Y 2008 Organic ferroelectrics *Nat. Mater.* **7** 357.
[233] Li J, Liu Y, Zhang Y, Cai H-L, Xiong R-G 2013 Molecular ferroelectrics: where electronics meet biology *Phys. Chem. Chem. Phys.* **15** 20786–96.
[234] Tayi A S, Kaeser A, Matsumoto M, Aida T, Stupp S I 2015 Supramolecular ferroelectrics *Nat. Chem.* **7** 281.
[235] Shi P-P, Tang Y-Y, Li P-F, Liao W-Q, Wang Z-X, Ye Q, et al 2016 Symmetry breaking in molecular ferroelectrics *Chem. Soc. Rev.* **45** 3811–27.
[236] Roberts S 1947 Dielectric and piezoelectric properties of barium titanate *Phys. Rev.* **71** 890.
[237] Wu J, Xiao D, Zhu J 2015 Potassium–sodium niobate lead-free piezoelectric materials: past, present, and future of phase boundaries *Chem. Rev.* **115** 2559–95.
[238] Bechmann R 1956 Elastic, piezoelectric, and dielectric constants of polarized barium titanate ceramics and some applications of the piezoelectric equations *J. Acoust. Soc. Am.* **28** 347–50.
[239] Ueberschlag P 2001 PVDF piezoelectric polymer *Sens. Rev.* **21** 118–26.
[240] Ramadan K S, Sameoto D, Evoy S 2014 A review of piezoelectric polymers as functional materials for electromechanical transducers *Smart Mater. Struct.* **23** 33001.
[241] Schmidt G C, Panicker P M, Qiu X, Benjamin A J, Quintana Soler R A, Wils I, et al 2021 Paper-embedded roll-to-roll mass printed piezoelectric transducers *Adv. Mater.* **33** 2006437.
[242] Jean-Mistral C, Basrour S, Chaillout J J 2010 Comparison of electroactive polymers for energy scavenging applications *Smart Mater. Struct.* **19** 85012.
[243] Harrison J S, Ounaies Z 2002 Piezoelectric polymers *Encycl. Polym. Sci. Technol.* **3** .

[244] Roh Y, Varadan V V, Varadan V K 2002 Characterization of all the elastic, dielectric, and piezoelectric constants of uniaxially oriented poled PVDF films *IEEE Trans. Ultrason. Ferroelectr. Freq. Control* **49** 836–47.
[245] Martins P, Lopes A C, Lanceros-Mendez S 2014 Electroactive phases of poly (vinylidene fluoride): determination, processing and applications *Prog. Polym. Sci.* **39** 683–706.
[246] Benz M, Euler W B, Gregory O J 2002 The role of solution phase water on the deposition of thin films of poly (vinylidene fluoride) *Macromolecules* **35** 2682–8.
[247] Gregorio Jr R 2006 Determination of the α, β, and γ crystalline phases of poly (vinylidene fluoride) films prepared at different conditions *J. Appl. Polym. Sci.* **100** 3272–9.
[248] Ducrot P-H, Dufour I, Ayela C 2016 Optimization of PVDF-TrFE processing conditions for the fabrication of organic MEMS resonators *Sci. Rep.* **6** 19426.
[249] Fu D-W, Cai H-L, Liu Y, Ye Q, Zhang W, Zhang Y, et al 2013 Diisopropylammonium bromide is a high-temperature molecular ferroelectric crystal *Science* **339** 425–8.
[250] Gao K, Liu C, Cui Z, Zhu J, Cai H-L, Wu X S 2015 Room-temperature growth of ferroelectric diisopropylammonium bromide with 12-crown-4 addition *CrystEngComm* **17** 2429–32.
[251] Gao K, Xu C, Cui Z, Liu C, Gao L, Li C, et al 2016 The growth mechanism and ferroelectric domains of diisopropylammonium bromide films synthesized via 12-crown-4 addition at room temperature *Phys. Chem. Chem. Phys.* **18** 7626–31.
[252] Yadav H, Sinha N, Goel S, Hussain A, Kumar B 2016 Growth and structural and physical properties of diisopropylammonium bromide molecular single crystals *J. Appl. Crystallogr.* **49** 2053–62.
[253] Zhang Y, Liu Y, Ye H, Fu D, Gao W, Ma H, et al 2014 A molecular ferroelectric thin film of imidazolium perchlorate that shows superior electromechanical coupling *Angew. Chemie Int. Ed.* **53** 5064–8.
[254] Gao W, Chang L, Ma H, You L, Yin J, Liu J, et al 2015 Flexible organic ferroelectric films with a large piezoelectric response *NPG Asia Mater.* **7** e189.
[255] Ma H, Gao W, Wang J, Wu T, Yuan G, Liu J, et al 2016 Ferroelectric Polarization Switching Dynamics and Domain Growth of Triglycine Sulfate and Imidazolium Perchlorate *Adv. Electron. Mater.* **2** 1600038.
[256] Zhang Z, Li P-F, Tang Y-Y, Wilson A J, Willets K, Wuttig M, et al 2017 Tunable electroresistance and electro-optic effects of transparent molecular ferroelectrics *Sci. Adv.* **3** e1701008.
[257] Bergenti I, Ruani G, Liscio F, Milita S, Dinelli F, Xu X, et al 2017 Highly Ordered Organic Ferroelectric DIPAB-Patterned Thin Films *Langmuir* **33** 12859–64.
[258] Pan Q, Xiong Y-A, Sha T-T, You Y-M 2021 Recent progress in the piezoelectricity of molecular ferroelectrics *Mater. Chem. Front.* **5** 44–59.
[259] Huang G, Khan A A, Rana M M, Xu C, Xu S, Saritas R, et al 2020 Achieving ultrahigh piezoelectricity in organic–inorganic vacancy-ordered halide double perovskites for mechanical energy harvesting *ACS Energy Lett.* **6** 16–23.
[260] Chen X-G, Song X-J, Zhang Z-X, Li P-F, Ge J-Z, Tang Y-Y, et al 2019 Two-dimensional layered perovskite ferroelectric with giant piezoelectric voltage coefficient *J. Am. Chem. Soc.* **142** 1077–82.
[261] Wang B, Hong J, Yang Y, Zhao H, Long L, Zheng L 2022 Achievement of a giant piezoelectric coefficient and piezoelectric voltage coefficient through plastic molecular-based ferroelectric materials *Matter* **5** 1296–304.
[262] Gao X, Wu J, Yu Y, Chu Z, Shi H, Dong S 2018 Giant piezoelectric coefficients in relaxor piezoelectric ceramic PNN-PZT for vibration energy harvesting *Adv. Funct. Mater.* **28** 1706895.
[263] Xu W-J, Li P-F, Tang Y-Y, Zhang W-X, Xiong R-G, Chen X-M 2017 A molecular perovskite with switchable coordination bonds for high-temperature multiaxial ferroelectrics *J. Am. Chem. Soc.* **139** 6369–75.
[264] You Y-M, Liao W-Q, Zhao D, Ye H-Y, Zhang Y, Zhou Q, et al 2017 An organic-inorganic perovskite ferroelectric with large piezoelectric response *Science* **309** 306–9.
[265] Liao W Q, Tang Y Y, Li P F, You Y M, Xiong R G 2017 Large Piezoelectric Effect in a Lead-Free Molecular Ferroelectric Thin Film *J. Am. Chem. Soc.* **139** 18071–7.
[266] Liao W Q, Tang Y Y, Li P F, You Y M, Xiong R G 2018 Competitive Halogen Bond in the Molecular Ferroelectric with Large Piezoelectric Response *J. Am. Chem. Soc.* **140** 3975–80.
[267] Harada J, Kawamura Y, Takahashi Y, Uemura Y, Hasegawa T, Taniguchi H, et al 2019 Plastic/Ferroelectric Crystals with Easily Switchable Polarization: Low-Voltage Operation, Unprecedentedly High Pyroelectric Performance, and Large Piezoelectric Effect in Polycrystalline Forms *J. Am. Chem. Soc.* **141** 9349–57.
[268] Liao W Q, Zhao D, Tang Y Y, Zhang Y, Li P F, Shi P P, et al 2019 A molecular perovskite solid solution with piezoelectricity stronger than lead zirconate titanate *Science* **363** 1206–10.
[269] Tang Y, Li P, Liao W, Shi P, You Y, Xiong R, et al 2018 Multiaxial Molecular Ferroelectric Thin Films Bring

Light to Practical Applications *J. Am. Chemcial Soc.*
[270] Vijayakanth T, Liptrot D J, Gazit E, Boomishankar R, Bowen C R 2022 Recent Advances in Organic and Organic–Inorganic Hybrid Materials for Piezoelectric Mechanical Energy Harvesting *Adv. Funct. Mater.* **32** 2109492.
[271] Zhang Y, Song X J, Zhang Z-X, Fu D, Xiong R-G 2020 Piezoelectric Energy Harvesting Based on Multiaxial Ferroelectrics by Precise Molecular Design *Matter* **2** 1–14.
[272] Ippili S, Jella V, Eom S, Hong S, Yoon S-G 2020 Light-Driven Piezo-and Triboelectricity in Organic–Inorganic Metal Trihalide Perovskite toward Mechanical Energy Harvesting and Self-powered Sensor Application *ACS Appl. Mater. Interfaces* **12** 50472–83.
[273] Ippili S, Jella V, Eom J-H, Kim J, Hong S, Choi J-S, et al 2019 An eco-friendly flexible piezoelectric energy harvester that delivers high output performance is based on lead-free MASnI3 films and MASnI3-PVDF composite films *Nano Energy* **57** 911–23.
[274] Ippili S, Jella V, Kim J, Hong S, Yoon S-G 2020 Unveiling predominant air-stable organotin bromide perovskite toward mechanical energy harvesting *ACS Appl. Mater. Interfaces* **12** 16469–80.
[275] Qin Y, Gao F-F, Qian S, Guo T-M, Gong Y-J, Li Z-G, et al 2022 Multifunctional Chiral 2D Lead Halide Perovskites with Circularly Polarized Photoluminescence and Piezoelectric Energy Harvesting Properties *ACS Nano* **16** 3221–30.
[276] Ippili S, Jella V, Thomas A M, Yoon S-G 2021 The recent progress on halide perovskite-based self-powered sensors enabled by piezoelectric and triboelectric effects *Nanoenergy Adv.* **1** 3–31.
[277] Lu J, Hu S, Li W, Wang X, Mo X, Gong X, et al 2022 A Biodegradable and Recyclable Piezoelectric Sensor Based on a Molecular Ferroelectric Embedded in a Bacterial Cellulose Hydrogel *ACS Nano* **16** 3744–55.
[278] Damjanovic D 1998 Ferroelectric, dielectric and piezoelectric properties of ferroelectric thin films and ceramics *Reports Prog. Phys.* **61** 1267.
[279] Stewart M, Battrick W, Cain M G 2001 Measuring piezoelectric d33 coefficents using the direct method.
[280] Ostwald W 1919. Die chemische Literatur und die Organisation der Wissenschaft Vol. 1. Akad. Verlag. Gesel.;
[281] Takacs L 2013 The historical development of mechanochemistry *Chem. Soc. Rev.* **42** 7649–59.
[282] Faraday M 1820 QJ Sci., Lit., Arts, 1820, 8, 374; *J. Therm. Anal. Calorim* **90** 81.
[283] Lea M C 1893 No Title *Am. J. Sci.* **46** 413.
[284] Stolle A, Szuppa T, Leonhardt S E S, Ondruschka B 2011 Ball milling in organic synthesis: solutions and challenges *Chem. Soc. Rev.* **40** 2317–29.
[285] Garay A L, Pichon A, James S L 2007 Solvent-free synthesis of metal complexes *Chem. Soc. Rev.* **36** 846–55.
[286] Yuan W, Friščić T, Apperley D, James S L 2010 High reactivity of metal–organic frameworks under grinding conditions: parallels with organic molecular materials *Angew. Chemie Int. Ed.* **49** 3916–9.
[287] Palazon F, El Ajjouri Y, Bolink H J 2020 Making by grinding: mechanochemistry boosts the development of halide perovskites and other multinary metal halides *Adv. Energy Mater.* **10** 1902499.
[288] Zhang Y, Wang Y, Yang X, Zhao L, Su R, Wu J, et al 2022 Mechanochemistry Advances High-Performance Perovskite Solar Cells *Adv. Mater.* **34** 2107420.
[289] Tanwar J, Vinjamur M, Scriven L E 2007 Design principles of integrated vacuum slot arrangement *AIChE J.* **53** 572–8.
[290] Ding X, Liu J, Harris T A L 2016 A review of the operating limits in slot die coating processes *AIChE J.* **62** 2508–24.
[291] Van Hest M F, Whitaker J B, Moore D, Wheeler L M, Berry J J, Zhu K, et al 2018 Roll-to-Roll Printing of Perovskite Solar Cells *ACS Energy Lett.* **3** .
[292] Galagan Y, Di Giacomo F, Gorter H, Kirchner G, de Vries I, Andriessen R, et al 2018 Roll-to-Roll Slot Die Coated Perovskite for Efficient Flexible Solar Cells *Adv. Energy Mater.* 1801935.
[293] Deng H, Dong D, Qiao K, Bu L, Li B, Yang D, et al 2015 Growth, patterning and alignment of organolead iodide perovskite nanowires for optoelectronic devices. *Nanoscale* **7** 4163–70.
[294] Rossander L H, Larsen-Olsen T T, Dam H F, Schmidt T M, Corazza M, Norrman K, et al 2016 In situ X-ray scattering of perovskite solar cell active layers roll-to-roll coated on flexible substrates *CrystEngComm* **18** 5083–8.
[295] Aliqué M, Simão C D, Murillo G, Moya A 2021 Fully-Printed Piezoelectric Devices for Flexible Electronics Applications *Adv. Mater. Technol.* **6** 2001020.
[296] Derby B 2010 Inkjet printing of functional and structural materials: fluid property requirements, feature stability, and resolution *Annu. Rev. Mater. Res.* **40** 395–414.

[297] Yang J, He P, Derby B 2022 Stability Bounds for Micron Scale Ag Conductor Lines Produced by Electrohydrodynamic Inkjet Printing *ACS Appl. Mater. Interfaces* **14** 39601–9.
[298] You Y-M, Liao W-Q, Zhao D, Ye H-Y, Zhang Y, Zhou Q, et al 2017 An organic-inorganic perovskite ferroelectric with large piezoelectric response *Science* **357** 306–9.
[299] Guo Q, Cao G Z, Shen I Y 2013 Measurements of piezoelectric coefficient d33 of lead zirconate titanate thin films using a mini force hammer *J. Vib. Acoust.* **135** 11003.
[300] Hauner I M, Deblais A, Beattie J K, Kellay H, Bonn D 2017 The dynamic surface tension of water *J. Phys. Chem. Lett.* **8** 1599–603.
[301] Kim J, Kim S, Zuo C, Gao M, Vak D, Kim D 2019 Humidity-tolerant roll-to-roll fabrication of perovskite solar cells via polymer-additive-assisted hot slot die deposition *Adv. Funct. Mater.* **29** 1809194.
[302] Andersen T R, Larsen-Olsen T T, Andreasen B, Bottiger A P L, Carlé J E, Helgesen M, et al 2011 Aqueous processing of low-band-gap polymer solar cells using roll-to-roll methods *ACS Nano* **5** 4188–96.
[303] Cotton F A, Francis R 1960 Sulfoxides as Ligands. I. A Preliminary Survey of Methyl Sulfoxide Complexes *J. Am. Chem. Soc.* **82** 2986–91.
[304] Katzin L I 1962 Ionization Differences Between Coordination States of a Cation. Octahedral—Tetrahedral Equilibrium of Transition-Element Chlorides in Dimethylformamide *J. Chem. Phys.* **36** 3034–41.
[305] Banerjee M, Jain A, Mukherjee G S 2019 Microstructural and optical properties of polyvinyl alcohol/manganese chloride composite film *Polym. Compos.* **40** E765–75.
[306] Cao J, Jing X, Yan J, Hu C, Chen R, Yin J, et al 2016 Identifying the molecular structures of intermediates for optimizing the fabrication of high-quality perovskite films *J. Am. Chem. Soc.* **138** 9919–26.
[307] Ghosh P S, Lisenkov S, Ponomareva I 2020 Phase switching as the origin of large piezoelectric response in organic-inorganic perovskites: A first-principles study *Phys. Rev. Lett.* **125** 207601.
[308] Harada J, Yoneyama N, Yokokura S, Takahashi Y, Miura A, Kitamura N, et al 2018 Ferroelectricity and Piezoelectricity in Free-Standing Polycrystalline Films of Plastic Crystals *J. Am. Chem. Soc.* **140** 346–54.
[309] Walker J, Scherrer S, Løndal N S, Grande T, Einarsrud M-A 2020 Electric field dependent polarization switching of tetramethylammonium bromotrichloroferrate (III) ferroelectric plastic crystals *Appl. Phys. Lett.* **116** 242902.
[310] Walker J, Miranti R, Skjærvø S L, Rojac T, Grande T, Einarsrud M-A 2020 Super-coercive electric field hysteresis in ferroelectric plastic crystal tetramethylammonium bromotrichloroferrate (III) *J. Mater. Chem. C* **8** 3206–16.
[311] Walker J, Marshall K P, Salgado-Beceiro J, Williamson B A D, Løndal N S, Castro-Garcia S, et al 2022 Mesophase Transitions in [(C2H5) 4N][FeBrCl3] and [(CH3) 4N][FeBrCl3] Ferroic Plastic Crystals *Chem. Mater.* **34** 2585–98.
[312] Scherrer S 2020. Synthesis, structure and properties of the organic-inorganic plastic crystal solid solution system [(CH2CH3) 4N] x [(CH3) 4N] 1-x [FeBrCl3] Wien;
[313] Praveen J P, Karthik T, James A R, Chandrakala E, Asthana S, Das D 2015 Effect of poling process on piezoelectric properties of sol-gel derived BZT-BCT ceramics *J. Eur. Ceram. Soc.* **35** 1785–98.
[314] Radzi M H M, Leong K S 2015. Investigation of the piezoelectric charge coefficient d33 of thick-film piezoelectric ceramics by varying poling and repoling conditions In: *AIP Conference Proceedings* AIP Publishing LLC; p. 70083.
[315] Kounga A B, Granzow T, Aulbach E, Hinterstein M, Rödel J 2008 High-temperature poling of ferroelectrics *J. Appl. Phys.* **104** .
[316] Harada J, Yoneyama N, Yokokura S, Takahashi Y, Miura A, Kitamura N, et al 2018 Ferroelectricity and Piezoelectricity in Free-Standing Polycrystalline Films of Plastic Crystals *J. Am. Chem. Soc.* **140** 346–54.
[317] Vazquez G, Alvarez E, Navaza J M 1995 Surface tension of alcohol water+ water from 20 to 50. degree. C *J. Chem. Eng. Data* **40** 611–4.
[318] Beekman C, Siemons W, Chi M, Balke N, Howe J Y, Ward T Z, et al 2016 Ferroelectric Self-Poling, Switching, and Monoclinic Domain Configuration in BiFeO3 Thin Films *Adv. Funct. Mater.* **26** 5166–73.
[319] Wang J, Wong K H, Chan H L W, Choy C L 2004 Composition control and electrical properties of PMN-PT thin films around the morphotropic boundary *Appl. Phys. A* **79** 551–6.
[320] Luo Y, Li X, Chang L, Gao W, Yuan G, Yin J, et al 2013 Upward ferroelectric self-poling in (001) oriented PbZr0. 2Ti0. 8O3 epitaxial films with compressive strain *Aip Adv.* **3** 122101.
[321] Yang J H, Ryu T, Lansac Y, Jang Y H, Lee B H 2016 Shear stress-induced enhancement of the piezoelectric properties of PVDF-TrFE thin films *Org. Electron.* **28** 67–72.
[322] Maji S, Sarkar P K, Aggarwal L, Ghosh S K, Mandal D, Sheet G, et al 2015 Self-oriented β-crystalline phase in the polyvinylidene fluoride ferroelectric and piezo-sensitive ultrathin Langmuir-Schaefer film. *Phys. Chem.*

Chem. Phys. **17** 8159–65.
[323] Liu J, Zhao Q, Dong Y, Sun X, Hu Z, Dong H, et al 2020 Self-polarized poly (vinylidene fluoride) ultrathin film and its piezo/ferroelectric properties *ACS Appl. Mater. Interfaces* **12** 29818–25.
[324] Li W, Tang G, Zhang G, Jafri H M, Zhou J, Liu D, et al 2021 Improper molecular ferroelectrics with simultaneous ultrahigh pyroelectricity and figures of merit *Sci. Adv.* **7** eabe3068.
[325] Zou R, Guo X, Yang J, Li D, Peng F, Zhang L, et al 2009 Selective etching of gold nanorods by ferric chloride at room temperature *CrystEngComm* **11** 2797–803.
[326] Guo Y, Kakimoto K, Ohsato H 2004 Structure and electrical properties of lead-free (Na0. 5K0. 5) NbO3-BaTiO3 ceramics *Jpn. J. Appl. Phys.* **43** 6662.
[327] Huan Y, Wang X, Fang J, Li L 2013 Grain size effects on piezoelectric properties and domain structure of BaTiO 3 ceramics prepared by two-step sintering *J. Am. Ceram. Soc.* **96** 3369–71.
[328] Ghosh D, Sakata A, Carter J, Thomas P A, Han H, Nino J C, et al 2014 Domain wall displacement is the origin of superior permittivity and piezoelectricity in BaTiO3 at intermediate grain sizes *Adv. Funct. Mater.* **24** 885–96.
[329] Arlt G, Hennings D, De With G 1985 Dielectric properties of fine-grained barium titanate ceramics *J. Appl. Phys.* **58** 1619–25.
[330] Waqar M, Wu H, Chen J, Yao K, Wang J 2022 Evolution from Lead-Based to Lead-Free Piezoelectrics: Engineering of Lattices, Domains, Boundaries, and Defects Leading to Giant Response *Adv. Mater.* **34** 2106845.
[331] Li D, Zhao X, Zhao H, Dong X, Long L, Zheng L 2018 Construction of Magnetoelectric Composites with a Large Room-Temperature Magnetoelectric Response through Molecular–Ionic Ferroelectrics *Adv. Mater.* **30** 1803716.
[332] Dong X, Fang X, Lv M, Lin B, Zhang S, Ding J, et al 2015 Improvement of the humidity stability of organic–inorganic perovskite solar cells using ultrathin Al 2 O 3 layers prepared by atomic layer deposition *J. Mater. Chem. A* **3** 5360–7.
[333] Hu Y, Parida K, Zhang H, Wang X, Li Y, Zhou X, et al 2022 Bond engineering of molecular ferroelectrics renders soft and high-performance piezoelectric energy harvesting materials *Nat. Commun.* **13** 1–10.
[334] Deswal S, Singh S K, Rambabu P, Kulkarni P, Vaitheeswaran G, Praveenkumar B, et al 2019 Flexible composite energy harvesters from ferroelectric A2MX4-type hybrid halogenometallates *Chem. Mater.* **31** 4545–52.
[335] Deswal S, Panday R, Naphade D R, Dixit P, Praveenkumar B, Zaręba J K, et al 2022 Efficient Piezoelectric Energy Harvesting from a Discrete Hybrid Bismuth Bromide Ferroelectric Templated by Phosphonium Cation *Chem. Eur. J.* e202200751.